Anomalous Structural Variations in III-Nitride Nanowire Heterostructures and Their Corresponding Optical Properties

Anomalous Structural Variations in III-Nitride Nanowire Heterostructures and Their Corresponding Optical Properties

by

Steffi Yee-Mei Woo, B.Eng.Society, M.A.Sc.

A Thesis
Submitted to the School of Graduate Studies
in Partial Fulfillment of the Requirements for the degree of
Doctor of Philosophy

Doctor of Philosophy (2017) (McMaster University)
(Materials Engineering) Hamilton, Ontario, Canada

TITLE:	Anomalous Structural Variations in III-Nitride Nanowire Heterostructures and Their Corresponding Optical Properties
AUTHOR:	Steffi Yee-Mei Woo, B.Eng.Society, M.A.Sc. (McMaster University)
SUPERVISOR:	Professor Gianluigi A. Botton
NUMBER OF PAGES:	xiv, 184

The thing about writing is
I can't tell if it's healing
or destroying me

Rupi Kaur, *milk and honey*

Abstract

Ternary InGaN and AlGaN alloys have been sought after for the application of various optoelectronic devices spanning a large spectral range between the deep ultraviolet and infrared, including light-emitting diodes, and laser diodes. Their non-ideal alloy mixing, and differences in bond energy and in adatom diffusion are established as the cause for various types of nanoscale compositional inhomogeneity commonly observed in nitride thin films. Growth in a nanowire geometry can overcome the phase separation, surface segregation, and chemical ordering by providing enhanced strain relaxation of the large lattice mismatch at the free surfaces. In this dissertation, the spectral and spatial luminescence distributions of ternary III-N alloy nanowire heterostructures are investigated and correlated to structural and chemical properties with scanning transmission electron microscopy.

Quantitative elemental mapping of InGaN/GaN dot-in-a-wire structures using electron energy-loss spectroscopy revealed compositional non-uniformity between successive quantum dots. Local strain mapping of the heterostructure showed a dependence of the incorporation of indium on the magnitude of the out-of-plane compressive strain within the underlying GaN barrier layer. Cathodoluminescence spectroscopy on individual nanowires presented diverse emission properties, nevertheless, the In-content variability could be directly correlated to the broad range of peak emission energies.

Atomic-level chemical ordering within the InGaN was then reported, and attributed to the faceted growth surface in nanowires that promotes preferential site incorporation by In-atoms that allows for better strain relaxation. Distinct atomic-scale alloy inhomogeneities were also investigated in AlGaN nanowires, which evidenced spatial localization of carriers taking place at the resulting energy band fluctuations. A high spectral density of narrow emission lines arose from such compositional modulations, whose luminescence behaviours exhibit a dependence on the nature of the compositional fluctuations from which they originate.

Acknowledgements

I consider myself very fortunate to have crossed paths with many individuals who have been influential to me in one way or another. This dissertation would not be the same (likely not even completed successfully) without them, and most definitely this Ph.D. journey of mine would not have been the same without them. I hope that with these simple words, I can convey my sentiment and begin to express my deepest gratitude for all their support.

First and foremost, I would like to thank my supervisor, Prof. Gianluigi Botton. I am truly grateful for the many opportunities he made available to me throughout my Ph.D. I greatly appreciate his support and encouragement in my many (sometimes far-fetched) endeavours, and gave me free rein to follow what inspired me most. This includes not one, but two research exchanges and other stopover visits abroad to chase what I hoped to seek.

My supervisory committee members, Profs. John Preston and Ray LaPierre, for their insight and pushing me beyond my perspective throughout the years. Prof. Preston, in particular, for his patience and sharing pieces of sage wisdom that will continue to resonant.

I would especially like to thank my collaborators, Prof. Zetian Mi and members of his research group from McGill University, in particular Drs. Hieu Nguyen, Songrui Zhao, Tony (Shizhao) Fan, Binh Le, and David Laleyan. It has been such an honour to work with such an inventive and inspiring group of people, whose ingenuity are beyond what I can ever imagine. I have been so fortunate to have the opportunity to explore materials that hold so much beauty and mystery.

My research group members, past and present, who have made my time as a Ph.D. student more bearable at the worst of times, and wholeheartedly unforgettable at the best of times. Thank you all for the joy and laughter, comaraderie for venting, being taste testers for my baked goods, and all the wonderful memories. Specific mentions include: Matthieu Bugnet, David Rossouw, Andrew Scullion, Sam Stambula, Alex Pofelski, Hanshuo Liu, Edson Bellido, Sagar Prabhudev, Isobel Bicket, Nicolas Gauquelin, Sherri Hadian. I am forever indebted to Matthieu for being a wonderful teacher while training me on the instruments and helping me fine-tune my skills, and Nicolas for performing with me my first experiments that catalyzed some of my early work.

The technical staff of the CCEM who keeps everything working smoothly behind the scene. Andreas Korinek and Andy Duft for keeping the microscopes in working order, and their willingness to help with troubleshooting and fixing bugs. Julia Huang and Travis Casagrande for the FIB preparation assistance. Andy especially for our many discussions on gastronomy and model building; it is always uplifting to see his cheery and friendly face in the CCEM. Travis, in addition for the softball, trivia and gamesnight fun over the years.

Special thanks to the STEM group at the LPS in Orsay, who made me feel welcome during my exchange and allowed me to refuel my curiosity and motivation during a difficult time period. Dr. Mathieu Kociak, for his infectious enthusiasm, and for relentlessly pushing during our early experiments together. Most of all, for showing interest in my ideas, and letting me find refuge within the STEM group to explore those ideas during a time in my Ph.D. when I needed it the most. Prof. Odile Stéphan for the gracious hospitality during my visits to Orsay, welcoming and trusting me to tinker with their one-of-a-kind tools. Dr. Luiz Tizei, for his guidance and reassurance, and also for his friendship both inside and outside the lab. I look forward to more (anti-)bunching together in our near future!

Last but not least, I would like to thank my family and friends, who have been a constant source of encouragement and moral support for this venture outside of the lab. Matthieu, for continuously supporting me every step of the way. Without whom, I am not sure that we would have arrived here at these pages of my Ph.D. thesis today. I do not know where this blind faith you have in me comes from, but thank you for teaching me to believe in myself when I didn't know how to. Thank you for giving me the courage to dream bigger than I would have ever allowed myself otherwise, and for never letting me give up on those dreams. Paige, despite being timezones away, still manages to find time to hear me w(h)ine. Priscilla and Cordelia, our friendship where time stands still, for reminding me where I came from, such that I can be proud of how far I've come. Charlie, for his fuzzy companionship during the thesis writing. Finally, I wish to thank my parents for their countless sacrifices, neverending patience, and sixth-sense for when something could simply be soothed by a home-cooked meal. It is because of their encouragement that I could continue working hard and make it this far.

To my parents, with love and gratitude

Contents

List of Figures

List of Tables

Chapter 1

Introduction

In response to the growing demand for energy resources given the ongoing global development and the depleting supply of natural resources, more sustainable ways to harvest and utilize energy need to be sought. Remaining at the forefront of technological relevance over the last few decades has been solid-state technologies based on group III-V compound semiconductors. A short list of suitable optoelectronic applications includes high-efficiency solid-state lighting and displays, photovoltaics, laser diodes, and high-power electronics. The group III-nitride materials system has enormous potential for various optoelectronic devices, but remains the top material of choice as the next generation of solid-state lighting devices with improved efficiency and longevity [1]. Heteroepitaxy of III-N materials into planar thin film device structures faces some fundamental challenges as no single lattice-matched native substrate exists. Highly lattice-mismatched interfaces continue to be the major roadblock in the growth of high quality planar thin films, as they can lead to structural defects that are detrimental to device performance. III-N materials are notorious for having very high density of dislocation from the plastic relaxation of mismatch strain.

The growth of semiconductor nanostructures, inclusive of nanowires, nanorods, and nanocolumns, offers a promising alternative to the high density of dislocations in planar structures. Nanowires have high surface-to-volume ratios and give rise to additional free side surfaces for lateral strain relaxation. The small cross-sectional interface allows for coherent elastic relaxation from biaxial strain for axial heterostructures [2], as the critical thickness for plastic relaxation is much larger in this type of geometry [3]. The small nanowire cross-section also lifts many limitations on the choice of (foreign) substrates, because remnant misfit dislocations are generally confined to the interfacial region or bent towards free surfaces. Residual strains are greatly reduced along the nanowire growth axis and the lattice eventually becomes fully relaxed. The use of silicon as substrate is an economical alternative to the sapphire commonly used for planar growth. Moreover, the monolithic integration of

III-V devices with the well-established silicon integrated circuitry technology is particularly attractive to increase functionality.

Focusing on InGaN/GaN quantum well (QW) structures for light-emitting diodes (LEDs) application already available in the market, the luminous efficiency drops significantly towards longer wavelengths as lattice strain builds from increasing the indium content. The two main limitations on the emission in (In,Ga)N materials has been nanoscale alloy inhomogeneity, and the generation of polarization-induced internal electric fields. However, the former has also been proposed as the reason for the exceptional luminescence efficiency in InGaN planar structures despite the high defect density. A topic continuing to receive significant attention is the role of nanoscale potential fluctuations as carrier localization centres in InGaN [4, 5], which provide a barrier against diffusion of carriers towards dislocations and other non-radiative recombination sites.

Alternatively, incorporation of similar InGaN/GaN heterostructures into nanowires can take advantage of the elastic strain relaxation to reduce the effects of piezoelectric polarization. From a broader prospective, it would be possible to extend the colour tunability across the entire visible spectral range, such that multi-coloured emitters can be realized within one material system integrated on a single chip [6, 7]. Different research groups have taken this direction in recent years, reporting on the growth of axial InGaN insertions within GaN nanowires utilizing both bottom-up and top-down approaches by molecular beam epitaxy and metalorganic chemical vapour deposition [8–16]. Some studies cite insignificant internal piezoelectric fields from the absence of the quantum-confined Stark effect due to the enhanced strain relaxation within nanowires [9, 11, 17–20].

The nanowire geometry does, however, have its own additional shortcomings. Self-organized nanowires from bottom-up epitaxy inevitably suffer from variability in nanowire size (diameter and length) or composition that are extremely sensitive to growth conditions and the surrounding environment. Negative contributions from surface effects are also emphasized in nanowires, including the surface depletion layer [21], and inhomogeneous lateral strain profile [22, 23]. Luminescence spectroscopy demonstrates that emission peaks from nanowire ensembles are very broad compared to conventional thin film structures [17]. The emission from a nanowire ensemble represents a superposition of spectra from single nanowires, thus the broad linewidth is likely caused by slight fluctuations in emission characteristics between individual nanowires related to composition and/or strain. It is therefore necessary to carry-out luminescence spectroscopy on single nanowires, in order to truly investigate the physical origin of spectral features.

Single nanowire spectroscopy, such as micro-photoluminescence or cathodoluminescence in a scanning electron microscope, can be technically challenging, let alone have sufficient

spatial resolution to gain information on the internal structure. Based on these considerations, it is advantageous to perform such investigations in a scanning transmission electron microscope where the high spatial resolution and the available analytical signals can provide additional insight. The correlation of optical properties to structural and chemical information at the nanoscale can uncover mechanisms governing the luminescence characteristics in individual InGaN/GaN nanowire heterostructures.

1.1 Thesis Overview

This thesis is structured as follows. To begin, the background fundamental concepts underlying this work are introduced in the remainder of Chapter 1. Namely, the discussion covers the usage of III-N materials for LED device application from a historical perspective, crystal structures of III-N semiconductors, spontaneous and piezoelectric polarization fields, effects of ternary InGaN alloys on carrier localization, as well as fundamentals of scanning transmission electron microscopy.

The experimental results portion of the thesis starts in Chapter 2 with discussions on the relationship between strain state and indium incorporation during the growth of InGaN/GaN dot-in-a-wire heterostructures. After which in Chapter 3, atomic-level chemical ordering of InGaN alloys are thoroughly investigated in similar InGaN/GaN dot-in-a-wire heterostructures. Steering towards local luminescence properties from cathodoluminescence spectroscopy, Chapter 4 encompasses the correlation of structural and chemical properties to optical properties in individual InGaN/(Al)GaN dot-in-a-wires. Shifting gears in Chapter 5 to focus on AlGaN *p-i-n* homojunction nanowires, where the influence of sub-nanoscale alloy (in)homogeneity on carrier localization varying with Al-composition is examined. Lastly, Chapter 6 summarizes the conclusions from this thesis and gives a future perspective beyond this work.

1.2 III-Nitride Materials for Light-Emitting Diodes

Wide-bandgap GaN and Ga-rich InGaN ternary alloys, with bandgap energies covering the near-ultraviolet (UV) to the blue-green, is the primary material system currently dominating solid-state lighting and laser diode technologies. The group III-nitride materials system as a whole has enormous potential in the application of optoelectronic devices [1]. As their direct bandgap energies can span from the infrared (IR) to the deep within the UV wavelengths [24], ranging from 0.64 eV for InN, 3.42 eV for GaN, to 6.2 eV for AlN as shown in Figure 1.1. A variety of devices that III-N based compounds have received tremendous inter-

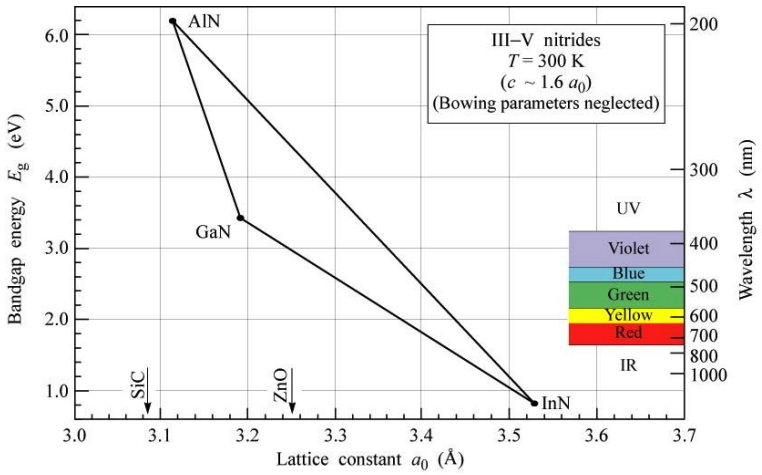

Figure 1.1: Bandgap energy versus lattice constant plot of III-nitride semiconductors at room temperature. From Schubert [25].

est for includes colour-tunable light-emitting diodes (LEDs) and laser diodes, photocatalytic generation of hydrogen gas, and photovoltaics. Particular emphasis has been placed on III-N materials to improving the efficiency and longevity of solid-state lighting devices and display technology [1]. The bandgap of InGaN alloys can provide complete coverage of the entire visible spectrum, thereby offering the possibility to fabricate full-colour optical devices with high quantum efficiency and tunable continuously-direct bandgaps within a single material class. However, there are still a number of fundamental obstacles that make the realization of In-rich InGaN in the active region of devices challenging.

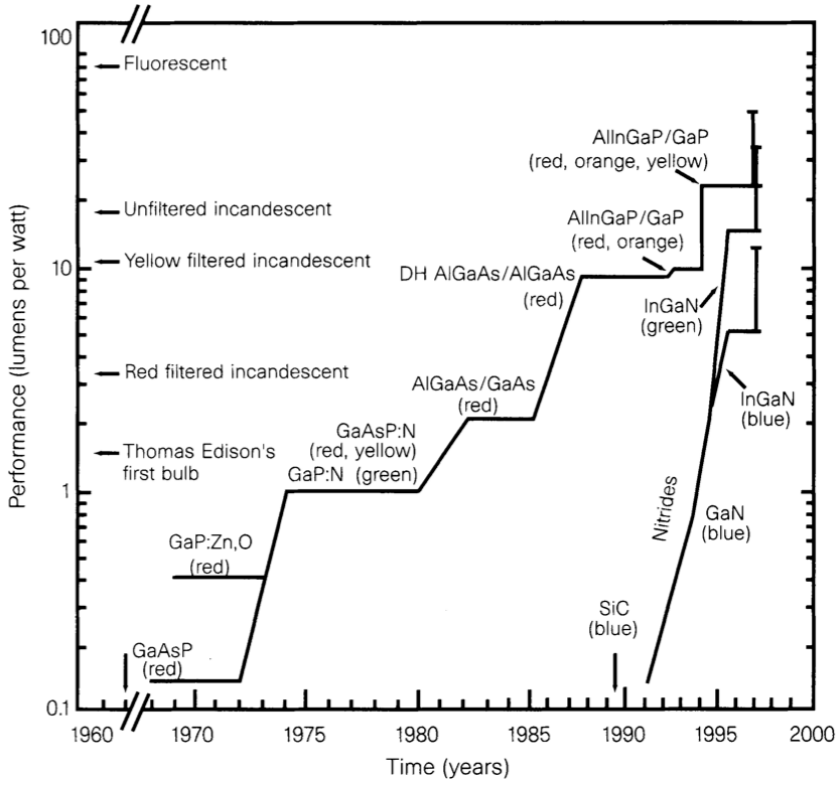

Figure 1.2: The evolution in performance of visible LEDs, where arsenides and phosphides dominate the red-to-yellow range, and nitrides have taken over the green-to-blue range. From Ponce and Bour [1].

The first report of III-N materials for successful commercially-viable application as LEDs was the use of InGaN in the active region as the first high-efficiency blue LED by Nakamura et al. [26]. Since then, this class of materials has attracted a lot of attention for lighting application alone, as it has a broadly appealing range of optical properties. A majority of the commercially important LEDs in the visible to IR spectral range (∼450 – 1500 nm) are made of III-V compound semiconductor thin films, and the evolution of their performance is illustrated in Figure 1.2. Aside from needing the large direct bandgaps to achieve the desired emission wavelengths for enhanced emission efficiency, high reliability, stability and high speed are also desirable properties for commercial application. III-N materials also exhibit very strong chemical bonding that makes them resilient against degradation under high current injection conditions and intense light illumination (common within the active regions of the device) [1].

The external quantum efficiency (EQE, the ratio of photons generated per injected electron) of LEDs for multiple III-V compounds (both phosphides and nitrides) suffer a significant drop at the green wavelengths (see Figure 1.3). Ironically, the 500 – 550 nm wavelengths in the yellow-green part of the visible spectrum coincide with the peak of the human eye sensitivity response [27], and has been dubbed the "green gap". The loss in quantum efficiency of green emission in III-Ps, namely GaP and AlGaInP, is due to the material's indirect bandgap and the direct-indirect bandgap transition from additional alloying with AlP and GaP, respectively. This makes GaP and AlGaInP devices more susceptible to thermal quenching of emission because electrons can be thermally excited into the secondary indirect gap valley, limiting the practical range to orange wavelengths. Additionally this quaternary system is also sensitive to atomic-ordering, where the non-random distribution

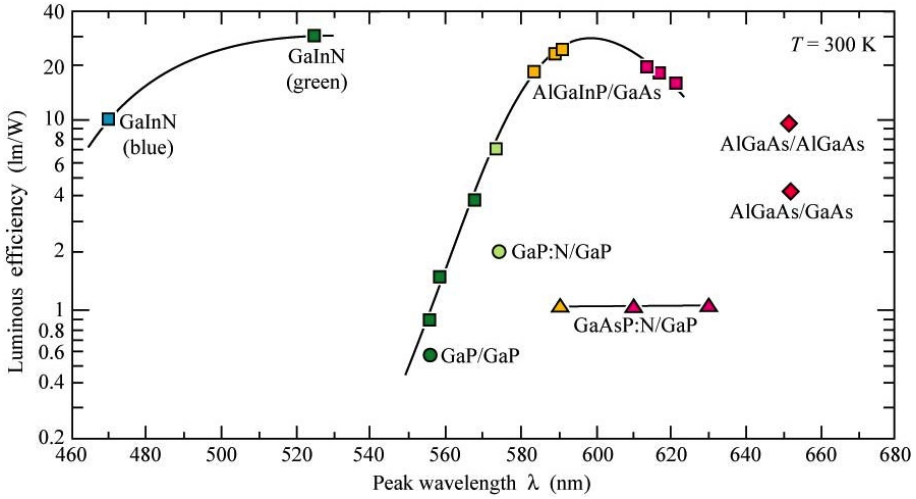

Figure 1.3: Overview of luminous efficiency of visible LEDs made from arsenide, phosphide, and nitride materials at room-temperature. From Schubert [25].

Table 1.1: Lattice parameters [30], thermal expansion coefficients for wurtzite binaries of AlN, GaN, InN [29], and common substrates such as sapphire, SiC and Si [31].

Parameters	AlN	GaN	InN	Sapphire	6H-SiC	Si
a (Å)	3.112	3.189	3.545	4.758	3.08	5.4301
c (Å)	4.982	5.185	5.703	12.991	15.12	*(cubic)*
$\Delta a/a$ (10^{-6}/K)	4.2	5.6	3.8	7.5	4.2	3.59
$\Delta c/c$ (10^{-6}/K)	5.3	3.2	2.9	8.5	4.68	*(cubic)*

of cations within the lattice can lower the effective bandgap [28]. The drop in efficiencies for emission at green and longer wavelengths in InGaN is attributed to multiple factors, some of which are growth-related and/or intrinsic to the material properties. This includes the spinodal decomposition of In-rich InGaN (*cf.* Section 1.4), polarization-induced quantum-confined Stark effect (*cf.* Section 1.3.4.3), and non-radiative recombination at native defects [29].

1.2.1 Group III-Nitride Material Growth Issues

Although GaN-based optoelectronic devices have already been commercialized with great success, such as the widespread use of a 405 nm "blue" laser diode in the Blu-ray optical storage media technology and phosphor-converted white LEDs by combining high-brightness blue InGaN LEDs with cerium-doped yttrium aluminum garnet (YAG:Ce) phosphors; some fundamental issues remain unsolved. A major limitation is the availability of suitable substrates for facile good quality crystal growth. Existing device structures of III-N materials are typically grown as planar thin films on costly substrates as no single lattice-matched native substrate of sufficient size exists. Firstly, the growth of nitride materials are done at high temperatures due to their strong chemical bonding nature, limiting the choice of suitable substrates to those that are stable at such elevated temperatures. Secondly, the most commonly used substrates, sapphire (α-Al_2O_3) and silicon carbide (6H-SiC), are highly mismatched in lattice parameters and thermal expansion coefficients with the nitride materials, as summarized in Table 1.1. Therefore the large lattice mismatch induces high dislocation densities or accumulation of thermal stress that leads to severe cracking. To this day, the combination of the two aforementioned challenges still contributes to the difficulty in growing high-quality epilayers of III-N materials.

The first nitride thin films had rough surfaces and cracking that were attributed to three-dimensional nucleation, due to the poor coverage and wetting of the substrate during growth. Two-dimensional growth mode was achieved after the introduction of a low-temperature growth of AlN as a buffer layer [32, 33]. Nevertheless, the resulting epilayers

have a high density of structural defects, including threading dislocations and stacking faults (more details in Section 1.3.3), both of which are known to have detrimental effects on optoelectronic properties of semiconductor materials. Despite these negative predictions, efficient GaN-based LED structures with dislocation densities as high as $10^{10}/cm^2$ (six orders of magnitude higher than other materials typically used for LED application) have been reported [1] , showing a significantly higher tolerance to dislocation density.

1.2.2 Device Challenges

The prospects of GaN-based materials as high-efficiency and high-brightness LEDs were recognized early on. However, research advancement was greatly hampered for many decades due to the combination of two attributes: i) the lack of *p*-*n* junctions due to poor *p*-type doping in III-Ns, and ii) poor crystalline quality due to the lack of native substrates. Several key breakthroughs in areas of materials design, synthesis, and fabrication of III-N system reignited research activity in GaN-based LEDs and laser diodes. For the former, this includes the successful demonstration of low resistivity *p*-type doping in GaN by activation of Mg-dopants induced by low-energy electron-beam irradiation (LEEBI) [34], and the eventual more reliable and reproducible method of dopant activation under high-temperature thermal annealing at 900 °C in a N_2 atmosphere [35]. For the growth of GaN on sapphire (0001) substrates by metalorganic chemical vapour deposition (MOCVD), the implementation of a two-step growth method involving a low-temperature AlN [32, 33] or GaN [36] buffer layer, the development of a two-flow MOCVD reactor to increase reactant flow to the growth surface [37], were pivotal to improving crystalline quality and wafer uniformity.

1.2.2.1 Physics of Semiconductor LEDs

LEDs as well as laser diodes fall under the general class of optoelectronic devices, in which an electrical-to-optical signal conversion is made possible by a *p*-*n* junction. LEDs emit spontaneous radiation, while laser diodes emit stimulated emission under suitable forward bias conditions. Under forward bias, electrons from the *n*-side and holes from the *p*-side of the *p*-*n* junction are injected into the junction. Recombination of these minority carriers with the majority carriers at the *p*-*n* junction produce a photon with energy corresponding to the bandgap of the semiconductor as per Figure 1.4. Such a process that generates light emission by electronic excitation is called *electroluminescence*, contrary to the thermal radiation of the tungsten filament in incandescent lamps and plasma discharge in fluorescent lights. The electronic transition pathways that lead to light emission are via a radiative recombination process, which is simultaneously competing with parallel non-radiative recombination

processes that can produce phonons or heating of the lattice. The main types of radiative recombination processes include band-to-band recombination, the dominant mechanism in direct bandgap semiconductors, excitonic recombination, and the capture and recombination of electrons and holes at highly localized luminescent (impurity) centres.

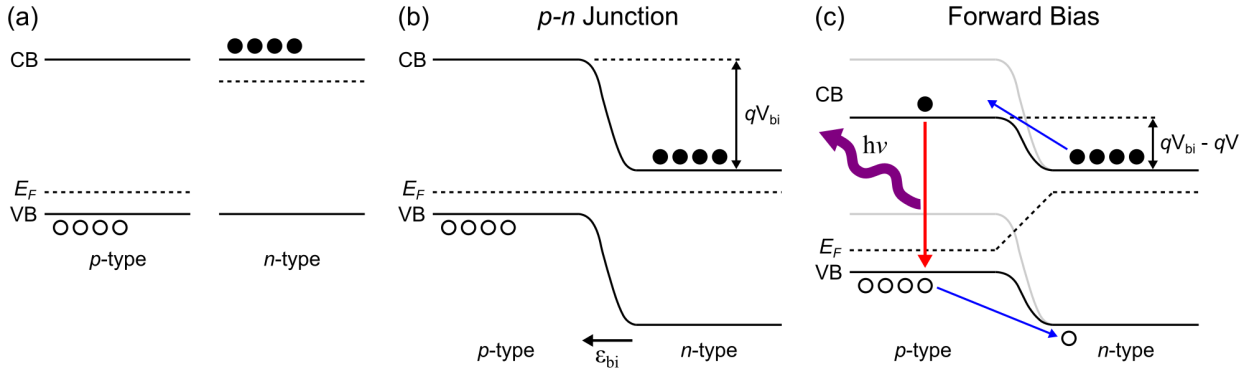

Figure 1.4: **(a)** Band structure of p- and n-type. Energy band diagram of p-n homojunction **(b)** under zero bias with Fermi level (E_F) aligned, and **(c)** under forward bias.

The probability for the interband radiative transition in a direct bandgap material is high because the conduction band minima and the valence band maxima have the same momentum, such that momentum is conserved upon recombination. Excess carrier density of electrons and holes must be equal to maintain charge neutrality after continuous injection of carriers. Therefore the excess carrier density ΔN is found to decrease exponentially from an initial excess carrier density ΔN_o with time relative to a characteristic recombination lifetime τ shown in Equation (1.1). The recombination lifetime contains both a radiative lifetime τ_r and non-radiative lifetime τ_{nr} shown in Equation (1.2). The internal quantum efficiency (IQE, η_{int}) is defined as the fraction of excited carriers that recombine radiatively to the total recombination, and can be expressed in terms of the ratio of the radiative to total recombination rates as given in Equation (1.3). It is desirable to have a short τ_r and long τ_{nr} such that the quantum efficiency approaches unity.

$$\Delta N = \Delta N_o \, exp\Big(- \frac{t}{\tau} \Big) \tag{1.1}$$

$$\frac{1}{\tau} = \frac{1}{\tau_{nr}} + \frac{1}{\tau_r} \tag{1.2}$$

$$\eta_{int} = \frac{{\tau_r}^{-1}}{{\tau_{nr}}^{-1} + {\tau_r}^{-1}} = \frac{\tau_{nr}}{\tau_{nr} + \tau_r} \tag{1.3}$$

1.2.2.2 Efficiency Droop

The internal quantum efficiency (IQE) can also be defined as the fraction of carriers in the active region that recombines through the process of photon emission [38]. Another relevant benchmark measure for LED efficiency is the external quantum efficiency (EQE)—the ratio of photons out per injected electron. EQE (η_{ext}) is the product of the current injection efficiency η_{inj}, radiative efficiency η_{int}, and light extraction efficiency η_{out} [27]. The current injection efficiency η_{inj} is defined as the fraction of injected current that recombine in the active region [27]. It is typical of LEDs of III-N materials, which is unlike other materials that have longer wavelengths, to experience a drastic decrease in its IQE (and EQE) with increasing injection current. This effect is known as the *efficiency droop* [39], where IQE peaks at low pump currents (<10 A/cm^2), followed by a significant gradual drop with increasing current density. This means that with increasing current densities, the number of carriers participating in non-radiative recombination increases more drastically than those participating in radiative recombination [38].

1.2.2.3 Auger Recombination Losses

Auger recombination in InGaN QWs has been a favourable proposed mechanism for efficiency droop, and regarded as the primary non-radiative recombination path for carriers at typical LED operating currents [40]. Auger recombination is associated with the loss of carriers to the dominant direct intraband process, and other indirect phonon-, disorder-, defect-assisted processes. However, the Auger losses through all the aforementioned means are debatably too weak, and their rates too low, to be responsible for the droop [38]. Furthermore, the evidence of relatively defect-free InGaN nanowires that show little to no significant droop up to 400 A/cm^2 [41]. This hinted at the presence of defects in planar quantum well (QW) structures, as well as the presence of local accumulation of carriers from an inhomogeneous indium distribution and QW width fluctuations [4] to be contributing factors during carrier delocalization. The thermal activation of defects with increasing temperature and trends in IQE that follow have also been reported and modeled according to a proposed density-activated defect recombination mechanism [38]. The model suggests that Auger losses decrease strongly with temperature, which is contrary to the intuitive assumption according to the usual temperature-activated dependence. More recent evidence of detecting Auger-electron emission concurrent to the onset of droop in InGaN/GaN LEDs [42] further supports Auger recombination as the dominant mechanism of efficiency droop.

1.2.2.4 Electron Leakage

Leakage of electrons away from the active region would mean that they do not recombine with holes, let alone recombine radiatively. Polarization fields common in III-N heterostructures lead to bending of the band edge potentials, allowing for the thermionic escape of carriers from the QW into the barrier layer. The much larger hole effective mass in comparison to electron effective mass in III-Ns dictates that the major contributor to carrier leakage will be from electron leakage [43]. Remedies for this problem include the introduction of a higher band gap material as an electron-blocking layer between the active regions and the origin of the holes in the *p*-doped region. The use of a multilayer structure (*e.g.* InGaN/AlGaN/InGaN) as barrier layer for InGaN QWs, in order to cater to appropriate carrier mobility dominance has also been suggested [44]. InGaN and AlGaN possess higher electron and hole mobility, respectively, and therefore appropriately modifying the energy band to minimize the serious energy band tilting in the case of GaN barriers.

1.3 III-Nitride Semiconductors: Material Properties

This section will give an introduction to some of the basic material properties of III-N semiconductors underlying the work presented in this thesis. Starting with the crystal structure and related structural properties, physical properties directly arising from the crystal symmetry, such as the spontaneous and piezoelectric polarization, are introduced. In heterostructures, where polarization discontinuities lead to internal electric fields, which then manifest themselves into the quantum-confined Stark effect.

1.3.1 Crystal Structure

All group III-N compounds can exist in either of two polytypes at ambient conditions, the more common thermodynamically-stable hexagonal wurtzite, and the metastable cubic zinc-blende (also known as sphalerite) crystal structure [31]. The latter cubic structure is analogous to the diamond crystal structure that group IV elements (such as Si and Ge) adopt. The wurtzite and zinc-blende structures are closely related in their bonding and electronic properties, differing only in the bond angle of the second nearest-neighbour. Crystallographically, both structures differs from that of diamond structure in that the two interpenetrating sublattices are exclusively occupied by one of the group III or V elements. Both crystal structures exhibits tetrahedral coordination and has the same configuration of nearest neighbours of the opposite element. Similar to other face-centred cubic and hexagonal close-packed structures, the {111} and (0001) planes are the closest packed planes with stacking sequence

of *ABCABC* and *ABABAB*, respectively.

The wurtzite structure, with basis vectors and coordinate system directions and common crystallographic planes indicated, is represented in Figure 1.5. The hexagonal unit cell is described by two basis vectors, a and c, the basal and axial lattice parameters, respectively. Within the primitive cell (dotted black line in Figure 1.5(a)), group III-atoms are situated at (0,0,0) and $(\frac{1}{3},\frac{2}{3},\frac{1}{2})$ positions, while there are N-atoms at $(0,0,u)$ and $(\frac{1}{3},\frac{2}{3},\frac{1}{2}+u)$. The unit cell-internal parameter, u, describes the interatomic distance between the anion and cation sublattice units, and is approximately $\frac{3}{8}$. The product of uc is defined as the group III-to-group V (cation-anion) bond length along the c-axis direction. The internal parameter u and axial ratio c/a can characterize the slight deviation from an ideal tetrahedron (with most dense hexagonal hard sphere packing) in the wurtzite structure. An ideal value of $u = \frac{3}{8} = 0.375$ or $c/a = \sqrt{\frac{8}{3}} = 1.633$ makes the next nearest tetrahedra the same between wurtzite and zinc-blende structures [27].

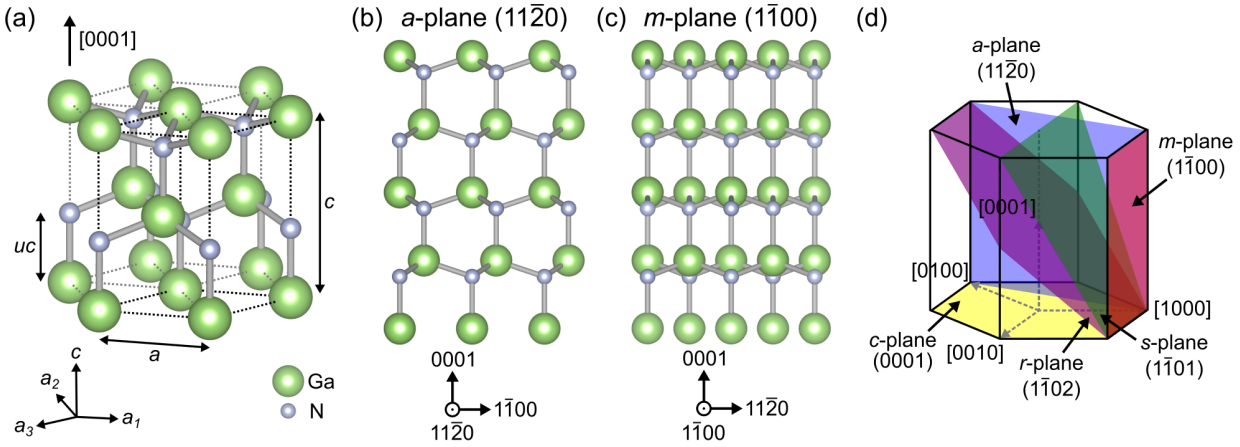

Figure 1.5: **(a)** Crystal structure of wurtzite GaN unit cell showing basis vectors, a, c, u, and its primitive cell outlined in dotted black line. **(b)** Atomic arrangement of a- and m-plane orientations of GaN. **(c)** Schematic illustration of various relevant crystallographic planes in a hexagonal unit cell.

Wurtzite and zinc-blende structures belong to point groups that lack inversion symmetry (or referred to as non-centrosymmetric), such that one or more polar axes exist. Because of this, the bonds are considered polar, meaning [0001] and [000$\bar{1}$] directions in wurtzite (or orthogonal directions such as [110] and [1$\bar{1}$0] in zinc-blende) are not equivalent. Consequently the polarity of the material can be designated based on the bonding from the group III to the group V element. The *6mm* point group of the wurtzite crystal implies that its polar axis lies along the c-axis perpendicular to the basal plane, which is the most common growth direction for wurtzite-GaN. Non-polar a- and m-planes, and semi-polar pyramidal planes (s- and r-planes) indicated in the hexagonal unit cell in Figure 1.5(c) have also been utilized as

growth surfaces.

1.3.2 Crystal Polarity

Non-centrosymmetric crystal structures exhibit different sequence of atomic layering along opposite directions parallel certain crystal axes, allowing crystal polarity to be observed. Polarity in the wurtzite crystal structure of III-N materials refer to the bond directionality of the III–N bond collinear to the *c*-axis within the unit cell. The conventional notation designates the vector from Ga-atom to the nearest-neighbouring N-atom as [0001], such that a structure with growth direction of [0001] is denoted Ga-polar, or Ga-face (Figure 1.6(a)). Conversely, a structure with growth direction of $[000\bar{1}]$ is denoted N-polar, or N-face (Figure 1.6(b)) [45, 46]. The resulting crystal polarity is highly dependent on a combination of factors, including the growth method, choice of substrate, specific growth parameters, the use of buffer layers [47], as well as geometry (planar thin film, or nanowire) to some extent.

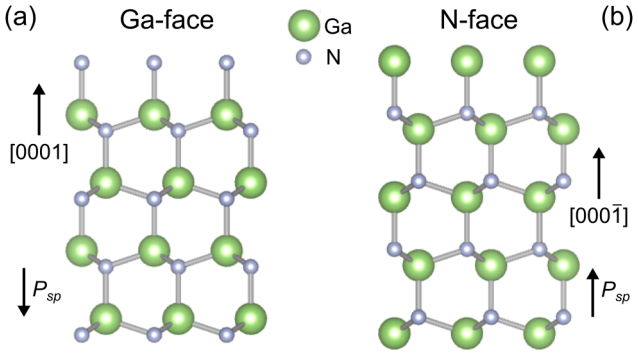

Figure 1.6: Schematic drawing of the wurtzite crystal structure with **(a)** Ga-face and **(b)** N-face GaN.

Reliable methods for polarity assignments in compound semiconductors with (scanning) transmission electron microscopy ((S)TEM) include convergent beam electron diffraction (CBED) with the use of simulated CBED patterns for comparison. Direct STEM-high-angle annular dark-field (HAADF) imaging of the dumbbells (atomic pairs of opposite ionicity) is possible in compound semiconductors with high-Z (atomic number) elements like GaAs and ZnTe; low-Z elements are typically not resolvable using the Z-contrast dependent imaging HAADF mechanism. More recently, annular bright-field (ABF) imaging, beneficial for imaging light elements, has been demonstrated as an effective technique for the local assignments of polarity in compound semiconductor nanowires with low-Z constituents, such as AlN, GaN and ZnO [48, 49].

1.3.3 Formation of Extended Defects

One of the biggest challenges in the epitaxial growth of group III-N semiconductors are the resulting structural defects. This is mainly due to mismatches in lattice parameters between the substrate and film, as well as mismatches in thermal expansion coefficients that become a larger contributing factor at high growth temperatures. III-N thin films are known to have notoriously high dislocation density as a result, up to 10^{10} cm^{-2} [50]. Despite of this, III-N thin film electronic devices have been able to achieve high quantum efficiencies, such that there are reasons to believe the influence of dislocations on device performance is smaller than expected [51]. Existing commercial devices do have difficulties achieving sufficient efficiencies in the yellow-green wavelength region, because of the hardship in obtaining high crystalline quality of high indium composition InGaN [52]. The reasons for this unusual phenomenon are still not fully understood and a topic of debate.

Other higher-dimensional extended crystalline defects tend to occur along the closest packed c-planes of (0001), such as basal plane stacking faults (BSFs), or the related, twinning. BSFs are interruptions in the $ABABAB$ stacking order in the (0001) planes, which are generally the fastest growth planes and the growth direction of the nanowires in most cases. Depending on the interruption, BSFs can be classified into different types under the two main categories of intrinsic (I) or extrinsic (E) [53]: I_1-type with $ABAB\underline{ABC}BCBC$, I_2-type with $ABAB\underline{ABC}ACAC$, I_3-type with $AB\underline{ABCBA}BA$, E-type with $ABAB\underline{C}ABAB$. The introduction of an I_1-, I_2- or E-type BSF induces a zinc-blende-like inclusion, in the sense that the stacking order resembles a zinc-blende (111) $ABCABC$ stacking. The formation energy of I_1-type BSFs are the lowest (10 meV and 19 meV per unit cell area for GaN and InN, respectively [54]). Therefore thermal fluctuations and other growth-related instabilities could easily overcome the thermodynamic barrier and cause BSF formation. Twins correspond to rotational defects, in which the structure is mirrored (180°) about a (0001) and {111} habit plane in wurtzite and zinc-blende structures, respectively. Mg-doping has been shown to have adverse effects on the formation of BSFs and twins within GaN nanowires [55].

1.3.4 Spontaneous and Piezoelectric Polarization Fields

1.3.4.1 Spontaneous Polarization

Group III-N compounds are unique amongst group III-V semiconductors due to the small size of the N-atom, and hence has the largest electronegativity within the group V elements. With nitrogen as the anion, III-N compounds have strong covalent bonds that are ∼20% shorter than other III-Vs [56], thus the metal-nitrogen bond has a highly ionic character. Their low-symmetry wurtzite structure and non-centrosymmetry in addition, results in a

Table 1.2: Lattice parameters [30], axial ratios (ideal value $c/a = 1.633$), internal parameters (ideal value $u = 0.375$), Born effective charge, calculated spontaneous polarization, and piezoelectric coefficients [60] for wurtzite binaries of AlN, GaN, InN.

Parameters	AlN	GaN	InN
a (Å)	3.112	3.189	3.545
c (Å)	4.982	5.185	5.703
c/a	1.601	1.626	1.609
u	0.380	0.376	0.377
Z^* (e)	−2.70	−2.72	−3.02
P_{sp} (C/m^2)	−0.081	−0.029	−0.032
e_{31} (C/m^2)	−0.60	−0.49	−0.57
e_{33} (C/m^2)	1.46	0.73	0.97

large non-zero macroscopic polarization along the polar [0001] direction even in equilibrium under no strain. Spontaneous polarization is due to the abrupt change in electronegativity at heterointerfaces. Each unit cell contains a charge dipole due to the spatial separation of the electron cloud negative charge (which is closer to the N-atom) and the nuclei positive charge, which does not normally manifest in the bulk as neighbouring unit cells will have dipoles that neutralize each other. Discontinuities at surfaces or interfaces lead to dipoles that do not get cancelled out, forming bound sheet charges. In a finite slab of strain-free GaN, the Ga-face and N-face surfaces develop a negative and positive sheet charge, respectively, such that the spontaneous polarization vector P_{sp} is negative and thus points towards the $[000\bar{1}]$ direction [57].

Asymmetric atomic positions within the wurtzite structure also plays a role in the physical origin of the spontaneous polarization. However in actuality, even within an ideal wurtzite structure, non-vanishing spontaneous polarization is still allowed based on symmetry [58, 59], with calculated values not negligible. Cubic zinc-blende structure on the other hand has zero spontaneous polarization in an infinite bulk by definition, and regarded as a reference state. Among the III-N system, the deviation of the c/a ratio or internal parameter u from the ideal ratio in wurtzite structure makes them more susceptible to spontaneous polarization because of the further separation of the positive and negative charge barycentres. Hence the larger this deviation (c/a gets shorter, u gets longer), the stronger the spontaneous polarization, as demonstrated in the P_{sp} values increasing from GaN, InN to AlN in Table 1.2.

1.3.4.2 Piezoelectric Polarization

In addition, heterostructures of these polar materials often tend to exhibit uncompensated strain due to lattice mismatch. When grown along a polar axis, as they generally are, such

strain fields will induce piezoelectric polarization because of the lack of inversion symmetry [61]. Piezoelectric effects in non-centrosymmetric materials such as III-V compound semiconductors can generate internal electric fields, which play a role in the resulting optical properties. This type of phenomenology has been well studied in strained QW layers, and the symmetry of the QWs makes the evaluation of the strain-induced electric field and its effect on the confined electronic states more straightforward [45, 62].

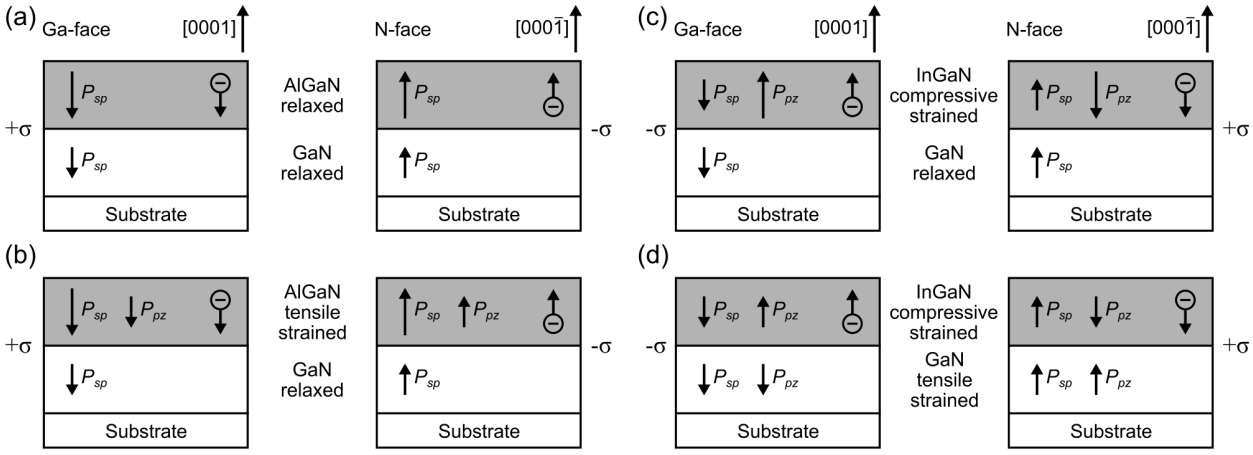

Figure 1.7: Schematic representation comparing various **(a, b)** AlGaN/GaN and **(c, d)** InGaN/GaN heterostructures and the resulting directions of spontaneous polarization and piezoelectric polarization (when applicable) based on the different strain states and crystal polarity. The polarization-induced sheet charge is also indicated. The length of the polarization arrows represent the relative magnitudes.

Calculated values of spontaneous polarization, piezoelectric coefficients for the three binary III-Ns using the Berry-phase approach [60] are summarized in Table 1.2. It should be noted that the piezoelectric constants of III-Ns follow the same sign as II-VI compounds but opposite to other III-Vs, and are about an order of magnitude larger than all other III-V and II-VI compounds. The former can be explained by the high ionicity of III-Ns, as manifested in the large values of effective charge Z^*. Piezoelectric polarization can be calculated from theory with known values for piezoelectric coefficients, elastic constants, strain along the c-axis, and isotropic in-plane strain. The sign of the resultant piezoelectric polarization, in conjunction with the polarity of the strained layer, dictates the direction of the induced piezoelectric field. The directions of spontaneous and piezoelectric polarization may or may not oppose each other, depending on the strain state of the heterostructures, as shown in Figure 1.7. In general relative terms, spontaneous polarization dominates over the piezoelectric polarization in AlGaN/GaN heterstructures, while spontaneous polarization is relatively small in comparison to the sizable strain-induced piezoelectric polarization in InGaN/GaN heterostructures. It is important to note that thermal stresses from the differences in thermal expansion coefficient between the epilayer and substrate can also contribute to

Table 1.3: Rules for defining *jk* in tensor notation by *j* in matrix (Voigt) notation, and *x,y,z* Cartesian coordinate notation for the strain and stress tensor.

Tensor Notation *jk*	11	22	33	23,32	13,31	12,21
Matrix Notation *j*	1	2	3	4	5	6
Cartesian Coordinate Notation	*xx*	*yy*	*zz*	*yz*	*xz*	*xy*

the piezoelectric effect within III-N materials.

The components of piezoelectric polarization vector P_i^{pz} (i = *x,y,z*) can be related to the stress tensor σ_{jk} by Equation (1.4) in tensor notation, where d_{ijk} is the piezoelectric moduli tensor (with units of pm/V). Matrix notation can be used to simplify the description such that σ_{jk} is redefined by σ_j as per Equation (1.5) and Table 1.3. Point group (*6mm* for wurtzite) symmetry operations reduce the non-vanishing components of d_{ij} to five, only three of which are independent components (d_{31}, d_{33} and d_{15}) and in matrix form becomes Equation (1.6).

$$P_i^{pz} = \sum_{j=1}^{3}\sum_{k=1}^{3} d_{ijk}\sigma_{jk} \tag{1.4}$$

$$P_i^{pz} = \sum_{j=1}^{3} d_{ij}\sigma_j \tag{1.5}$$

$$\begin{pmatrix} P_1^{pz} \\ P_2^{pz} \\ P_3^{pz} \end{pmatrix} = \begin{pmatrix} 0 & 0 & 0 & 0 & d_{15} & 0 \\ 0 & 0 & 0 & d_{15} & 0 & 0 \\ d_{31} & d_{31} & d_{33} & 0 & 0 & 0 \end{pmatrix} \begin{pmatrix} \sigma_1 \\ \sigma_2 \\ \sigma_3 \\ \sigma_4 \\ \sigma_5 \\ \sigma_6 \end{pmatrix} \tag{1.6}$$

Stress and strain can be interchanged in the piezoelectric polarization vector P_i^{pz}, as stress σ_{ij} and strain ϵ_{kl} are related by Hooke's law (Equation (1.7)), where C_{ijkl} is the stiffness tensor (more commonly referred to as elastic constants). Symmetry of the *6mm* point group reduces the stiffness tensor to a 6×6 matrix with 12 non-vanishing components made up of five independent elastic stiffness constants (C_{11}, C_{12}, C_{13}, C_{33} and C_{44}) as shown in Equation (1.8). Using Equation (1.6) and Equation (1.8), the relationship between piezoelectric polarization P_i^{pz} and strain ϵ_{ij} can be expressed by a matrix of piezoelectric coefficients e_{ij} as shown in Equation (1.9). For a hexagonal structure, the relationship between the non-zero piezoelectric modulus and coefficients are listed in Equation (1.10). Conversion between the tensor notation, matrix (Voigt) notation, and the *x,y,z* Cartesian

coordinate system commonly used to describe lattice strain is detailed in Table 1.3.

$$\sigma_{ij} = C_{ijkl}\epsilon_{kl} \tag{1.7}$$

$$\begin{pmatrix}\sigma_1\\ \sigma_2\\ \sigma_3\\ \sigma_4\\ \sigma_5\\ \sigma_6\end{pmatrix} = \begin{pmatrix} C_{11} & C_{12} & C_{13} & 0 & 0 & 0\\ C_{12} & C_{11} & C_{13} & 0 & 0 & 0\\ C_{13} & C_{13} & C_{33} & 0 & 0 & 0\\ 0 & 0 & 0 & C_{44} & 0 & 0\\ 0 & 0 & 0 & 0 & C_{44} & 0\\ 0 & 0 & 0 & 0 & 0 & \frac{1}{2}(C_{11}-C_{12}) \end{pmatrix} \begin{pmatrix}\epsilon_1\\ \epsilon_2\\ \epsilon_3\\ \epsilon_4\\ \epsilon_5\\ \epsilon_6\end{pmatrix} \tag{1.8}$$

$$\begin{pmatrix}P_1^{pz}\\ P_2^{pz}\\ P_3^{pz}\end{pmatrix} = \begin{pmatrix} 0 & 0 & 0 & 0 & e_{15} & 0\\ 0 & 0 & 0 & e_{15} & 0 & 0\\ e_{31} & e_{31} & e_{33} & 0 & 0 & 0 \end{pmatrix} \begin{pmatrix}\epsilon_{xx}\\ \epsilon_{yy}\\ \epsilon_{zz}\\ \epsilon_{yz}\\ \epsilon_{xz}\\ \epsilon_{xy}\end{pmatrix} = \begin{pmatrix} e_{15}\epsilon_{xz}\\ e_{15}\epsilon_{yz}\\ e_{31}(\epsilon_{xx}+\epsilon_{yy})+e_{33}\epsilon_{zz} \end{pmatrix} \tag{1.9}$$

$$\begin{aligned} e_{kl} &= \sum_{j=1}^{6} d_{kj}C_{jl}; k = 1,2,3; l = 1,...,6\\ e_{31} &= (C_{11}+C_{12})d_{31} + C_{13}d_{33}\\ e_{33} &= 2C_{13}d_{31} + C_{33}d_{33}\\ e_{15} &= C_{44}d_{15} \end{aligned} \tag{1.10}$$

$$P_{pz}^{[0001]} = e_{31}(\epsilon_{xx}+\epsilon_{yy}) + e_{33}\epsilon_{zz} \tag{1.11}$$

The strain tensor in Equation (1.9) encompasses normal components ϵ_{xx}, ϵ_{yy}, ϵ_{zz}, and shear components ϵ_{xy}, ϵ_{xz}, ϵ_{yz}. It is a sufficient approximation to neglect the shear strains in the case of epitaxial growth along low-index orientations, leaving only P_3^{pz} along the polar c-axis direction (Equation (1.11)). For instance, a thin film with relaxed (equilibrium) lattice constant a_0 is grown coherently strained on a lattice-mismatched substrate with lattice constant a_s just along the [0001] direction, such that the deformed lattice constant $a = a_s$. Assuming pseudomorphic growth (such that biaxial strain approximation holds with out-of-plane stress $\sigma_{zz} = 0$), if the in-plane strain is isotropic, it is given by:

$$\epsilon_{xx} = \epsilon_{yy} = (a - a_0)/a_0 \tag{1.12}$$

$$\epsilon_{zz} = -2\frac{C_{13}}{C_{33}}\epsilon_{xx} \tag{1.13}$$

$$P_{pz}^{pseudo} = 2\epsilon_{xx}(e_{31} - e_{33}\frac{C_{13}}{C_{33}}) \tag{1.14}$$

In the case where $a_0 > a_s$, the in-plane strain is compressive, and the out-of-plane strain ϵ_{zz} is tensile due to the Poisson effect related by Equation (1.13) through elastic constants. The pseudomorphic biaxial strain conditions allows to simplify the piezoelectric polarization to Equation (1.14) as a function of only the in-plane strain, piezoelectric coefficients, and elastic constants. Other possible stress state conditions that can be considered include uniaxial ($\sigma_{xx} = \sigma_{yy} = 0$) and hydrostatic stresses (σ_{xx}, σ_{yy}, $\sigma_{zz} \neq 0$).

1.3.4.3 Quantum-Confined Stark Effect

Electric field effects induced by spontaneous and piezoelectric polarization can exert a substantial influence on the concentration, distribution and recombination of free carriers in strained group III-N heterostructures. Observations of Franz-Keldysh-oscillations and Stark-effects in InGaN/GaN and AlGaN/GaN QW structures provide direct evidence for the presence of strong electric fields caused by gradients in spontaneous and piezoelectric polarization. These fields significantly influence the distribution and lifetime of free carriers in InGaN and GaN QWs and can have an important impact on the performance of AlGaN/GaN and InGaN/GaN based optoelectronic devices. For light-emitting applications, fast radiative recombination rates are highly beneficial, however strong polarization fields in III-N materials are susceptible to the quantum-confined Stark effect (QCSE) [4]. The QCSE suggests that electric fields perpendicular to the dimensionally-confined direction changes the potential shape the carriers are subject to, pulling the electrons and holes towards the opposite sides (of the QW, for example, as shown in the schematic in Figure 1.8). This spatial separation of electron and hole wavefunctions in nanostructures reduces the net energy of an electron-hole pair, corresponding to a Stark shift in the exciton absorption [63]. In addition to an observed redshift of the interband transition energy, there is also a strong reduction in the transition oscillator strength (probability of radiative recombination), which leads to an increased radiative recombination lifetime and hence compromises the recombination rate [64]. The transition energy redshift increases with QW thickness, but can also become diminished at increased carrier density within the QW that screens the internal electric field [4].

Time-resolved photoluminescence measurements have been used to demonstrate that the QCSE is greatly reduced in nanowire heterostructures compared to two-dimensional QWs, as explained by a reduction in the piezoelectric polarization in the nanowires [64]. It has been shown using tight-binding methods, that internal fields in nanowires can be screened to a larger extent by the charges that are pulled axially out the top of the nanowire heterostructures [65]. Spontaneous polarization and its effect on optical properties are polarity dependent; therefore polarity determination is important in understanding the confinement and localization of carriers inside heterostructures (*cf.* Figure 1.7). Identifying GaN nanowires grown on Si substrates as N-polar has been crucial in confirming the predictions of charges being pulled out from the top surface of nanowires could minimize the effects of QCSE [46].

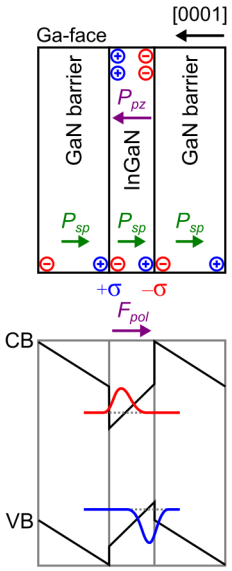

Figure 1.8: Schematic illustration of the spontaneous and piezoelectric polarization directions, and the resulting polarization field (F_{pol}) within a Ga-face InGaN/GaN QW grown on the polar *c*-plane. The energy band diagram due to the field-induced QCSE shows band bending in the conduction band and valence band profiles, the electron and hole wavefunctions (red and blue lines) are also indicated. A 70:30 CB:VB offset ratio is assumed.

1.3.4.4 Internal Fields and Charge Distributions in Nitrides

Due to the strong presence of piezoelectric fields in nitride heterostructures (such as InGaN/GaN QWs) grown along polar directions, with the combination of spontaneous polarization intrinsic to the wurtzite crystal structure, the study of these internal electric fields have been of great interest. Based on *ab initio* methods, the internal field strengths in isolated InGaN QWs have been predicted to be as high as 15 MV/cm [66]. Since the presence of these fields can cause a separation of carriers within the active region due to the QCSE, a better understanding of the nature and strength of the fields, as well as their effect on carrier radiative recombination is fundamentally important. Electron holography, a TEM technique, has been a good prospect for profiling these electrostatic potentials with high-resolution, as first demonstrated by Cherns et al. [67].

The total polarization P is the sum of the spontaneous polarization P_{sp} intrinsic to the wurtzite structure and the strain-induced piezoelectric polarization P_{pz}. The relationship between polarization P and the surface charge density follows Gauss' law, such that the bound charge density $\rho_s = -\nabla P$. If a ternary $A_xB_{1-x}N$ layer with Ga-face polarity grown pseudomorphic to a GaN buffer layer is considered in the following. Firstly, surface charges can be assumed to be completely screened by charge from the ambient or charge surface defects. At the interface of the $A_xB_{1-x}N$/GaN heterostructure, the abruptly changing total polarization leads to a bound polarization charge σ at the interface given by Equation (1.15). If the polarization-induced charge density is positive ($+\sigma$), free (mobile) electrons will tend to accumulate to compensate the polarization, resulting in the formation of a two-dimensional electron gas (2DEG) with sheet carrier concentration of n_s [57]. A very large resulting number of electrons in the range of 10^{13} cm^{-2} due to the polarization charge in the case of AlN/GaN heterostructures is not uncommon.

$$\begin{aligned} P &= P_{sp} + P_{pz} \\ \sigma_{ABN/GaN} &= P_{GaN} - P_{ABN} \\ &= (P^{sp}_{GaN} + P^{pz}_{GaN}) - (P^{sp}_{ABN} + P^{pz}_{ABN}) \end{aligned} \tag{1.15}$$

In the case of a single pseudomorphically-grown InGaN/GaN QW, it can be assumed that the polarization-induced charge at all surfaces are fully screened except for the GaN/InGaN bottom and InGaN/GaN top interfaces. An electric field in the well under a constant field approximation can be described by Equation (1.16), where ϵ_r and ϵ_0 are the dielectric constant and the permittivity of free space, respectively. For a set of $In_{0.25}Ga_{0.75}N$/GaN QWs, the electric field is predicted to be as large as 4.4 MV/cm, which would cause severe band bending to turn the potential distribution from the otherwise square to triangular. A representation of such a QW structure, relating the growth polarity, strain, polarization charges and the polarization-inducted electrostatic fields F_{pol} is sumarized in Figure 1.8. The large InN/GaN lattice mismatch ($\Delta a/a = 11\%$) makes the piezoelectric polarization dominant, leading to a polarization field that points from the top to the bottom interface (along $[000\bar{1}]$). The inclined band profile causes the QCSE, leading to the spatial separation of the electron and hole wavefunctions to opposite sides of the quantum well. In addition, the inclined band profile also leads to a redshift of the transition energy, which is dependent on the band discontinuity and band-offset ratio (ΔE_C:ΔE_V) that influence the confinement potentials for electrons and holes.

$$E_{well} = \frac{P^{total}}{\epsilon_0(\epsilon_r^{InGaN} - 1)} = \frac{P_{GaN}^{total} - P_{InGaN}^{total}}{\epsilon_0(\epsilon_r^{InGaN} - 1)} \tag{1.16}$$

1.4 Alloy Effects on Physical Properties

Chemical properties like the composition affect the lattice parameter of a semiconductor alloy, which can be scaled roughly by the use of Vegard's law. Composition can then also indirectly contribute to the strain of a system, particularly in heterostructures. Both composition and strain can be commonly measured in thin films using X-ray diffraction or Raman spectroscopy; however, the contributions from the two components cannot be so easily decoupled. While this task is more achievable at a macroscopic level in combination with techniques such as Rutherford backscattering spectroscopy [68], it is the variations of composition and strain on a nanometer scale that is of greater interest. Superior spatial resolution can be achieved using various methods available from (scanning) transmission electron microscopy ((S)TEM). To investigate strain, there are diffraction techniques such as convergent beam electron diffraction (CBED) [69] and nanobeam electron diffraction (NBED) [70], and imaging techniques such as geometric phase analysis (GPA) [71], peak pairs analysis (PPA) [72], and interferometry techniques like electron holography [73]. Any of these aforementioned techniques alone does not provide the ability to separate contributions from strain and composition, as their evaluation involves the crystal lattice spacing from a reciprocal or real-space perspective, which depends on both components. The integration of electron holography and GPA techniques has been successful in obtaining 0.1% and 5% accuracy in lattice strain and composition, respectively [74, 75].

1.4.1 Phase Segregation and Elemental Distribution

Elemental mapping of composition in InGaN is of special interest, as the existence of composition fluctuations as a result of phase segregation into indium-rich regions remains a topic of ongoing debate [76, 77]. The same chemical instability is also responsible for the various surface segregation [68], and chemical ordering [78, 79] processes commonly observed in both InGaN and AlGaN alloys. All of Chapter 3 is devoted to atomic-level chemical ordering in InGaN alloys, and will be further discussed there. To achieve homogeneity in the growth of InGaN in the form of QWs, it is desirable to try and suppress the phase separation caused by spinodal and binodal decomposition. However, on the other hand, the strong phase separation behaviour of InGaN can actually be advantageous when growing InGaN QD structures [80]. Spinodal and binodal decomposition describe the phase separation of

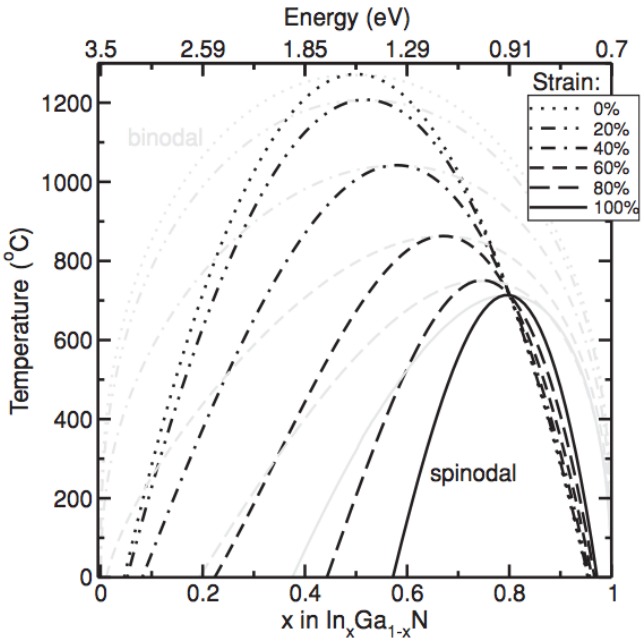

Figure 1.9: Spinodal (black) and binodal (grey) lines calculated using an interaction constant of 25700 J/mol for different strain states of the InGaN layer on *c*-plane GaN, where 0% is completely relaxed and 100% is completely strained laterally to the GaN. From Tessarek et al. [80].

compounds where there is no barrier to nucleation [81], based on the minimization of the Gibbs free energy (G) of the system. Where the binodal line denotes the absolute minima of the Gibbs function of the system ($\partial G/\partial x = 0$), but it does not dictate the spontaneous phase separation unless the spinodal conditions ($\partial^2 G/\partial x^2 = 0$, at points of inflection) are also satisfied. Spontaneous phase separation does not occur in the positive curvature regions of the Gibbs function ($\partial^2 G/\partial x^2 > 0$), as this would indicate local maxima in the free energy curve [82].

The calculated spinodal phase diagram for InGaN has been able to elucidate some insight into the large unstable phase region from the miscibility gap at typical growth temperatures, however, experimental reports are not in full agreement. This disagreement regarding the experimentally observed reduction of the unstable region has been attributed to the presence of strain, common in the growth of the lattice-mismatched InGaN/GaN system [83]. The influence of strain on the InGaN spinodal phase diagram (Figure 1.9), while considering an InGaN layer grown on GaN that can be completely relaxed (0% strain) to completely strained laterally to the GaN substrate (100%), has been calculated by Tessarek et al. [80]. These results suggest a strong dependence of the spinodal decomposition behaviour on the strain state of the material. With increasing strain in the $In_xGa_{1-x}N$ layer, the miscibility gap remains, but the critical temperature of decomposition decreases and shifts towards higher x (higher In-content). Similar tendencies towards spinodal decomposition have also been observed in InAlN alloys [84].

Growth temperature control is crucial in minimizing the compositional instabilities. Due to the weaker bond energy of In–N, the In has a high mobility on the surface during growth,

and can easily be desorbed into the gas phase [80]. Since the composition can be directly related to the optical properties, quantification of the In-content with high spatial resolution is crucial to understanding factors that influence In-incorporation [15], and obtaining controlled emission properties. Small variations in growth temperature (∼20 °C) are sufficient to enhance InGaN phase separation, leading to inhomogeneous broadening and unstable emission characteristics from the formation of clusters with higher In composition [85]. Despite the promising bandgap ranges that can be covered by InGaN ternary alloy alone, spanning the near-UV to the near-IR wavelengths, there are considerable challenges in obtaining high-quality epilayer structures across the entire compositional range.

1.4.2 Origin of Carrier Localization in InGaN Alloys

The InGaN/GaN system at various compositional ranges have demonstrated the presence of a significant Stokes-like shift of 49 meV even at room-temperature [86], which is the redshift of the spontaneous emission peak (from electroluminescence or photoluminescence spectroscopy) compared to its absorption edge (from photovoltage, electroreflectance, or photoluminescence excitation spectroscopy). It differentiates the emission from localized energy tail states and the absorption over the high density of states (DOS) in the conduction band, indicating that carriers or excitons involved in the radiative recombination process in InGaN alloys take place at localized states.

Localization mechanisms in InGaN alloys occurring at varying lengthscales ranging from the atomic-scale to few-to-tens of nanometers have been postulated [87]:

(i) Strong hole localization around –In–N–In– atomic chains and related atomic-scale chemical ordering has been proposed in zinc-blende and wurtzite InGaN from pseudopotential calculations [88, 89] and experimentally demonstrated by positron annihilation spectroscopy [90]. Such –In–N–In– chains can form even within statistically random InGaN alloys with a probability that increases with In-concentration.

(ii) Quantum dot-like In-clustering self-assembled within InGaN alloys were first confirmed by high-resolution TEM imaging and attributed to phase instability [5, 91]. Specifically, the In-rich clusters become strong localization centres for excitons, such that the diffusion to nearby dislocations or trapped by other non-radiative recombination centres is negligible. The hypothesis for preferential carrier capture into efficient localized radiative recombination centres is supported by short radiative lifetimes (τ_r) and long non-radiative lifetimes (τ_{nr}) in InGaN and AlInN thin films [90].

The compositional inhomogeneity and subsequent local bandgap fluctuations has been a controversial topic of interest. Discrepancy from other research groups utilizing different

growth methods and conditions later argued the strong contrast fluctuations in TEM imaging were actually electron-beam damage artifacts [77, 92]. It is expected that such local potential minima in the energy band of the active region are responsible for the high tolerance to threading dislocations in III-N LEDs.

Evidence of various emission behaviours has been proposed to be the outcome of radiative recombination from localized states in InGaN/GaN structures, some of which will be described in the following. Emission spectra of InGaN alloys exhibit much larger broadening than intrinsically from alloy broadening alone [93], suggesting disorder from In-composition and/or local monolayer QW width fluctuations [94]. It should be noted that monolayer thickness fluctuations in binary III-V QWs (*e.g.* GaAs, InP, GaN) that exhibit no compositional inhomogeneity can also provide localized band tail states. The large alloy broadening in (Al,In)GaN alloys can be understood by the small effective Bohr radius of excitons ($a_B \approx 2.7$ – 3.4 nm in GaN [4, 95]), such that excitons are extremely sensitive to local bandgap variations down to these nanometer lengthscales [96]. Additionally, significant blueshift in peak energy has been observed using PL and EL spectroscopy as a function of excitation (power and current, respectively) density. Taking into account the presence of polarization-induced fields in *c*-plane InGaN structures, this spectral non-linearity was attributed to the combined effect of Coulombic screening of the QCSE and band-filling of localized states [4]. Furthermore, anomalous *S*-shape (redshift–blueshift–redshift) temperature-dependence of peak PL emission energy concomitant with spectral narrowing (broadening) during the redshift (blueshift) is characteristic of changes in carrier dynamics in the presence of band tail states. Time-resolved PL measurements also shows increased carrier lifetimes at low-temperatures (below the redshift–blueshift transition), providing sufficient duration for carriers to relax down into and recombine at the lower-energy tail states caused by the potential fluctuations. Carrier lifetimes then see a dramatic decrease in the intermediate temperature regime, explaining the peak energy blueshift and concurrent broadening on the higher energy side [97].

The very low DOS at these localized tail states could explain the large band filling effect and weak localization at low In-composition ($x < 0.15$). The degree of exciton localization enhances significantly with In-composition beyond $x > 0.15$ – 0.2, with deep traps (in the order of 100 – 250 meV based on the measured Stokes-shift [98]). The spectral broadening in this case can be attributed to inhomogeneous broadening due to size and compositional fluctuations in the self-organized quantum dots within InGaN QW layers. As macroscopic optical spectroscopy reflects the properties of an ensemble of such quantum dots whose quantized levels vary with size and potential depth. The small compositional fluctuations in the former low In-composition case leads to mobile excitons within the local potential

minima, as the localized states would not be energetically separated from the extended states at elevated temperatures or high injection conditions.

1.5 Group III-Nitride Nanowire Structures

Exploring these same heterostructure designs in a nanowire geometry on lower cost substrates such as (111)-oriented silicon has demonstrated great success [10, 41]. The alternative of growing devices in a nanowire geometry can lead to more improvements aside from those that are structurally beneficial, such as the additional lateral free surface for improved strain relaxation to minimize the density of threading dislocations. From a device design standpoint, the growth in the nanowire morphology can also provide a new roadmap of unique device structure design possibilities that cannot be achieved easily, let alone in one single growth step, with the conventional planar thin film heterostructure geometry. However, some of the existing challenges with the use of III-N materials do not necessarily disappear, and new obstacles can arise with the introduction of a larger surface to volume ratio, such as the increased non-radiative surface recombination and band bending near the surfaces. The idea of introducing embedded axial heterostructures into nanowires is still at its early stages of development, including an unclear designation as to whether such unique structures would behave like QWs or quantum dots [64]. The electronic properties of such heterostructures are influenced significantly by lateral inhomogeneous distribution of strain, and also carrier concentration induced by band bending at the nanowire surfaces [99].

1.5.1 Self-Organized GaN Nanowire Growth

Semiconductor nanowires can be achieved by direct epitaxial growth (bottom-up) or by post–growth etching (top-down) approaches. Molecular beam epitaxy (MBE), an ultrahigh vacuum physical vapour deposition technique, is the growth method of choice for III-V compounds as it offers a high degree of growth control, even layer thicknesses down to the atomic-scale. A common growth method for nanowires is by vapour-liquid-solid (VLS), where liquid metal droplets (*e.g.* Au, Ni, Fe) deposited first onto the substrate act as a catalyst [100]. The liquid metal droplets get supersaturated with the source species before it precipitates out below the droplet.

The growth of GaN nanowires alternatively can be grown spontaneously and catalyst-free, as referred to as self-induced or self-organized growth mode [101], and has been demonstrated on AlN buffer layers [102, 103] and on Si substrates [104, 105]. Growth parameter of V/III flux ratio much greater than one, *i.e.* nitrogen-rich conditions, is used and enhances the

axial growth rate while simultaneously suppressing the lateral growth rate [106, 107]. Substrate temperature is another critical growth parameter, which governs both the diffusion and the desorption of Ga atoms impinging on the substrate. The self-induced growth of GaN nanowires in radio-frequency (rf) plasma-assisted MBE (PAMBE) is possible within an optimal temperature range of 750 – 830 °C [108]. The growth temperature has to be sufficiently high to promote surface diffusion of adsorbed atoms to the nanowire nuclei, but sufficiently low to limit the desorption of atoms.

The self-induced GaN nanowire growth mechanism is a two-step process: a nucleation phase governed by thermodynamics, followed by a kinetically-driven anisotropic growth phase. The nucleation phase consists of a relatively long incubation period given the low probability of GaN nucleation, during which time a few nm-thick amorphous SiN_x layer forms from the nitridation of the Si substrate [104, 105]. The nanowire nuclei takes on a hexagonal prism shape, terminated by c-plane top surface and m-plane lateral sidewalls to minimize surface energies [103]. The axial growth of GaN nanowires is diffusion-limited, and governed by the differential sticking coefficients on the c- and m-planes [107]. Axial incorporation occurs with adatom species from a combination of direct impingement on the top facet, and impingement then subsequent diffusion along the sidewalls [109]. Adatoms impingent on the sidewalls within the surface diffusion length diffuse to the top surface driven by the lower chemical potential at the top surface [107, 109].

The availability of the reaction species is always higher near the top of the nanowire due to the geometric position of effusion cells and plasma sources in MBE growth chambers and shadowing effects for moderate and high nanowire densities [110]. As a consequence, many self-induced GaN nanowires grown by PAMBE have an inversely tapered geometry, *i.e.* the nanowire diameters increase along the length. Additionally, self-organized GaN tend to exhibit random tilt and twist misorientations and in-plane rotations that inevitably can lead to the formation of defects (low-angle grain boundaries, dislocation network) from coalescence of neighbouring nanowires [111]. Self-induced GaN nanowires are found to grow N-polar on (111)-oriented Si (or specifically on the SiN_x interlayer) [46, 49]; on AlN, the GaN nanowire growth follows the substrate polarity, and is more typically Ga-polar or of mixed polarity [112, 113].

1.6 Scanning Transmission Electron Microscopy

Electron microscopy has played an important role within understanding the carrier localization phenomena in InGaN alloys. The superior spatial resolution has made scanning electron microscopy (SEM) and (scanning) transmission electron microscopy ((S)TEM) versatile char-

acterization techniques of choice to investigate the structure, morphology and chemistry for various materials including III-N semiconductors. In this section is an overview of the established STEM techniques utilized within this thesis work, in order to provide the necessary background for interpreting the results presented in subsequent thesis chapters.

1.6.1 Interaction of Fast Electrons with Matter

The vital electron-matter interactions in an SEM and STEM between the high-energy incident electrons and the specimen undergo different events of scattering, diffraction, and transmission. Each of which produce various types of signals, and contain a breadth of structural and chemical information that are of particular interest. Some of the different signals that originate from electron-matter interaction events are demonstrated in Figure 1.10. These scattering events can be further differentiated conveniently into elastic and inelastic scattering processes (Figure 1.11). Elastic scattering with the atomic nuclei caused by Coulombic forces involves negligible amount of energy transfer given the large mass difference (Figure 1.11(a)). Elastic scattering brings about the high-energy back-scattered electrons (BSE), diffraction, and electron channeling patterns in a crystalline solid giving rise to electron back-scatter diffraction (EBSD). Inelastic scattering involves the excitation of inner- and outer-shell core-level or valence electrons of the target atom into higher-energy unoccupied states. The energy transfer during this type of scattering event leads to the emission of electromagnetic radiation at the energy difference between the (final) excited state and (initial) ground state during de-excitation (Figure 1.11(b)). Inelastic scattering interactions in a solid provide a variety of signals, including the generation of secondary electrons (SE), Auger electrons, characteristic X-rays, and high-energy electron-hole pairs (hot carriers).

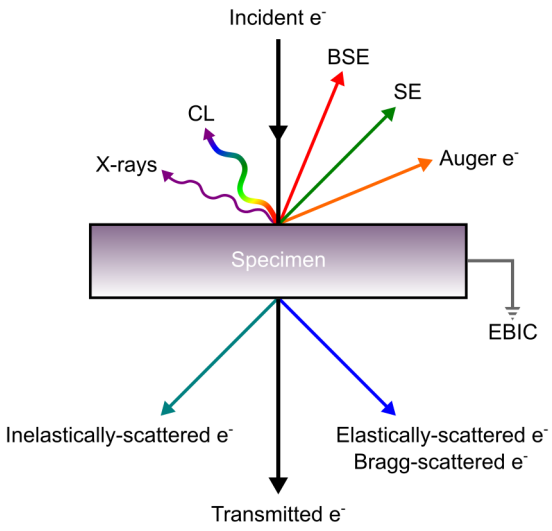

Figure 1.10: Schematic diagram of the the various types of interaction of fast electrons with the specimen and the resulting measurable signals.

The collection of SE, BSE, Auger electrons, transmitted and diffracted electron can be used to form images to investigate the morphology, chemistry, and crystal structure of the specimen. The additional characteristic X-rays and electron-hole pairs generated from inelastic scattering are secondary events. SE and Auger electrons are of low-energy particles and hence have a small escape depth, and only detected from the near-surface region of the specimen. The X-rays and Auger electrons are characteristic of the atoms involved in the transition, and therefore can supply elemental composition information about the specimen. Characteristic X-rays are the signals collected in energy-dispersive X-ray (EDX) spectroscopy. The electron-hole pairs are generated from transitions involving electrons in the valence band promoted into the conduction band, leaving behind a hole. The electron-hole pairs then relax near the band-edge or any other levels within the bandgap, and can recombine to emit photons (cathodoluminescence spectroscopy, detailed later in Section 1.6.4) or phonons otherwise. The energy of the emitted photon depends on the irradiated material and give information about its band structure. The recombination of the electron-hole pairs can additionally provide a complementary signal of electron-beam induced current (EBIC) if an electric field from a *p*-*n* junction or Schottky junction is present to separate the electron-hole pairs. The EBIC signal generation is governed by the diffusion of minority carriers to the junction depletion region, recombination at electrically-active defect sites and their collection by drift in the electric field. Current collecting contacts made to the sample allows the resulting current to be measured in an external circuit.

1.6.2 Imaging Contrast Mechanisms in STEM

The fairly recent development of spherical aberration (C_s) correction in a TEM has revolutionalized high-resolution (S)TEM imaging capabilities by compensating for the lens aberrations that have plagued the spatial resolution of high-resolution imaging in both TEM and STEM modes of operation. A C_s-corrector system implemented at the probe-forming lenses before the specimen is used to form an intense sub-Ångström-sized probe for STEM mode, which allows for atomically-resolved imaging. A brief overview of relevant imaging techniques in STEM will be given in this section. The elastic scattering of incident electrons approaching the atomic nuclei due to Coulombic attraction get deflected at high-angles following an angular distribution described by Rutherford scattering. A majority of the incident electrons traverse the target atom farther away from the nucleus, where the electrostatic field is partially screened by the atomic electrons (*cf.* Figure 1.11(a)). Thus most incident electrons scatter at typically a few degrees (10^0 – 10^1 mrad) for electrons with 100 keV energy.

The detected intensities within these angular ranges using an annular detector become

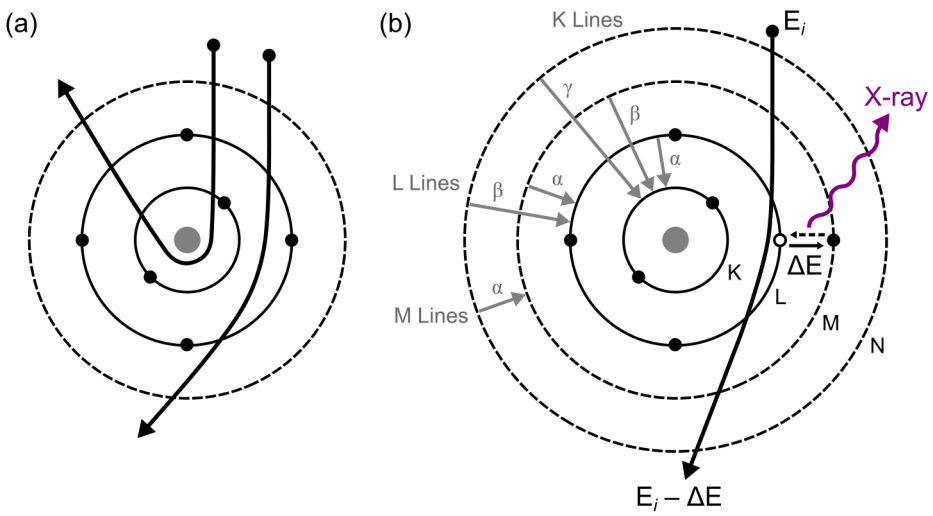

Figure 1.11: Classical particle picture showing electron scattering of a fast electron with a target atom: **(a)** elastic scattering caused by Coulombic attraction by the nucleus, and **(b)** inelastic scattering caused by Coulombic repulsion with the atomic electrons. In **(b)**, an outer-shell electron is excited to a higher unoccupied energy state, while the fast electron loses energy ($E_i - \Delta E$) equal to the energy gained (ΔE) by the excited electron. The de-excitation is marked by the dashed arrow (and the release of an X-ray portrayed here). Naming convention for specific transitions of characteristic X-ray emission and the energy levels involved is also labeled.

highly sensitive to the atomic number given the Rutherford scattering approximation. This atomic-number (Z) dependent imaging contrast mechanism, referred to as high-angle annular dark-field (HAADF), has a scattering cross-section that approximates proportionally to $\sim Z^{1.64}$ [114]. Mass-thickness contrast also contributes to the HAADF signal intensity. The cross-section forms an object function strongly peaked at the atomic sites, such that each atom can be considered to be a separate scattering source, and the detected intensity is a convolution of that object function with the probe intensity profile. Unlike the phase contrast transfer function of bright-field (BF) imaging (described later), the Fourier-transform of the probe intensity (known as the optical transfer function) contains no contrast reversals and exhibits a monotonic decay with spatial frequency. This allows for direct interpretation of HAADF images in terms of atom type and positions (bypassing the phase problem in BF imaging), as changes in defocus and specimen thickness does not cause contrast reversals [115]. An annular detector is used to collect electrons scattered into a finite angular range, typically $\sim$100 – 200 mrad for HAADF, which is a function of the camera length in practice. In STEM mode, rastering of a focused probe results in diffracted discs (CBED discs), with radii equivalent to the convergence semi-angle (α) of the probe, incident on the annular detector. Signal intensity is integrated across the angular collection range of the annular detector at each pixel of the scan raster. One of the drawbacks for HAADF imaging is the small scattering cross-section and hence low sensitivity for low-Z elements (*e.g.* B, C, N). In

the case of III-N materials, the weakly scattering N-atoms are overwhelmed by the adjacent group-III atomic columns and usually not visible above excess background intensity with typical HAADF imaging conditions. Only in AlN are the N-columns visible [116].

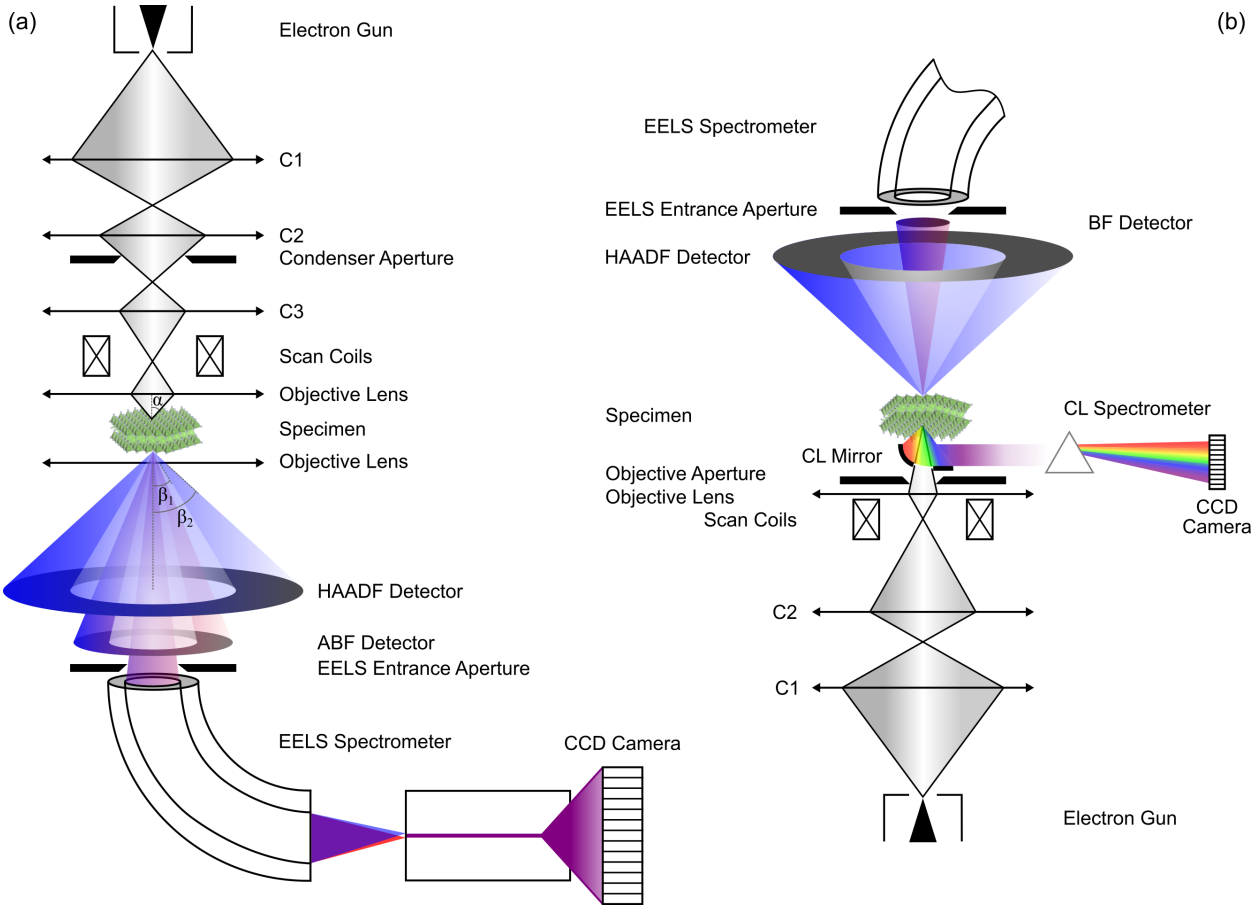

Figure 1.12: Simplified schematic and ray diagrams of **(a)** a three-condenser TEM/STEM system with an EELS spectrometer (with projection lenses and aberration correctors omitted), like the FEI Titan Cubed, and **(b)** a dedicated STEM with CL detection and EELS spetrometer, like the VG HB-501 used in this thesis. Notable scattering geometry angles (α, β_1 and β_2 for the HAADF detector) are also marked in **(a)**.

Other common complementary imaging modes are accessible in STEM by varying the angular range of collection angle (β) with respect to the probe convergence angle (α) from the selection of different detector geometries. Some of these detector geometries are illustrated schematically in Figure 1.12. Collecting the transmitted electrons that have been deflected at very low-angles ($\beta \ll \alpha$) with a circular detector produces bright-field (BF) images. Collecting electrons that exit the specimen at low-angles but omitting the direct beam with an annular detector produces annular bright-field (ABF) images. Electrons scattering to low-angles tend to be more sensitive to strain-fields, as a result of the displaced atoms along an atomic column de-channeling the electron probe. Variations of annular dark-field

(ADF) modes which take advantage of the low-angle strain-contrast sensitivity also exist, including medium-angle ADF (MAADF) imaging and low-angle ADF (LAADF) modes by progressively decreasing the inner collection angle (β_1). On the other hand, HAADF imaging typically uses an inner collection angle (β_1) $2-3\times$ larger than the probe illumination cone (α) to avoid dynamical diffraction effects. ABF imaging involves spanning the annular detector within the range of the illumination cone to also contain part of the directly scattered beam (optimally $\beta_1 = \alpha/2$, outer collection angle $\beta_2 \leq \alpha$) [117]. The contrast of ABF images is mainly associated with the s-state channeling effect (tightly-bound Bloch states), and beneficial for the visualization of low-Z elements that often lead to low detectability in HAADF imaging [118]. The resulting ABF image allows for the simultaneous visualization of light and heavy atomic columns, which becomes useful for crystal polarity determination of III-Vs and II-VIs. However, as the coherence effects are not completely suppressed with contributions from the low-angle scattered electrons, the ABF image is directly interpretable only within a narrow range of defocus [117].

1.6.3 Electron Energy-Loss Spectroscopy

Electron energy-loss spectroscopy (EELS) is an analytical technique which measures the amount of energy lost by the fast electrons after they have undergone inelastic scattering with atoms from the TEM specimen. The basic physical interaction can be described as the following. Through the excitation process by the incident electrons shown in Figure 1.13, the target electron is promoted to a higher-energy unoccupied state or into the continuum with an excitation energy of ΔE. From the energy transfer, the fast electron experiences an equivalent loss in kinetic energy ($E_i - \Delta E$) and is characteristic of the transition of the target electron. Measuring the energy-loss of the inelastically-scattered electrons post-specimen with an EELS spectrometer comprised of a dispersive magnetic prism generates a spectrum, which consists of the probability of energy transfer at each energy-loss value.

A typical EELS spectrum (spanning 0 – 2000 eV energy range) has several notable features that can be subdivided into different regions: i) an intense zero-loss peak (ZLP) centred at 0 eV from elastic scattering of electrons that did not suffer any or minimal loss of energy, ii) low-loss regime in the 0 – 50 eV energy range that involves excitations from the valence band to conduction band, iii) core-loss regime for energy range $>$ 50 eV that involves ionization of core-level electrons into the conduction band (and beyond). The width (or full-width half-maximum, FWHM) of the ZLP is used to dictate the energy spread of the electron source and other contribution from the lens optics, and ultimately determines the energy resolution of EELS. The low-loss region include a variety of transitions that have different

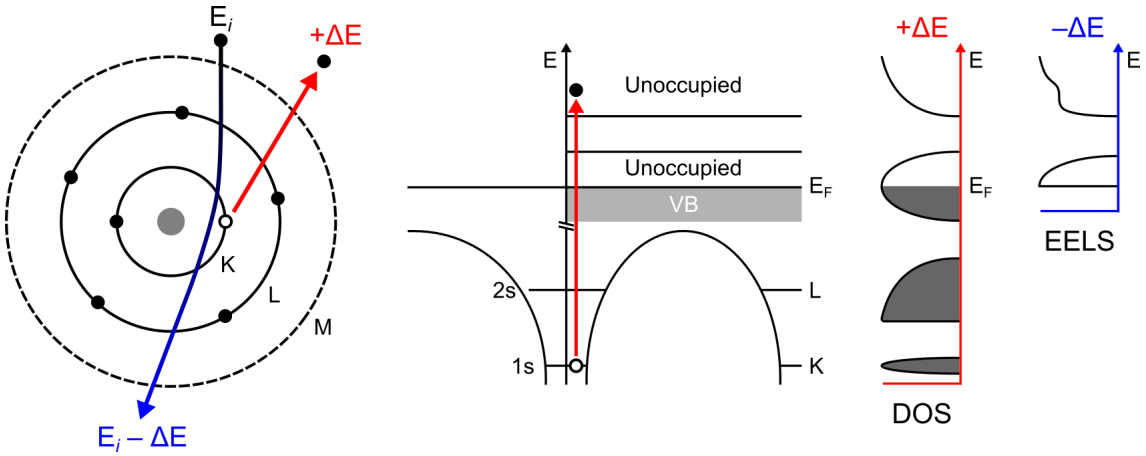

Figure 1.13: Schematic representation of the energy-loss ($-\Delta$E) of the incident fast electron (with initial energy E_i) and the energy gained ($+\Delta$E) by the target electron from an inner-shell in a solid, leaving behind a core-hole. The core-loss edge arises from transition between the the core-level to unoccupied states above the Fermi level (E_F) and valence band (VB, grey band). The relationship between free atomic levels and the associated bands in a solid are represented. The correspondence between the density of states (DOS) and the energy-loss in core-loss EELS is also shown.

physical original, including collective excitations of surface and bulk plasmons, inter- and intraband transitions.

For core-loss EELS, the excitation appear as edges (instead of peaks), superimposed over an intense decaying background, at a characteristic ionization energy threshold corresponding to the core-levels for any given element. The background under the core-loss ionization edges can be modeled using a power-law function AE^{-r}, and is removed using the standard approach of least-squares fitting over an energy window prior to the edge of interest [114]. The core-loss EELS energy signature can be used as a means for elemental identification to provide local chemical information about the specimen. The area under a given edge is also proportional to the concentration of elements for the excited atom, and is useful for elemental quantification if the scattering cross-sections are known. Furthermore, a relationship between the excitation of target electrons into unoccupied levels above the Fermi level in the density of states (DOS) and energy-loss measured in core-loss EELS is portrayed in Figure 1.13. Core-loss EELS additionally has the capability to provide information on the electronic structure for certain transition edges, as the excitation of core ionization edges effectively maps out the density of unoccupied states. Intensity modulations, or fine-structures, in a core-loss edge after the threshold energy (edge onset) are sensitive to the local environment about the target atom, as shown in the N K-edges related to InGaN alloys in Figure 1.14(a). The so-called energy-loss near-edge structures (ELNES) close to the edge onset, and extended energy-loss fine-structures (EXELFS) from ~50 eV beyond the onset, contain valuable information on local bonding, coordination, valence state, and charge transfer. Using AlN as an example

in Figure 1.14(b), correspondence in the ELNES in the various core-loss edges arrowed, namely Al K, N K, and Al $L_{2,3}$, reflects the covalent bonding that involves bands made up by characters from both elements.

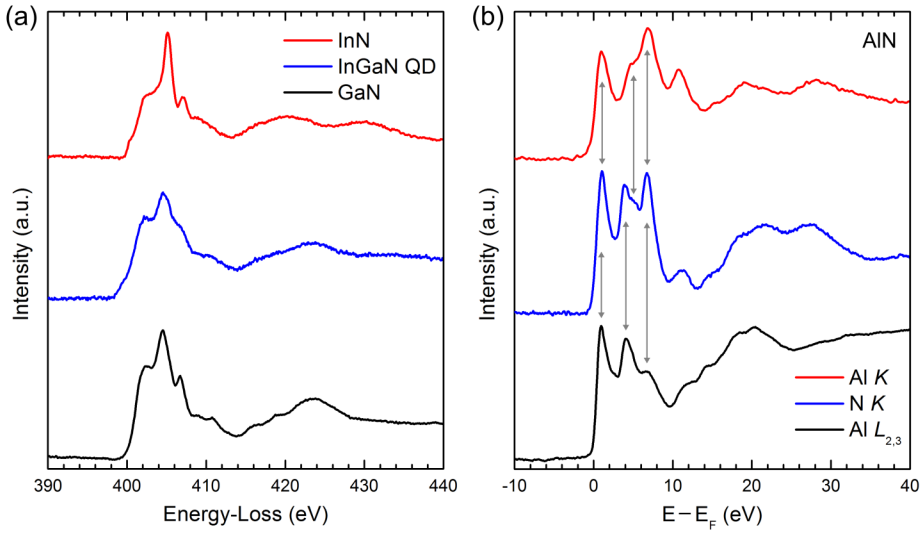

Figure 1.14: Experimental core-loss EELS edges of wurtzite III-nitrides: **(a)** variation in the N K near-edge fine-structures between binary GaN and InN compared with InGaN, **(b)** correspondence in ELNES of various Al (K and $L_{2,3}$) and N (K) edges in AlN due to the covalent bonding. Spectra in **(b)** have been aligned relative to the edge onset.

1.6.3.1 Spectrum Imaging Technique

An added benefit of STEM-HAADF imaging is that it allows for the simultaneous acquisition of other signals that are scattered directly and at low-angles, like BF an ABF imaging. Or more importantly yielding a powerful analytical data acquisition geometry depicted in Figure 1.12(a), the combined collection with other analytical signals such as the characteristic X-rays with an EDX detector and the inelastically-scattered electrons with an EELS spectrometer. This variant of the STEM-EELS imaging technique, or spectrum imaging, involves scanning the electron probe on the sample to collect the HAADF intensity and the full EELS spectrum sequentially at each pixel within the rastered area. Spectrum images are obtained in the form of a datacube: a 3-D array containing structural information from the HAADF signal in two dimensions (spatial coordinates x, y) and the full EELS spectrum in the third dimension (energy-loss coordinate E) at each spatial position. Such data acquisition allows for finer spectral sampling and produces datasets where more advanced post-processing methods can be utilized to better extract information. The strength in the spectrum imaging technique is the point-to-point correlation of structure and property from spectroscopy at the nanometer-scale and even down to the atomic-scale.

1.6.4 Cathodoluminescence Spectroscopy

When a solid is bombarded by an incident radiation, that incident energy can be absorbed, resulting in the promotion of electrons into an excited state. The excited final state E_f can then relax by dropping back down to its initial state E_i, coupled with the emission of electromagnetic radiation. The luminescence process can be categorize based on the type of excitation source, where the most common are electroluminescence (applied electric field), photoluminescence (photon excitation), and cathodoluminescence (high-energy electrons) [119]. The inelastic scattering interaction of the fast electrons with a semiconductor that leads to cathodoluminescence (CL) has already been described briefly in Section 1.6.1. The electron-hole pair generated, made up of the promoted electron and the hole left behind, then relax near the band-edge or any other levels within the bandgap, and can recombine to emit a photon radiatively or phonon non-radiatively. The energy of the emitted photon ($h\nu = E_f - E_i$) corresponds to the electronic transition, and the probability that a photon and not a phonon will be emitted depends on the nature of the irradiated material, presence of impurities, and defect states.

In terms of instrumentation, a focused electron beam in a SEM or STEM is utilized for excitation, and the emitted CL photons are collected with appropriate optics. Some of the main components include a parabolic mirror to couple the light from inside the electron microscope column to be wavelength-dispersed by a diffraction grating spectrometer (monochromator) before collecting with a photomultiplier tube (PMT) or CCD camera for serial or parallel detection, respectively. Conventional serial collection with a PMT can be carried out in different CL imaging modes: filtering at select wavelengths for monochromatic mode (narrow bandwidth window) or bypassing the monochromator for panchromatic (all of the emitted light) mode. CL detection systems are more commonly found integrated within SEM, sometimes with additional temporal-resolution read-out capabilities [120], and only in the last decade it is gaining momentum implemented within STEM [121–124]. A schematic representation of a CL detection system within a dedicated STEM, is shown in Figure 1.12(b).

Analogous to STEM-EELS, CL spectroscopy can also be carried out with spectrum imaging acquisition to allow for concurrent multi-modal imaging capabilities in both SEM (SE, BSE signals) and STEM (ADF, BF, even EELS signals) set-ups. CL hyperspectral imaging, as it is more oftenly referred to, greatly improves the spectral-spatial correlative power of the technique than the conventional monochromatic or panchromatic imaging modes mentioned previously. CL spectroscopy, and more specifically CL hyperspectral imaging, has been regarded as a particularly suitable spectroscopic characterization tool for investigating the optical properties in semiconductor nanostructures. By virtue of the nanometric elec-

tron probe size, the material optical response can be excited locally, drastically improving the spatial resolution beyond analogous far-field spectroscopy methods. Detectibility of CL signals in a STEM would allow for direct optical property-structure correlation from BF imaging for visualization of strain or defects and HAADF imaging for compositional contrast with improved resolution over SEM. Another advantage of STEM-CL is the smaller lateral spreading of the electron beam due to the thin specimen thickness, which can greatly improve the spatial resolution. In addition, the higher-energy incident electrons in STEM experience reduced interactions with the specimen whose thickness is on the order of the inelastic mean-free path, limiting the number of scattering events. A major challenge is the limited CL intensity from a small volume, which manifests to a high inherent noise level in CL hyperspectral imaging when the light is spectrally dispersed into multiple channels.

1.6.4.1 Luminescence Centres

The various radiative transitions that can lead to emission in semiconductor materials include those intrinsic to the material, the near band-edge (NBE) emission from the recombination of excitonic states corresponding to the bandgap of the material. The thermal distribution of carriers in this type of interband transition between states close to the band-edges will generally lead to a broadened emission spectrum. The probability of a direct electron-hole pair is actually quite small, and the absorption and emission usually occurs at different centres after some carrier diffusion in their respective bands and obtain thermal equilibrium. Additional extrinsic luminescence process is due to the presence of localized states caused by impurities (such as donors and acceptors in semiconductors). It can involve the recombination of free carriers with trapped carriers of the opposite type (donor to free hole $D^{\circ}h$, and free electron to acceptor eA°), and the donor-acceptor pair (DAP, $D^{\circ}A^{\circ}$). DAPs can give rise to a series of emission lines; aside from dependence on the binding energies of the donor and the acceptor, the pair separation can dictate whether the emission line will be sharp and discrete or form a continuum [119]. Electron-hole pairs that form bound excitons have their states just below the conduction band at low temperatures. Both excitons that remain free or bound to neutral impurity donors ($D^{\circ}X$) or acceptors ($A^{\circ}X$) can undergo recombination transitions. Therefore, luminescence at low temperatures is always dominated by excitonic emission. However, for GaN, excitonic emission can play a role even up to room-temperature, as their high exciton binding energy ($E_{FX} \approx 26.7$ meV [125]) is close to $k_BT = 25.8$ meV at T = 300 K.

A schematic of the various recombination pathways described is presented in Figure 1.15. The recombination of electron-hole pairs does not necessarily lead to the emission of photons during the release of energy. Non-radiative recombination describes such processes where the

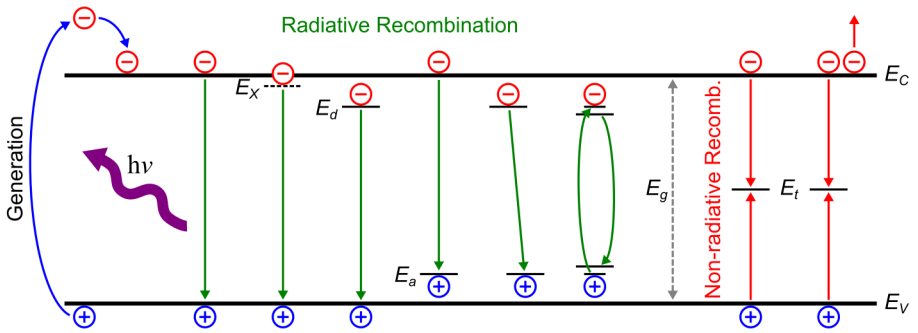

Figure 1.15: Schematic illustration of carrier generation and different radiative and non-radiative recombination mechanisms between the conduction band (E_C) and valence band (E_V) in semiconductors. Blue arrows: carrier generation and relaxation to the band-edge via an intraband transition. Green arrows (from left to right): band-to-band (interband) transition, exciton decay from exciton level (E_X), free-to-bound recombination (donor to free hole $D^{\circ}h$, and free electron to acceptor eA°), spatially separate donor-acceptor pair (DAP or $D^{\circ}A^{\circ}$) recombination, as well as the excitation and radiative excitation of an impurity with incomplete inner shells like a rare-earth or transition metal element. Red arrows: non-radiative recombination via a deep (mid-gap E_t) energy level as well as through an Auger-assisted process.

energy is dissipated via alternate pathways, which are in direct competition with the radiative processes described previously and quench the luminescence. The simultaneous emission of a phonon, typically longitudinal optical (LO) phonon, causes a characteristic reduction in emission energy given by the material-specific LO phonon energy resulting in phonon replicas of the zero-phonon line. The presence of defects in a crystal often introduces much deeper level states localized within the band gap, which have large capture cross-sections for trapping both types of carriers and are therefore efficient recombination centres. Some of the non-radiative recombination processes possible include: intraband transitions where an electron is excited well above the conduction band-edge and reaches thermal equilibrium through phonon or phonon-assisted emission, other multiple phonon emission, Auger recombination common in high concentration of excess carriers, and recombination at surface states [119].

The radiative transition mechanism leading to photon emission through photoluminescence (PL) and CL are very similar, involving the same luminescent centres [119]. An exemplary temperature-dependent PL spectra and the dependence of emission line energies of undoped GaN grown by MOCVD in the range of T = 9 – 250 K is presented in Figure 1.16. PL emission depends strongly on the excitation energy, and can be used to selectively excite, for example, only the InGaN within InGaN/GaN QWs. On the other hand, electron-beam irradiation could excite all luminescence mechanisms, which is beneficial for high bandgap semiconductors that would require costly optical setups. While the two methods do differ significantly in their electron-hole pair generation process, they are effectively providing close to equivalent spectral signatures on the carrier recombination taking place [126, 127]. This allows STEM-CL to be regarded as an appropriate below diffraction limit counterpart of PL.

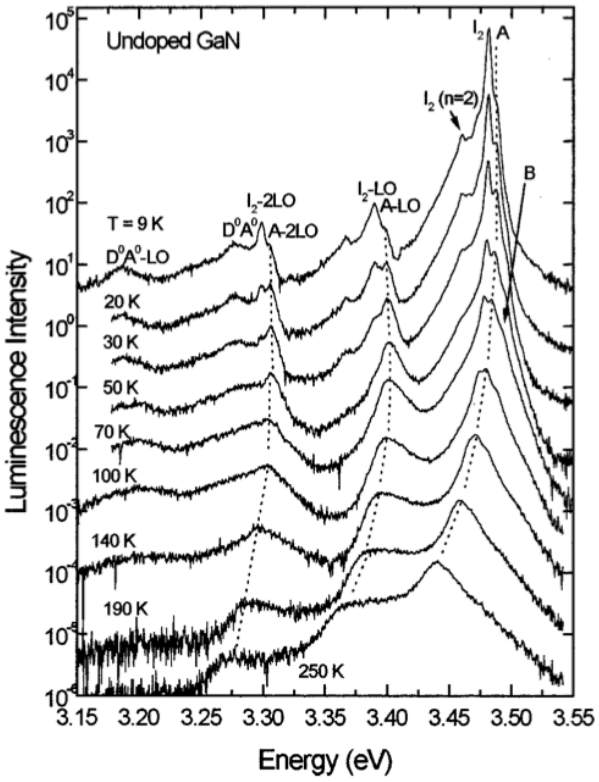

Figure 1.16: Typical temperature dependence of PL spectra of high-quality undoped GaN grown by MOCVD. Assigned transitions include: A and B for the free exciton lines, I_2 line for the $D^\circ X$, $D^\circ A^\circ$ for the neutral donor-acceptor pair, and LO for phonon replicas of the associated recombination. From Leroux et al. [128].

1.6.4.2 Carrier Diffusion and Spatial Resolution

The spatial resolution of CL spectrosccopy in S(T)EM is determined by three parameters [129, 130]: i) the electron probe size (diameter of electron beam); ii) the excitation volume in the sample from which electron-hole pairs are generated, related to the beam penetration range; iii) the material-dependent minority carrier diffusion length. The first two factors can be optimized within limitations, as both are a function of the acceleration voltage. Beam spreading is directly related to the successive electron scattering events within the sample in a randomized trajectory, resulting in electron penetration range in the order of tens of microns for typical III-V semiconductors at incident energy $E_b > 30$ keV. The last factor of carrier diffusion length is purely a material property, and can only be influenced minimally by the operator. Carrier diffusivity, including the minority carrier lifetime (both radiative and non-radiative components), is strongly affected by specimen temperature. Therefore increasing temperature can improve the spatial resolution by shortening diffusion length, but trading off signal intensity because of the increased non-radiative recombination. Thinner specimens for STEM-CL can also experience reduced diffusion length caused by the additional likelihood of non-radiative recombination at surface states.

Cathodo-generated carriers in a semiconductor become free to undergo diffusion away from the site of excitation before recombining, which has adverse effects on the spatial resolu-

tion of CL measurements. The diffusion of excess minority carriers for continuous irradiation can be described by a differential equation of continuity in Equation (1.17) for electrons in a p-type semiconductor, valid under low-injection conditions and when the motion of excess carriers is purely diffusive in the absence of depletion zones or applied fields.

$$D\nabla^2(\Delta n) - \frac{\Delta n}{\tau} + g(r) = 0 \tag{1.17}$$

where D is the diffusion coefficient, Δn is the excess minor carrier density, τ is the minority carrier lifetime, and $g(r)$ is the excess carrier generation rate as a function of radial distance. The carrier diffusion length (L) is related to the lifetime by $L = \sqrt{D\tau}$. Counter-intuitively, the material quality has an inverse relationship with carrier diffusion length, and hence also with spatial resolution. Better material quality with negligible structural/chemical variations would produce emission intensity patterns smeared out by the long diffusion length [130]. The recombination lifetime τ contains competitive contributions from radiative lifetime τ_r and non-radiative lifetime τ_{nr}, as already demonstrated earlier in Equation (1.2) from Section 1.2.2.1. Alternatively, the (non-)radiative lifetime (τ_{nr}, τ_r) can be described in terms of the density of recombination centres (N_{nr}, N_r) and their capture cross-section (σ_{nr}, σ_r) using the relation $\tau_{(n)r} = (N_{(n)r}\sigma_{(n)r}V_{th})^{-1}$. V_{th} is the carrier thermal velocity [119]. The CL emission rate is proportional to the radiative recombination efficiency (or IQE) η defined as the ratio of radiative recombination rate to total recombination rate, also shown earlier in Equation (1.3) from Section 1.2.2.1.

$$I(r) = I_0\Big[1 - exp\Big(-\frac{r}{L}\Big)\Big] \tag{1.18}$$

From the nature of electron-matter interaction, the pear-shaped interaction volume approximates well to the generation volume of charge carriers, which serves as the lower limit to the spatial resolution in CL. The size of the interaction volume, or electron beam range R_e, can be estimated by Monte-Carlo simulations [131] or semi-empirically from the Kanaya-Okayama expression [132]. An advantage of the higher acceleration voltage and thinner specimens used in STEM-CL relative to SEM-CL is to minimize the lateral beam spreading effect beyond the electron probe size that would otherwise degrade the spatial resolution from the site of excitation. Comparatively, the excitation volume in TEM specimens is limited to only the narrow neck region in the pear shape. As such, the material-dependent carrier diffusion length becomes the bottleneck limiting STEM-CL spatial resolution. On the other hand, CL measurements can be used to determine carrier diffusion length (L) in semiconductors [133–136]. This is carried out by monitoring the exponential decay of emission intensity ($I(r)$) away from an emission centre approximated by the expression in

Equation (1.18), where I_0 is the maximum emission intensity, and r is distance from the carrier sink.

Chapter 2

Interplay of Strain and Indium Incorporation

2.1 Introduction

Ternary InGaN alloys have been investigated extensively for the application of high-efficiency light-emitting diodes (LEDs) during the last decades because of bandgap energies (0.7 eV for InN and 3.4 eV for GaN) that can be tailored to have emission wavelengths spanning the entire visible spectrum [137]. However, the development of device structures of group III-nitride materials does experience a number of inherent growth challenges in obtaining high-quality structures across the entire compositional range. The two major growth-related issues are the lack of native substrates leading to a high density of threading dislocations, and the predicted miscibility gap [138] contributing to various phase segregation processes. The high amount of indium incorporation, necessary to achieve high In-content InGaN for longer wavelength (green and red) emission, has also been problematic due to a compromise between good crystalline quality and targeted emission wavelength [138]. High growth temperatures are needed to achieve optimum crystalline quality in InGaN epilayers, but are deleterious to efficient In incorporation since In–N bonds readily decompose at high temperatures. The growth of III-N compounds in a nanowire (NW) geometry as axial heterostructures has been a promising alternative because of their inherent strain relaxation laterally to prevent the formation of dislocations, and thereby also have the potential for suppressing piezoelectric polarization. Although high performance green and phosphor-free white LEDs have been demonstrated with the use of InGaN/GaN nanowire heterostructures [8, 11, 19, 41, 52, 139], the understanding of the underlying mechanism for In-incorporation, the compositional and strain variation, and their impact on the device performance is limited [15, 140–143] and

have remained elusive.

The many intrinsic properties of In-containing III-V alloys, including the deviation from ideal mixing, are due mainly to the large difference in cation covalent radii [68]. Therefore knowledge of cation incorporation behaviours of In-based III-V heteroepitaxy by molecular beam epitaxy (MBE), which are greatly controlled by growth kinetics [9], is of fundamental importance to the growth of many III-Vs. The much-lower sticking coefficient of In is strongly dependent on the substrate temperature and plays an important role in the In incorporation efficiency by affecting the desorption of surface In-atoms [144]. In ternary InGaN alloys, the differences in thermal stabilities between the two binary constituents (InN and GaN) leads to a large disparity in the Ga and In sticking coefficients, and to additional loss through thermal dissociation of In–N bonds at higher growth temperatures [145]. The influence of elastic strain on the InGaN spinodal phase diagram and hence the stability against phase separation [83], as calculated by Tessarek et al. [80] in accordance with the theory by Karpov, suggests a strong shift of the spinodal decomposition limit to higher In-content with increased lateral strain state of the InGaN layer grown on GaN. Wurtzite III-N materials are also prone to a combination of both spontaneous polarization and piezeoelectric polarization components, due to their large polarization constants. The polarization fields and the resulting quantum-confined Stark effect negatively affect the spatial separation of carriers within the device active region, resulting in a decrease in the radiative recombination rate [143]. Therefore, the appreciable effects of strain on the properties of III-N heterostructures are three-fold, from the formation of defects, the effect on alloy miscibility, and the generation of polarization-induced internal electric fields. In nanowires, the growth and stability of ternary III-Ns, and the resulting strain state are expected to be more complex and have remained largely unexplored.

With the successful achievement of high-quality, almost defect-free III-N heteroepitaxy within a nanowire geometry, further characterization with scanning transmission electron microscopy (STEM) is necessary to correlate their structural properties to device properties. In this chapter, the quantification of compositional and strain distribution within InGaN/GaN nanowire heterostructures at high spatial resolution using STEM is demonstrated, showing that strain states of GaN barriers play a role in the formation and strain relaxation of InGaN quantum dots (QDs) within such structures. Further calculations of the expected piezoelectric polarization from such local strain and composition measurements indicate a significant reduction compared to bulk thin films, but nevertheless, remains not negligible in overall magnitude.

The nanowire architecture introduces a building block with immense potential to form new and diverse heterostructures that can exist in both radial and axial (longitudinal) vari-

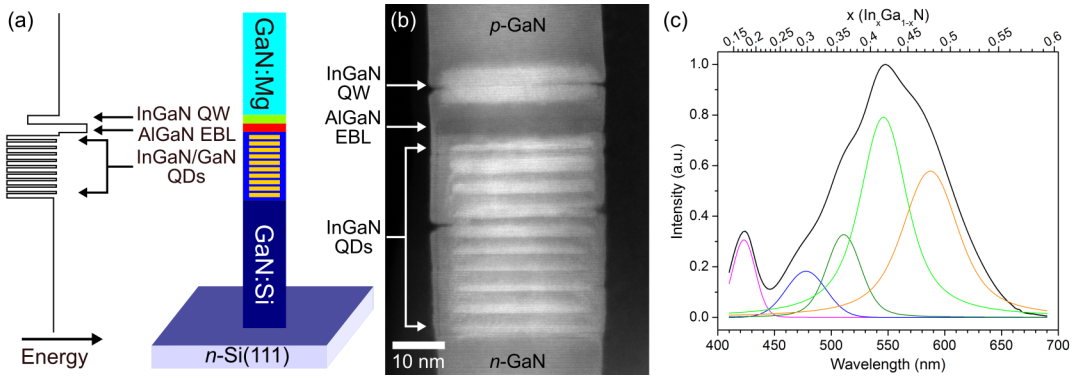

Figure 2.1: **(a)** Schematic illustration of the InGaN/GaN DWire LED design, with an additional *p*-InGaN test well and *p*-AlGaN EBL between the QD active region and the *p*-GaN section, shown alongside its corresponding flat conduction band energy diagram. **(b)** STEM-HAADF image showing the varying Z-contrast in the different regions in the structure. **(c)** Room-temperature PL spectrum of the nanowire LED device (thick black line), represented with additional fitting curves with Voigt functions (coloured lines) to emphasize the presence of multiple shoulders within the main emission peak at 550 nm. The emission peak at ∼430 nm is from the InGaN QW.

ations. The different forms of kinetically-limited phase separation processes in InGaN alloys that often hinder the growth of In-rich InGaN quantum wells (QWs) can actually be advantageous in the formation of QDs [80], as in the recently developed InGaN/GaN dot-in-a-wire (DWire) nanostructures [10, 19, 85]. A schematic of the InGaN/GaN DWire LED design investigated in this study is shown in Figure 2.1(a). The InGaN/GaN DWire LEDs show broader than anticipated emission peaks from room-temperature photoluminescence (PL) spectroscopy measurements of an ensemble of nanowires [85], as shown in the spectrum in Figure 2.1(c). Since the InGaN composition in the active region of such devices can be directly related to the emission wavelength, a quantification of the In-content at high spatial resolution is thus crucial in order to understand factors that can influence In incorporation [15]. Hence elemental mapping of the local composition in InGaN at high spatial resolution is of tremendous interest, because of known issues of compositional fluctuations [146] as a result of phase segregation into In-rich regions [80, 147], or composition gradients along the growth direction due to composition pulling effect caused by In surface segregation [68]. In addition, the intrinsic optical properties need to be established primarily before considering the effects of quantum confinement or strain-induced modifications like the quantum-confined Stark effect. Definitive prediction of the optical and electrical properties of nitride heterostructures requires taking into account the strain-relaxation mechanisms. This remains to be a critical task in obtaining targeted emission properties through the precise control and full compositional range tunability of alloyed nanowires.

2.2 Experimental Methods

2.2.1 MBE Growth

Multiple InGaN/GaN DWire nanostructures are grown on Si(111) substrates by *rf* plasma-assisted MBE under nitrogen-rich conditions without the use of any external catalyst, as described in further detail in Ref. [19, 85]. A 10 InGaN QD series, each capped by a GaN barrier layer, is centrally confined within the nanowire active region embedded between *n*- and *p*-doped GaN in the nanowire heterostructure. Additional components in the device structure include the *p*-AlGaN electron-blocking layer (EBL) and the *p*-InGaN test well towards the *p*-GaN, used to mitigate and evaluate electron overflow, respectively.

2.2.2 Scanning Transmission Electron Microscopy

Characterization of the nanowire heterostructures was carried out using aberration-corrected scanning transmission electron microscopy (STEM). The experiments were performed with a FEI Titan Cubed 80-300 monochromated, probe- and image-corrected STEM equipped with a Gatan GIF Tridiem 866 imaging filter for electron energy-loss spectroscopy (EELS), and a high-brightness field emission gun (X-FEG) operated at 200 kV. Atomic-resolution, Z-contrast sensitive STEM high-angle annular dark-field (HAADF) images were processed using geometric phase analysis (GPA) from algorithms originally developed by Hÿtch et al. [71], and implemented as a plugin within Gatan DigitalMicrograph by HREM Research Inc.

2.2.3 EELS Quantification

A multiple linear least-square (MLLS) fitting routine [148] implemented within DigitalMicrograph was used to treat the EELS spectrum images to separate the spectral contributions of the N K-edge (399 eV) from that of the In $M_{4,5}$-edge (451 eV in InGaN). The N K-edge from the nearby GaN region as internal reference combined with the In $M_{4,5}$-edge from an InN nanowire as an external reference were used for the MLLS fitting. The basic principles of the composition quantification method from the separation of the EELS spectral components and subsequent normalization is presented in Equation (2.1). $S(E)$ is the fitted spectrum, AE^{-r} is the Power-law background; A_n and $S(E_{x=0})$ are the fitting coefficient for N (without In), and its reference spectrum from *n*- or *p*-GaN region of the nanowire being analyzed, respectively; B_n and $S(E_{x=1})$ are the fitting coefficient for In (without Ga), and its reference spectrum from an InN nanowire, respectively. An assumption was made that group III-nitride nanowires are stoichiometric, such that the III:N ratio equates to unity for $In_xGa_{1-x}N$ alloys of compositional range of $x = 0 - 1$. Therefore subsequent normalization

of the resulting MLLS-fitted In-map with the N-map (fitting coefficients B_n/A_n) produces a projected-thickness normalized In-content map that should contain values (x in $In_xGa_{1-x}N$) corresponding to the In-composition within each pixel.

$$S(E) = AE^{-r} + A_nS(E_{x=0}) + B_nS(E_{x=1}) \tag{2.1}$$

2.2.3.1 Method Accuracy

Sources of error in the quantitative MLLS analysis of EELS can arise from the intrinsic spectral differences (EELS near-edge fine structure) in the N K-edge between InN and GaN used as reference spectra, or from differences in thickness between the standard specimens and the analyzed specimen. The latter was avoided by utilizing (n- or p-doped) GaN reference spectra internal to the (nanowires) nanowires being analyzed, and external reference spectra of InN nanowire only summed from regions with similar ranges of thickness.

The method of composition determination by EELS spectrum imaging on InGaN/GaN nanowire heterostructures demonstrated in this study is implemented on binary InN nanowire to illustrate the accuracy and precision of the quantification, as a measure of the outcomes of any sources of error. Quantification of the In-content in the InN nanowire is achieved using identical methods of MLLS fitting routine within DigitalMicrograph, followed by subsequent normalization of the resulting In-map with the N-map. In group III-nitride materials, the III:N ratio equates to unity to maintain stoichiometry, therefore the expected projected thickness normalized In-content map for an InN nanowire should contain values corresponding to one. The reference spectra used include the N K-edge from the n-GaN region in the nanowire heterostructure, and the In $M_{4,5}$-edge from the InN nanowire, similar to the ones later used in the elemental maps of Figure 2.5. The quantification of the In-content in the binary InN nanowire, presented in Figure 2.2, shows statistical variations with a mean In/N

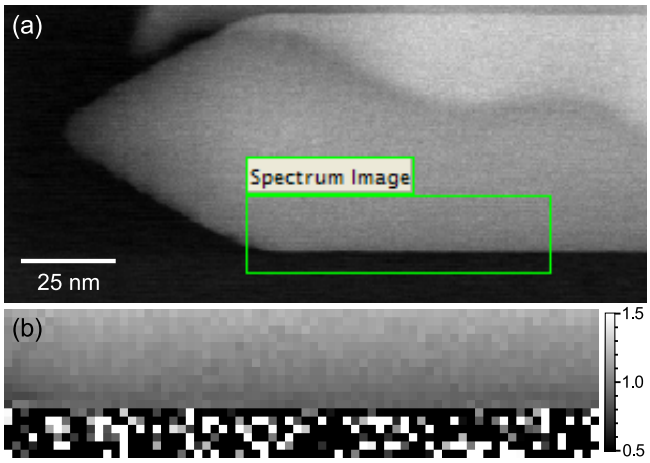

Figure 2.2: **(a)** STEM-HAADF image of the InN nanowire used for reference spectrum of the In $M_{4,5}$-edge in the MLLS fitting. **(b)** Normalized In-content map using the same method in Figure 2.5(d), showing the validity of the quantification with In/N ratios within reasonable error. The bottom six rows of pixels is vacuum, and are omitted in the statistics.

ratio of $\bar{x} = 1.02357$, with a standard deviation of $\sigma = 0.09785$. A similar assessment of the p- and n-GaN regions in the analyzed nanowire of Figure 2.5 also shows the statistical variations from an expected In/N ratio of 0. A mean In/N ratio of $\bar{x} = 0.01300$ with a standard deviation of $\sigma = 0.02177$ for the p-GaN and $\bar{x} = 0.00271$ with a standard deviation of $\sigma = 0.02119$ for the n-GaN (where the reference spectrum was obtained).

2.2.3.2 Correction for Embedded Quantum Dots

It is worth noting that the quantitative elemental mapping methods using STEM-EELS implemented in this work, are still prone to projection effects common in most TEM techniques. However, the use of this quantification method in planar nitride heterostructures (made into wedge-shaped TEM specimen geometry, for example) would avoid the projection issues and increase the quantification accuracy greatly. Additionally, this quantification method will be equally as applicable in coaxial nanowire heterostructures to concurrently account for changes in projected thickness towards the nanowire surface.

The InGaN/GaN QDs are centrally embedded by a surrounding GaN shell at the nanowire sidewalls, whose N K contributions are included along the electron beam direction and within the N-map of Figure 2.5(b). Because the In-content map in Figure 2.5(d) is projected along the beam direction, it underestimates the In-composition contained only within the InGaN QD itself. Similar to the work on composition measurement in buried In(Ga)As QDs grown on planar GaAs [149], substantial approximations need to be made about the shape of the QD in order to deduce its resulting two-dimensional projection surrounded by a GaN shell and obtain quantitative compositional information. The overall shape of the QD is estimated to be a hexagonal disk that is axisymmetric about the centre of the nanowire. A correction factor, as determined from the ratio in lateral dimension of the QD within the nanowire based on the HAADF image intensity profile across the QD (example shown in Figure 2.3(b)), was applied to the EELS-measured In-content of each QD in Figure 2.5(d). Table 2.1 summarizes the In-composition, the correction factor, and the GaN shell-corrected In-composition of each $In_xGa_{1-x}N$ QD from Figure 2.5(d).

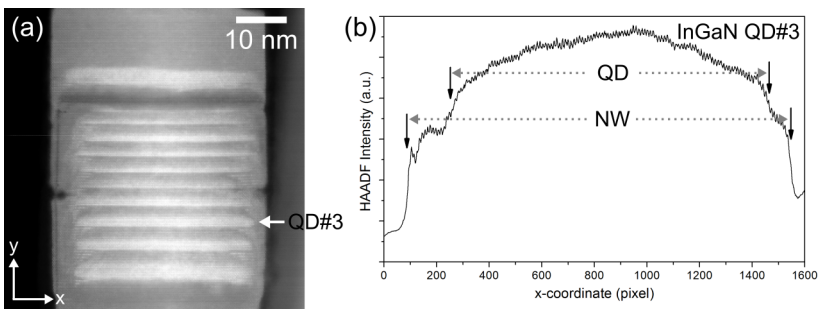

Figure 2.3: **(a)** STEM-HAADF image of the nanowire studied using STEM-EELS spectrum imaging in Figure 2.5, and **(b)** Line profile of the HAADF intensity across QD#3, counting from the bottom along the growth direction, demonstrating how the correction factor listed in Table 2.1 was calculated for each QD.

2.3 Structural and Compositional Analysis of InGaN/GaN Dot-in-a-Wire

Atomic number (Z-contrast) sensitive STEM-HAADF imaging in Figure 2.1(b) demonstrates that the 10 InGaN QD series are centrally confined within the active region, embedded between n- and p-doped GaN in the nanowire heterostructure. Additional components visible in the device structure include the p-AlGaN electron-blocking layer (EBL, dark band arrowed) and the p-InGaN test well towards the p-GaN, used to mitigate and evaluate electron overflow, respectively. Other notable features within the nanowire include the varying intensity of the HAADF signal within each QD and between different QDs, as well as changes in the height and lateral size of QDs within the series. The intrinsic projected thickness variation of the QDs within the nanowire could be a probable cause for the observed HAADF intensity changes; though they can also be attributed to changes in composition between the QDs. Elemental analysis of these structures using energy dispersive X-ray spectroscopy (EDX) in STEM was previously reported in Ref. [85]. Line profiles acquired along the centre of the nanowire through the QDs showed qualitative variations in the In L_α signal, suggesting a non-uniformity in their composition. However, a quantitative comparison of the EDX results remained inconclusive due to thickness variations inherent in the nanowires along the growth direction, differences in QD size, and radial projected thickness changes of the QD.

To explain the HAADF intensity variations between the InGaN QDs in this study, core-loss electron energy-loss spectroscopy (EELS) was used to evaluate the elemental distribution within the DWire structures in the boxed area of Figure 2.4(a). Extracted spectra from different regions containing the elements of interest—specifically the N K, In $M_{4,5}$, and Ga $L_{2,3}$-edges (Figure 2.4(b))—show a good correspondence between the different elements in the ternary alloys present. The In-rich regions (such as the QDs and QW, spectra in red and blue, respectively) show the rise of a broad In-peak (451 eV) and a slight decrease in the Ga-peak (∼1150 eV). The latter can also be observed in the Al-rich (and hence Ga-deficient) AlGaN EBL (green spectrum). Elemental maps of Ga and In can be obtained from the spectrum image, as shown in Figures 2.4(c) and 2.4(d), respectively. There is good complementarity in the distribution of Ga and In signals within the QDs based on their elemental maps (In-enrichment = Ga-deficiency). It is also noteworthy to point out that there is significant signal within the In-map (Figure 2.4(d)) from the regions that should not contain any In, and that the boundaries of the InGaN regions are not sharp. This outcome is due to the close proximity of the N K (399 eV) and In $M_{4,5}$ (451 eV in InGaN) edges, such that a background subtraction on the In $M_{4,5}$-edge to obtain the elemental map cannot completely exclude contributions from the N K-edge. Therefore, the N K contributions from

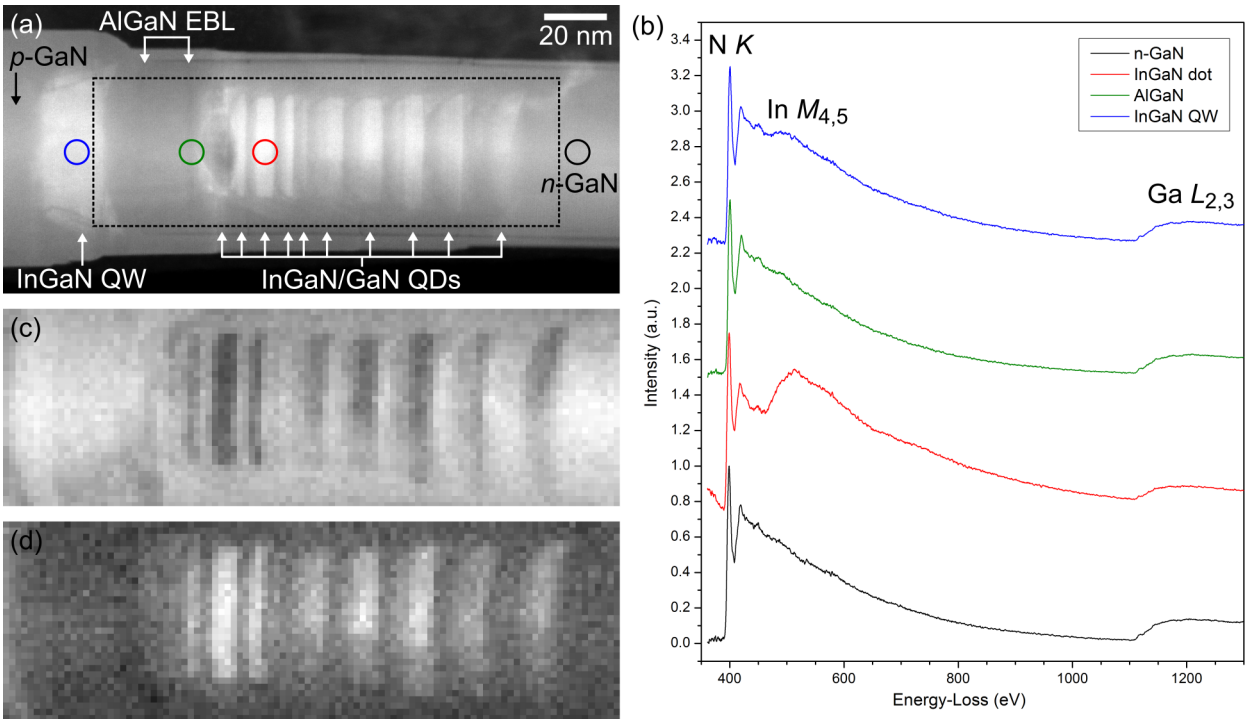

Figure 2.4: **(a)** STEM-HAADF image of the InGaN/GaN DWire structure studied using STEM-EELS spectrum imaging technique, identifying the boxed area of the spectrum image acquisition. **(b)** EELS spectra containing the N K, In $M_{4,5}$, and Ga $L_{2,3}$-edges extracted from different regions (circled in their respective colours in **(a)**), normalized to the maximum intensity in the N K-edge and vertically offset for clarity. Elemental maps of the boxed region in **(a)** extracted from the **(c)** Ga $L_{2,3}$-edge, and **(d)** In $M_{4,5}$-edge showing the localization of In within the QDs.

the GaN regions are also included in the In-map, resulting in the apparent non-zero intensity at the GaN regions.

2.3.1 Variation of Indium Content amongst Quantum Dots

The true In-distribution is evaluated after the separation of the N K contributions from the In $M_{4,5}$ with the use of a MLLS fitting routine [148]. The results of the MLLS fitting on an EELS spectrum image of a DWire structure are presented in Figure 2.5. The MLLS-fitted In-map (Figure 2.5(c)) shows clearly defined InGaN QDs and a non-uniform In-content distribution radially within each QD, as well as variation along the growth direction between the different QDs in the series. Due to the intrinsic thickness variation within the nanowires along the c-axis (growth direction, denoted as y-axis in the figure), and the projection-effect induced thickness changes across the nanowire diameter, the measured intensities must be compensated for these factors. Since the ratio of group III elements to N-atoms stays constant within III-N materials [146], the MLLS-fitted N-map (Figure 2.5(b)) can be used to provide

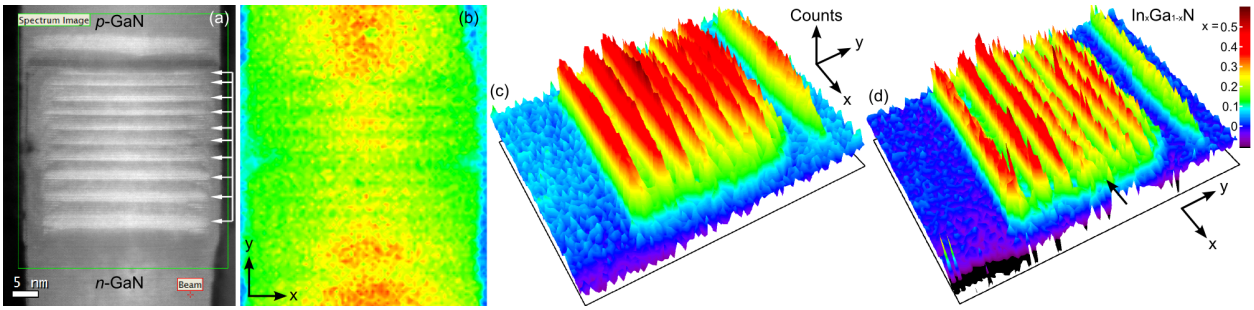

Figure 2.5: **(a)** HAADF-STEM image the InGaN/GaN DWire structure studied using STEM-EELS spectrum imaging, followed by subsequent MLLS fitting using combined internal and external reference spectra. **(b)** Colour map of the MLLS fitting coefficients output for the N-component. **(c)** Surface plot of the MLLS fitting coefficients output for the In-component, interpreted directly as the relative In-content projected through thickness. The surface plot representation emphasizes the variation in relative In-content both radially (along x-axis), and along the growth direction (y-axis). **(d)** Surface plot of the thickness-corrected In-content map, generated from normalizing the MLLS-fitted In-map of **(c)** with the MLLS-fitted N-map in **(b)**. The In-composition shown in **(d)** is underestimated, as it does not take into account the proportion of the GaN shell projected through thickness.

local thickness information, as the gradual change to higher signal towards the centre of the nanowire can be directly correlated to the increased thickness. It is important to note that the changes in the N-map visible within the QDs are due to minor spectral differences in the N K-edge between GaN and InGaN. These small differences can introduce minor artifacts into the MLLS fitting, thereby limiting the usage of the MLLS-fitted N-map as a mere pseudo-thickness map.

The normalized MLLS-fitted In-content map, corrected for thickness projection using the MLLS-fitted N-map (Figure 2.5(b)), is shown in Figure 2.5(d). The apparent non-uniform In-content radially is mostly nullified by the normalization, most evidently seen in the InGaN QW, therefore justifying its origin solely to the projected thickness changes. More interestingly, the variation in In-content ($x = 0.12 - 0.38$) between the $In_xGa_{1-x}N$ QDs along the growth direction is still present. As the growth conditions of the whole active region were kept constant to target a nominal composition, the observed compositional variation must be an effect of the intrinsic growth dynamics during the formation of the InGaN/GaN QDs within the active region. This systematic occurrence, and the mechanism by which it occurs is elaborated further within the discussion. It has to be noted that the In-composition shown in Figure 2.5(d) is underestimated for the InGaN QDs, as the N-signal includes a contribution from the GaN shell at the nanowire sidewalls projected through thickness, the proportion of the GaN shell must be taken into account. For example, adjusting for the GaN shell in QD#3 (with highest relative In-content), the measured $In_xGa_{1-x}N$ composition would increase from $x = 0.38$ to $x = 0.45$ (see Section 2.2.3.2 for further details of the correction).

A non-uniform composition amongst the QDs has been observed in all nanowires surveyed; however, there does not appear to be a statistically evident trend of the relative In-content change along the growth direction between different nanowires examined. On the other hand, the compositional variation within individual nanowires can be explained as follows. The sudden drop in In-content within QD#5 can be linked to the presence of the surface crack that propagates past only the GaN shell (marked in Figure 2.5(d)), which is indicative of strain relief. Surface cracks have been observed in other nanowires to typically not propagate past the GaN shell, in the vicinity of high In-content QDs or thick InGaN layer such as the QW in the nanowire of Figure 2.1(b). Because the formation of the InGaN QDs within the DWire structure is due to strain-induced self-organization, it is postulated that the strain relaxation within individual nanowires plays a determinant role directly affecting the incorporation of In during the formation of each QD.

2.4 Mapping Local Lattice Deformation

In combination with EELS mapping to further correlate the composition in the InGaN QDs and strain, geometric phase analysis (GPA) [71] was applied to the corresponding atomic-resolution HAADF images to better understand the strain distribution, as presented in Figure 2.6. The MLLS-fitted relative In-content map measured using EELS in Figure 2.6(a) already shows a strong correlation with the image intensity of the HAADF image in Figure 2.6(b), acquired along the $\langle 1\bar{1}00\rangle$ viewing direction (m-plane). Reciprocal lattice vectors, $\mathrm{g} = 0002$ and $\mathrm{g} = 11\bar{2}0$, were selected from the image's power spectrum to calculate the phase images and generate the subsequent two-dimensional strain tensors during the GPA processing. Seen laterally across the nanowire diameter (denoted as the x-axis) in the ϵ_{xx} map (Figure 2.6(d)) there is a ~2.5% lattice expansion (positive $\Delta a/a^{ref}_{GaN}$ lattice spacing) within the QD heterostructure compared to the fully relaxed GaN sidewalls used as reference. Additionally, the InGaN QDs show no discernible in-plane lattice spacing changes with respect to the underlying GaN and appear to form both coherent GaN/InGaN and InGaN/GaN interfaces. Corollary to coherent planar bilayer structures that are elastically compliant, the uniform in-plane spacing within the short-period heterostructure, together with the observed expanded a-spacing within the GaN barriers (compared to the relaxed shell) is indicative of strain partitioning [150] within the coherent InGaN/GaN nanowire heterostructure. No misfit dislocations have been observed at any GaN/InGaN interface within the active region, indicating a tendency towards elastic relaxation.

Concerning the growth direction (denoted as the y-axis) in the ϵ_{yy} map (Figure 2.6(c)) showing the $\Delta c/c^{ref}_{GaN}$ spacing, there are large systematic variations corresponding to the

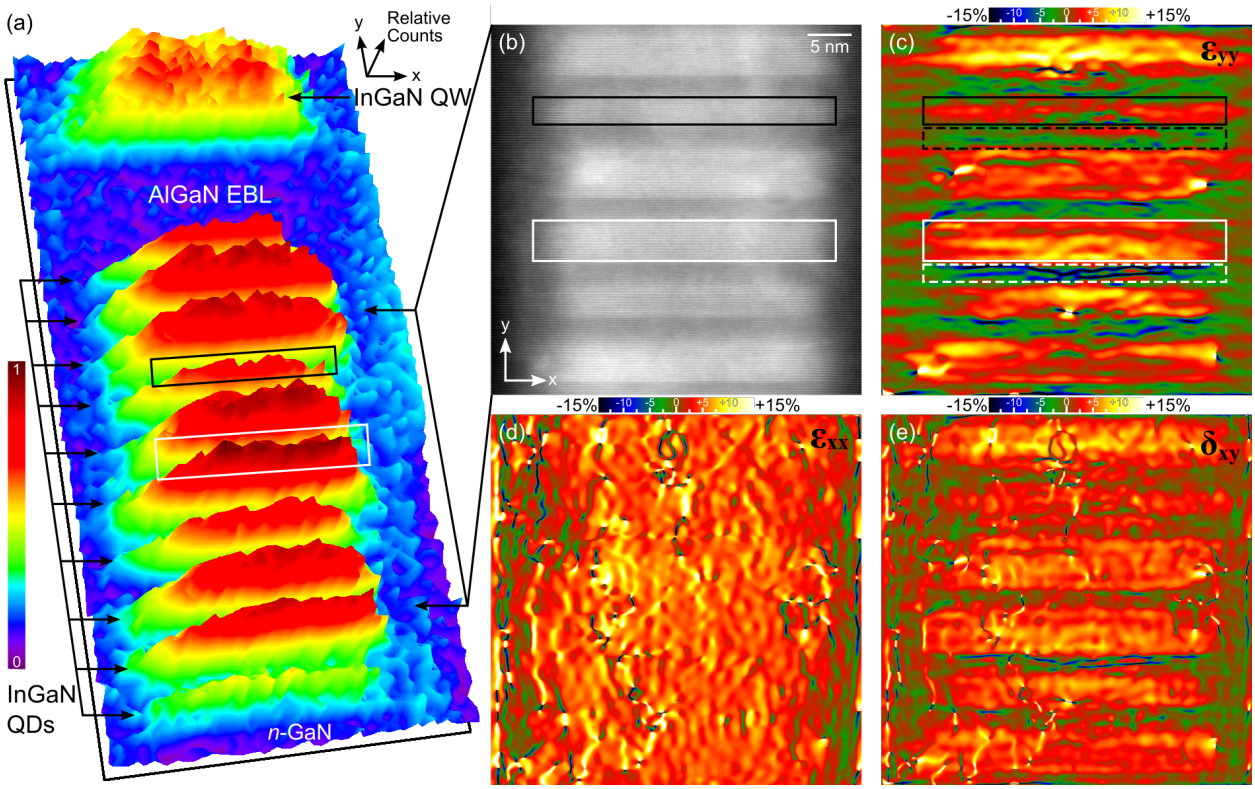

Figure 2.6: **(a)** Surface plot representation of the MLLS-fitted *relative* In-content map from EELS with internal references, relative counts scaled to fit-coefficients from QD boxed in white from 0 – 1. **(b)** Corresponding HAADF-STEM image showing the In-rich QDs (bright areas). Strain maps **(c)** along the growth direction, ϵ_{yy}, **(d)** along the in-plane direction, ϵ_{xx}, and **(e)** dilatation matrix, δ_{xy}. The strain maps show that there is a direct correlation between the In-content as highlighted in **(a)** and the strain along the growth direction **(c)**, while compressive strain towards the nanowire centre in the in-plane direction **(d)** indicates the enhanced surface relaxation. Colour scale legend of each GPA strain map indicates the percent change relative to the reference region.

locations of the QDs. The calculated displacement shows that there is a 2 – 5% lattice expansion along the c-axis within the InGaN QDs, while the GaN barrier layers are compressively strained ($\Delta c/c^{ref}_{GaN} = -2 - 6\%$). Isolating one of the QDs with high In-content (as boxed in white) and comparing it to another QD with low In-content (as boxed in black), a direct relationship between the degree of c-spacing expansion and the EELS-measured In-content can be postulated. As more In-atoms are incorporated within the structure, the lattice parameter is expected to increase monotonically following Vegard's law, and thus presents as an apparent positive strain. Furthermore, in the GaN barrier layers just below the QDs (marked with dashed boxes), there is also a direct correspondence between their degree of compressive strain to the In-content in the subsequent QD. Therefore it is concluded that the more compressive-strained a GaN barrier layer is along the growth direction, the more In is incorporated into the subsequent QD during the growth sequence, as demon-

strated in all GaN barrier/QD pairs from Figure 2.6 summarized in Figure 2.7. The system will respond in such a manner to accommodate the strain through the intrinsic physical properties of the InGaN alloy during growth, namely the phase segregation behaviour and the high mobility of In adatoms, in order to achieve the necessary lattice expansion for optimal strain relaxation. The enhanced or suppressed incorporation of In during the formation of InGaN QDs can thus aid in distributing the elastic energy more evenly across interfaces, and locally minimize the total energy. The mean dilatation matrix, δ_{xy}, an average of ϵ_{xx} and ϵ_{yy}, indicating the overall lattice deformation as determined from the GPA algorithm, is also shown in Figure 2.6(e). The compressed c-planes within the GaN barriers are a result of the tensile constraints observed in-plane due to the Poisson effect, in which the tetragonal distortion in the GaN barrier is more apparent within the δ_{xy} map in Figure 2.6(e).

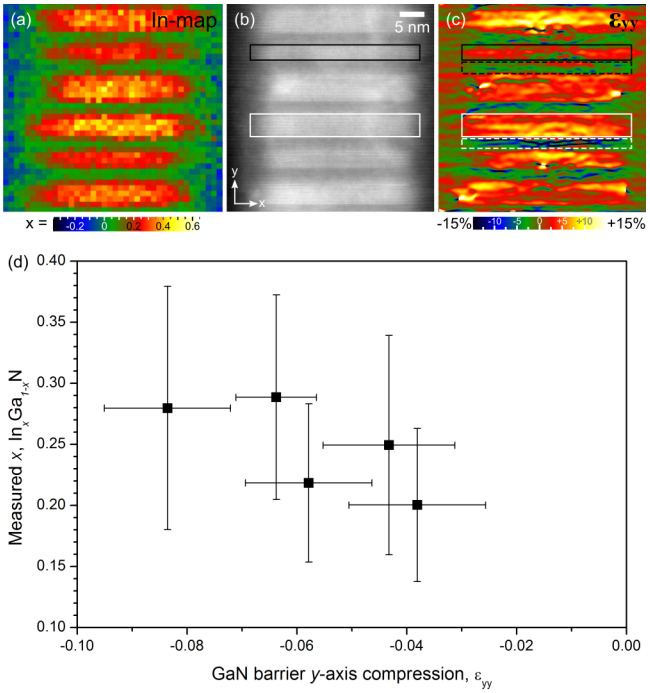

Figure 2.7: Graphical representation of the same nanowire and its measured In-content and strain state shown in Figure 2.6. **(a)** Colour map of the thickness-corrected MLLS-fitted STEM-EELS In-map. **(b)** Same STEM-HAADF image with GPA applied, and **(c)** its strain map along the growth direction, ϵ_{yy}, from Figure 2.6(b) and **(c)** with emphasis boxes also present. **(d)** Plot of corresponding out-of-plane compression and measured In-content in GaN barrier/InGaN QD pairs grouped along the growth direction within **(a – c)**, showing a correlation between the degree of compression in GaN barriers and the measured In-content in the subsequent QD. Error bars represent standard deviations from the measurement averaging over a local area, separate for the STEM-EELS and GPA techniques used per feature averaged.

2.4.1 Measured In-content and Barrier Strain State

The amount of In incorporated into a particular quantum dot (QD) depends on the strain state of the GaN barrier below, in particular the degree of out-of-plane compression within the GaN barrier, as demonstrated in the combined relative In-content map and strain maps in Figure 2.6. Aside from highlighting the extreme cases for comparison in Figure 2.6, this hypothesis is further exemplified in Figure 2.7 by comparing the averaged In-content versus the averaged out-of-plane strain state (ϵ_{yy}) of the corresponding GaN barrier within each QD/barrier pair from Figure 2.6. The (thickness-normalized) In-content map in Figure 2.7(a)

is similar to the *relative* In-content map in Figure 2.6(a), but with additional normalization with the N K-edge. The proportional trend between the magnitude of y-axis compression in a particular GaN barrier (number n) and the In-content in the subsequent QD (number $n+1$) is most evident in the plot of Figure 2.7(d). As the magnitude of compression in a particular GaN barrier increases, the In-content in the subsequent QD also increases.

2.5 Strain Accommodation within the Nanowire Heterostructures

Strain accommodation has been pinpointed as the driving force of compositional pulling in thicker InGaN layers [68], where surface-segregated In is only partially incorporated during the growth of InGaN and results in a gradual enrichment towards the surface [151]. The incorporation of In atoms in the InGaN lattice is enhanced by the volume change introduced by alloying that opposes the in-plane strain state [152]. It has been reported that InGaN/GaN multiple quantum well (MQW) LED structures can experience enhanced hole injection efficiency with the use of thinner barriers and/or thinner QWs from various graded-thickness heterostructure designs [153, 154]. Therefore, the use of InGaN/GaN MQW structures with short-periods and thin QWs can lead to better remediation against efficiency droop at high operating current. The strain state of both the thin InGaN QW and GaN barriers is likely not fully relaxed and might lead to compensations by other means. For example, two-dimensional heterostructures are typically susceptible to a very high density of dislocations, where the strain is relieved plastically [155]; the large aspect ratio of nanowires, on the other hand, could favour a regime of elastic-strain relaxation. It can even be postulated that their strain relaxation occurs in a purely elastic manner, as Landré et al. [155] demonstrated in GaN/AlN nanowire superlattices.

The in-plane strain state of the InGaN QDs in this work is determined to be different than planar InGaN QWs, exhibiting additional relaxation at the nanowire free surface and approaching an elastic regime. See additional strain maps and extended discussion on the same nanowire from Figure 2.5 in the Figure 2.10 appearing in a later section (2.6.1.1). From strain maps of the whole active region using n-GaN as reference lattice, QD#1 grown on the n-GaN base shows negligible a-spacing expansion, demonstrating that it is grown pseudomorphically. However, assessing the ϵ_{xx} map sequentially along the growth direction shows a gradual transition towards positive $\Delta a/a^{ref}_{GaN}$ spacing starting at the first GaN barrier before reaching an average 2.5% a-spacing expansion within QD#3 (see Figure 2.10(b)). In Figure 2.6, the positive $\Delta a/a^{ref}_{GaN}$ spacing within the GaN barriers compared to the GaN ref-

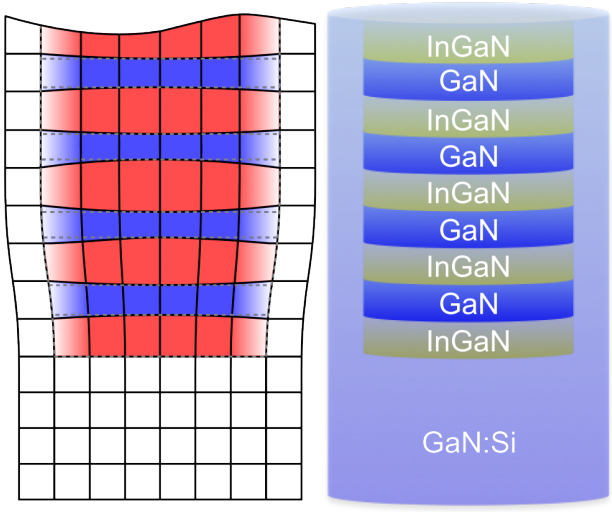

Figure 2.8: Schematic illustration of the lattice distortions in the InGaN/GaN QD heterostructure due to strain partitioning, as well as the c-axis constraints caused by the surrounding GaN shell. The in-plane compression within InGaN QDs (red) and the in-plane tension within GaN barriers (blue) are responsible for the out-of-plane distortions, in particular the compressed c-planes in the GaN barriers. The grey dashed lines show the estimated difference in lattice distortion within an ideal axial nanowire heterostructure in the absence of a GaN shell.

erence lattice at the nanowire shell indicates that they are strain partitioned with the InGaN QDs in the heterostructure. Strain partitioning describes how coherency at the heterostructure interface is achieved [150], such that the in-plane strains in adjacent layers of InGaN and GaN have opposite sign, representing their compressive and tensile strains, respectively. As explained by the Poisson effect, the tensile strain along the a-axis induces compressive strains (negative $\Delta c/c^{ref}_{GaN}$) in the GaN barriers along the growth direction. As suggested by Kehagias et al. [143] in similar lattice strain analysis of InGaN/GaN nanowire superlattices along the growth direction, the interfacial misfit within coherent nanowire heteroepitaxy can be minimized by means of distributing the strain in the adjoining lattices.

Compared to strain partitioning in thin coherent planar bilayer structure, where the elastic compliance is maintained only by the in-plane lattice spacing, both layers do not fully relax in-plane, and normal stresses are zero (as per biaxial strain condition). Heterostructures within nanowires would also experience identical in-plane strains, but differences arise depending on whether the layers have free sidewall surfaces. Ideal axial nanowire heterostructures of QWs with free surfaces can have an inhomogeneous lateral strain distribution due to the lateral elastic relaxation in both materials [156], while embedded nanowire heterostructures can exhibit additional non-zero normal stresses. A comparison of the expected differences in lattice distortions for the two scenarios within nanowire heterostructures is presented in Figure 2.8. The accommodation of interfacial misfit of the InGaN/GaN DWire is accomplished by partial strain partitioning in-plane, as shown in the ϵ_{xx} map of Figure 2.6(d). The partial compliance (strain in the bilayer not balanced to zero) is observed after the progressive lateral expansion starting at the first GaN barrier and reaches a plateau at QD#3, as described previously, where compliance of all subsequent layers is to the expanded QD#3 lattice (can see also Figure 2.10(b) in a later section).

In this study, the presence of a surrounding GaN shell (not considered to be part of the strain partitioned heterostructure) imposes additional c-axis constraints to the alternating InGaN/GaN layers, and can further encourage an out-of-plane strain accommodation in the alloy layers within the superlattice. Specifically, the tensile and compressive in-plane strains within GaN barriers and InGaN QDs, coloured blue and red, respectively, in Figure 2.8, will also lead to an out-of-plane distortion through the Poisson effect. However, this distortion does not occur fully within the InGaN/GaN layers, and residual strains remain to match the constraints from the surrounding GaN shell, as visible within the GaN barriers in the ϵ_{yy} map of Figure 2.6(c). Growth of a subsequent InGaN QD can accommodate the residual compressive ϵ_{yy} strain in the underlying GaN barriers through the InGaN alloy by affecting the incorporation of In during its formation to counteract the volumetric distortion. It should be noted that higher incorporation of In into a subsequent InGaN QD will have some additional compression on the underlying GaN barrier lattice, but it is expected to be minimal; because the GaN barrier is already compliant to the prior InGaN QD, back propagation of additional strain into QDs formed previously during the sequence is unlikely. Due to the complexity of the DWire structure in the presence of a GaN shell, further calculations using finite-elemental modeling (FEM) could assist in interpreting the three-dimensional strain accommodation. Existing FEM done on similar InGaN/GaN nanowire heterostructures that also include a GaN shell [15, 140], however, shows an opposite trend for the in- and out-of-plane strains in the GaN shell compared to related GPA measurements, even though those same experimental results are in agreement with this study. The discrepancy can be due to the insufficient resolution, as well as indirect measurements of the in-plane direction with high-resolution X-ray diffraction (HRXRD) used by Knelangen et al. [15]. Additional input parameters, such as those from in-plane distortions measured locally and directly in this study, can further improve the interpretation of strain accommodation in such structures with the help of FEM.

2.6 Independent Determination of Strain and Composition

Elemental mapping providing compositional information at very high spatial resolution is crucial for understanding the growth of nitride heterostructures, in particular for those contained in a nanowire geometry, which show even more fluctuations in their structural parameters. Composition determination within nanowire structures is significantly more difficult than in epilayers, as structural parameters have shown drastic fluctuations in composition,

demonstrated using conventional HRXRD [142]. Significant success has been achieved on planar heterostructures; however quantification of alloy composition is overall hindered by the inherent inhomogeneity that has been observed to occur over nm-lengthscales in nitride alloys [15, 80, 144], and by the inability to resolve these nanoscale variations with HRXRD. Another obstacle is the commonly convoluted effects of both the epilayer composition and strain state, effects which are not so straightforwardly disentangled [146, 156]. Determining composition using (S)TEM lattice images generally involves measuring the local out-of-plane lattice parameter, and subsequently calculating the composition [15, 142, 143] based on assumptions about the in-plane strain state (InGaN layer grown pseudomorphically to GaN). This assumption does not hold within the InGaN/GaN heterostructure presented in this study, where the InGaN QDs were shown to be partially strain-relaxed. A more direct and accurate quantification method of individual atomic column intensity in HAADF images is possible [147], but requires comparison with calculation-intensive image simulations that takes into account the varying statistical distribution of In/Ga-atoms and the resulting atomic displacements due to the large disparity in neighbouring atom sizes within an alloy. It has been reported recently that both the In-content and the thicknesses of InGaN insertions in axial InGaN/GaN nanowire heterostructures contribute to the combined effects of polarization potentials and surface potentials on carrier localization [157]. The nanowire structures in this study are expected to have weaker surface potentials in the presence of a thin passivating GaN shell, but will also vary proportionally with the overall nanowire diameter [157]. Therefore, the ability to determine both the composition and strain accommodation of InGaN QDs simultaneously, and independently, with their size and morphology at high spatial resolution facilitates a better assessment of the relationship between structural and optical properties.

It is worth noting that the quantitative elemental mapping methods using STEM-EELS implemented in this chapter, as demonstrated in InGaN QDs centrally-embedded within nanowires, are still prone to projection effects common in most TEM techniques. Similar to the work on composition measurement in buried In(Ga)As QDs grown on planar GaAs [149], substantial approximations need to be made about the shape of the QD in order to deduce its resulting two-dimensional projection surrounded by a GaN shell and obtain quantitative compositional information. However, the use of this quantification method in planar nitride heterostructures (made into wedge-shaped TEM specimen geometry, for example) would reduce the projection issues and increase the quantification accuracy greatly. The validity of the quantification method was already demonstrated in Figure 2.2 within an earlier Section 2.2.3.

Several additional important points can be made based on the high-resolution imaging

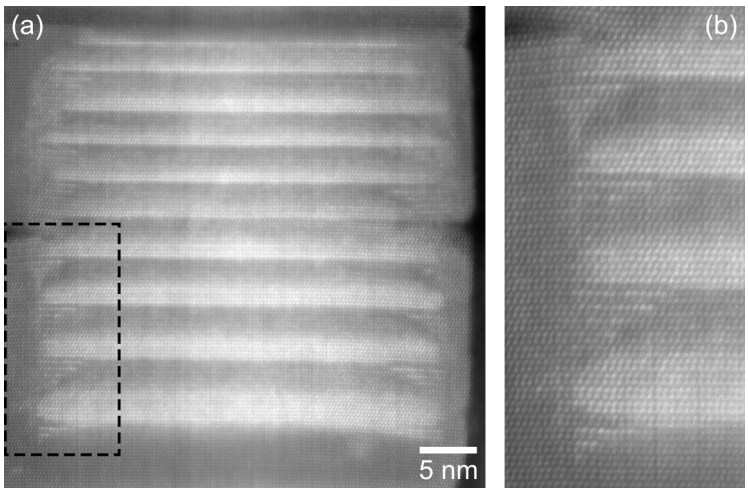

Figure 2.9: **(a)** STEM-HAADF image of the nanowire studied using STEM-EELS spectrum imaging in Figure 2.5, and **(b)** higher magnification image of the boxed area in **(a)** showing the presence of alternating bright and dark *c*-planes in the tails of the InGaN QDs, suggestive of atomic-level chemical ordering into In-rich and Ga-rich layers. Also visible in **(b)** is the atomic displacement near the crack with visible extra planes.

and quantification with EELS. Drastic interdiffusion of In within the active region can be ruled out from the sharp GaN/InGaN interface observed in atomically-resolved HAADF images (most evident in examples such as Figures 2.1(b) and 2.9(a)), which is further supported by high-resolution elemental mapping. Other composition determination methods in (S)TEM for buried QDs involving digital processing of lattice images require assumptions made about the strain state [143], and do not exclude the likely strain effects on the lattice parameter. Whereas the independent determination of the InGaN QD composition from EELS has negligible dependence on strain, such that the strain state can be deduced separately, as demonstrated in this study.

The large range of composition measured in individual nanowires using STEM-EELS suggests that the resulting InGaN alloy composition within these short-period nanowire heterostructures may not depend only on parameters controlled within the growth recipe, such as the substrate temperature, and In/Ga flux ratios. Additional factors such as the strain state of the underlying GaN layer during growth are suggested to play a role in enhancing or suppressing the In incorporation during the formation of the InGaN QDs. Furthermore, unusual bright/dark contrast modulations in single *c*-planes observed within InGaN tails just below the QDs, visible in the HAADF image of Figure 2.5(a) (seen in higher magnification in Figures 2.9(a) and 2.9(b)), are suggestive of the occurrence of atomic ordering in the InGaN alloy [79]. In fact, theoretical predictions for cubic-InGaN have suggested that biaxial strain within the alloy suppresses phase segregation but alternatively provides driving force for other types of spinodal decomposition, such as chemical ordering [158]. The confirmation of atomic ordering in the InGaN alloys within the nanowire heterostructures, as well as their implications on the resulting optical properties, will be detailed in its entirety in Chapter 3.

2.6.1 Piezoelectric Polarization Estimate

As an additional benefit of combined independent measurements of composition and strain within the InGaN/GaN QD heterostructure, they can be used to experimentally derive the resulting piezoelectric polarization, in order to understand the effects of these aforementioned structural properties on polarization. In particular, the GaN-shell-corrected In-compositions in the nanowire of Figure 2.5, in conjunction with the strain maps providing the $\Delta a/a^{ref}_{GaN}$ and $\Delta c/c^{ref}_{GaN}$ (Figures 2.10(b) and 2.10(d), respectively), were also used to calculate the actual ϵ_{xx} and ϵ_{yy} (more typically referred to as ϵ_{zz} or ϵ_{33} in the literature) within each QD, to be detailed in Section 2.6.1.1. Furthermore, the piezoelectric polarization, P_{pz}, within each QD is calculated according to the relationship between the strain tensor and piezoelectric constants (e_{31} and e_{33}) and listed in Table 2.1. As compared to equivalent pseudomorphic planar QW heterostructures of identical composition, the strain mapping of Figure 2.10 (and also in the other example in Figure 2.6) shows that the QD heterostructures are drastically more strain-relaxed in the in-plane direction as a result of the strain partitioning. The decreased ϵ_{xx} would directly translate to a $> 50\%$ decrease in the P_{pz} alone in the QDs. However, additional constraints along the y-axis from the GaN shell contribute to an out-of-plane component (non-zero normal stresses) that counteracts the in-plane component. Nevertheless, the calculated total P_{pz} in the high-In content InGaN QDs in this study (Figure 2.5) are still suppressed with respect to equivalent planar QWs by 30% on average, and similar in magnitude to those reported by Lähnemann et al. [140] for their InGaN insertions in GaN nanowires with the same range of In-content [15]. These P_{pz} values confirm that the magnitude of internal piezoelectric fields within nanowire heterstructures, while reduced due to enhanced lateral strain relaxation, is still significant ($\sim$4.5 MV/cm). In addition, the limitation on the field reduction predicted in nanowires is dominated by residual strains in the growth direction in embedded heterostructures.

2.6.1.1 Translating Lattice Deformations to Lattice Strain

The GPA method [71] was applied to atomic-resolution HAADF images corresponding to the same nanowire in Figure 2.5 to better understand the strain distribution, as shown in Figure 2.10. The HAADF images of Figures 2.10(a) and 2.10(c), were acquired along the $\langle 11\bar{2}0\rangle$ viewing direction (a-plane), and reciprocal lattice vectors, g = 0002 and g = $1\bar{1}00$, were selected for the GPA analysis. Seen laterally across the nanowire diameter (denoted as the x-axis) in the ϵ_{xx} map (Figure 2.10(b)), there is on average a 2.5% lattice expansion within the InGaN/GaN QD heterostructure with respect to the fully relaxed n-GaN region used as reference. Additionally, the GaN shell does not show a discernible difference in $\Delta a/a^{ref}_{GaN}$ to

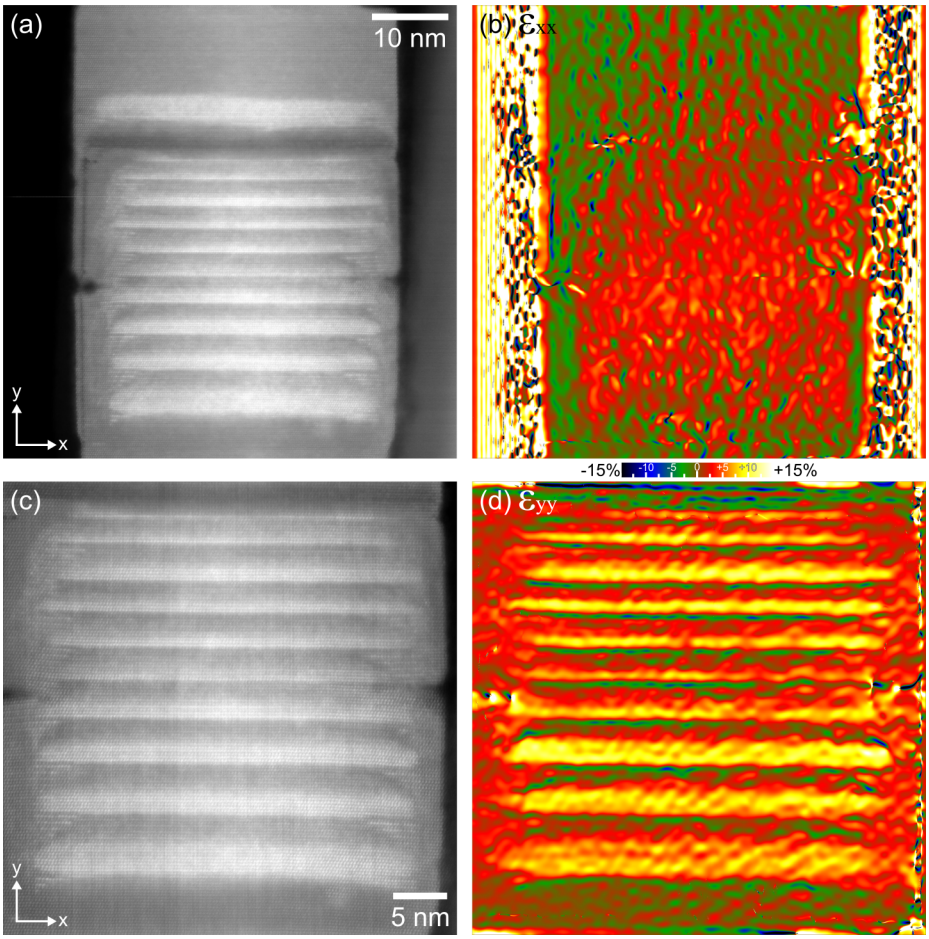

Figure 2.10: **(a)** STEM-HAADF image of the nanowire studied using STEM-EELS spectrum imaging in Figure 2.5, and **(b)** its corresponding strain map along the in-plane direction, ϵ_{xx}. **(c)** STEM-HAADF image of the same active region, acquired 90 degree rotated to minimize scan distortion effects along the slow-scan direction then displayed with rotation corrected, and **(d)** its corresponding strain map along the growth direction, ϵ_{yy}.

the n-GaN, justifying that the GaN shell and n-GaN have very similar a-spacing. Along the growth direction for the whole active region in Figure 2.10(c) (denoted as the y-axis), the ϵ_{yy} map (Figure 2.10(d)) shows similar results as Figure 2.6(c). The larger field of view in Figure 2.10(c) allows the n-GaN base to be used as reference lattice, which illustrates that the GaN shell is partially elongated along the c-axis to accomodate to the large expansion in the adjacent InGaN/GaN QD heterostructure.

$$\begin{aligned} \epsilon_{xx}^{InGaN} &= \frac{a_0^{GaN}(1+\Delta a/a_{GaN}^{ref}) - a_0^{InGaN}}{a_0^{InGaN}} \\ \epsilon_{zz}^{InGaN} &= \frac{c_0^{GaN}(1+\Delta c/c_{GaN}^{ref}) - c_0^{InGaN}}{c_0^{InGaN}} \end{aligned} \tag{2.2}$$

Table 2.1: Calculated in-plane (ϵ_{xx}) and out-of-plane (ϵ_{zz}) strains, and the resulting piezoelectric polarization (P_{pz}, C/m^2) for each InGaN QD from the nanowire in Figures 2.5 and 2.10, and compositionally equivalent InGaN QWs grown pseudomorphically on GaN. The measured and corrected composition and lattice parameter changes of each QD according to Section 2.2.3.2 is also shown. QDs are numbered by their sequence along the growth direction (from bottom to top).

				Theoretical QWs			From GPA	Experimental QDs		
QD Number	Measured x	Correction Factor	Corrected x	ϵ_{xx}^{QW}	ϵ_{zz}^{QW}	P_{pz}^{QW}	$\Delta c/c_{GaN}^{ref}$	ϵ_{xx}	ϵ_{zz}	P_{pz}
10	0.115	0.673	0.171	−0.0187	0.0105	0.0270	0.0555	+0.0058	0.0377	0.0233
9	0.201	0.841	0.239	−0.0260	0.0149	0.0382	0.0830	−0.0016	0.0578	0.0471
8	0.302	0.850	0.355	−0.0381	0.0229	0.0582	0.0948	−0.0141	0.0573	0.0613
7	0.302	0.849	0.356	−0.0382	0.0230	0.0584	0.0901	−0.0142	0.0527	0.0577
6	0.327	0.804	0.406	−0.0434	0.0266	0.0674	0.0758	−0.0195	0.0338	0.0483
5	0.266	0.759	0.351	−0.0377	0.0226	0.0574	0.0621	−0.0136	0.0262	0.0354
4	0.288	0.811	0.354	−0.0381	0.0229	0.0581	0.0708	−0.0140	0.0342	0.0424
3	0.378	0.830	0.456	−0.0484	0.0302	0.0763	0.0855	−0.0246	0.0383	0.0580
2	0.367	0.832	0.440	−0.0469	0.0291	0.0736	0.0771	−0.0230	0.0317	0.0507
1	0.321	0.851	0.377	−0.0404	0.0245	0.0621	0.0667	−0.0164	0.0280	0.0400

$\Delta a/a_{GaN}^{ref} = 0.025$ was used for all QDs to calculate ϵ_{xx}.

$$P_{pz} = e_{31}(\epsilon_{xx} + \epsilon_{yy}) + e_{33}\epsilon_{zz} \tag{2.3}$$

The corrected In-compositions in Table 2.1 and the lattice distortions from the strain maps providing the $\Delta a/a_{GaN}^{ref}$ and $\Delta c/c_{GaN}^{ref}$ were also used to calculate the actual ϵ_{xx} and ϵ_{zz} (referred to as ϵ_{yy} in the GPA strain map of Figure 2.10) within each QD in Figure 2.10 with Equation (2.2). The piezoelectric polarization P_{pz} within each QD is calculated according to the relationship between components in the strain tensor and piezoelectric constants, given in Equation (2.3), where $\epsilon_{xx} = \epsilon_{yy}$ due to isotropic hardness along the basal plane in wurtzite-structured III-nitride materials [159]. In addition, the corrected In-compositions in Table 2.1 were used to calculate the piezoelectric polarization (P_{pz}^{QW}) expected in corresponding planar InGaN quantum wells (QWs) of the same composition grown pseudomorphically on GaN, assuming biaxial strain conditions. A linear composition-dependence of the piezoelectric constants (e_{31} and e_{33}) and material elastic constants (C_{13} and C_{33}) is assumed for the alloy, so that the alloy material constants can be interpolated between the values for GaN and InN listed in Table 2.2.

The GPA strain mapping shows that the QD heterostructures are drastically more strain relaxed in the in-plane direction than the corresponding pseudomorphic QW heterostructures, as a result of the strain partitioning. The decreased ϵ_{xx} directly translates to a >50% decrease in the in-plane strain contributions to P_{pz} alone in all QDs when compared to the theoretical QWs. However, additional constraints along the z-axis from the GaN shell contributes to an out-of-plane component that counteracts the in-plane component due to the opposite signs of piezoelectric constants e_{31} and e_{33} (to account for the opposite signs of ϵ_{xx}

Table 2.2: Lattice parameters [30], elastic constants [30] and piezoelectric constants [60] for wurtzite binaries of GaN and InN used to calculate parameters for the InGaN alloy according to Vegard's Law.

Parameters	GaN	InN
a (Å)	3.189	3.545
c (Å)	5.185	5.703
C_{13} (GPa)	106	92
C_{33} (GPa)	398	224
e_{31} (C/m^2)	−0.49	−0.57
e_{33} (C/m^2)	0.73	0.97

and ϵ_{zz}). In the nanowire example of Figure 2.10, the effect of the counteracting in-plane and out-of-plane strain components on the P_{pz} is particularly strong in the last four QDs, where the changes relative to P_{pz}^{QW} of the pseudomorphic QW are insignificant or even leading to an increase in P_{pz}. Nevertheless, the magnitudes of the calculated P_{pz} in the high-In content $In_xGa_{1-x}N$ QDs (x ≈ 0.40) in this study are similar to those reported by Lähnemann et al. [140] of 0.044 C/m^2 for the In-rich surface-segregated region (x ≈ 0.39) within their much larger InGaN insertions [15].

2.6.1.2 Implications on Optical Properties

The role of these compositional variations on the optical properties in nanowire heterostructures can be further interpreted. Assuming a linear dependence of the bandgap as a function of alloy composition given by Vegard's law and neglecting possible bandgap bowing, the composition is estimated relative to emission wavelength and is also marked for the PL spectrum of Figure 2.1(c). Without taking into account strain and quantum confinement effects, the range of compositional variation amongst the InGaN QDs within individual nanowires measured by EELS can be the main contributor to the broad linewidth and asymmetric spectral shape of the main emission peak from the nanowire LEDs shown in Figure 2.1(c). The main peak at 550 nm contains prominent shoulders that can be deconvolved into multiple emission peaks with narrower linewidths, and also demonstrated in Figure 2.1(c) using Voigt functions, where each peak could effectively originate from different QD compositions.

Notably, the range of InGaN compositions that corresponds to the prominent shoulders in the PL spectrum overlaps only with the upper end of the EELS-measured alloy composition. Interpretation of the PL spectrum is not as straightforward with the InGaN QW present, but despite measuring QDs with composition that would correspond to emission at λ = 420 – 450 nm, only a singular peak assigned to the InGaN QW was present. Furthermore, in the absence of the InGaN test well (*cf.* LED III in Ref. [85]), no discernible PL intensity is observed in the same wavelength range despite nanowires showing similar

structural composition in the active region (results not shown). These results are in agreement with the monotonic decrease in PL intensity with decreasing In-content previously observed in nanowire MQWs [142], as well as with the high total P_{pz} calculated for the low In-content QDs ($x \approx 0.2$ – 0.25) in this work, which are contradictory to the properties of planar MQWs. The anomalous trend in similar InGaN/GaN nanowire heterostructures was explained by the severe lateral separation of carriers at low In-content due to a strong influence from surface potentials [157]. While the spectral fitting shown in Figure 2.1(c) is not unique, it illustrates that individual InGaN QDs with a variable range of compositions can produce a series of overlapping emission peaks. Higher intensity emission will likely occur towards the longer wavelengths, as the InGaN QDs with lower In-content will be more strongly affected by piezoelectric polarization and the effects of the surface potential, and will have a reduced lateral electron-hole overlap. The effect is further manifested in an ensemble of nanowires that contain individual nanowires each exhibiting slightly varied ranges of composition, resulting in the broad emission peak with apparent shoulders.

2.7 Conclusion

In summary, a correlative investigation of composition and local strain state in InGaN/GaN DWire structures has combined strain mapping from HAADF imaging and independent composition determination from core-loss EELS elemental mapping using scanning transmission electron microscopy. The nanowires exhibit unique structural characteristics, including an inhomogeneous lateral strain distribution, and accommodation within the heterostructure by strain partitioning. However, it is the residual strains along the growth direction that is the main determinant of various properties, namely the indium incorporation and magnitude of piezoelectric polarization. The out-of-plane strain within GaN layers is suggested to be responsible for the observed compositional variation within the series of ternary QDs, as a result of the strain evolution along the growth direction. Both of these effects can contribute to the unexpectedly broad emission peaks observed within these nanowire structures with room-temperature PL. Additionally, the measured strains and compositions are used to calculate the expected local piezoelectric polarization, which shows a significant suppression compared to equivalent planar QWs, but is still not negligible. These findings are discussed in terms of the interplay of effects on the optical properties that needs to be understood in order to obtain controlled emission properties. This study therefore provides critical insight into the epitaxial growth and characterization of In-containing III-nitride nanowire heterostructures, which have demonstrated potential in emerging applications for solid-state lighting, photovoltaics, imaging and displays.

Chapter 3

Atomic Ordering of InGaN Alloys within Nanowire Heterostructures

3.1 Introduction

Ternary InGaN compounds have been studied for optoelectronic applications spanning a large spectral range between the ultraviolet and infrared, including light-emitting diodes (LEDs), and laser diodes [26, 160]. The large difference in cation covalent radii [68] is the cause of the alloy non-ideal mixing behaviours, as described by the theoretically calculated miscibility gap in the InGaN system [138]. This thermodynamic instability has been related to experimental evidence of various phase separation, surface segregation [68], and chemical ordering [78, 79] processes involving the cation species that result in compositional fluctuations and inhomogeneity within InGaN epilayers. The existence of In-clustering as-grown in InGaN alloys, which effectively localizes carriers within LEDs overcoming the high threading dislocation density, remains an ongoing controversy whether or not they were due to electron beam damage [76, 77]. Additionally, the heteroepitaxy of InGaN alloys, often on substrates or buffer layers with smaller lattice parameters (typically GaN), are affected by biaxial compression. The presence of strain also plays a role in the alloy stability [80], and spontaneous ordering or formation of compositional superlattice in III-Ns [161–163].

Atomic ordering in ternary and quaternary III-V alloys is not uncommon within epitaxial thin films of various cubic III-V arsenides and phosphides, whose degree of ordering has shown a strong dependence on the growth conditions [164]. However, the hexagonal nitride ternary alloys are notorious for their several distinctly different optical properties as compared to other As- and P-compounds, including the large bandgap bowing and large Stokes shift [24]. Strong exciton localization in nitride alloys has been attributed to these anomalous

properties, which are even affected by fluctuations in the distribution of nearest-neighbors on the atomic-scale [165]. Experimental observation of chemical ordering in both InGaN [79] and AlGaN [78] alloys have been reported in wurtzite-structured layers deposited on hexagonal substrates (typically sapphire or 6H–SiC) using molecular beam epitaxy (MBE) or metalorganic chemical vapor deposition methods. Most studies reported the existence of atomic ordering with a 1:1 periodicity along the [0001] direction of growth, based on the presence of the otherwise forbidden diffraction peaks or spots in a wurtzite crystal structure from θ–2θ X-ray diffraction (XRD) [78] or electron diffraction in transmission electron microscopy [79]. These additional superlattice reflections (*e.g.* 0001 and $000\bar{1}$, or other $000l$ where l is odd) indicate a break in the symmetry along the c-axis caused by a non-random atomic site occupancy of the group-III atoms within the two unique cation sublattice positions ((0,0,0) and $(\frac{1}{3},\frac{2}{3},\frac{1}{2})$) in a wurtzite unit cell [166]. The preferential site occupation within the cation sublattice is consistent with a superlattice structure of alternating c-planes of Ga-rich and In(Al)-rich monolayers. Existence of other more complex ordered structures with longer periods has also been established [163, 166–169].

The spontaneous formation of ordered ternary nitride alloys is still largely not understood due to the nature of these growth processes occurring far from equilibrium conditions, but has been often regarded as a kinetically-limited growth surface-induced process. However, there is evidence of some composition dependence for their formation that can be explained using a thermodynamical approach, with the ideal ordered $(Al/In)_xGa_{1-x}N$ alloy at composition of $x = 0.5$ based on the relative superlattice XRD peak intensity maxima [78]. First-principle calculations of ordering in both InGaN [170] and AlGaN [165] have suggested that $\{10\bar{1}1\}$ pyramidal microfacets expose surface sites on alternating c-planes that exhibit different N-coordination, leading to preferential incorporation of the larger cation at the reduced N-coordination site in an ordered fashion. Overall, experimental evidence differentiating the two unique cation site positions and their elemental occupancy is lacking, and requires further investigations at atomic-resolution that allows the visualization of both group III and N-atoms. Furthermore, atomic ordering demonstrates a bandgap reduction of the nitride alloy both theoretically [171] and (compared to its random AlGaN alloy equivalent) experimentally [165], and may significantly modify other electronic properties including optical and transport properties [165, 172], as well as their intrinsic piezoelectric properties [173]. More recent calculations of microscopic ordering in compressively strained InGaN layers with a $\sqrt{3} \times \sqrt{3}$ pattern periodicity along the in-plane direction, which corresponds more closely to the nanoscale lateral phase separation [174], can instead increase the bandgap by 0.1 – 0.15 eV [175].

In this chapter, InGaN/GaN nanowire (NW) heterostructures, grown on Si(111) sub-

strates by MBE [176], were investigated using various techniques in scanning transmission electron microscopy (STEM) to understand the formation of bilayer atomic ordering with 1:1 periodicity in InGaN alloys. The InGaN/GaN dot-in-a-wire structures show a high degree of crystallinity and little to no defects (some stacking faults, but no threading dislocations). Thus nanowires provide the model system to understand the alloy ordering mechanism and conditions that favour their occurrence, as well as any benefits or implications on device properties. The techniques carried out at atomic-resolution, including local crystal polarity determination and elemental analysis, allow to distinguish the two unique cation sublattice positions within a wurtzite unit cell, and confirm the localization of In-atoms preferentially within one of the cation sites. Comparison of nanowires with a single and multiple InGaN QDs also demonstrates that the growth of highly atomic ordered InGaN QDs can be systematically induced.

3.2 Experimental Methods

3.2.1 MBE Growth

Catalyst-free, vertically-aligned InGaN/GaN dot-in-a-wire heterostructures were grown on 2-inch Si(111) substrates using a Veeco Gen II molecular beam epitaxy (MBE) system at McGill University equipped with a radio frequency plasma-assisted nitrogen source under nitrogen-rich conditions. Si substrates were first cleaned in hydrofluoric acid (10%) to remove surface oxide before loading to the MBE chamber. Subsequently, the substrates were in situ degassed at ∼770 °C in the growth chamber prior to the growths. During the growth process, the nitrogen flow was kept at 1.0 standard cubic centimeter per minute (sccm) with a forward plasma power of ∼350 W. The light-emitting diode (LED) active region consisting of 10 InGaN/GaN dots, each composed of ∼3 nm InGaN and ∼3 nm GaN barrier layer, was grown on ∼0.4 μm GaN:Si nanowire base as schematically shown in Figure 3.1(a). The remaining LED structure also consists of a ∼10 nm p-doped AlGaN electron blocking layer (EBL) grown in between the LED active region, and ∼0.2 μm GaN:Mg segment. Finally, an AlGaN layer of ∼40 nm was grown on top of the nanowire for the formation of an AlGaN shell layer. The GaN:Si and GaN:Mg segments were grown at ∼750 °C. The InGaN/GaN quantum dot (QD) active region was grown at relatively low temperatures (∼610 – 630 °C) to enhance In incorporation in the QDs. The growth rate for the InGaN/GaN QD active region is ∼1 nm/min. Typical nanowire diameters are ∼50 – 75 nm. The single InGaN QD in GaN nanowire samples were grown at similar growth conditions but without the additional AlGaN EBL and top AlGaN layer, as illustrated in Figure 3.1(b). A 3-dimensional model of

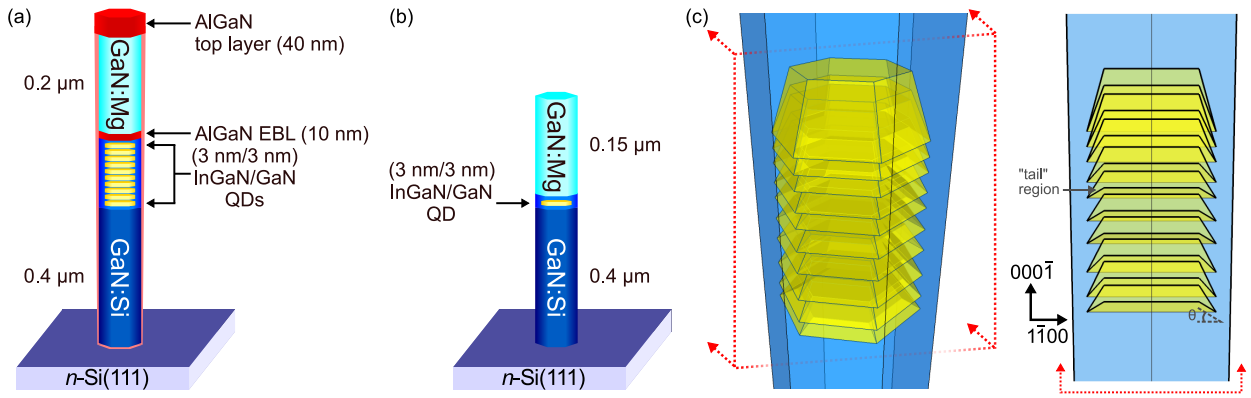

Figure 3.1: Schematic illustration of the InGaN/GaN dot-in-a-wire heterostructure with **(a)** multiple (10) QDs and additional AlGaN EBL and top AlGaN layer, and **(b)** a single InGaN QD. **(c)** 3-D schematic model of the multiple dot-in-a-wire structure and a corresponding cross-sectional cut-out along a-plane at the center of the nanowire, section plane is outlined by dotted red box along direction of the arrows. The "tail" region and the angle of inclination relative to the c-plane, θ, are also marked in the cross-section view.

a multiple dot-in-a-wire structure, detailing the complex bent morphology of the QDs that originated from a faceted growth front, and resulted in their nested-like nature along the growth direction is presented in Figure 3.1(c).

3.2.2 STEM Characterization

The scanning transmission electron microscopy (STEM) was performed using a FEI Titan Cubed 80-300 STEM, fitted with a high-brightness field-emission gun (X-FEG), aberration-correctors on both the probe- and image-forming lens systems, a monochromator, and a high-resolution electron energy-loss spectrometer (Gatan GIF Quantum 966). All experiments were carried out at an accelerating voltage of 200 kV, except for the annular bright-field (ABF) imaging which was done at 300 kV, with 19 mrad convergence angle. Atomic-number sensitive (Z-contrast) high-angle annular dark-field (HAADF) images were obtained using a detector angular range of 63.8 – 200 mrad, and ABF images using a detector angular range of 5 – 31 mrad. Elemental mapping by electron energy-loss spectroscopy (EELS) in STEM mode was done with the N K, In $M_{4,5}$, and Ga $L_{2,3}$-edges using the spectrum imaging technique. Typical beam currents and dwell times used during STEM imaging are 40 – 45 pA, and 6 – 20 μs, respectively. Beam current and dwell time used during the atomic-resolution STEM-EELS mapping are 50 – 60 pA, and 5 ms, respectively, with the total acquisition time of each spectrum image under 30 s.

Based on these acquisition conditions for imaging and spectroscopy in STEM, the estimated current density with a ~1 Å probe is ~$5.1 - 5.7 \times 10^5$ A/cm^2 and $6.4 - 7.6 \times 10^5$ A/cm^2,

respectively. The range of total electron dose sustained during STEM imaging, dependent on the dwell time and pixel size, is ∼5 – 160 C/cm^2 and well below the 7700 C/cm^2 threshold dose for electron beam damage reported in Ref. [77]. The total dose for the EELS spectrum imaging is ∼3200 – 3800 C/cm^2, which is half of the damaging dose from Ref. [77], but can be exceeded due to oversampling at atomic-resolution. Therefore a high-dose technique like EELS could induce radiation damage within the InGaN, resulting in an inhomogeneous strain distribution. However, images before and after (Figures 3.5(a) and 3.5(b), respectively) the elemental mapping in Figure 3.5 showed no significant electron beam damage. Furthermore, the conclusions regarding the atomic-ordering can be confirmed from the lower-dose STEM imaging alone. The elemental mapping is solely to confirm the chemical composition origin of the modulated Z-contrast in the ordered InGaN alloys.

3.2.2.1 Sample Preparation

The as-grown nanowires samples were mechanically removed from the Si substrate, dispersed in anhydrous ethanol, and deposited on carbon-coated TEM support grids for observation. Longitudinal cross-sectional samples of nanowires were prepared by focused ion beam (FIB) milling using a Zeiss NVision 40 dual-beam system with deposited W as protection layer, followed by subsequent low-energy Ar-ion thinning using a Fischione Model 1040 NanoMill®. Nanowires shown in Figure 3.2(a) (same in Figures 3.4 and 3.9), Figure 3.5, and Figure 3.6 are separate as-grown nanowires, while nanowires in Figure 3.2(b), and Figure 3.3 (same in Figures 3.7 and 3.8) are separate FIB cross-sections. Extraneous dot-like contrast on FIB cross-sections is a result of redeposition of W particles during the Ar-ion thinning and plasma cleaning.

3.2.2.2 Spectral Analysis

A multiple linear least-square (MLLS) fitting routine implemented within DigitalMicrograph was used to treat the EELS spectrum images to separate the N K-edge (399 eV) contributions from that of the In $M_{4,5}$-edge (451 eV in InGaN). The N K-edge from the nearby n-GaN region as internal reference (from a spectrum image of the same nanowire done at low magnification) combined with the In $M_{4,5}$-edge from an InN nanowire as an external reference were used for the MLLS fitting. Quantification of the In-content in the nanowire is achieved by subsequent normalization of the resulting In-map with the N-map derived from their respective MLLS fitting coefficients as described in Chapter 2. In group III-nitride materials, the III:N ratio equates to unity to maintain stoichiometry, therefore the projected thickness normalized In-content map from the use of the N-signal in $In_xGa_{1-x}N$ should contain values

corresponding to the In-composition (x).

3.3 Atomic-Scale Image Intensity Modulations

Atomic-number (Z-contrast) sensitive STEM high-angle annular dark-field (HAADF) imaging of the overall nanowire heterostructure is presented in Figure 3.2(a), illustrating the 10 centrally-embedded InGaN quantum dots (QDs) appearing as bright regions, each capped by a GaN barrier layer. The InGaN/GaN QDs make up the device active region between n- and p-doped GaN segments along the growth direction for these nanowire LEDs (see further details of the overall nanowire structure in Figure 3.1). Typically the InGaN QDs exhibit outer edges that are slightly to severely bent downwards (opposite the growth direction), with an angle of inclination (θ) from the c-plane ranging $\sim$15 – 60°, henceforth referred to as the QD "tails". The degree of bending observable in STEM depends on the particular zone-axis (a- or m-plane), demonstrated by the differences in projected shape for the nanowire in Figures 3.2(a) and 3.4. This establishes that the QD surface facets lie on $\{10\bar{1}l\}$ with $l = 1, 2, 3$, in order to be seen edge-on along a-plane orientation. Detailed imaging of the QDs along the c-axis growth direction in detail (Figure 3.2(b)) shows the presence of oscillatory HAADF intensity occurring at the atomic-level, exhibiting alternating bright/dark c-planes within the bulk of some QDs and at the outer QD "tails" when viewed in the $\{11\bar{2}0\}$ orientation. This is suggestive of 1:1 bilayer atomic ordering, as seen in the image intensity line profile in Figure 3.2(c).

3.4 Local Nano-Beam Electron Diffraction

Electron diffraction patterns (DPs) recorded from the ternary InGaN QDs were obtained in the $\{1\bar{1}00\}$ zone-axis in STEM mode (as convergent beam electron diffraction patterns with small discs due to the small 0.91 mrad convergence angle) to confirm the presence of superlattice reflections without any ambiguity from possible double diffraction common in the $\{11\bar{2}0\}$ orientation. The DP of Figure 3.3(b) and its corresponding intensity line profile (Figure 3.3(c)) along the c-axis show the presence of the otherwise forbidden 0001 and $000\bar{1}$ superlattice reflections with local intensity maxima at half the 0002 position, unambiguously confirming the presence of 1:1 bilayer atomic ordering within the ternary InGaN [79].

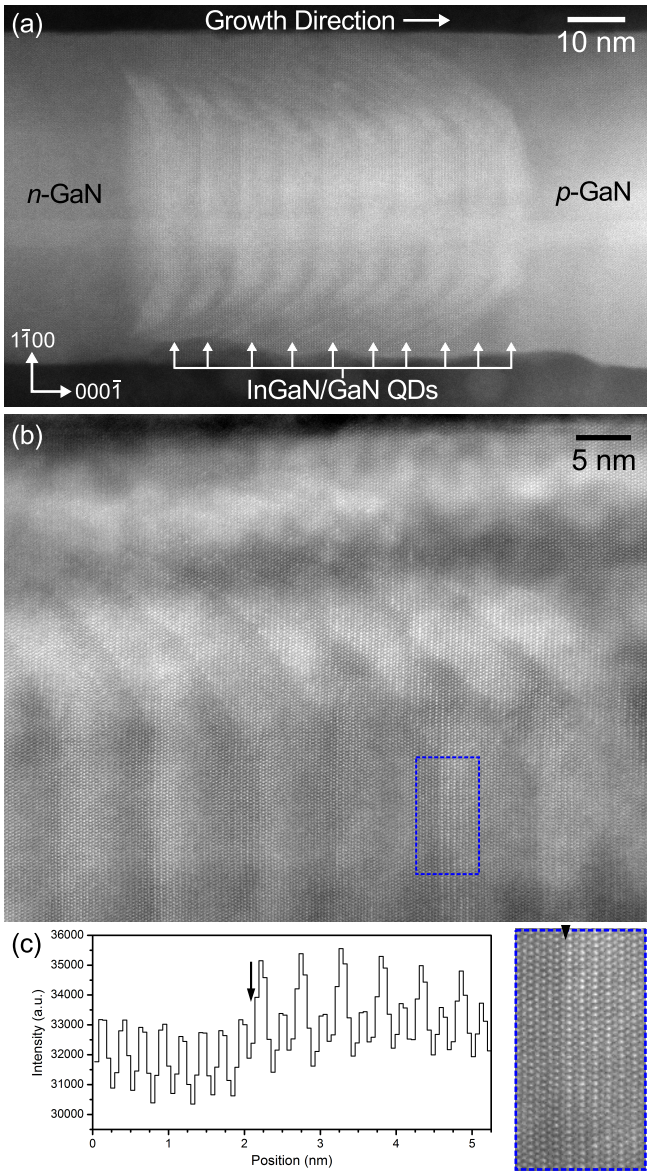

Figure 3.2: **(a)** STEM-HAADF Z-contrast image showing an overview of nanowire LED structure along the $\{11\bar{2}0\}$ zone-axis, namely the active region containing 10 InGaN/GaN QDs between the n-GaN and p-GaN segments. **(b)** High-magnification view of the active region, showing the oscillatory image intensity at the atomic-level within the bulk and the "tails" of the InGaN QDs. **(c)** Detailed view of the boxed region in **(b)** and its integrated intensity line profile.

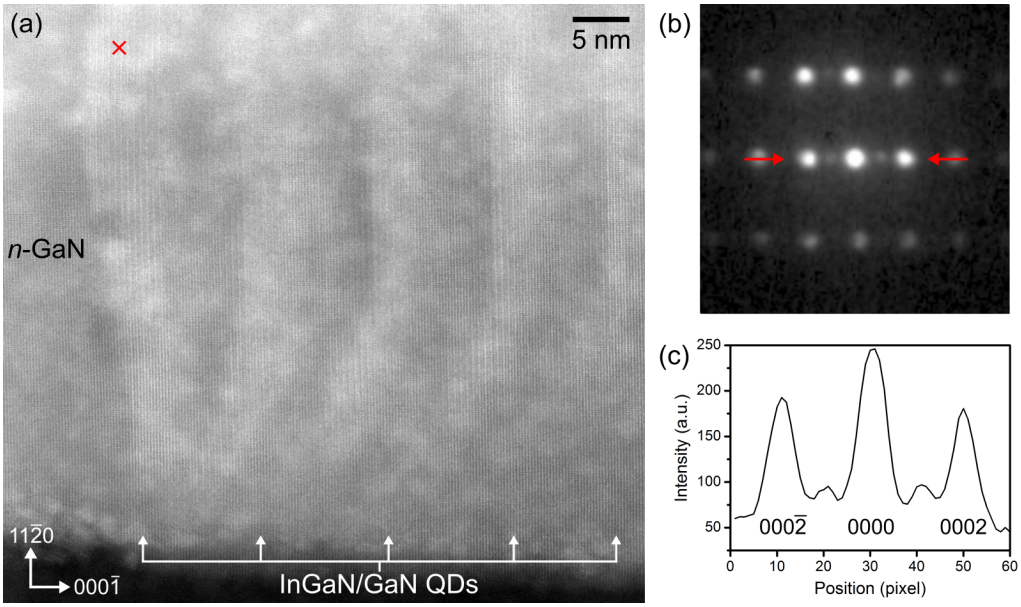

Figure 3.3: **(a)** STEM-HAADF image of the first four QDs in the active region, showing moderate variations in image intensity within the InGaN alloy viewed along the $\{1\bar{1}00\}$ zone-axis. **(b)** DP collected from QD#1 with the probe positioned in the area marked by a red cross in **(a)** showing the presence of superlattice reflections at half the periodicity of the fundamental reflections. **(c)** Intensity line profile of the DP in **(b)** between the arrows. Extraneous circular bright contrast in **(a)** is from redeposition of W particles during Ar-ion thinning and plasma cleaning.

3.4.1 Degree of Ordering

The prevalence for high degree of ordering within the first QD in the multiple QD nanowire heterostructures, and similarly in the single QD nanowires, is demonstrated in the diffraction pattern (DP) "spectrum image" of Figure 3.4 using the nanowire from Figure 3.2(a). Local DPs extracted along the $\{1\bar{1}00\}$ zone-axis were acquired using a ~nm-sized probe in STEM mode using a small convergence angle of ~0.91 mrad along the growth direction. Specific DPs (Figure 3.4(a)) from marked InGaN QD positions in Figure 3.4(b) exhibit the presence of superlattice reflections, further confirming the presence of atomic ordering within the InGaN alloy as also visible in the HAADF images along the two main orientations in Figures 3.4(c) and 3.4(d). Varying relative intensities between the superlattice *0001* and fundamental *0002* reflections are also observed between the different DPs, suggestive of a varying degree of ordering between the different InGaN QDs, *i.e.* different fraction of In-atoms occupying their preferred site at a particular composition. Specifically, the strongest superlattice spots commonly originate from within the tails of the first QD (red boxed DP in Figure 3.4(a)) or the bulk of the first QD in the nanowires observed.

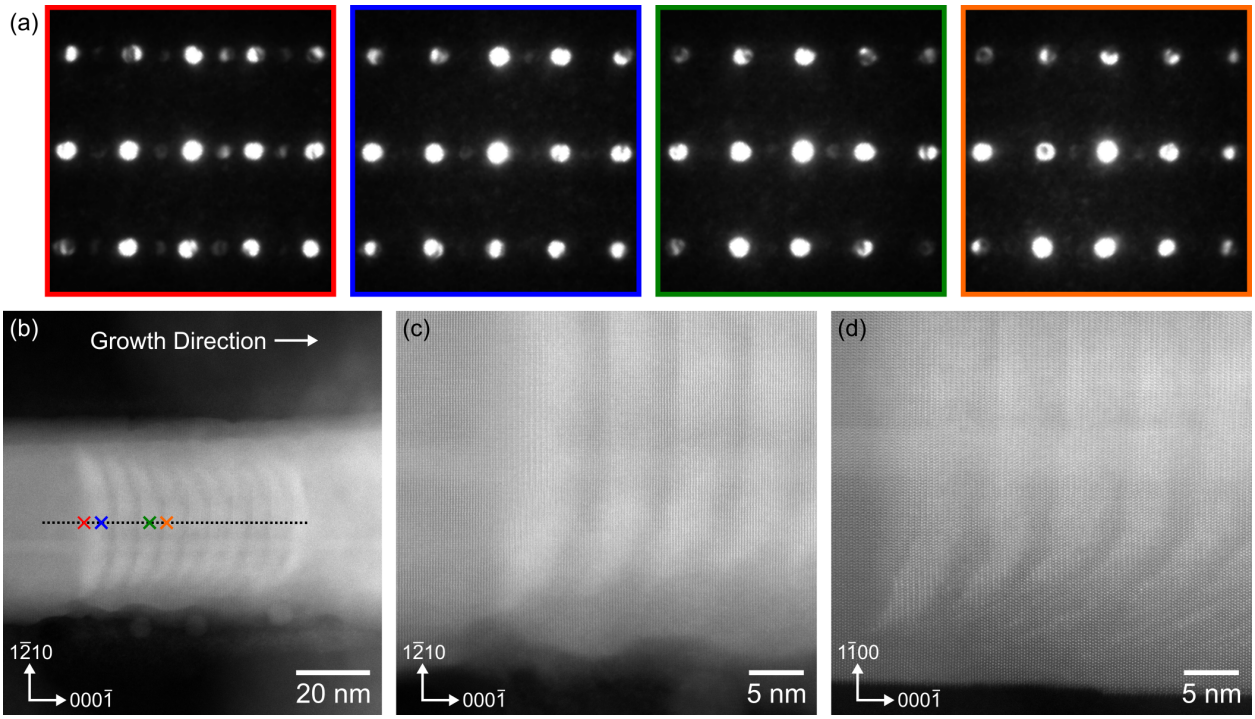

Figure 3.4: **(a)** $\{1\bar{1}00\}$ DPs collected with the probe positioned at different areas along the black-dotted line on the nanowire, each DP is color-coded with its position marker in (b). STEM-HAADF image of the nanowire from Figure 3.2(a) along the $\{1\bar{1}00\}$ zone-axis, **(b)** a low-magnification view with the probe positions of the DPs in **(a)** marked by colour-coded crosses, and **(c)** a detailed view of the QD#1–4 where intensity modulations in this orientation are also visible. **(d)** A detailed view of the same QD#1–4 along a $\{11\bar{2}0\}$ zone-axis tilted 30° away (same as in Figure 3.2(a)), where the intensity modulations due to ordering are more pronounced. The brightness and contrast of the DPs in **(a)** have been adjusted equally to emphasize the weaker superlattice reflections.

3.5 Localization of Indium Distribution in Single Dot Nanowires

The extent of the localization of indium in alternating planes within the ordered InGaN was further examined from atomic-resolution elemental mapping using electron energy-loss spectroscopy (EELS). The STEM-HAADF image of the InGaN QD within a single QD nanowire (comparable to first QD in the 10 dot-in-a-wire samples) and a high-magnification view demonstrating its ordering within its bulk is shown in Figures 3.5(a) and 3.5(b). The acquisition area of the spectrum image is boxed within Figure 3.5(b). Signal from the relevant In $M_{4,5}$-edge was extracted using multiple linear least-squares (MLLS) fitting methods described in Ref. [177] using external reference spectra from binary GaN and InN nanowires.

An In-map derived from the MLLS fitting coefficients (Figure 3.5(d) and its line profile in (g)) shows an In-enrichment in alternating c-planes that match the maxima in the HAADF

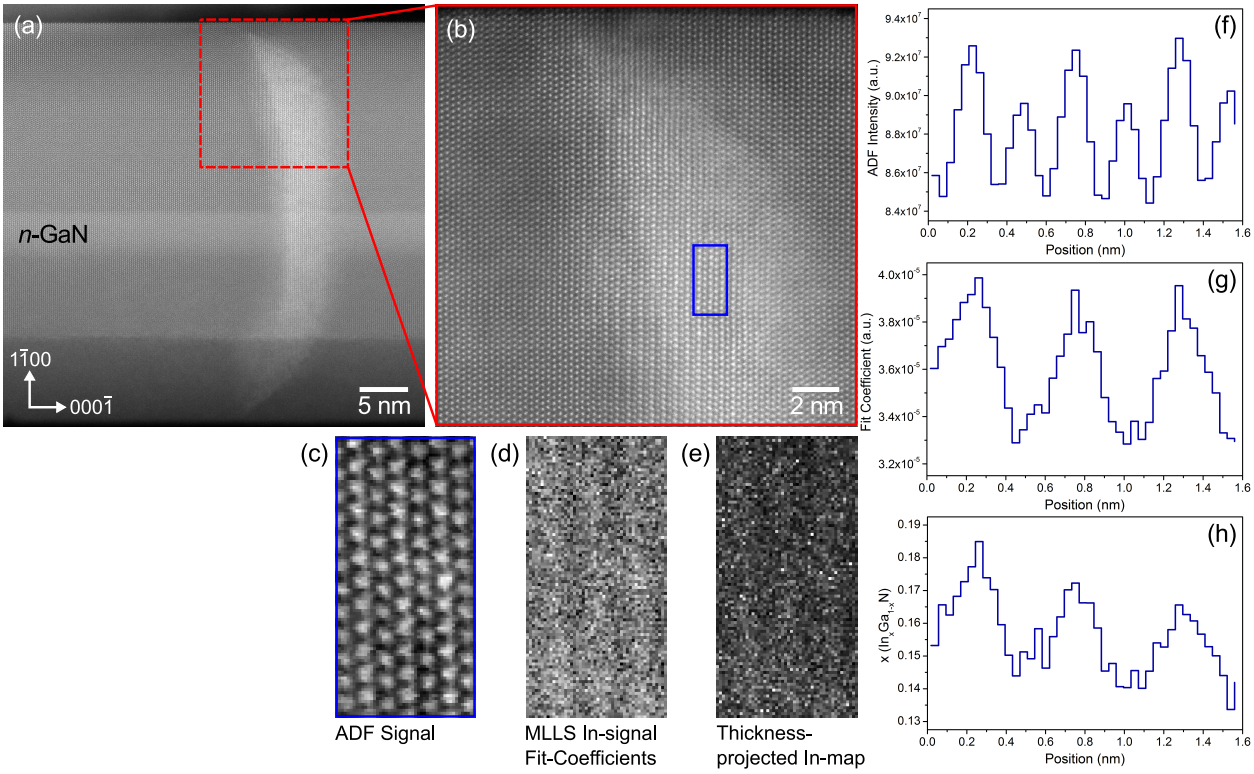

Figure 3.5: **(a)** STEM-HAADF image of the single QD and **(b)** its high-magnification view along the $\{11\bar{2}0\}$ zone-axis, showing the high degree of ordering within the bulk and the "tails" of the QD. Atomic-resolution STEM-EELS spectrum imaging of the region boxed in **(b)**, showing **(c)** the ADF signal collected concurrently, **(d)** the MLLS fit-coefficient map of the In-signal, and **(e)** the thickness-projected In-content map. Line profiles of the STEM-EELS maps in **(f)**–**(h)** shows that the localization of In corresponds to the ADF intensity maxima. Horizontal bands of contrast in **(a)** are likely planar defects seen inclined along the projection direction.

signal collected concurrently (Figure 3.5(c) and its line profile in (f)). Furthermore, following the pseudo-thickness normalization with the N K-edge signal described in Section 3.2.2.2 and detailed in a previous chapter (Section 2.2.3), a thickness-projected In-content map (Figure 3.5(e)) is also generated, showing that the In-content variation in alternating c-planes is significant. The average In-content within the bulk of this ordered $In_xGa_{1-x}N$ QD in Figure 3.5 is $x \approx 0.12 \pm 0.02$, approximate to the In-deficient planes composition. On the other hand, the In-rich planes exhibit an average deviation from the local mean composition by >25%, as shown in the line profile in Figure 3.5(h). Similar enrichment in additional elemental map of ordered QD in multiple dot-in-a-wire is shown in Figure 3.6. Due to the centrally-embedded nature of the QDs, the magnitude of the measured In-content variation between adjacent planes is expected to be underestimated due to additional contributions from the GaN shell present along the projected-thickness. In addition, beam broadening effects along the projection direction in a relatively thick specimen (∼35 nm) would also dampen out the relative difference in the STEM-EELS signal between the In-rich and Ga-rich planes.

It is important to note that superlattice peaks in XRD can also be attributed to the presence of nitrogen vacancy ordering [166, 178]. Extracted EELS spectra (see Figures 3.6(f) and 3.6(g)) from the In-rich c-planes show a significantly higher intensity in the In $M_{4,5}$-edge compared to the adjacent In-deficient planes. Conversely, the Ga $L_{2,3}$-edge (after normalizing the integral before the edge onset) shows the corresponding trend confirming the In-deficient planes are Ga-rich, supporting the suggestion of cation ordering as the cause for the superlattice reflections in the DP of Figure 3.3(b). A previous study of much larger-scale (few nm period fringes) compositional modulations in $In_{0.5}Ga_{0.5}N$, using energy dispersive X-ray spectroscopy in TEM, showed comparable systematic modulations in Ga and In concentration change distributed across the fringes [169]. Additional EELS analysis in the same study [169] showed a significant increase in the Ga $L_{2,3}$-edge intensity in spectra collected from the Ga-rich fringe, and no change in the N K-edge, but the direct contributions to the In $M_{4,5}$-edge in close proximity was neglected.

3.5.1 Localization of Elemental Signal in Multiple Dot-in-a-wire

The localization of indium between alternating planes within ordered $In_xGa_{1-x}N$ in multiple dot-in-a-wire samples was also demonstrated using atomic-resolution elemental mapping with STEM-EELS in Figure 3.6. The measured In-content in the tail of this ordered QD#1 is overall higher than the single QD in Figure 3.5, showing ranges between $x = 0.16 – 0.25$ in Figure 3.6(j). The In-rich planes exhibit an average enrichment of ∼32% from the local mean

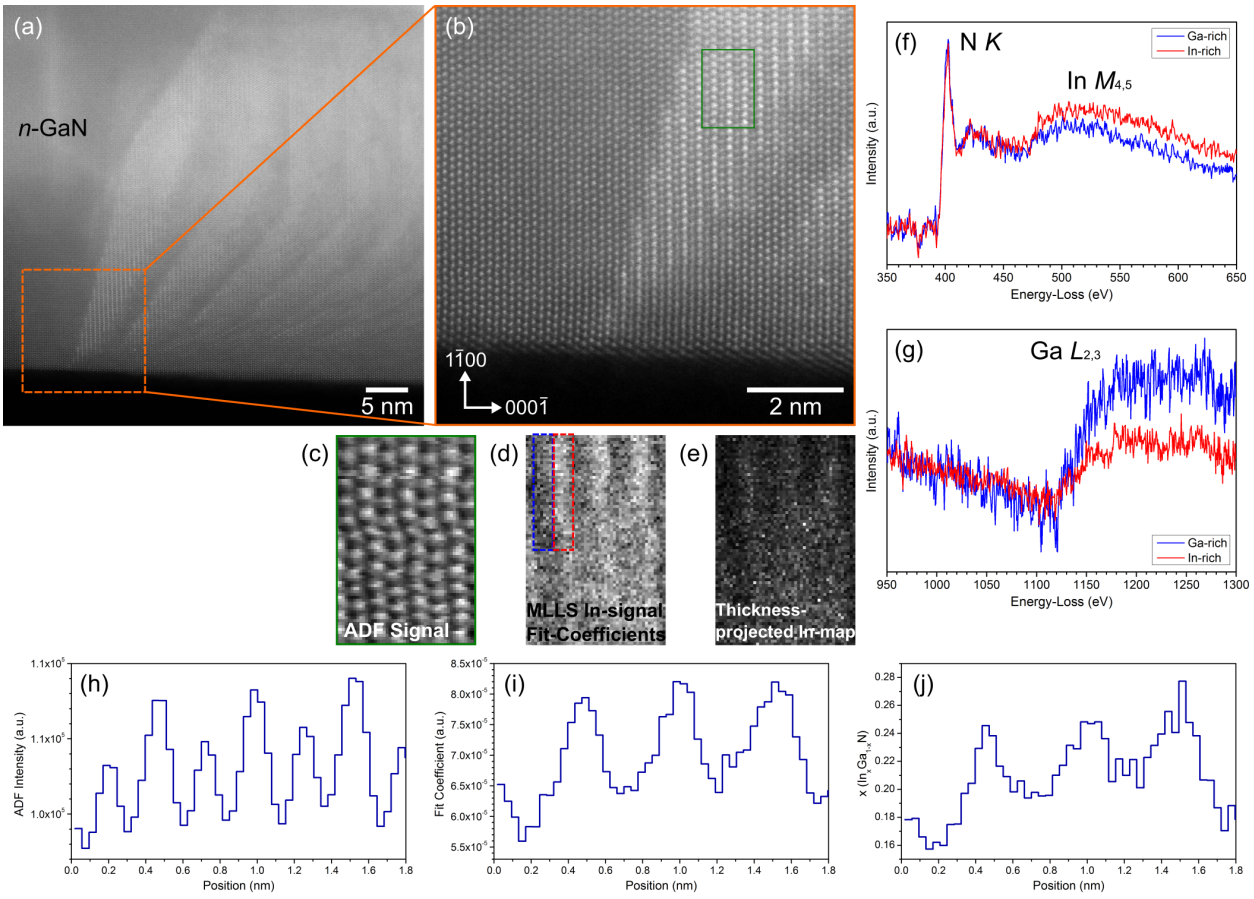

Figure 3.6: **(a)** STEM-HAADF image of a 10 dot-in-a-wire and **(b)** high-magnification view of QD#1, showing its high degree of ordering within the bulk and "tail" of this QD. Atomic-resolution STEM-EELS spectrum imaging of the region boxed in (b), showing **(c)** the ADF signal collected concurrently, **(d)** the MLLS fit-coefficent map of the In-signal, and **(e)** the thickness-projected In-content map. EELS spectra extracted from adjacent In-rich (red) and Ga-rich (In-poor, blue) single atomic-planes from same-sized regions boxed in (d), showing **(f)** the N *K* and In $M_{4,5}$-edges, and **(g)** the Ga $L_{2,3}$-edge (with integral before the edge onset normalized). **(h)**–**(j)** Corresponding line profiles of the STEM-EELS maps show that the localization of In is consistent with the ADF intensity maxima. The distortions in the spectrum image are due to specimen drift during acquisition.

composition of $x = 0.19$ where the spectrum image was done, as shown in the line profile in Figure 3.6(j). At the extreme, comparison between the Ga-rich plane and In-rich plane boxed in blue and red, respectively in Figure 3.6(d), even demonstrates a ∼55% relative increase. Extracted EELS spectra from the In-rich *c*-planes (red spectrum in Figure 3.6(f)) show a significantly higher intensity in the In $M_{4,5}$-edge (∼451 eV) compared to the adjacent In-deficient planes (blue spectrum). Conversely, the Ga $L_{2,3}$-edge (Figure 3.6(g), after normalizing the integral before the edge onset) shows the complementary trend confirming the In-deficient planes are Ga-rich, affirming cation ordering as the cause for the superlattice reflections in the DP of Figure 3.3(b).

3.6 Crystal Polarity Determination

Complementary STEM annular bright-field (ABF) imaging, which enables the visualization of atomic columns with light elements such as N [48, 179], was used to directly determine the crystal polarity within the III-N nanowires, as demonstrated at the InGaN/GaN:Si interface in Figure 3.7(a). Validation that the *n*-GaN/InGaN interface in Figure 3.7(a) is situated on a faceted growth surface *inclined* along the *a*-plane projection direction shown, is presented in Figure 3.8 and schematically in Figure 3.9. The InGaN QD, seen in high-magnification images (Figure 3.7(b)), and line profiles of the atomic dumbbells (Figure 3.7(c)) show clear distinctions between In- and Ga-atoms as well as the relative location of N-atoms to deduce the nanowire as N-face polar. This particular assignment of polarity indicates that the In-atoms have a preferential occupation at the lower-coordination site (N=2) along a pyramidal surface facet, such as the $(10\overline{1}\overline{1})$ plane shown in the crystal structure model of Figure 3.7(d). This finding provides equivalent experimental evidence for the *T1* site (a lower-coordination site which forms only one N-bond) on a $\{10\overline{1}1\}$ surface from the theoretical model proposed by Northrup et al. [170] for ordering in Ga-polar InGaN layers, which also similarly applies for N-polar InGaN layers.

Within the nanowire heterostructures, it should be emphasized that the InGaN QDs have a bent morphology (see Figure 3.2) that formed their given shape from a highly faceted growth front with strong non-basal components, which propagated from growth conformal to the top surface facet of the *n*-GaN base [143]. Thus, the QD exhibit vicinal facets that are inclined with respect to the basal plane ranging from ∼15 – 60°, encompassing $\{10\overline{1}\overline{1}\}$, with a large majority close to 35° or 45° corresponding to $\{10\overline{1}\overline{3}\}$ and $\{10\overline{1}\overline{2}\}$, respectively. The theoretical calculations from Ref. [170] were used to propose a mechanism for bilayer atomic ordering in InGaN alloys, where site energy differences at the $\{10\overline{1}1\}$ surface steps can drive the preferential occupation of In/Ga-atoms. As Rao et al. [180] experimentally demonstrated that faceting promoted ordering within InGaN epilayers grown on faceted GaN, the present results also suggest a similar surface energy origin for atomic ordering within the nanowires. The faceted growth front in nanowires can provide $\{10\overline{1}\overline{1}\}$ or similar vicinal surfaces (between the *c*- and *m*-plane) exposing the two differently-coordinated sites to assist in the preferential occupation of In into the lower-coordination site (two-fold in N-polar case). It should be noted that high degree of ordering is most prevalent but not exclusive at the QD "tails" originating from growth on vicinal facets, as ordering is also observed in regions where the GaN/InGaN interface is abrupt along *c*-plane (Figure 3.2(c)). Due to the longer In–N bond with weaker bond energy, In-adatoms have relatively high mobility on surfaces [80]. An exchange reaction between In-adatoms and incorporated surface Ga-atoms is even possible

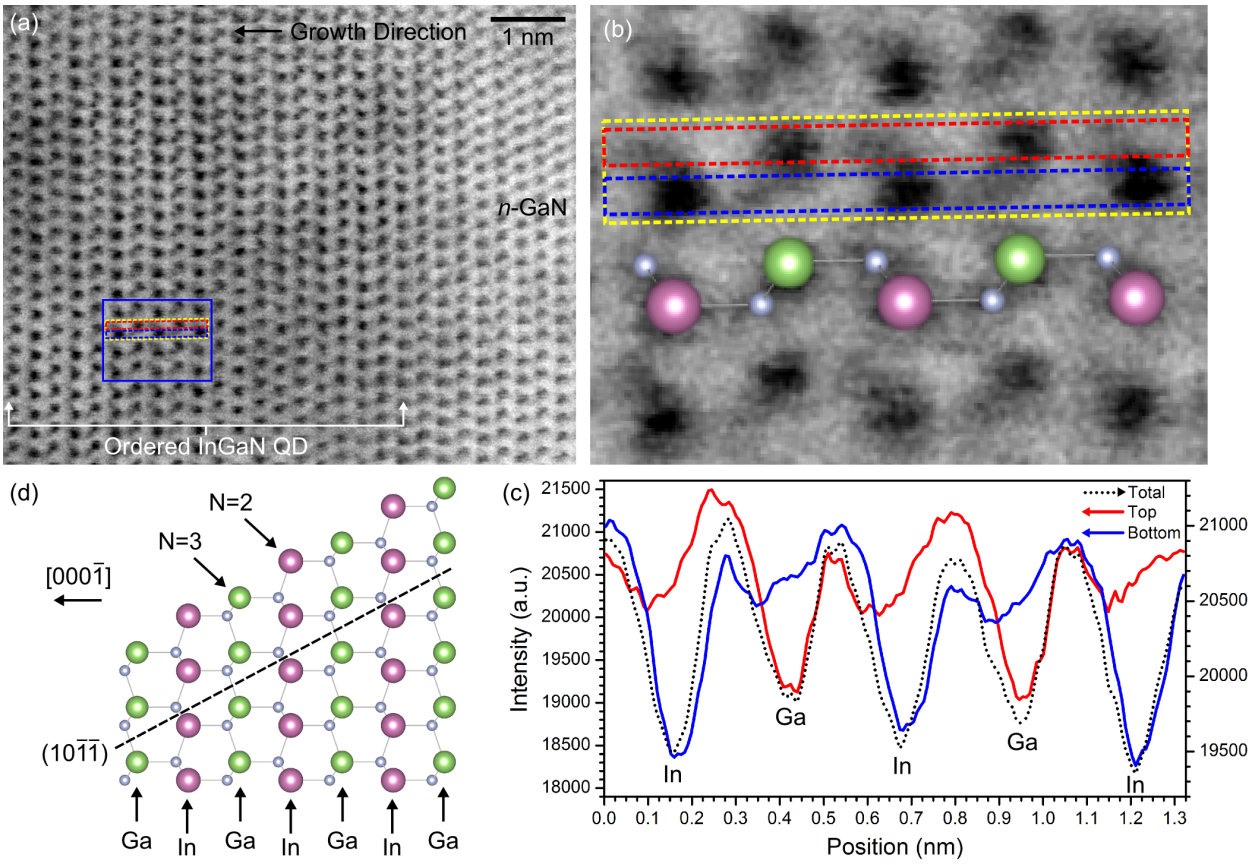

Figure 3.7: **(a)** STEM-ABF image of QD#1 exhibiting ordering at the InGaN/GaN:Si interface and **(b)** a high-magnification view of area boxed in blue in **(a)**. Gaussian-smoothing has been applied to the ABF image. **(c)** Line profiles of the ABF signal along atomic dumbbells, including both projected columns (Total, black dashed line from yellow dashed box in **(b)**), and separating into Top (red dashed box) and Bottom (blue dashed box) columns to emphasize the weaker minima from the N-atoms. Identification of the In- and Ga-atoms is differentiated by the minima in the Total profile, deducing the nanowire as N-polar. **(d)** Model of bilayer-ordered InGaN alloy with N-face polarity from the preferential incorporation of In at the reduced N-coordination site (two-fold coordinated, N=2) and Ga at the three-fold coordinated site (N=3) along a $\{10\bar{1}\bar{1}\}$ surface facet.

along c-plane surface, but most energetically favourable at an edge site on vicinal surfaces [181]. Furthermore, a site substitution between an incorporated bulk-site In-atom with Ga-atoms at a surface site, can also take place lowering the overall energy of the system [170].

3.6.1 Identification of Interfacial Region in ABF Image

The specific region shown in the ABF image of QD#1 in Figure 3.7(a) was identified by comparison with other lower magnification HAADF images by locating similar features, as presented in Figure 3.8. Ordering has been confirmed in this boxed region in Figure 3.8(a) from STEM-HAADF (Figures 3.8(c) and 3.8(d)) and diffraction techniques to correspond to the differentiation between the two cation sites and its elemental occupancy from STEM-ABF. The HAADF intensity line profile in Figure 3.8(d) shows a smooth transition with a sloping background intensity across the n-GaN/InGaN interface, in contrast to the abrupt transition at the GaN/InGaN interface shown in Figure 3.2(c) that is suggestive of a c-plane growth front at that location. Therefore the profile in Figure 3.8(d) is indicative of a non-

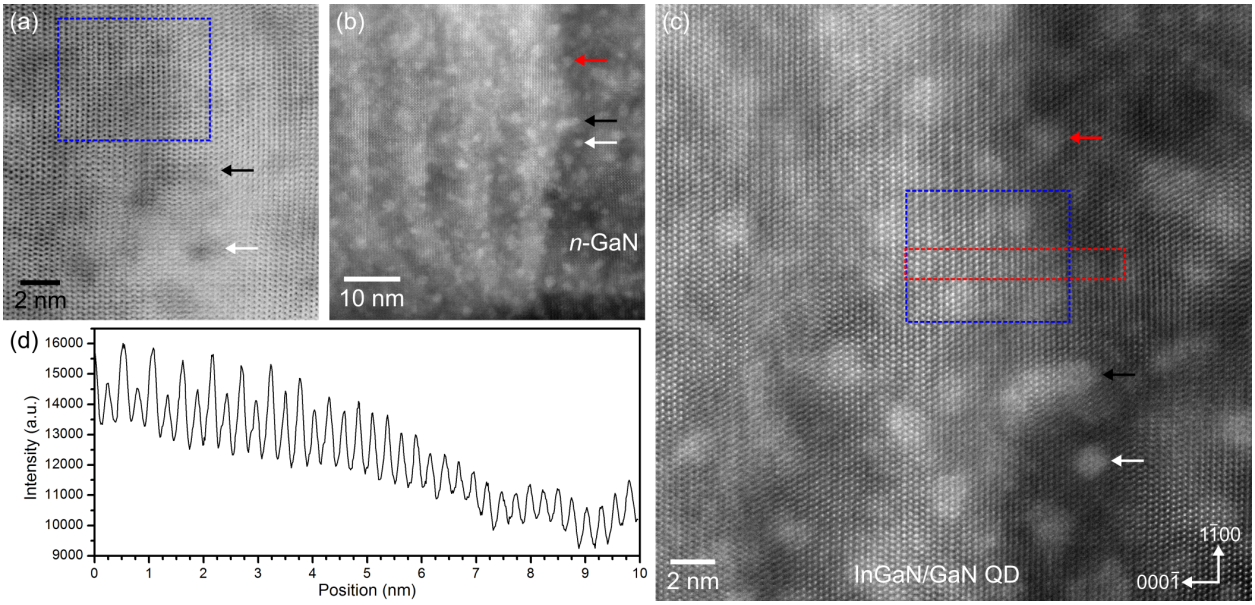

Figure 3.8: **(a)** STEM-ABF image of the InGaN/GaN:Si interface, containing the cropped region (boxed in blue) that is Figure 3.7(a), as a raw image without Gaussian-smoothing applied. STEM-HAADF images of the same nanowire, including **(b)** the low magnification view of n-GaN and QD#1–4, and **(c)** detailed view of the InGaN/GaN:Si interface with the region corresponding to the boxed area in **(a)** also indicated. Features in common between images **(a)**–**(c)**, from extraneous contrast caused by redeposition of W particles during Ar-ion thinning and plasma cleaning, are marked using colour-matched arrows. All images are viewed along the $\{11\bar{2}0\}$ zone-axis, with growth direction towards the left. **(d)** Integrated HAADF intensity line profile from the red dashed box region in **(c)**, showing the oscillatory image intensity from QD#1, and the sloping background intensity supporting the presence of a faceted growth front inclined along the projection direction at this InGaN/GaN:Si interface.

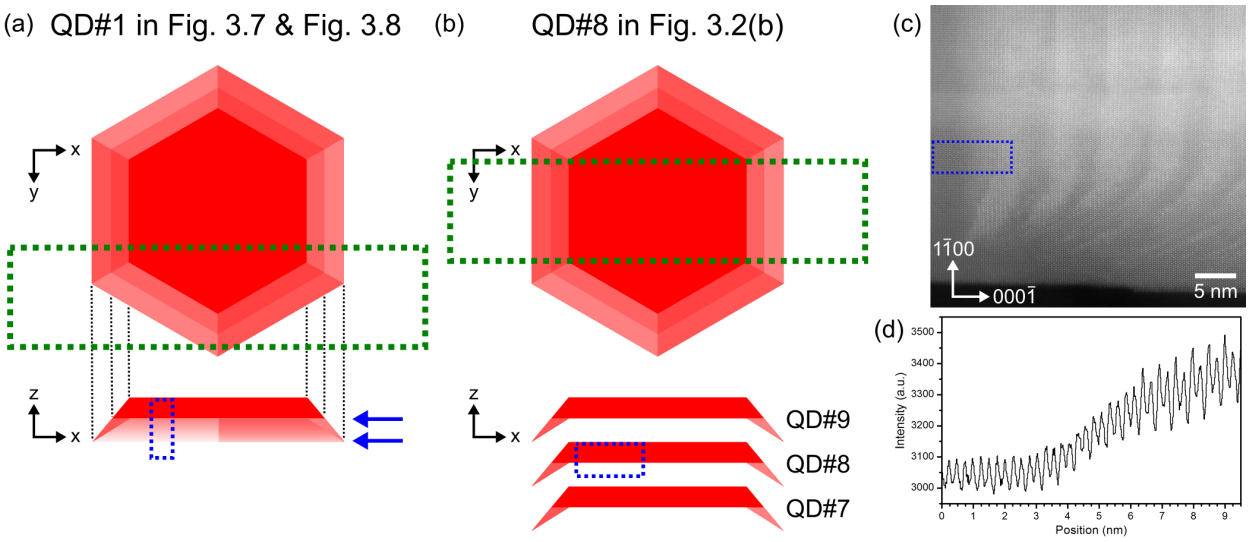

Figure 3.9: Schematic diagrams of the proposed location of the lift-out lamellae from FIB cross-sections of nanowires featured in **(a)** Figure 3.7 and Figure 3.8, and **(b)** Figure 3.2(b), as boxed in green dashed line in the top-down view. Shades of red are assigned as InGaN QDs, varied to differentiate adjacent facets, with darker shade within a single facet to indicate more projected thickness, and the white background as GaN layers. The resulting HAADF intensity line profiles of the GaN/InGaN interface integrated within the blue dashed boxes in the side view (same projection as observed in STEM), shows **(a)** a smooth transition (light to dark shade between blue arrows) at the QD tails, and **(b)** an abrupt transition due to the milling away of tails. **(c)** Same STEM-HAADF image as Figure 3.4(d), of the as-grown nanowire presented in Figure 3.2(a) viewed along $\{11\bar{2}0\}$ zone-axis, with blue dashed box marked at the n-GaN/InGaN interface to assess the nature of the interface. **(d)** Integrated intensity line profile from the blue dashed box region at QD#1 in **(c)**, showing the sloping background intensity supporting the presence of a faceted growth front inclined along the projection direction at base regions of the QD (its tails) that grew on an vicinal growth surface on the underlying n-GaN.

basal plane *inclined* along the projection direction shown due to presence of the QD tails in the center of the nanowire. This validates that Figure 3.7(a) corresponds to the base regions of the QD, situated on a faceted growth surface on the underlying n-GaN.

Schematic diagrams depicting the differences between the two proposed FIB cross-section locations across the QDs in Figure 3.7 and Figure 3.2(b), by comparing the two HAADF intensity line profile outcomes, are presented in Figures 3.9(a) and 3.9(b), respectively. Demonstration of a sloping background intensity in the highly-ordered base regions at the centre of the nanowire, evident in QD#1 from Figure 3.2(a) (also shown in detail in Figure 3.4(d)), is presented in Figures 3.9(c) and 3.9(d). The resulting intensity profile from this as-grown nanowire represents well the situation depicted in Figure 3.9(a), confirming that a vicinal growth surface is indeed present, where the QD tails are only not visible edge-on in the zone-axis shown in the Figures 3.8(c) and 3.8(d) (same area as in Figure 3.7(a)).

3.7 Discussion

The first InGaN QD, grown pseudomorphically to the underlying n-GaN base, similar to InGaN/GaN thin films, is unlike the other nine QDs in the series. The latter QDs have been shown to be strain partitioned with the GaN barrier layers and partially relaxed along the in-plane direction, discussed previously in Section 2.5. The prevalence for the highest degree of ordering in QD#1 (see Figure 3.4) suggests that the higher degree of in-plane compressive strain could favour the preferential site occupation of the larger In-atoms into the N=2 sites for better bond relaxation. Although the local strains within and between single atomic layers in the ordered QDs is not detectable within the limits of current imaging methods, it can be surmised that the different covalent radii of In- and Ga-atoms can impart slight compressive and tensile strains into their respective In-rich and Ga-rich layers [165]. Therefore ordered alloys can better accommodate strain at a coherent interface than a random alloy due to the simultaneous accommodation of two different bond lengths [161]. A higher degree of in-plane compressive strain, such as that observed in QD#1, can provide additional driving force for this modulated strain distribution in adjacent layers [163], further promoting the formation of ordered alloys while suppressing phase separation [162]. Based on these strain considerations, single InGaN QD nanowires, such as in Figure 3.5, were investigated systematically to illustrate that a high degree of ordering can be induced with high probability. The single InGaN QD is comparable to QD#1 in the 10 dot-in-a-wire samples, exhibiting similar bent morphology, In-content, and strain-state (coherent to the underlying n-GaN base). Most importantly, all single InGaN QD nanowires observed exhibit strong atomic-ordering as confirmed from HAADF imaging and/or electron diffraction.

In consideration of the effects on optical properties, atomic ordering within InGaN alloys can be proposed as a new path to achieve high-efficiency long visible wavelength photonic devices, in particular in the nanoscale devices demonstrated in this letter. High In-compositions often lead to In-clustering due to phase separation [76], resulting in broad linewidths undesirable for laser and single-colour LED applications. Due to the expected reduction in bandgap [165, 171], ordered InGaN alloys can reach longer wavelengths without as much In incorporated, and hence exhibit smaller lattice strain. Photoluminescence and cathodoluminescence spectroscopies suggest a similar red-shift behavior within the ordered-only single InGaN QD nanowires relative to the multiple dot-in-a-wire. However, experimental comparison with identical random alloy counterparts of equivalent (or at least similar) compositions, in particular within nanowire heterostructures, remains to be a challenge. The reduced strain will also likely suppress defect formation, enhancing carrier transport due to less carrier scattering. In addition, with an overall decrease in piezoelectric coefficients (e_{31} and e_{33}) calculated

for ordered InGaN alloys [173], a reduction in piezoelectric polarization compared to random alloys is expected. The growth kinetics unique to nanowires, such as contributions from sidewall adatom diffusion, and the resulting low density of defects, make nanowires an excellent platform to understand fundamentally the formation and stability of ordered III-V alloys and other kinetically-driven effects. Therefore, atomic ordering within nanowire heterostructures can ultimately provide another method to control compositional fluctuations and structural disorder by simultaneously suppressing phase separation. Furthermore, this study highlights the potential for the controlled formation of such atomic ordering to provide an atomic-scale band engineering approach to tune the emission wavelengths from deep green to red spectral range, which has been difficult to realize previously using InGaN materials.

3.8 Conclusion

To summarize, atomic-level chemical ordering in wurtzite InGaN alloys within InGaN/GaN nanowire heterostructures was confirmed using electron diffraction and direct visualization at atomic-resolution. Experimental evidence shows that the degree of In-enrichment in In-rich layers is significant, and the preferential site occupation of In-atoms into reduced N-coordination sites at vicinal surface facets validates the existing theoretical model based on surface site energetics. The prevalence for ordering of InGaN alloy is explained by a combination of the non-flat growth front that progressed along the nanowire heterostructure, and the in-plane strain relaxation of the alloy relative to the underlying GaN. Atomic ordering offers an alternative against larger-scale compositional inhomogeneity, which could be advantageous for obtaining high-quality InGaN/GaN heterostructures to realize full wavelength tunability towards the deep visible spectrum.

Chapter 4

Correlative Nanoscale Luminescence and Elemental Mapping

4.1 Introduction

Ternary InGaN compounds show great promise for light-emitting diode (LED) applications because of bandgap energies (0.7 – 3.4 eV) that can be tailored to have emission wavelengths spanning the entire visible spectrum. Given the large lattice mismatch strain present in conventional planar *c*-plane growth of InGaN epilayers or quantum wells (QWs) on GaN, the formation of a high density of threading dislocations can be detrimental for obtaining high optical-quality materials. Additionally, the wurtzite-structured III-nitrides, when grown along its polar *c*-axis also exhibit large magnitudes of spontaneous and piezoelectric polarization at heterointerfaces. Such polarization-induced electrostatic fields can also have a substantial effect on the optical and electrical properties of InGaN/GaN QW structures. Despite the less than desirable crystalline quality, InGaN alloys have managed to achieve high efficiency as light emitters in practical applications for solid-state lighting and diode lasers for optical storage with huge commercial success. The inherently high luminescence efficiency is believed to be caused by carrier localization taking place at nano- and atomic-scale compositional inhomogeneity. Such localization behaviour holds even in random In-containing (In,Al)GaN alloys with characteristic disorder at statistical fluctuations [90]. This localization phenomenon, however, also results in inhomogeneouos broadening of the emission, accompanied with strongly retarded recombination dynamics, and significant Stokes-type shift due to localized states at potential minima [98].

Nanowire (NW) or nanorod geometries, both bottom-up (catalyzed or self-catalyzed) epitaxial growth and top-down etching of planar epilayers, have been proposed to have en-

hanced strain relaxation due to the additional free surfaces. The nanowire geometry also opens up the variety and complexity of device design opportunities. Complex III-N device heterostructures have been incorporated into GaN nanowires recently, but exhibit emission linewidths that are broader than expected for their corresponding planar counterparts using photoluminescence (PL) spectroscopy [17, 85]. It is thus critical to understand how the overall structural and chemical properties interplay with optical and electrical properties within individual nanowire structures, using combined spectroscopic methods that can resolve different localized signals at the nanoscale within analytical scanning transmission electron microscopy (STEM).

Although the bulk of GaN nanowires are considered relatively strain-free, the integration of axial InGaN/GaN heterostructures have demonstrated that the presence of misfit strain still arise at the heterointerfaces [15, 141]. The presence of strain can have an influence on the resulting morphology and faceting of the InGaN insertions (also referred to as quantum dots or quantum discs), as well as the incorporation of indium already discussed previously in Chapter 2. Irrespective of the total number of successive QDs in short-period heterostructures, inhomogeneity arises in the relative In-content within individual nanowires. Additionally, this also further leads to a different degree of elastic strain relaxation [143], which already is inherently dependent on the radial distance to the free sidewall surface [156] and the overall nanowire diameter [182]. Affected by the enhanced relaxation at the free surfaces, such nanowire heterostructures (NWH) are susceptible to an inhomogeneous strain distribution in the radial direction; theoretical studies suggest it is the culprit to the broadened luminescence common in nanowire structures [23].

Several studies utilizing nanometer-resolved cathodoluminescence (CL) spectroscopy in STEM have already demonstrated the viability of the technique for correlating nanoscale structural and chemical properties in InGaN insertions within GaN nanowires to optical properties probed locally. In the work of Tourbot et al. [141] regarding thicker InGaN insertions with thicker GaN barriers (15 nm and 10 nm, respectively), the emission appears localized to the thickness of single InGaN insertions of ∼15 nm. Despite the higher In-content at the top of the insertions due to compositional pulling effect quantified using energy-dispersive X-ray (EDX) spectroscopy, such a compositional gradient did not correspond to any spectral shift in the CL emission. In particular, the emission is most intense at the high In-content upper portion of each insertion and non-radiative in the lower In-content, suggestive of their relative carrier capture strength as radiative recombination centres. On the contrary, Zhou et al. [183] have more recently reported in GaN nanorods containing four InGaN nanodisks of similar dimensions, that carrier diffusion can be as large as 50 nm. It is important to note that the first two nanodisks were intended to target green emission

and the last two along the growth direction for red emission (nominal In-content of 20 – 30% and 40%, respectively). The resulting emission energy does show correspondence to the intentional variation in composition amongst InGaN nanodisks, determined from the relative amount of In using EDX. In order to gain a fundamental understanding of the nanoscale optical properties, both of the aforementioned studies were performed on model InGaN/GaN heterostructures with few number of insertions with large thickness and spacing. Furthermore, without intentional doping, these heterostructures do not represent fully the behaviour in short-period multiple quantum well/dot typical of LED device structures.

In this chapter, multiple InGaN/(Al)GaN quantum dot (QD)-embedded NWH for LED application, with tunable emission wavelengths within the visible spectral range, were characterized by CL in STEM. Previous observations using electron energy-loss spectroscopy (EELS) in STEM have shown a systematic non-uniformity of In-content between successive InGaN QDs (already detailed in Chapter 2). Additionally, from PL spectroscopy measurements from an ensemble of nanowires, the dot-in-a-wire structures show broader than anticipated emission peaks, as compared to linewidths expected from corresponding planar multiple QWs. STEM-CL hyperspectral imaging or spectrum imaging can provide spatially-resolved spectroscopic information regarding the emission process at the nanoscale. Thus, optical signatures can be directly assigned to structural features, including the morphology, elemental distribution, strain state, and even the presence of defects acting as (non-)radiative recombination centres. Therefore the purpose of the CL study is in an effort to correlate the In-content variation between the InGaN QDs in individual nanowires, with the broad emission band from an ensemble of the nanowires observed at the macroscopic level.

4.2 Methods

4.2.1 MBE Growth

Multiple InGaN/GaN and InGaN/AlGaN dot-in-a-wire nanostructures are grown on Si(111) substrates by *rf* plasma-assisted molecular beam epitaxy under nitrogen-rich conditions without the use of any external catalyst, as described in further detail in Ref. [85, 184]. For the InGaN/GaN nanowire heterostructures, identical to those discussed in Chapter 2, a 10 InGaN QD series, each capped by a GaN barrier layer, is centrally confined within the nanowire active region embedded between *n*- and *p*-doped GaN in the nanowire heterostructure. Additional components in the device structure include the high-bandgap *p*-AlGaN electron-blocking layer (EBL) and the *p*-InGaN test well towards the *p*-GaN, used to mitigate and evaluate effects of electron overflow, respectively. The single InGaN QD in

GaN nanowire samples were grown at similar growth conditions but without the additional AlGaN EBL and InGaN test well (described in Chapter 3). The InGaN/AlGaN nanowire heterostructures also consists of a 10 InGaN QD series, but each capped by a p-doped AlGaN barrier layer that function simultaneously as distributed EBLs and surface passivation.

4.2.2 Scanning Transmission Electron Microscopy

4.2.2.1 Nano-Cathodoluminescence

Nanometer-resolution STEM-cathodoluminescence (nanoCL) spectral imaging on individual dot-in-a-wire structures was performed using a custom-built system on a VG HB-501 dedicated STEM at the Université de Paris-Sud XI. The in-house high collection efficiency CL spectrum imaging detection set-up is described in detail by Zagonel et al. [122]. The microscope is equipped with a high-brightness cold field-emission gun capable of very high beam currents, operated at 60 kV with typical probe currents of 50 – 100 pA with ∼1 nm probe size. In the absence of aberration-correction, typical spatial resolution obtained is ∼1 nm. Specimens were cooled to ∼150 K with liquid nitrogen to further minimize effects of beam damage and concurrently increase radiative emission efficiency by surpressing phonon-assisted non-radiative recombination. Photons are collected by a parabolic mirror with a large solid-angle, coupled into a fibre optic bundle and dispersive optical spectrometer (150 grooves per mm diffraction grating blazed to 500 nm) read-out in parallel onto an electron-multiplying charge-coupled device (EMCCD). Such a set-up allows for high-speed acquisition while maintaining high-spectral resolution and high signal-to-noise ratio in the full emission spectrum.

Experiments were performed in spectrum imaging mode for concurrent acquisition of spatial information from bright-field (BF) and annular dark-field (marked ADF in figures for simplicity) signals, allowing for a point-to-point comparison between the full CL emission spectrum collected at every pixel. Four-dimensional datasets $I_{CL}(x, y, \lambda)$ are recorded at each pixel as the beam rasters over the area of interest, which allows for the facile extraction of local spectra $I_{CL}(x_i, y_i, \lambda)$ or two-dimensional monochromatic CL images or maps $I_{CL}(x, y, \lambda_i)$ by applying a spectral band-pass. Calibration of the dispersive grating and the parallel-detection onto the CCD is carried out using pairs of emission lines from a Hg vapour lamp for the visible wavelengths. The as-grown nanowires samples were mechanically exfoliated from the Si substrate, dispersed in anhydrous ethanol, and deposited on carbon-coated TEM support grids for observation.

4.2.2.2 High-Resolution STEM

Subsequent characterization of the same nanowire heterostructures was carried out using aberration-corrected scanning transmission electron microscopy (STEM). The possible generation of point defects caused by knock-on damage in GaN is undesirable for CL signal collection, as they greatly quench the radiative recombination. The threshold for such electron-beam damage in (In)GaN has been reported as 120 keV [185], and later refined to ∼70 keV specific to the decay of CL signal from InGaN [186]. Therefore the STEM-CL experiments below the damage threshold were performed first, then followed by the high-resolution STEM to study the atomic structure and elemental distribution. The high-resolution experiments were performed with a FEI Titan Cubed 80-300, fitted with a high-brightness field-emission gun (X-FEG), aberration-correctors on both the probe- and image-forming lens systems, a monochromator, and a high-resolution electron energy-loss spectrometer (Gatan GIF Quantum 966). All experiments were carried out at an accelerating voltage of 200 kV with 19 mrad convergence angle. Atomic-number, Z-contrast sensitive high-angle annular dark-field (HAADF) images were obtained using a detector angular range of 63.8 – 200 mrad. Elemental mapping by electron energy-loss spectroscopy (EELS) in STEM mode was done with the N K, In $M_{4,5}$, and Ga $L_{2,3}$-edges using the spectrum imaging technique. Multiple linear least-squares (MLLS) fitting was used to separate the N K, In $M_{4,5}$-edges within the EELS spectrum images to extract the In-distribution for quantifying the In-composition, as described in detail in Chapter 2.

4.3 InGaN/GaN Dot-in-a-wire Heterostructures

InGaN/GaN heterostructures in both axial and radial configurations have been widely implemented within the nanowire platform by many research groups. The (In)GaN system should benefit most of this architecture from taking advantage of the strain relaxation of the very large lattice mismatch at free surfaces. Relatively dislocation-free nanowire arrays can be grown given a small diameter. Nevertheless, there are still challenges in optimizing device properties, including controlling electron overflow that can contribute to efficiency droop, and improving the carrier injection efficiency to increase the output power of nanowire LEDs. Electron overflow contributes to the efficiency degradation by the leakage of electrons outside the active region at high current densities, which can be prevented by the addition of the high bandgap AlGaN electron-blocking layer (EBL) [85]. The in-depth structural characterization of the InGaN/GaN dot-in-a-wire nanostructures with AlGaN EBL (and InGaN test well) has already been highlighted in Chapter 2, therefore the current section will mainly

focus on the nanoscale optical properties from individual nanowires examined using nanoCL.

Individual InGaN/GaN nanowire heterostructures examined using nanoCL show diverse optical responses, but most nanowires exhibit multiple sharp emission peaks (25 – 50 nm at FWHM) centred between 500 – 625 nm in the yellow-green wavelengths from the active region, identified using the bright-field (BF) or annular dark-field (ADF) signals collected concurrently. Multiple spectral features arise from the active region, showing an apparent spatial origin dependence of changes in emission wavelength. The spatially overlapping peaks spanning a wavelength range of ∼100 nm within individual nanowires is consistent with the unusually broad emission peaks measured from an ensemble of nanowires using room-temperature PL spectroscopy. This indicates that the broad emission originates from within single nanowires and is not an inhomogeneous broadening. Subsequent aberration-corrected STEM-HAADF images on the same nanowires were acquired to evaluate their structural properties, such as the size and morphology of the ten QDs within the nanowire heterostructure (NWH). The elemental distribution was assessed using STEM-EELS, and the local alloy composition was quantified. The luminescence intensity within nanowires shows a direct relationship to the thickness of the GaN shell surrounding the InGaN/GaN heterostructure and the presence of an AlGaN shell formed during the growth of the AlGaN EBL due to sidewall incorporation from direct impingement. Both enhance the in-plane confinement of carriers, hence reducing non-radiative surface recombination. Additionally, absence or even poor coverage of the additional AlGaN shell drastically changes the luminescence spatial symmetry. The effects of the presence of built-in and polarization fields on the excitation probability and resulting emission intensity distribution will also be discussed.

4.3.1 Alloy Composition and Polychromaticity in Single Nanowires

Atomic number (Z-contrast) sensitive high-angle annular dark-field (HAADF) imaging using high-resolution STEM (HRSTEM) in Figure 4.1(a) demonstrates a typical nanowire viewed along a $\langle 11\bar{2}0 \rangle$ zone-axis, with the ten InGaN/GaN QD series centrally confined within the nanowire's active region, embedded between n- and p-doped GaN segments in the NWH. Additional components visible in the device structure include the p-AlGaN EBL (dark band) and the p-InGaN test well (thick bright band) towards the p-GaN, included to mitigate and evaluate electron overflow, respectively. It is noteworthy to mention that variations in QD morphology, height, diameter, and HAADF image intensity in individual nanowires are not uncommon. Furthermore, visible clearly near the bottom nanowire sidewall is an Al-rich AlGaN shell (thin dark band arrowed in yellow) that formed spontaneously during the growth of the AlGaN EBL from the sidewall impingement and minimal sidewall diffusion

of Al-adatoms. Despite the relatively low surface recombination velocity in GaN nanowires ($\sim 10^3$ – 10^4 cm/s [187, 188]), non-radiative recombination at nanowire surface states will have a strong effect on the carrier diffusion within such nanowires. The additional higher-bandgap AlGaN shell provides carrier confinement in the radial direction and sufficiently passivates the surface [176].

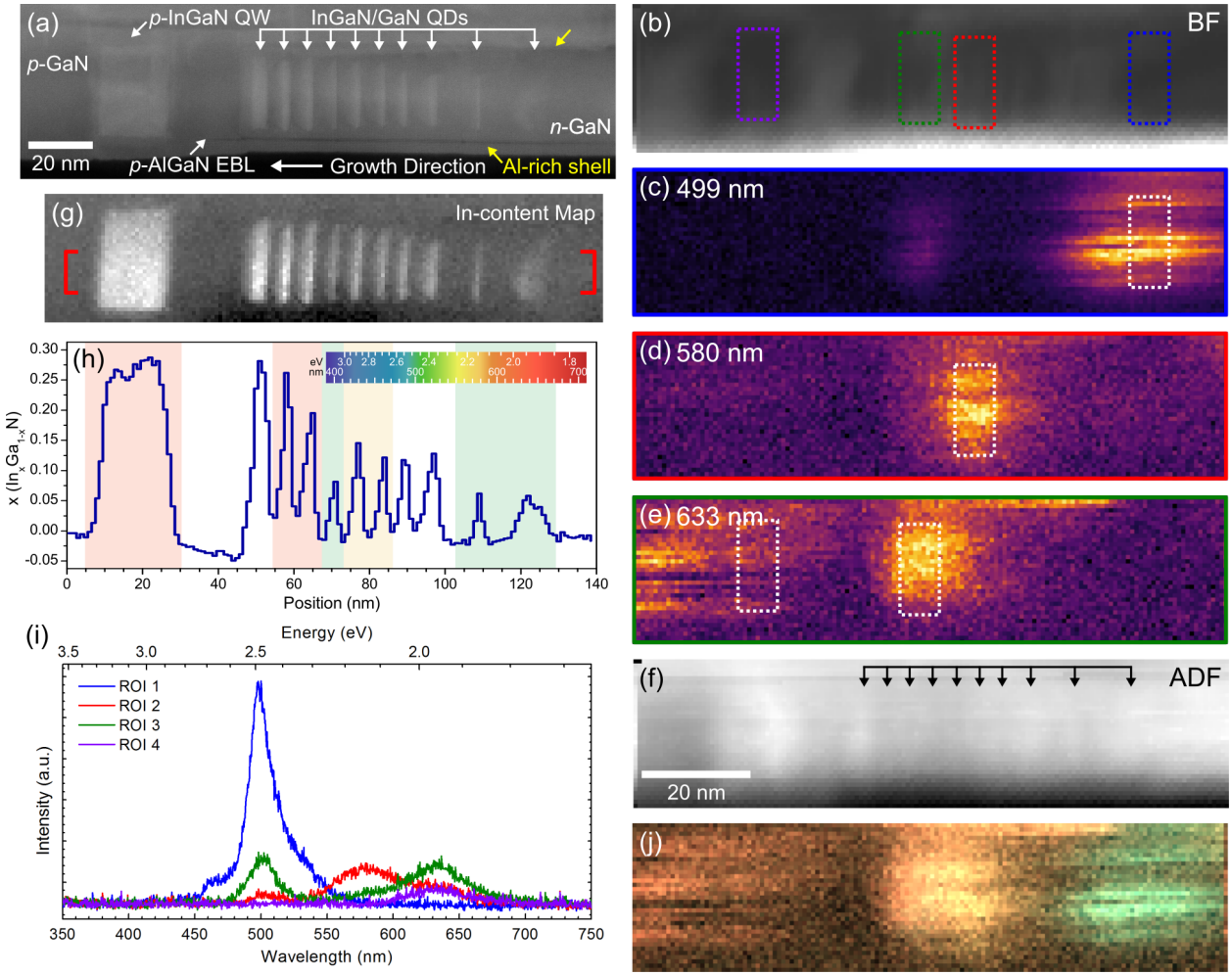

Figure 4.1: **(a)** HRSTEM-HAADF image along $\langle 11\bar{2}0 \rangle$ zone-axis showing the InGaN/GaN active region in detail. NanoCL on the same nanowire: **(b)** BF and **(f)** ADF images acquired simultaneously during STEM-CL spectral imaging, and **(c – e)** spatial maps of spectral features centred about the wavelengths labeled. Four marked regions of interest (ROIs) that exhibit unique emission spectra are shown in **(i)**. Correlative HRSTEM: **(g)** quantitative EELS In-content map, and **(h)** corresponding line profile of the red-bracketed region in **(g)**. The line profile is overlaid with emission wavelengths colour-coded matching **(j)** the RGB composite stack of multi-coloured wavelength-filtered CL maps showing the emission wavelength variations according to the visible spectrum legend inset in **(h)**.

BF and ADF images of the same nanowire acquired concurrently during the nanoCL spectrum imaging, with marked locations of the four regions of interest (ROIs) that exhibit unique emission characteristics are shown in Figures 4.1(b) and 4.1(f), respectively. The

insufficient spatial resolution and lack of specimen tilting during the nanoCL experiments usually leaves poor interfacial contrast, and often hinders the identification of individual InGaN QDs that are only 3 – 5 nm in height. The orientation of the nanowire presented in Figure 4.1 was sufficiently close to the basal plane, allowing the QDs to be distinguished using the combination of line profiles from the BF and ADF images (approximate locations marked in Figure 4.1(f)). The corresponding CL spectra from the four ROIs are presented in Figure 4.1(i). When examining the CL spectra, firstly the emission intensity varies drastically between the different emission peaks, with the most intense peak (at ∼500 nm) five times higher in intensity than other spectral features. Secondly, the emission wavelength of the most intense features spanned a range of ∼150 nm, consistent with the broad FWHM of the emission peaks measured using PL. The two notable features suggest that the emission characteristics are inhomogeneous even within individual nanowires.

Isolating the distinct emission bands within the CL spectra, the origin of these spectral features can be revealed from within the spectrum image as spatial distribution maps based on the corresponding electron probe position. Wavelength-filtered spatial maps of specific spectral peaks centred about the wavelengths labeled is shown in Figure 4.1(c) – (e). Each spatial map is summed slices within the spectrum image centred at the wavelengths as labeled, with an integrated width of ∼50 nm (in wavelength) and a linear extrapolation of the background using a three-window method. The CL maps demonstrate a clear localization of specific emission peaks to areas ∼15 – 30 nm in size within the active region along the nanowire growth axis, but also at the *p*-InGaN test well (Figure 4.1(e)). In addition, some InGaN QDs appear to not emit at all or significantly less compared to adjacent QDs. Similar CL quenching behaviour has been reported in other multiple InGaN insertions in GaN nanowire structures previously [141, 183]. Zhou et al. [183] attributed the non-radiative recombination in the active layers specifically to the large number of I_1-type basal plane stacking faults in the higher In-content nanodisks. In the current nanowire, correlation with HRSTEM of the same nanowires allows to eliminate sub-par crystalline quality and any resulting structural defects as a probable cause for the observed CL quenching across specific InGaN QDs within the active region. Carriers generated within the active region that diffuse towards the InGaN QDs have a tendency to recombine at the lowest available potential minima within its diffusion range [189]. Therefore CL quenching can also indicate carrier diffusion away from the incident electron beam position.

HRSTEM-HAADF imaging on the same nanowire (Figure 4.1(a)) corroborates with the approximate spacing between QDs identified in the nanoCL BF/ADF image pairs. The 10 QDs within the NWH exhibit a gradual increase in diameter along the growth direction, and a morphological change along the growth direction from crescent-shaped (in particu-

lar QD#1) to more flat and disc-like. Additional electron energy-loss spectroscopy (EELS) spectrum imaging, together with multiple linear least-squares (MLLS) fitting, was used to extract the In-distribution to quantify the In-composition projected through the thickness of the nanowire (Figure 4.1(g)). An integrated line profile of the red-bracketed region in Figure 4.1(g) is displayed in Figure 4.1(h). The origin of each individual emission peak cannot be directly assigned to a single InGaN QD, as the localized CL signals in the 2D maps (Figure 4.1(c) – (e)) span a distance that encompasses at minimum two QDs and its surrounding barriers. The effect of the diffusion of generated carriers on CL signal delocalization, and hence the spatial resolution of nanoCL spectral imaging, needs to be accounted for, but will be discussed in a later section. An apparent spatial-spectral correlation is made between shifts in the CL emission wavelength to the relative In-content between successive QDs from the STEM-EELS In-content map (Figures 4.1(g) and 4.1(h)). Regions in the Figure 4.1(h) profile are colour-coded to the corresponding CL emission wavelength, matching the RGB (red-green-blue) composite stack of polychromatic wavelength-filtered CL map in Figure 4.1(j) based on the visible spectrum legend inset in Figure 4.1(h).

A second nanowire exhibiting a prominent gradient in CL emission wavelength along the nanowire growth axis, and later confirmed gradation in InGaN QD size and composition, is presented in Figure 4.2. The CL emission from this nanowire spans wavelengths with a majority in the yellow-green with minor intensities in the blue-green (Figure 4.2(d)), displayed visually in the RGB composite stack of multi-coloured wavelength-filtered CL maps in Figure 4.2(b). Concurrent spatial and spectral variations in a CL spectrum image can be represented globally using the principles utilized in these references [127, 190]. Furthermore, since the emission in this case lies in the visible, the representation can be even more direct and true to tone. The polychromatic CL map has been obtained by summing a stack of the wavelength-filtered images from the CL spectrum image, each of which have been RGB-encoded corresponding to the colour of its emission wavelength using the visible spectrum directly as colour-scale. Individual QDs are not resolved for this nanowire, so only the approximate locations of the QDs and the InGaN test well are marked in the BF image from the CL spectrum image in Figure 4.2(c).

In Figure 4.2(d) is a few select CL spectra summarizing the spectral variations from different ROIs in this nanowire marked in the ADF image (Figure 4.2(a)). The InGaN test well luminesces strongly in the yellow-green from a broad peak centred at 540 nm with 200 meV FWHM (ROI 1 spectrum), which is about twice as broad as the emission originating from the InGaN QDs (*cf.* ROI 2 spectrum). The ROI 3 spectrum features multiple emission peaks, some of which are recurrent across the ROI 1 and 2 spectra, but slightly redshifted in ROI 3. Such proximity effects will be described in a later section (Section 4.3.4). Also

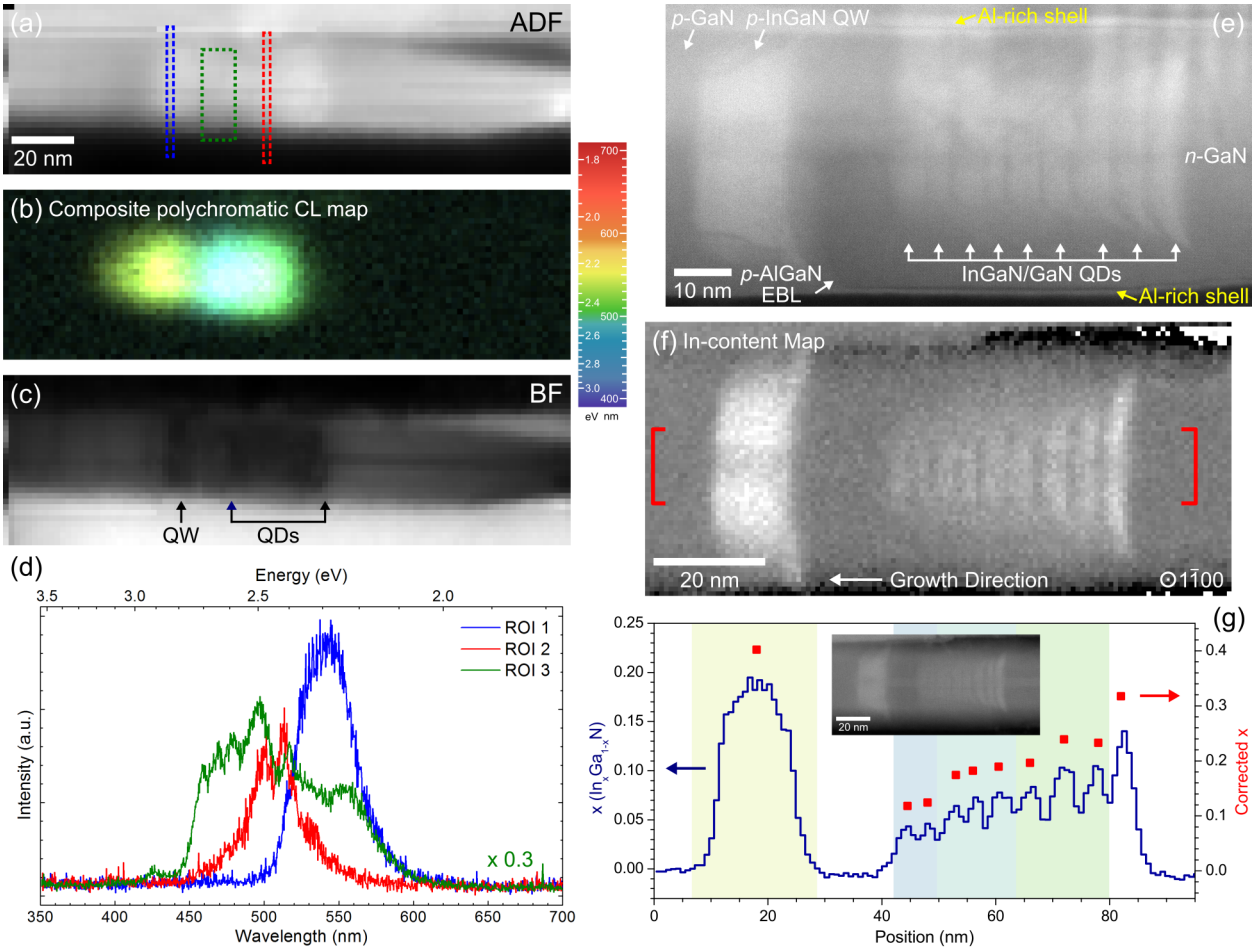

Figure 4.2: **(a)** ADF and **(c)** BF images acquired simultaneously during STEM-CL spectral imaging, with three ROIs marked in **(a)** that exhibit unique emission spectra shown in **(d)**. Intensity scaling of spectra in **(d)**, when applicable, is indicated by a multiplier. **(b)** RGB composite stack of polychromatic wavelength-filtered CL maps showing the emission wavelength variations according to the visible spectrum legend. **(e)** HRSTEM-HAADF image along $\langle 11\bar{2}0 \rangle$ zone-axis showing the active region in detail, including the thin Al-rich AlGaN shell (dark band) that formed along the nanowire sidewall (arrowed in yellow). **(f)** Quantitative EELS In-content map obtained along adjacent $\langle 1\bar{1}00 \rangle$ zone-axis (HRSTEM image inset in **(g)**), and **(g)** corresponding line profile of the thickness-projected In-content and the In-content corrected for QD diameter variations, overlaid with emission wavelengths colour-coded according to the visible spectrum legend in **(b)**.

noteworthy are the four peaks towards higher energy between $\lambda = 450 - 500$ nm, which could not be individually excited (nor changing relative intensities of single peaks) within the whole region boxed in by ROI 3 in Figure 4.2(a). Wavelength-filtered CL images across these four peaks exhibits, with increasing wavelength, a gradually more asymmetric emission pattern towards the n-GaN direction (opposite the growth direction). This suggests that these multiple recombination centres of different energy levels are within close proximity to each other within the carrier diffusion length, and only excited simultaneously during the electron beam rastering. The different methods of extraction and representation of the CL spectrum image all describe a decreasing gradient in emission wavelength in the QD active region along the growth direction. Same as the example in Figure 4.1, the InGaN test well emission is again the longest wavelength in the whole nanowire.

A notable structural feature observed during nanoCL includes the dark band along the length of the wire in the BF image (Figure 4.2(c)). HRSTEM-HAADF imaging along the closest zone-axis (m-plane) from the specimen tilt during the nanoCL experiment identifies that same feature (inset in Figure 4.2(g)) as an inclined planar defect. Observing the planar defect edge-on in the adjacent a-plane zone-axis (Figure 4.2(e)) confirms it is likely an inversion-domain boundary. The presence of this defect appears to have some correlation to the local In-content variation, but little to no effect on the CL emission. Along both m- and a-plane orientations reveal only nine InGaN QDs of decreasing diameters along the growth direction, each with a crescent-shape from having bent tails on semi-polar planes (seen edge-on in Figure 4.2(e)). Visible again in the a-plane orientation HAADF image is the thin Al-rich AlGaN shell (arrowed in yellow) that extends from the AlGaN EBL along both of the nanowire sidewalls towards the n-GaN segment. The relevance of this few atomic-plane-thick AlGaN shell to the overall emission from a surface passivation point of view will be discussed in a later section (Section 4.3.3).

Quantitative STEM-EELS mapping of the In-distribution, as shown in Figure 4.2(f), was carried out when viewing down m-plane instead to avoid overlap with the adjacent nanowire whose contributions are visible at the top of the image in Figure 4.2(e). Because of the drastic changes in QD diameters seen in the lateral direction, the thickness-projected In-content map (Figure 4.2(f)) does not fully represent the composition within the QDs themselves. Therefore according to the procedure already described in Section 2.2.3.2, a correction for the GaN shell contributions, taking into account the proportion of centrally embedded QD in the total through-thickness must be considered. The correction factors are ratios of the QD diameter at the basal plane portion to the overall nanowire diameter measured from the HAADF image intensity profiles while viewing down $\langle 11\bar{2}0 \rangle$. The correction is applied to the integrated line profile of the red-bracketed region in Figure 4.2(f) and shown as the

red datapoints alongside the uncorrected line profile in the plot of Figure 4.2(g). An overlay of the colour-coded CL emission wavelengths to the approximate locations in the nanowire is included in Figure 4.2(g). The overall decreasing trend of the measured In-composition remains approximately the same after correction, and correlates to the emission wavelength changes within the active region and at the InGaN test well measured from nanoCL.

In combination with the small scatter in the range of emission wavelengths observed between different nanowires, the effects of broadening are only amplified during the PL measurements illuminating an ensemble of nanowires. Nevertheless, it can be concluded that the observed variation in emission characteristics is occurring at an individual nanowire level, and not due solely to the macroscopic broad-beam nature of the PL measurement technique itself. Isolating distinct emission bands from the active region in single nanowires show FWHM of 100 – 150 meV, however, averaging within individual nanowires still remain rather broad. The present InGaN/GaN dot-in-a-wires exhibit a variation range in peak emission energy of ∼500 – 600 meV. Compared to the literature, previous works have reported a FWHM of 200 meV for individual (15 nm thick) InGaN insertions in nanowires [141], and up to 300 meV for nanowires with multiple InGaN insertions [189]. In contrast, values for the FWHM on the order of 100 – 150 meV are reported from PL on planar (In,Ga)N QW structures emitting in the green spectral range [191, 192]. Interestingly, the even broader emission peaks from the 15 – 20 nm thick InGaN test well is consistent with other thicker InGaN insertions of similar composition in literature.

4.3.2 Dot Morphology and Luminescence Intensity Distribution

The thorough structural characterization of the multiple InGaN/GaN dot-in-a-wire nanostructures in the previous chapters have outlined various effects on the formation of the InGaN QDs, including the effect of strain mitigation on the composition, and the combined contributions of strain state and growth front faceting on atomic-level alloy ordering and overall QD morphology. In the following section, examples of nanowires with less than perfect QD morphology that deviates from the expected flat disc geometry, and how it plays a role in the luminescence properties, will be presented. Figure 4.3 displays a nanowire that demonstrates two instances of asymmetry in the CL intensity distribution from the active region. Firstly, the excitation pattern of the emission peak from the first few QDs (ROI 1 spectrum and Figure 4.3(b)) is highly asymmetric and lobed towards the top free surface of the nanowire. Secondly, the last few QDs exhibit an emission pattern from the main peak (ROI 2 spectrum Figure 4.3(c)) that is unevenly localized laterally within the plane of the QDs and concentrated towards the nanowire sidewalls. The CL intensity localization is further emphasized

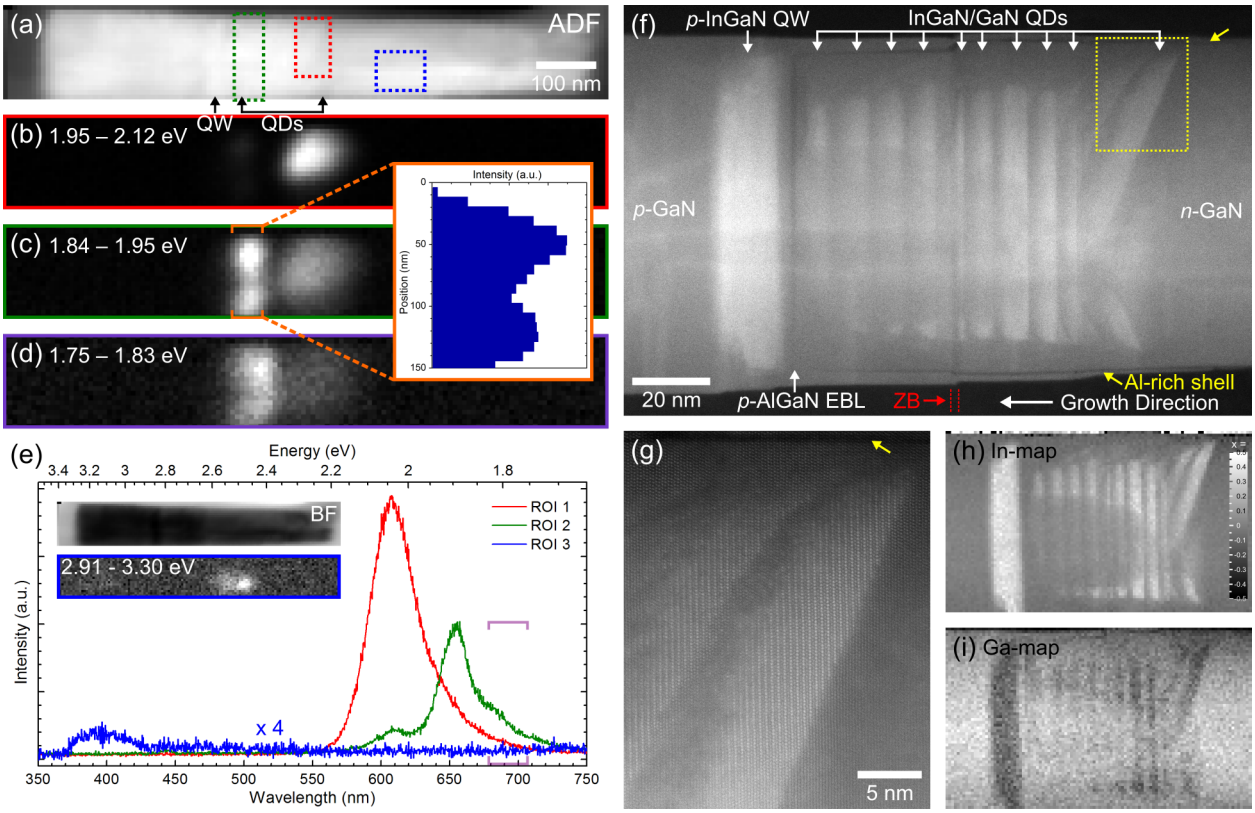

Figure 4.3: NanoCL spectral imaging: **(a)** ADF image with three ROIs marked that exhibit unique emission spectra shown in **(e)**, and **(b – d)** spatial maps of emission features within spectral range labeled. Concurrently acquired BF image and CL map of a weak emission peak from ROI 3 is also shown inset in **(e)**. Intensity scaling of spectra in **(e)**, when applicable, is indicated by a multiplier. Correlative HRSTEM: **(f)** HRSTEM-HAADF image along $\langle 11\bar{2}0 \rangle$ zone-axis showing the active region in detail, including the thin Al-rich AlGaN shell (dark band) that formed along both nanowire sidewalls (arrowed in yellow) and the few ML thick ZB insertion (delimited by dashed red lines). **(g)** High-magnification view of the tail region of the first two InGaN QDs boxed in **(f)** that demonstrate a high-degree of atomic-ordering. **(h)** Quantitative EELS In-content map with corresponding intensity scale (x in $In_xGa_{1-x}N$), and **(i)** Ga-signal map generated using the concurrently collected Ga $L_{2,3}$-edge showing the reciprocal nature of the group III elemental distribution.

in the inset line profile of the emission pattern radially across this area. Two local maxima with a peak-to-peak spacing of ∼70 nm is evident in the profile, as well as an intensified local maxima towards the nanowire top surface. A similar, only more delocalized distribution is also observed when filtering across the low-energy shoulder (marked by purple brackets across ROI 2 spectrum in Figure 4.3(e)) in Figure 4.3(d). Figure 4.3(e) summarizes the CL emission spectra originating from various ROIs marked in the ADF image (Figure 4.3(a)). Inset in Figure 4.3(e) includes the BF image and CL map of a weak band from the n-GaN segment (marked as ROI 3) assigned to the states related to nanowire coalescence in the local area.

Comparison with the HRSTEM-HAADF image of the same nanowire in Figure 4.3(f)

shows that the first few QDs (#1 – 3) have prominent bent tail components, with QD#1 even made up entirely of semi-polar components. Along this $\langle 11\bar{2}0 \rangle$ zone-axis view, the bent tail morphology of QD#1 – 3 is more heavily weighted towards the top free surface, which can explain the asymmetric CL signal distribution. Figure 4.3(g) is a detailed view of the tail region of QD#1 and 2 (boxed area in Figure 4.3(f)), and illustrates the same 1:1 *c*-plane bilayer atomic-ordering discussed in Chapter 3 of the InGaN alloy in this area. The remaining InGaN QDs in the nanowire have the expected flat-disc shape. Additional contrast changes in the HAADF image at the nanowire central region across QD#5 – 10 that coincides with another lenticular-shaped extended defect along the nanowire length require further investigation.

Subsequent STEM-EELS mapping was used to determine the elemental distribution within the active region. The In-content map in Figure 4.3(h) illustrates that the image contrast changes are due to the local area devoid of In and the QDs split into two laterally. However, when comparing with the complementary Ga-signal map generated using the concurrently collected Ga $L_{2,3}$-edge in Figure 4.3(i), the local area shows a reciprocal distribution of In- and Ga-atoms. Therefore the enrichment of Ga concludes that the *void* is not an empty cavity, but only deficient in indium. The thickness-projected In-content of the $In_xGa_{1-x}N$ alloy varies between x $\approx$ 0.05 across QD#7 – 10 at the nanowire centre to x $\approx$ 0.20 at the split dots near the top surface. This subtle change in In-composition local at QD#5 – 10 provides sufficient lateral confinement to induce the carrier localization observed in the CL intensity pattern in Figure 4.3(c). The peak-to-peak spacing from the inset CL intensity profile and the higher intensity maxima corresponds well to the relative spacing between the split dots and the larger width of the split dot near the top surface, respectively. Also worth mentioning is the position along the active region where CL emission is very low, such as the gap between the marked areas of ROI 1 and 2 visible in the emission pattern in Figure 4.3(c). This location approximates to QD#6, within which a 6 ML thick zinc-blende (ZB) insertion intersects (delimited by dashed red lines in Figure 4.3(f)). Coinciding with the start of the ZB insertion, the overall nanowire diameter increased and Al-rich AlGaN shell switched to a semi-polar plane within the insertion (its l-index deviates from $l = 0$ in $\{1\bar{1}0l\}$). Such stacking fault-related ZB insertions have formed as a result of errors in the stacking sequence, and confirms a previous finding of their role in CL quenching at InGaN nanodisks containing stacking faults in GaN nanowires [183].

4.3.3 Surface Passivation and Excitation Probability

Due to the limited incorporation of In onto the *m*-plane sidewalls, which can be explained by the strain-induced segregation of InGaN alloys and the higher In-adatom mobility, each InGaN QD is covered by a GaN shell towards the nanowire surface. Such a self-organized core/shell-like InGaN/GaN structure is beneficial because they provide an intrinsic higher bandgap material at the nanowire sidewalls for passivation against non-radiative surface recombination. Other post-growth surface treatment methods with aquaeous solutions of inorganic sulphides are also popular amongst III-V semiconductors in general against the effects of surfaces states on carrier recombination [193]. Surface states can vary the radiative and non-radiative recombination rates directly, or they can contribute to the degradation of PL intensity under UV illumination over time in air [194]. The luminescence intensity within nanowires is related to the presence of such GaN or AlGaN shell surrounding the InGaN/GaN nanowire heterostructures, formed due to sidewall incorporation during the growth of each of the subsequent GaN barriers and *p*-GaN segment, and *p*-AlGaN EBL, respectively. Both can enhance the in-plane confinement of carriers, hence reducing non-radiative surface recombination.

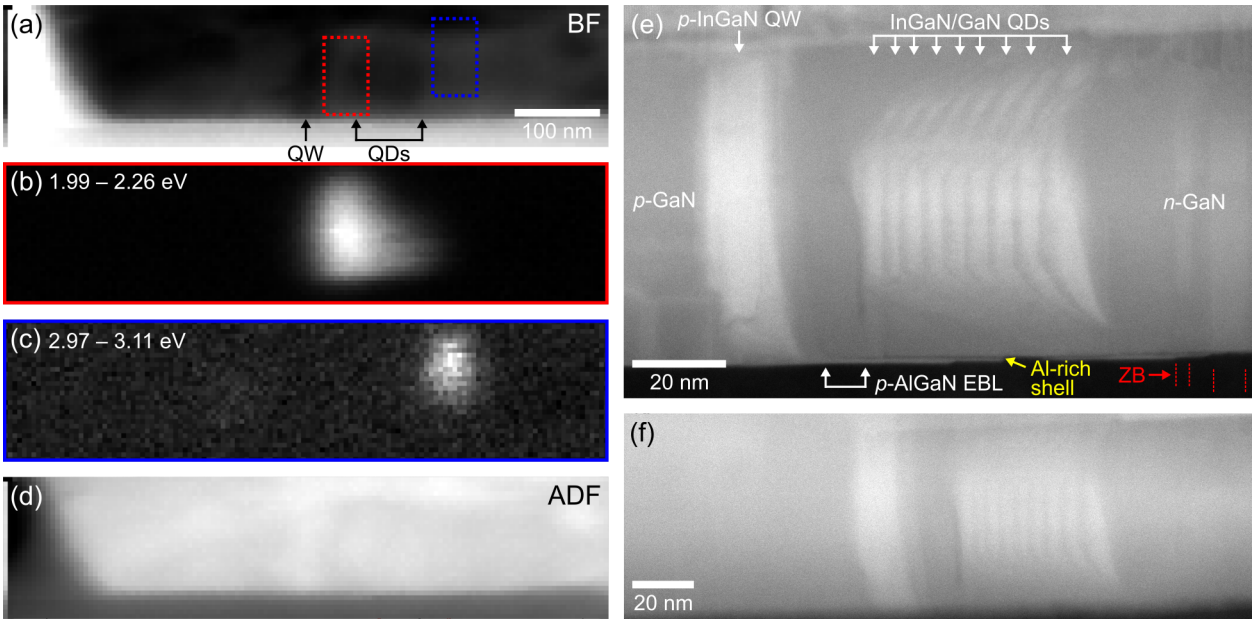

Figure 4.4: **(a)** BF and **(d)** ADF images acquired simultaneously during STEM-CL spectral imaging, with ROIs marked in **(a)** that exhibit the main emission peaks shown in the CL maps in **(b)**–**(c)**. **(e)** HRSTEM-HAADF image along $\langle 11\bar{2}0 \rangle$ zone-axis showing the active region in detail, including the thin Al-rich AlGaN shell (dark band) that formed along only the bottom nanowire sidewall (arrowed in yellow at bottom edge) and the pair of few ML thick ZB insertion (delimited by pairs of dashed red lines). **(f)** HRSTEM-HAADF image taken at zero-tilt to mimick the view during nanoCL.

Demonstrated in Figure 4.4 is a nanowire with an incomplete coverage of the QD active region by the Al-rich AlGaN shell at the nanowire sidewall, and how it has contributed to the spatial asymmetry of the CL signal. Typically this Al-rich shell is only a few atomic-planes thick (up to ∼1 nm) on m-plane, and therefore only visible when viewing along a $\langle 11\bar{2}0 \rangle$ zone-axis. This also means that within the specimen tilt range in the microscope, at any one time only two of six m-plane sidewall facets can be confirmed to contain an Al-rich shell or not. The other four facets may or may not contain such an Al-rich shell layer, but any Z-contrast from its contributions will be averaged out through the thickness in projection. NanoCL of the nanowire in Figure 4.4 exhibits comparatively fewer number of emission peaks, including only two from within the QD active region isolated in the ROIs boxed in the BF image in Figure 4.4(a) (and their corresponding CL spectra later in Figure 4.6(b)). The main emission band from ROI 2 is rather broad (FWHM ∼230 meV) and asymmetric towards higher energy, but more interestingly, the wavelength-filtered image across this peak (Figure 4.4(b)) has a highly asymmetric distribution of the luminescence intensity lobed towards the bottom free surface of the nanowire. The asymmetry can, as a first approximation, be related to the underlying QD morphologies. This hypothesis is later excluded based on the HRSTEM-HAADF imaging along the nearest a-plane zone-axis as well as at zero-tilt to mimick the projection during the nanoCL experiment (Figures 4.4(e) and 4.4(f)). The nine identifiable InGaN QDs in the HAADF image in Figure 4.4(e) have strongly bent tail components towards both sidewalls, however, the morphology is not as severely asymmetric towards the bottom free surface to explain the CL signal profile.

Alternatively, an Al-rich shell is visibly absent on the top edge of this nanowire, whereas the shell coverage is continuous at the bottom edge (arrowed in yellow in Figure 4.4(e)). This particular nanowire in Figure 4.4 appears to be partially coalesced with its neighbouring nanowire since the n-GaN segment, visible in both orientation views (Figures 4.4(e) and 4.4(f)). Al-adatoms have minimal diffusion at the growth temperatures used during the growth of the AlGaN EBL, which is actually optimized for (In)GaN growth. Therefore the sidewall incorporation of Al-adatoms relies on the directly impinging flux instead of sidewall diffusion of adatoms from the c-plane growth front. As a result, geometrical shadowing by neighbouring wires and coalescence will play a dominant role in the spontaneous formation of the AlGaN shells, and can explain the incompleteness in shell coverage. The absence or partial coverage of this high band-gap AlGaN layer can explain the asymmetric luminescence distribution, because it disrupts the balance of non-radiative to radiative recombination towards the unpassivated surface. As the probe position approaches the uncovered surface, diffusion of carriers towards surface states which subsequently recombine non-radiatively becomes more probable.

4.3.3.1 Shell Coverage and Emission Rate

The nature of a nanoCL investigation on isolated nanostructures has some intrinsic bias within its data sampling, where typically individual nanowires are first surveyed for its overall emission intensity before carrying out more in-depth spectrum imaging measurements. However, the study of nanowires with reduced emission rates is also of equal importance for understanding the physical mechanisms that lead to CL quenching. Figure 4.5 displays such a nanowire where the overall emission intensity was quite low despite being obtained under very similar experimental conditions as other nanowires investigated. A comparison between the ADF image (Figure 4.5(a)) and the later acquired HRSTEM-HAADF image (Figure 4.5(b)) identifies the various layers within the active region. It should be pointed out that part of the *p*-GaN segment in this nanowire is missing, and could have resulted from fracture during sample preparation. Other nanowires measured that were missing portions of their *n*- or *p*-GaN segments did not demonstrate adverse effects on the CL emission. The energy-filtered CL maps in Figures 4.5(c) and 4.5(d) show emission intensity across the *p*-InGaN test well and InGaN QDs corresponding to ROI 1 and 2, respectively. The intensity scaling of the CL maps are individually adjusted to illustrate the full dynamic range in each map. The CL map corresponding to the emission from the InGaN test well (Figure 4.5(c)),

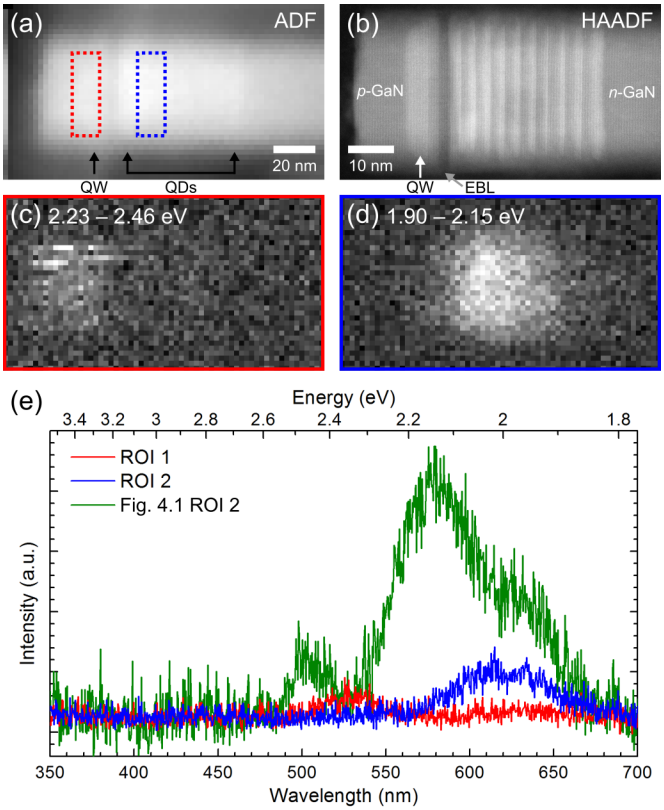

Figure 4.5: **(a)** ADF image acquired during the STEM-CL spectral imaging, and **(b)** HRSTEM-HAADF image along $\langle 1\bar{1}00 \rangle$ zone-axis showing the active region highlighting the minimal GaN shell coverage along the nanowire sidewalls. **(c – d)** Spatial maps of emission features within spectral range labeled, from the two ROIs marked in **(a)** that exhibit unique emission spectra shown in **(e)**. Plot in **(e)** includes a spectrum covering similar wavelengths, but of relatively weak emission intensity, from a previously presented nanowire (ROI 2 of Figure 4.1) for comparison. All three CL spectra have been calibrated according to their respective electron-hole pair generation rate per unit volume [$\mathrm{nm}^{-3}\ \mathrm{s}^{-1}$].

in particular, has very low signal-to-noise ratio. Inspecting the CL spectra from ROI 1 and 2 alone does not emphasize their low signal intensities. Therefore to provide grounds for comparison, a weakly emitting band from Figure 4.1's ROI 2 has been normalized according to its electron-hole pair generation rate per unit volume and presented in Figure 4.5(e). Furthermore, the CL spectra from ROI 1 and 2 have been treated with the same volumetric carrier generation rate calibration of the summed areas of ROI 1 and 2, and also shown alongside in Figure 4.5(e). The low emission intensity from two bands in the current nanowire becomes seemingly evident with the calibrated spectra, which are a factor of five lower in intensity.

No extraneous image contrast or visible defects, such as those associated with stacking faults, are identified within the active region in the Figure 4.5(b) HAADF image that can be associated to the CL quenching. The GaN shell that formed around the InGaN QDs during the growth of the GaN barriers is otherwise particularly thin ($\sim$2 – 4 nm) within this $\langle 1\bar{1}00 \rangle$ projection view. Analogous to the Al-rich AlGaN shell discussed previously, the GaN encapsulation also lies on m-planes; thus only the GaN shell portion at the ridges connecting two m-plane facets is visible when viewing along a $\langle 1\bar{1}00 \rangle$ zone-axis. Albeit unambiguous confirmation of an Al-rich shell cannot be possible in this m-plane orientation view of the nanowire, the GaN shell thickness is significantly thinner than other nanowires of similar diameter (such as the nanowire in Figure 4.1). Given the minimal passivation layer on the nanowire in Figure 4.5, the poor in-plane carrier confinement leads to enhanced non-radiative recombination rates taking place at the nanowire surface.

4.3.4 Proximity-Related Non-Linearity Effects

Other influences on luminescence properties that can be inferred from apparent changes in CL spectral characteristics with an excitation density dependence is also of interest and investigated for the same nanowire from Figure 4.4 in the following. To maintain a quantitative visualization of emission centres and their spatial distribution along the nanowire length concurrently, a two-dimensional spectral profile representation of the full spectrum image can be used. While spatial information lateral across the nanowire diameter is lost in this representation, any asymmetry in the luminescence distribution can already be assessed in the wavelength-filted CL map of the main emission peak (Figure 4.4(b)). Figure 4.6(c) shows such a 2D spectral profile plotting the emission energy/wavelength as a function of the probe position along the nanowire growth axis within the spectrum image. Relatively weaker intensity emission bands are straightforwardly revealed in the 2D spectral profile, including the pair of bands at the p-GaN segment (2.41 eV, 2.51 eV), and two narrow bands barely

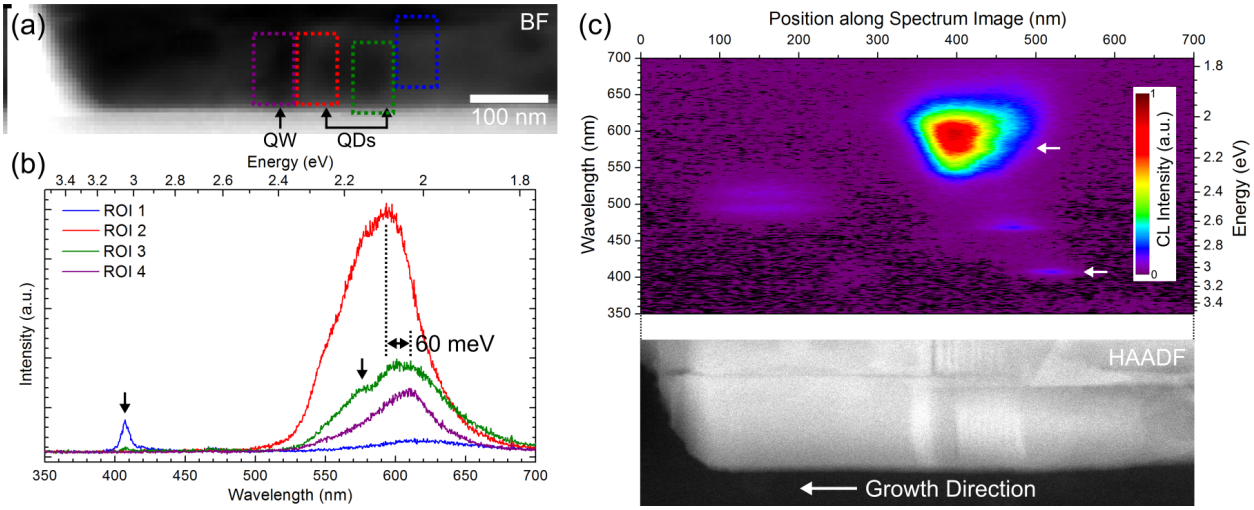

Figure 4.6: **(a)** BF image with ROIs marked that exhibit relevant emission spectra shown in **(b)**, including ROI 1 and 2 from Figure 4.4 of the same nanowire. **(c)** CL spectral profile integrated across the nanowire diameter as a function of the emission wavelength/energy and position along the nanowire axis in the spectrum image, shown alongside a HRSTEM-HAADF image taken at zero-tilt to mimick the view during nanoCL. A few minor spectral features appearing simultaneously in **(b)** and **(c)** have been marked using black and white arrows, respectively.

visible in the ROI 1 spectrum in Figure 4.6(b) from the n-GaN and near the first InGaN QDs at 3.04 eV and 2.65 eV, respectively. The weak bands at 2.41 eV, 2.51 eV, 2.65 eV are in fact residual contributions from the neighbouring nanowire (deduced from CL maps not shown). The emission line from n-GaN is presumably defect related, and a repeated occurrence in other nanowires studied. In detail, the narrow 3.04 eV peak from n-GaN arrowed in Figures 4.6(b) and 4.6(c) is close to the transition energy interval of few monolayer-thick ZB inclusions (whose boundaries are delimited by pairs of red-dashed lines in Figure 4.4(e)'s zone-axis HAADF image) that form ZB/WZ heterostructures in GaN [195]. It should be emphasized that these four aforementioned bands remain invariant in energy with position.

It can be assumed that the location of a peak CL intensity maximum coincides with the physical location of that particular emission centre. The peak intensity maximum evident at 2.09 eV, the same as the peak portrayed in the ROI 1 spectrum in Figure 4.6(b), its recombination centre can be designated approximately to the last QDs within the active region. More notable is the simultaneous peak energy redshifting and spectral narrowing (from 230 meV to 185 meV) as the electron beam moves away from this intensity maximum along both directions in position, where the emission intensity decreases up to one full order of magnitude. The 50 – 60 meV redshift is evident from the energy shift in the maximum intensity distribution with position in the spectral profile in Figure 4.6(c), and replicated in the CL spectra from ROI 3 and ROI 4 on the right and left sides of the ROI 2 maximum

in Figure 4.6(b). Or in other words, as the incident probe position approaches the physical location of the recombination centre, the emission peak both broadens and blueshifts. This behaviour is typical of band-filling effects, such as at localized states, and therefore suggestive of carrier localization as a probable cause [196, 197]. As the incident probe gets closer to the recombination centre, the excess carrier density effectively increases due to diffusion until eventual direct excitation. The proximity of the excitation volume to a recombination centre achieves an equivalent scenario as increasing the excitation (current or power) density locally [99], both of which affect the generation rate of electron-hole pairs. The increased charge carrier density progressively fills the lowest lying band-tail states, leading to recombination also at higher energies, resulting in the blueshift in emission energy.

Coulombic screening of the internal polarization field and hence reducing the quantum-confined Stark effect (QCSE) is another possible root cause for the blueshift, but its combined outcome is often not distinguishable from band-filling effects [4]. Furthermore, a reduction of the internal fields generally leads to little variance in the emission linewidth [198], and even decreased linewidths if the influence of thickness and compositional fluctuations is diminished [197]. Therefore in contradiction to the concurrent peak broadening and blueshifting observed with excitation proximity, the QCSE cannot be the sole contributor to the radiative recombination processes here. The appearance of a high-energy feature at 2.15 eV arrowed in the ROI 3 spectrum of Figure 4.6(b) can also be contributing partly to the peak broadening. Other possible factors that can contribute to peak broadening with increased excitation density unique to nanowires include: inhomogeneous lateral strain distribution and inhomogeneous screening of internal fields in the presence of surface depletion layers [99].

4.3.4.1 Evidence of Quantum-Confined Stark Effect

The CL emission distribution of luminescence centres in more basic InGaN/GaN heterostructures can be used to better understand the complex optical behaviour in the dot-in-a-wire structures, in particular the excitation density dependent effects. As expected in nanowires with a single InGaN QD introduced in Figure 4.7, the presence of only one InGaN QD results in fewer emission peaks. In most cases, only one main peak is identified, eliminating the influence of spatial and spectral overlap for peak assignments. Within the energy-filtered CL map in Figure 4.7(b), the maximum intensity is peaked across the QD but not clearly defined to the outlines of the QD, as identified in the ADF image (Figure 4.7(a)). In addition, the emission intensity exhibits a fair degree of spatial asymmetry between the two sides of the QD, with the distribution elongated towards the n-GaN direction.

Unlike in the previous section describing the dot-in-a-wire samples with an AlGaN EBL,

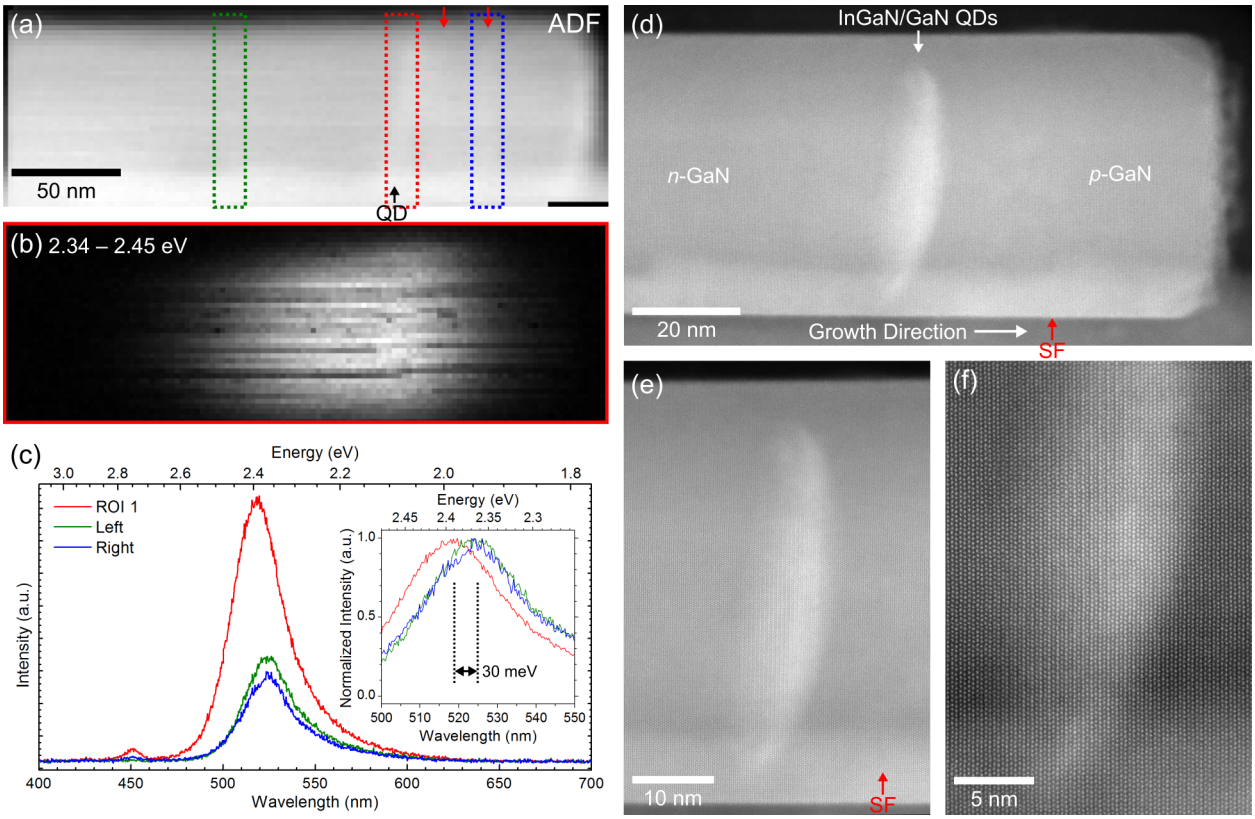

Figure 4.7: Single InGaN/GaN dot nanowire. **(a)** ADF image acquired simultaneously during STEM-CL spectral imaging, **(b)** spatial map of main emission peak within spectral range labeled from ROI marked in **(a)** and the spectra shown in **(c)**. **(d)** HRSTEM-HAADF image along $\langle 11\bar{2}0 \rangle$ zone-axis showing the InGaN QD, and a stacking fault is marked in the *p*-GaN by a red arrow. **(e, f)** High-magnification views in the vicinity of the QD, including **(e)** a separate stacking fault within the *p*-GaN (arrowed in red with SF label), and **(f)** the tail region of the area boxed in **(d)** that details the high-degree of atomic-ordering.

where the contributions of the Al-rich shell coverage had to be considered for radial asymmetries, only the QD morphology would be relevant in this case. HRSTEM imaging was used to evaluate the QD morphology, which instead shows that the crescent-shaped QDs are bent towards the *n*-GaN segment in Figure 4.7(d). Such a hollow truncated pyramid shape is typical of the first QD within the growth order for both single and multiple InGaN/GaN QD nanowire structures. This asymmetric CL emission intensity behaviour, which can be excluded as a result of the InGaN QD morphology, was confirmed in all single InGaN QD nanowires examined using combined nanoCL and HRSTEM. Furthermore, the scan raster direction during spectral imaging with respect to the growth direction also has no effect on the intensity distribution asymmetry. Other structural characteristics of the single dot nanowires are summarized in the following. As already described in the previous chapter (Chapter 3) where the single InGaN dot nanowires were first introduced, a high degree of 1:1 bilayer atomic-ordering in the InGaN QDs is prevalent. The atomic-ordering is evidenced in

Table 4.1: Lattice parameters and elastic constants [30], and spontaneous and piezoelectric constants [60] for wurtzite binaries of AlN, GaN and InN.

Parameters	AlN	GaN	InN
a (Å)	3.112	3.189	3.545
c (Å)	4.982	5.185	5.703
C_{13} (GPa)	108	106	92
C_{33} (GPa)	373	398	224
P_{sp} (C/m^2)	−0.081	−0.029	−0.032
e_{31} (C/m^2)	−0.60	−0.49	−0.57
e_{33} (C/m^2)	1.46	0.73	0.97

the HAADF images of the QD tail region in Figures 4.7(e) and 4.7(f). In addition, minimal defects are identified within the active region in individual nanowires, with the exception for stacking faults typically in the p-GaN segment (Figures 4.7(d) and 4.7(e)).

A proximity dependence of the CL peak emission energy can also be noted in the nanowire in Figure 4.7. The peak intensity maximum at the InGaN QD, as denoted by the ROI 1 spectrum in Figure 4.7(c), is centred at 2.39 eV. Energy shifts are apparent in the spectra taken from the two sides of the QD, also summarized in the spectra in Figure 4.7(c). Both the left (green spectrum) and right (blue spectrum) sides of the QD demonstrate a ∼30 meV redshift relative to the main peak noted in the inset normalized spectra. A small additional peak at 2.75 eV is assigned to the stacking faults identified in the p-GaN segment (CL map not shown), whose locations are marked by the red arrows in Figure 4.7(a). The spectral linewidth remains mostly invariant on the two sides of the QD relative to the linewidth at the InGaN QD (FWHM of 150 meV), with a FWHM of 147 meV from the n-GaN side and 143 meV from the p-GaN side. This contrasts the previous example discussed in Section 4.3.4, where the emission peak concurrently broadens and blueshifts as the incident probe position approaches the emission centre. Therefore within the limited magnitude in emission intensity variation, QCSE alone can be ascribed to govern the luminescence behaviour in these InGaN QDs (without indications of simultaneous band-filling effects). The cathodo-generated carrier density increases with proximity of probe position to the QD, which screens the internal polarization field and reduces the QCSE, and subsequently causes the emission energy blueshift. A suppression of QCSE in III-N nanowire structures relative to their planar counterparts have been demonstrated by several studies, including in GaN/AlN QDs in nanowires [64, 198] and InGaN QWs in GaN nanowires [9, 17]. Nonetheless, QCSE is not diminished to negligible levels, as favourable elastic strain relaxation in a nanowire geometry only relieves the piezeoelectric component of polarization. Naturally, this advantage will benefit more the larger lattice-mismatched InGaN/GaN structures, but the spontaneous po-

larization component in GaN/AlN heterostructures remains dominant. A comparison of the spontaneous polarization constants (P_{sp}) between binary III-Ns is listed in Table 4.1 to highlight the dissimilar P_{sp} values for GaN and AlN. As already demonstrated in Section 2.6.1 on the InGaN/GaN dot-in-a-wire structures, an estimate of the piezoelectric polarization (P_{pz}) directly from lattice deformation measurements averages a 30% decrease compared to equivalent planar QWs. Therefore, it still remains important to assess the relevance of QCSE on carrier recombination processes in order to design high-efficiency device structures.

4.3.5 Spatial Resolution of Cathodoluminescence in STEM

Factors contributing to the spatial resolution of CL spectroscopy in S(T)EM have already been detailed in Section 1.6.4.2. The interaction volume is generally a good indicator of the generation volume of electron beam-induced charge carriers, which may diffuse away before recombining elsewhere. An advantage of the higher acceleration voltage and thinner specimens used in STEM-CL relative to SEM-CL is to minimize the lateral beam spreading effect that degrades spatial resolution from the site of carrier generation. Therefore, the material-dependent minority carrier diffusion length becomes the bottleneck limiting STEM-CL spatial resolution. It should be emphasized that both carriers that recombine locally at the incident electron beam position, as well as those that diffuse away from the point of excitation, are attributed to the same beam position [189]. Therefore, the interpretation of CL spectroscopy cannot be simply generalized. Other influences, such as the presence of defects, surfaces, and external perturbations from temperature, electric field, and stress, all have to be taken into consideration when analyzing CL spectra. In the case of heterostructures with Type I (straddled) band alignment such as InGaN/(Al)GaN or GaN/Al(Ga)N heterostructures, carrier confinement can reduce the effective diffusion length [199]. At the limits of the CL signal delocalization and further complicated by the spatially and spectrally overlapping emissions, the attribution of specific spectral features to individual InGaN QDs can be ambiguous within the 2D monochromatic CL images. Furthermore, the presence of electric fields can contribute to additional carrier drift, such as from strong polarization-induced fields [200, 201], intrinsic built-in fields from p-n junctions [182, 202], or even externally applied bias [203].

4.3.5.1 Diffusion and Drift of Carriers within Nanowire Structure

Epitaxial growth of bottom-up self-catalyzed GaN nanowires on Si(111) have been known to exhibit a wurtzite (WZ) structure, with a large majority of which have N-face polarity, or grown along $[000\bar{1}]$ direction [46]. Given the large hole effective mass in GaN materials,

the hole mobility in (In)GaN is orders of magnitude lower. As a consequence, the diffusion length of holes in GaN is intrinsically small [204], and the effects of carrier diffusion and drift is limited by the holes. Since CL emission is dominated by the recombination of the minority carriers (holes in most regions), diffusion and drift of holes control the excitation efficiency during indirect excitation of recombination centres. The observed spatial asymmetry in the luminescence intensity distribution, which is affected by charge carrier diffusion and drift in the presence of spontaneous and piezoelectric polarization fields in the InGaN/GaN NWHs, will be addressed in this section.

The spatial asymmetry induced by an excitation probability difference of the same emission centre can be attributed to the influence on carrier drift due to internal and built-in electric fields generated by polarization and the *p*-*n* junction potential, respectively. An analogous asymmetry in CL emission distribution was first proposed to be induced by the effects of carrier drift in the presence of internal electric fields in the case of unintentionally-doped (*n*-type) single GaN quantum disk in AlN nanowires [201]. A comparison between the two types of polar double heterostructures—the current InGaN/GaN, and GaN/AlN in literature, will be outlined in the following.

Given the growth along a polar *c*-axis with the non-centrosymmetric wurtzite structured III-N, a crucial property is the crystal polarity. It can be safely assumed that under the N-rich growth conditions used results in III-N nanowires with N-polarity such that the growth direction aligns to $[000\bar{1}]$. A direct comparison of the resulting CL emission is illustrated schematically in Figure 4.8. At first glance, the asymmetry with respect to the growth direction is reversed between the InGaN/GaN and GaN/AlN cases, lobed towards [0001] and $[000\bar{1}]$ in Figures 4.8(a) and 4.8(b), respectively. Recall that the directionality of hole drift actually lies anti-parallel to the excitation probability asymmetry. It is solely the underlying dominant type of polarization that differentiates the two cases. Both heterostructure types have components of spontaneous polarization (P_{sp}), whose vector always points from the nitrogen-atom to the group III-atom along $[000\bar{1}]$. Assuming in both cases that the thin QD is grown pseudomorphically on the underlying binary III-N nanowire, the in-plane strain state of the QD is compressive in both scenarios. The resulting piezoelectric polarization (P_{pz}) is a positive value and hence points along [0001], and anti-parallel to the spontaneous polarization vector. The polarization-induced sheet charge (σ), and resulting electrostatic field vectors (F_{pol}) are shown accordingly in Figure 4.8. A list of the relevant parameters for spontaneous and piezoelectric polarization are summarized in Table 4.1. The similar P_{sp} values for GaN and InN and large InN/GaN lattice mismatch makes the piezoelectric polarization component dominant, leading to a polarization field that points along $[000\bar{1}]$. On the other hand, the two anti-parallel polarization vectors within the GaN QD are close to cancelling out completely

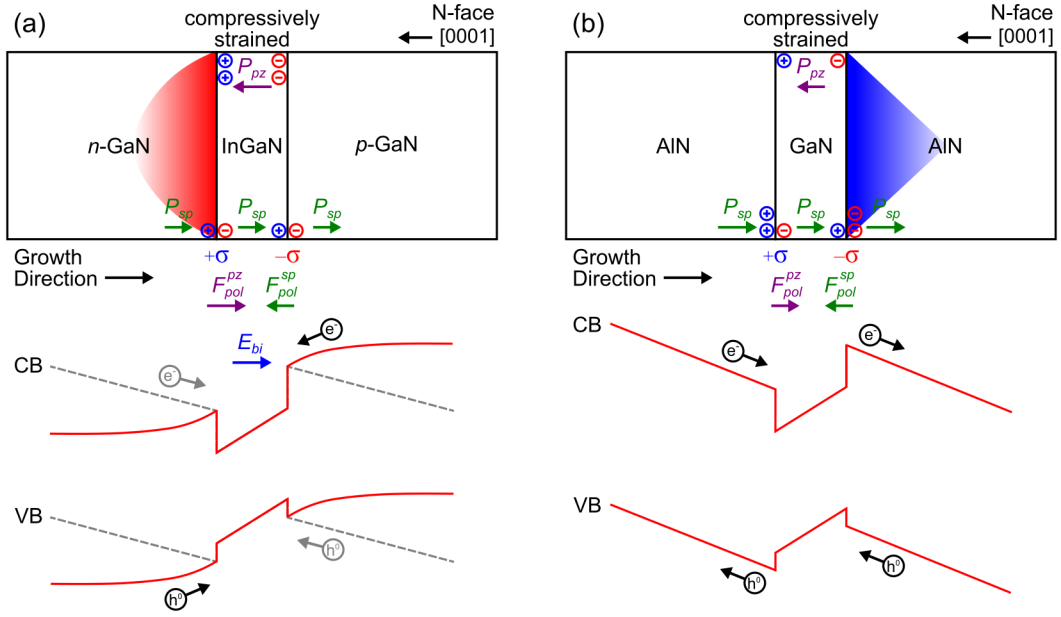

Figure 4.8: Schematic representation comparing **(a)** n-GaN/i-InGaN/p-GaN and **(b)** unintentionally-doped AlN/GaN/AlN double heterostructures and the experimentally observed asymmetric CL intensity distribution marked by the shaded area in red and blue, respectively. The spontaneous polarization and piezoelectric polarization directions are deduced according to the compressive strain state and N-face polarity, and gives the resulting polarization field (F_{pol}). The polarization-induced interfacial sheet charge (σ) as a result of the dominant polarization type (denoted by the longer F_{pol} arrow) is also indicated. The length of the polarization arrows represent the relative magnitudes in the different materials. A qualitative model of the energy band diagram at the hetero-junction is also shown to illustrate the field-induced band tilting and the carrier drift for each case. Note the additional built-in electric field (E_{bi}) from the p-n junction in **(a)**, where the band diagram (and carrier drift) in grey only considers only P_{sp} and P_{pz} (similar to in **(b)**), the band diagram in red also includes contributions from the built-in field.

at the -2.41% compressive in-plane strain. The P_{sp} value differences for GaN and AlN is sufficiently large, and governs the sheet charge at the GaN/AlN interfaces.

A qualitative representation of the band diagram including the effects of band tilting caused by polarization fields and the resulting carrier drift motion at the two types of heterostructures is also included in Figure 4.8. It is evident that, in spite of the identical internal polarization field vectors (and resulting interfacial sheet charge) between the InGaN/GaN and GaN/AlN scenarios, the observed CL intensity asymmetry is completely opposite. The only other underlying difference is the presence of the built-in electric field (E_{bi}) from the p-n junction potential in the current InGaN/GaN system. Another CL study on very similar single InGaN quantum disk in GaN p-n nanorods, but formed by top-down etching of Ga-polar epilayers, reveals two corroborating pieces of evidence [182]. Firstly, the GaN near-band edge emission is detected exclusively from the n-GaN segment. Second, the CL emission distribution from the InGaN QD is severely asymmetric towards the n-GaN segment facing $[000\bar{1}]$. The switch to Ga-face polarity reverses directions of all polarization fields (F_{pol}).

However, the hole drift direction remains the same in the direction of the build-in electric field (E_{bi}), which is now parallel to the (spontaneous) polarization field outside of the InGaN disk. Therefore, it can be concluded that the CL emission asymmetry in the current N-polar InGaN/GaN single dot nanowires (Figure 4.7(b) and schematically in Figure 4.8(a)) is not driven by polarization fields, but instead dominated by the prevailing built-in junction field.

4.4 Incorporating Al within the Barrier Layers

The integration of an AlGaN EBL in InGaN/GaN NWH has demonstrated mitigation against effects of electron overflow [85], and additional surface passivation benefits from the Al-rich AlGaN shell spontaneously formed at the nanowire sidewalls discussed in the previous Section 4.3. The carrier dynamics in nanowire devices is adversely dominated by non-radiative surface recombination, resulting in short carrier lifetimes of ∼0.4 ns or less [176, 205]. Therefore, the utilization of the larger bandgap AlGaN as barrier layers, which then function as distributed EBLs and simultaneous surface passivation, was also explored. In such quantum well/dot structures, the band offset governs the degree of carrier confinement [206], as such, the use of AlGaN barriers is also expected to enhance the carrier confinement. The AlGaN barriers are additionally modulation-doped p-type to enhance hole transport during electrical injection. The InGaN/AlGaN NWHs exhibit a nested core-shell structure made up of an Al-rich AlGaN shell surrounding the InGaN QDs along both axial and radial directions. The nested shell nature results from significant radial incorporation during the growth of AlGaN barriers, leading to a gradual increase in nanowire diameter along the growth direction. In most cases, the nanowire diameter increase is coupled with a progressive increase in QD diameter. Evidence of Al-segregation within the AlGaN barriers is attributed to the reduced growth temperatures for the heterostructure optimized for In-incorporation, as well as the modulation doping with Mg that alters the incorporation rate of Al-adatoms. STEM-CL spectral imaging shows a progressive redshifting of the peak emission energy along the growth direction. The spatial localization of individual spectral features suggests superior three-dimensional carrier confinement, which can be assigned to specific QDs as resolved with sufficient clarity in the BF image acquired without aberration-correction.

HRSTEM-HAADF imaging of an exemplary InGaN/AlGaN NWH is shown in Figure 4.9 along $\langle 11\bar{2}0 \rangle$ a-plane orientation, presenting clearly from the atomic-number contrast the ten InGaN/AlGaN QDs in the GaN nanowire. A view of the active region in Figure 4.9(a) shows that the ten InGaN dots (in bright contrast) are centrally-confined and capped by the AlGaN barriers (in dark contrast), each of which form an Al-rich core-shell at the nanowire sidewall. The overall high crystalline quality of the dot-in-a-wire core-shell heterostructures

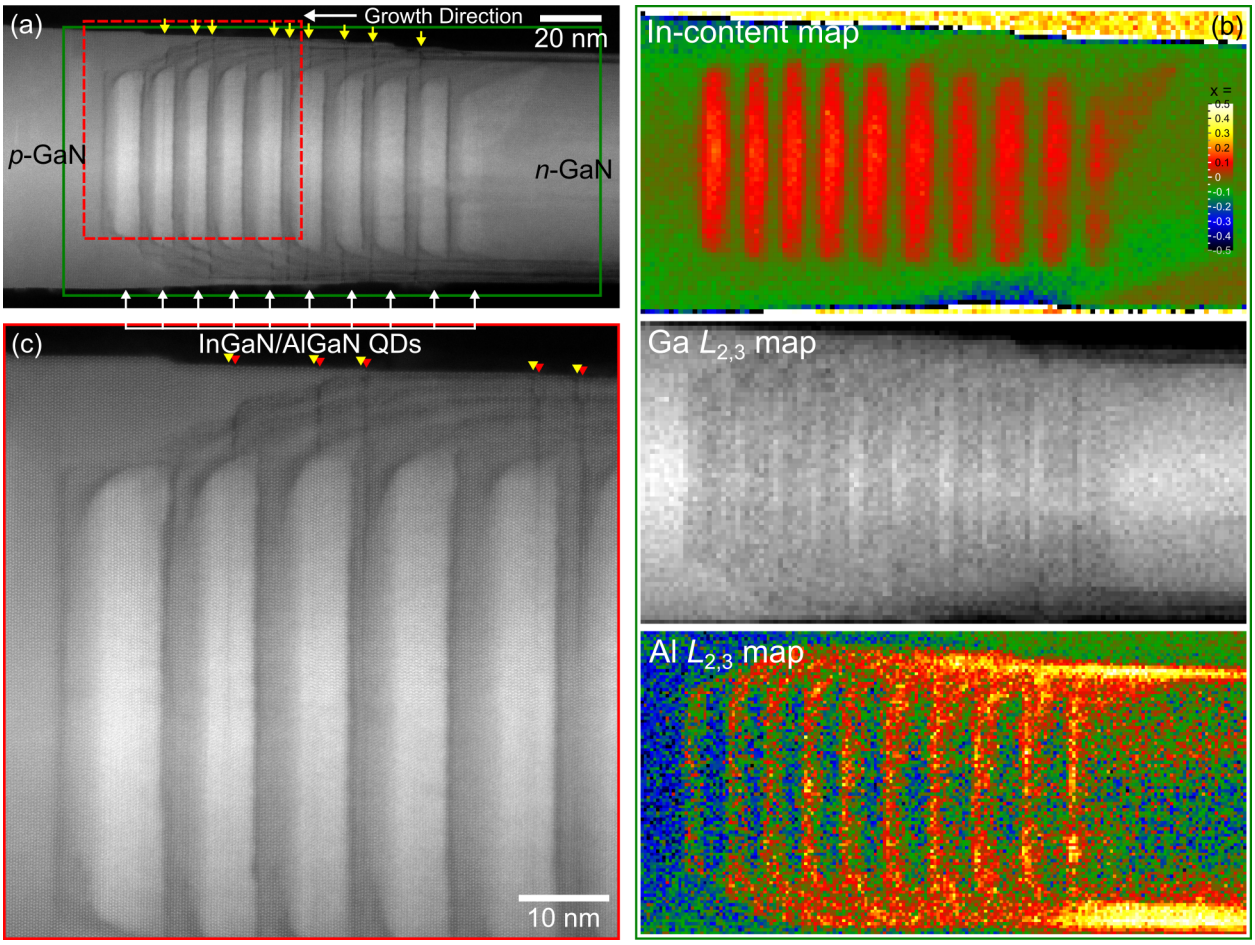

Figure 4.9: InGaN/AlGaN dot-in-a-wire core-shell heterostructures. **(a)** STEM-HAADF images showing the InGaN dots, AlGaN barriers, and the Al-rich core-shell by atomic-number contrast. The acquisition area of the EELS spectrum image is boxed in green in **(a)**. **(b)** Elemental mapping from EELS spectrum imaging of the green area marked in **(b)** of the group III elements extracted from the In $M_{4,5}$, Ga $L_{2,3}$, and Al $L_{2,3}$-edges. **(c)** Higher-magnification, atomically-resolved HAADF image of the selected region (boxed in red dashed line) in **(a)** showing the AlGaN core-shell and barriers in detail. Arrowed in yellow in **(a)** are E-type basal plane stacking faults. Noted in **(c)**, the same stacking faults are marked by yellow triangles, red triangles mark the Al-rich *c*-planes, and between each pair of triangles is the step-wise increase in nanowire diameter.

is demonstrated in the atomic-resolution images of Figures 4.9(a) and 4.9(c). It should be remarked that the uniformity in QD morphology and size is greatly improved with the use of AlGaN barriers. The QD approaches the flat disc-like shape with smooth sides and minimal bent semi-polar tails. With the exception of QD#1 that continues to exhibit a hollow truncated pyramid shape grown on the *n*-GaN segment. Elemental analysis was performed using STEM-EELS on the nanowire in Figure 4.9. Elemental maps from spectrum imaging in Figure 4.9(b) illustrate the distribution variation of the three group III elements in the different regions. The In-map, representing the thickness-projected In-content extracted

from the In $M_{4,5}$-edge, shows a strong localization in only the QDs. The Ga-map shows a signal maximum towards the centre of the nanowire because of the increased projected thickness for the *a*-plane viewing orientation, as well as an overall deficiency in the active region and at the sidewalls in the presence of In or Al alloying elements.

4.4.1 Al Segregation within Barrier Layers

Most notable is the Al distribution in the AlGaN barrier layers and the Al-rich core-shell in the Al-map extracted with the Al $L_{2,3}$-edge (Figure 4.9(b) bottom). The Al-rich core-shell is continuous from each of the AlGaN barriers, and present throughout the whole active region as it propagates well into the *n*-GaN segment (also visible in Figure 4.9(a)). A higher-magnification HAADF image of the core-shell (Figure 4.9(c)) highlights the continuity of the core-shell from the AlGaN barriers, suggesting their formation during the growth of the AlGaN barriers from the facile sidewall incorporation due to minimal lateral diffusion of Al-adatoms. Examining the InGaN/AlGaN heterostructure in detail reveals numerous I_1-type basal plane stacking faults ($ABAB\underline{ABC}BCBC$) that extend the full nanowire diameter: five at InGaN QDs (#4, 5, 6, 8, 9) and four at AlGaN barriers (#2, 3, 5, 7), marked by yellow arrows in Figure 4.9(a). Each of these stacking faults coincide with two events within the two preceeding atomic planes: i) a single atomic (*m*-)plane step-wise increase in nanowire diameter (between red and yellow triangle pairs); ii) a single Al-enriched *c*-plane at the nanowire near-surface region, deduced based on the locally darker HAADF image contrast intersecting with the Al-rich AlGaN shell visible in Figure 4.9(c) marked by red triangles. The intersection of the Al-rich shell and the stacking fault-adjacent Al-rich *c*-plane is a feature easily recognizable at low-magnification, and was later used to locate stacking faults in a straightforward manner.

Other areas with significant Al-segregation within the AlGaN barriers include the regions covering the curved outer edges of the InGaN QDs and at the top *c*-plane surface of each AlGaN barrier before the next QD. The former can be related to the additional Mg-dopant introduced to achieve modulation doping in the AlGaN barriers. The latter is most prominent at the last AlGaN barrier (#10), where the transition to *p*-GaN is abrupt (*cf.* Figures 4.9(c) and 4.10(a)). The significant Al-enrichment prior to the growth of the next QD can be described by the surface segregation of Al-adatoms at the low growth temperatures of the active region optimized for In-incorporation. The axial Al-segregation within the AlGaN barrier layers is further emphasized in the Al-map performed within the heterostructure (on a separate nanowire) at a higher spatial sampling in Figure 4.10(b). Multiple I_1-type stacking faults are also identified in the nanowire in Figure 4.10(a) marked by yellow triangles. The

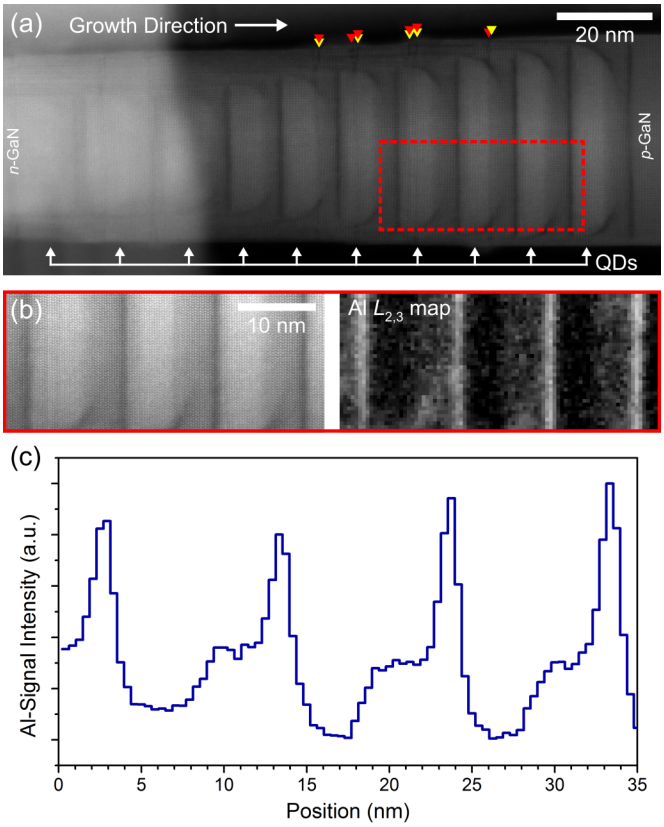

Figure 4.10: **(a)** HRSTEM-HAADF image along $\langle 11\bar{2}0 \rangle$ zone-axis showing the active region highlighting the general characteristics of the InGaN/AlGaN heterostructure. Noted are stacking faults marked by yellow triangles, and Al-rich *c*-planes marked by red triangles. **(b)** Higher-magnification HAADF image and Al-map (Al $L_{2,3}$-edge) of the selected area (boxed in red dashed line) in **(a)**. **(c)** Integrated line profile of the Al-signal map in **(b)**.

integrated line profile (Figure 4.10(c)) highlights a step-wise then sudden onset increase of the Al-signal projected through thickness. It is important to note that the nested nature of the AlGaN barrier layers presents some inherent difficulty to decouple compositional change with 3D shape change within the Al-rich shells. However, the existence of a highly Al-rich *c*-plane layer terminating the top of each AlGaN barrier layer can be deduced with certainty, as confirmed in other adjacent zone-axes about *c*-axis.

The observed Al-rich shells can serve as chronological growth markers to evaluate the axial and lateral growth rates within the active region, and further investigate the kinetics of nanowire formation. Similar use of AlN or Si-doping as growth markers have been demonstrated in both GaN nanowires [207, 208] and coalescence in patterned structures [209, 210]. The Al-rich markers illustrate concentric radial growth during the deposition of each AlGaN barrier layer (Figures 4.9(a) and 4.10(a)), which gradually increases the overall nanowire diameter. The general trend in a majority of InGaN/AlGaN NWH shows the gradual increase in nanowire diameter is also concomitant with a progressive increase in the QD diameter along the growth direction. The limited Al-adatom mobility smoothing the growth front can factor into the improved QD uniformity, as In-incorporation remains largely on the *c*-plane surfaces of the growth front instead of also on the semi-polar edge facets.

4.4.2 Enhanced Carrier Confinement with AlGaN Barriers

The incorporation of higher bandgap AlGaN as barrier layers has tremendous effects on the nanoscale optical properties within individual nanowires. The InGaN/AlGaN nanowires show similar range of polychromaticity in its emission energy as the InGaN/GaN dot-in-a-wires in Section 4.3, but isolated emission bands spanning the same wavelength range have broader linewidths. The spatial localization of individual spectral features suggests superior three-dimensional carrier confinement with the AlGaN barrier layers. A generic trend in the evolution of emission energy along the growth direction, as well as regions of local CL quenching, can be identified and correlated to specific structural features. Also worth noting is the drastically improved resolution of individual InGaN QDs in the nanoCL BF image (Figure 4.11(a)) because of the larger Z-difference between InGaN and AlGaN. Isolated emission spectra from the active region shows a successive redshifting of the peak emission energy along the growth direction (ROI 1 – 3 in Figure 4.11(f)). There are overlapping of peaks, but through peak-fitting demonstrate individual emission peaks have a broad linewidth, up to 200 meV at FWHM. More noticeable is the effect of improved axial carrier confinement in the energy-filtered CL maps across the three emission peaks, as summarized in Figure 4.11(b)–(d). The CL maps have been filtered on the high-energy side of each emission peak to minimize the negative impact of directional diffusion from high- to low-bandgap areas (or even similarly from band-filling effects) on spatial resolution and contrast [130, 189]. The individual features are localized to a spatial width of ∼15 nm, which approximates to the thickness of a barrier-dot-barrier section and can be assigned to specific InGaN QDs. Because of the overlapping nature of the peaks, the CL intensity is maximum at the locations of the ROIs, but also recurrent across other QDs.

Subsequent HRSTEM-HAADF imaging on the same nanowire along *a*-plane orientation (Figure 4.11(g)) shows good correspondence to the approximate spacing between QDs identified in the nanoCL BF image. Three basal plane stacking faults have been located intersecting QD#1, 3, 4, identified with red triangles based on the intersection of the Al-rich shells and Al-rich *c*-planes outlined previously. The 10 InGaN QDs within this NWH exhibit a gradual increase in diameter along the growth direction, concurrent to a steady decrease in the AlGaN shell thickness. The emission energy redshift along the growth direction is consistent with changes in the deformation potential caused by these changes in the shell-to-core volume ratio, as a result of the concentric nature of the Al-rich shells formed during the AlGaN barrier layers. As the core radius increases at a constant shell thickness, the out-of-plane component of the strain-induced deformation potential is decreased, leading to a smaller blueshift. Simultaneous core radius increase with shell thickness decrease, such as observed in this Figure 4.11 nanowire, further enhances this out-of-plane strain effect on the

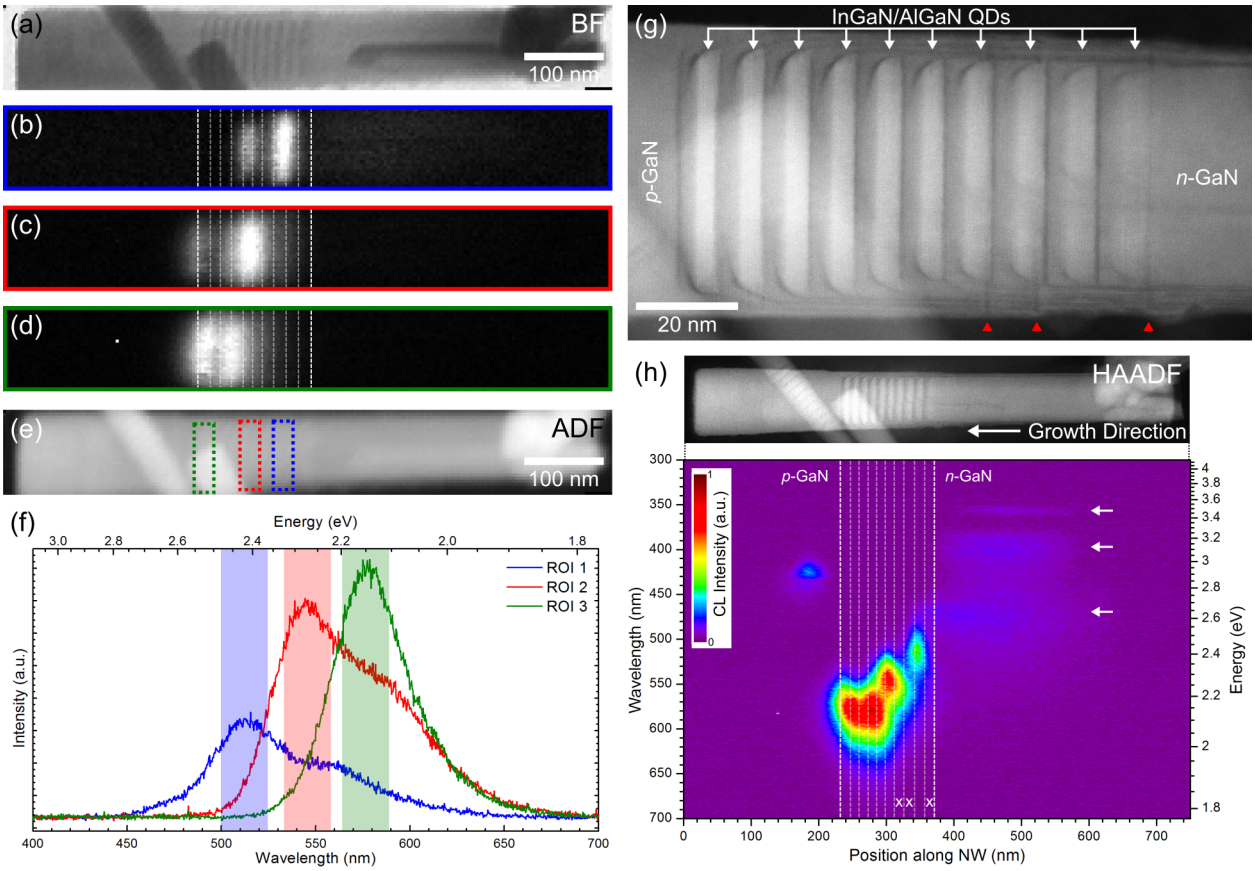

Figure 4.11: **(a)** BF and **(e)** ADF images acquired concurrently, and wavelength-integrated CL maps **(b – d)** of spectral features marked in CL spectra **(f)** from ROIs shown in **(e)**. **(g)** HRSTEM-HAADF image showing the Al-segregation within the AlGaN barriers and stacking faults marked by red triangles, **(h)** CL spectral profile integrated across nanowire diameter (bottom), and HRSTEM-HAADF image taken at zero-tilt to mimick the projection during nanoCL (top). Dashed lines in **(b – d)** and **(h)** mark the locations of AlGaN barriers in the active region as guides to the QD separation.

transition energy. It should be noted that the shell-to-core ratio effect on the deformation potential is a first approximation for the general trend, and does not yet take into account the in-plane strain component at the InGaN/AlGaN heterostructure, nor any changes in In-composition between InGaN QDs also taking place.

Minimal radial asymmetry in the CL distribution (*cf.* Figure 4.11(b)–(d)) encourages the use of a 2D spectral profile representation of the full spectrum image for better visualization of simultaneous spatial and spectral variations within the active region. Presented in Figure 4.11(h) is the 2D spectral profile plotting emission energy/wavelength as a function of the probe position along the nanowire growth axis within the spectrum image. Weaker intensity emission bands, including the GaN near band-edge (NBE) at 3.5 eV and related phonon replicas from the *n*-GaN segment (arrowed in white), and an extraneous band at

3 eV from the nanowire overlapping the p-GaN segment, can also be identified in the 2D spectral profile. The GaN NBE is typically not detectable from either p- nor n-GaN in the InGaN/GaN dot-in-a-wire structures with (and without) AlGaN EBL. The spontaneously-formed Al-rich shell is generally only a single layer of ∼1 nm thick, in comparison to multiple Al-rich layers making up the ∼5 nm thick shell for the InGaN/AlGaN heterostructures. The sufficient surface passivation from the distributed AlGaN EBL overcomes the non-radiative surface recombination at the n-GaN segment as well as the efficient carrier capture into the active region that normally led to the lack of n-GaN emission. The emission energy redshift along the growth direction is strikingly evident within the the 2D spectral profile. The BF image (Figure 4.11(a)) was used to identify the boundaries of the AlGaN barrier layers drawn as dashed-line markings for the spatial-spectral correlation. Local intensity maxima are isolated to single QDs (#2, 5) or can be isolated to specific QDs (#7, 9) in the overlapped intensity distribution. Also evident is where the emission is quenched within the active region at QD#1, 3, 4 (marked by X's in Figure 4.11(h)), which coincides with where stackings faults are located. As already demonstrated in the InGaN/GaN dot-in-a-wire example in Section 4.3.2, basal plane stacking faults and related stacking error-induced ZB insertions are the designated culprit to local CL quenching within the active region.

4.5 Conclusion

In summary, the polychromaticity in emission wavelength from InGaN/(Al)GaN NWH is deduced using nanometer-scale CL spectral imaging to also be occurring at the single nanowire level. The inhomogeneous broadening can be attributed to the compositional variation between InGaN QDs. Isolating individual emission bands from multiple and single dot-in-a-wire structures illustrates that the non-uniform lateral strain distribution in nanowires contributes to the intrinsically broad linewidth. Various structural features, including the InGaN QD morphology, the GaN and Al-rich AlGaN surface passivating shell and presence of stacking fault defects, govern the CL intensity distribution by way of affecting the excitation probability of recombination centres. Excitation density-dependent behaviours can also be pinpointed to alter the local spectral characteristics, namely contributions from band-filling and QCSE. Lastly, the underlying electrostatic fields (polarization and built-in potential) are confirmed to have adverse effects on the carrier drift in such polar nanostructures.

Chapter 5

Carrier Localization at Atomic-Scale AlGaN Compositional Fluctuations

5.1 Introduction

Considerable interest has been generated to develop highly efficient deep ultraviolet (DUV) emitters using AlGaN-based alloys with direct bandgaps between 3.4 – 6.1 eV for a broad range of applications. AlGaN light-emitting diodes (LEDs) have thus far made good progress in the UV-A and UV-B bands (315 – 400 nm, and 280 – 315 nm, respectively), achieving relatively high internal quantum efficiencies (IQE) of ∼50% [211]. However, device performance experiences significant degradation towards the UV-C band (100 – 280 nm), with the IQE dropping drastically to $< 10^{-3}$% approaching the AlN near band-edge at $\lambda = 210$ nm [212, 213]. Conventional AlGaN quantum well lasers made up of epitaxial AlGaN layers similarly demonstrate degraded performance with decreasing emission wavelength. To date, the shortest wavelength reported for electrically-injected AlGaN (multiple) quantum well laser diodes at room-temperature are in the UV-A at 336 nm with threshold current densities that remain high in the order of few tens kA/cm^2 [214]. Alternatively, lasing of AlGaN quantum well lasers in the UV-B and UV-C bands at room-temperature can be achieved through optical pumping [215], but require threshold power densities up to 100 kW/cm^2 [216, 217].

Conventional planar AlGaN DUV devices, in particular electrically-injected solid-state lasers and LEDs, experience limited efficiencies due to the high dislocation density (up to 10^{10}/cm^2 [50]) from the lattice mismatch, and inefficient p-type impurity doping using Mg in Al-rich AlGaN with increasing Al-content. The ionization energy of Mg acceptors in AlN is reported upwards of 500 – 600 meV [212, 218], as compared to 170 meV in GaN [219], significantly limiting the free charge carrier density with only 1% of Mg-atoms getting

thermally-activated at room-temperature. In addition, the achievement of p-type conductivity is further impeded due to strong compensation by the presence of intrinsic defects, such as nitrogen vacancies (V_N), or other common unintentional shallow donors. Further regarding native defects, group III vacancy-related complexes (V_{III}–X) in $Al_xGa_{1-x}N$ alloys are prone to form acceptor-type defects that act as non-radiative recombination centres, in which the occurrence of V_{Al} increases with x due to its smaller formation energy than V_{Ga} [90].

From a light-extraction efficiency standpoint in conventional top (or bottom) emitting c-plane devices, the unusual switching of emitted light with transverse electric (TE, $E \perp c$) polarization to transverse magnetic (TM, $E \| c$) polarization with increasing Al-concentration in AlGaN alloys is also problematic towards wavelengths below 300 nm [220]. This phenomenon originates from valence band structure differences between the binary constituents of GaN and AlN, where a reversal in sequence between the heavy hole/light hole (HH/LH) and crystal-field split-off hole (CH) bands unique in AlN leads to a cross-over in these two bands in AlGaN alloys above a critical Al-composition [220]. Additional factors such as the strain state of the active region also have an effect on the relative splitting/order between the HH/LH and CH bands, and can be engineered to control the emission polarization, as demonstrated previously by Northrup et al. [221] in AlGaN/GaN quantum well systems. The polarization of the light emission from an AlGaN active region within a device depends on the character of the lowest-energy hole state at the valence band maximum. If the lowest-energy transition involves a HH or LH, TE polarization is dominant like in binary GaN; if the lowest-energy transition involves a CH, the polarization of the emitted light is strongly TM, as in AlN. Consequently, the light propagating along c-axis to be extracted from the top-surface must have TE polarization [221], or limiting conventional c-plane planar Al-rich AlGaN light-emitters to only be side-surface extracted to accommodate the intrinsic TM polarization [222].

Nanowire (NW) structures can be a promising alternative to enhance strain relaxation and p-doping, both mediated by the additional free surfaces. Firstly, the surface segregation of dopants [223, 224] could enhance the incorporation of Mg-dopants during III-N nanowire growth. Secondly, the nitrogen-rich growth environment that promotes nanowire growth also simultaneously suppresses the formation of compensating nitrogen vacancies [218, 225]. The strong light scattering and coupling in nanowire structures have also demonstrated that light extraction can be improved for AlN as the TM polarized emission can be extracted directly from the top c-plane surfaces of AlN nanowire arrays [226]. Furthermore, the self-organized, randomly-distributed nanowires provide strong photon confinement by way of recurrent multiple scattering in the random nanowire array cavity, *i.e.* Anderson localization

[227, 228], for electrically-injected AlGaN nanowire lasers that can operate at $\lambda = 289$ nm at room-temperature with low threshold current densities [229].

Such high Al-content AlGaN nanowires, developed as emitters in the DUV, have reported exceptionally high IQE up to 80% as determined using temperature-dependent photoluminescence (PL) spectroscopy [229, 230]. The reduced temperature quenching of PL intensity suggests strong spatial and energy localization of charge carriers at potential fluctuations that leads to minimal losses through non-radiative recombination [231]. Other temperature-dependent optical signatures of carrier localization include: sharp emission lines at low-temperatures due to localized exciton emission, coupled with linewidth broadening at high-temperatures, and a S-shape variation in emission energy characteristic of delocalization-localization behaviour [231–233]. Further structural characterization revealed nanoscale alloy inhomogeneities within the AlGaN nanowires that demonstrate some dependence on growth temperature, and believed to be driven by growth kinetics. The compositional variations lead to local potential minima in the energy band, and recognized as the origin of the carrier confinement in these AlGaN alloys producing very high spectral density of lines with few meV linewidths at low-temperature [231]. Comprehensive photon correlation experiments were able to isolate individual emission lines in single nanowires to demonstrate anti-bunching behaviour, confirming each line stems from a discrete level, *i.e.* a single localization centre. Together with a lack of evidence showing the thermalization of neutral donor-bound exciton (D^0X) towards a free exciton (FX) with increasing temperature, this is indicative of quantum dot-like confinement behaviour as the main localization mechanism at the Ga-rich AlGaN regions [234]. In a similar manner, atomic-scale compositional modulations have even been reported recently in high Al-concentration AlGaN nanowires and suggested to act as efficient localization centres to enhance radiative recombination [229, 230]. However, a comprehensive understanding of emission characteristics in such spontaneously-formed compositional fluctuations in AlGaN nanowires, from directly correlating the localized optical response to structural/chemical properties at relevant lengthscales is still lacking.

Following the previous chapters discussing alloy-related effects in InGaN-based nanowires, this chapter instead focuses on AlGaN nanowires, specifically the similarities and differences in alloy (in)homogeneity with varying Al-concentration and the resulting local optical properties. High and low Al-content $Al_xGa_{1-x}N$ p-i-n homojunctions were grown on Si-doped GaN nanowire templates on Si(111) substrates by plasma-assisted molecular beam epitaxy. Characterization on single nanowires using nanometer-scale cathodoluminescence (nanoCL) spectral imaging at 150 K was performed, and subsequently correlated to their structural information obtained with aberration-corrected scanning transmission electron microscopy (STEM). In this context, the current chapter is organized to distinguish the two low and high

Al-concentration AlGaN nanowires in separate sections, starting with the low Al-content AlGaN nanowires in Section 5.3. The low Al-content nanowires demonstrate structural and chemical characteristics as expected from AlGaN homojunction nanowires with no intentional changes in composition, as well as exhibit optical properties that infer minimal confinement potential within individual nanowires. In contrast, the high Al-content nanowires presented in Section 5.4 display extensive alloy fluctuations throughout the AlGaN layers, varying in size (down to the atomic-scale) and faceting nature between the differently doped *p*-*i*-*n* segments. The corresponding nanoCL mapping shows an abundance of emission peaks with spatially localized origins at locations with alloy fluctuations. Tendencies for specific bandwidths from certains regions with specific compositional fluctuations can also be drawn and discussed.

5.2 Methods

5.2.1 MBE Growth

Catalyst-free high and low Al-concentration $Al_xGa_{1-x}N$ *p*-*i*-*n* homojunctions were grown on Si-doped GaN nanowire templates on Si(111) substrates by a Veeco Gen II radio frequency plasma-assisted molecular beam epitaxy (MBE) system at McGill University under nitrogen-rich conditions. The Si wafers were cleaned by standard solutions (HCl, H_2O_2, HF, typical in RCA clean procedures) prior to loading into the system. The Si surface oxide was thermally desorbed at 770 °C *in situ*. Before growth initiation, a thin Ga seeding layer was utilized to promote the nanowire nucleation and formation. Schematically shown in Figure 5.1, the nanowire structure consists of Si-doped GaN (∼250 nm), *p*-*i*-*n* AlGaN homojunction (each layer ∼100 nm), and a thin (∼10 nm) Mg-doped GaN contact layer. The growth conditions include a nitrogen flow rate at 1.0 standard cubic centimeter per minute (sccm), a forward plasma power of 350 W, Ga beam equivalent pressure (BEP) in the range of 5×10^{-8} to 7×10^{-8} Torr, and Al BEP in the range of 8×10^{-9} Torr to 4×10^{-8} Torr. The nominal Ga/Al BEP ratios correspond to 11% and 88% Al-concentration in the low and high Al-content AlGaN nanowires, respectively. The growth temperatures for GaN and AlGaN layers are 780 °C and 800 °C, respectively. The Si and Mg dopant concentrations for *n*- and *p*-AlGaN regions were estimated to be 1×10^{18} cm^{-3} and 1×10^{20} cm^{-3} based on calibrations from Si and Mg-doped epilayers grown under similar conditions, respectively. The Mg concentration in AlGaN nanowires, however, may be lower, due to the Mg surface desorption at the growth temperature of AlGaN nanowires.

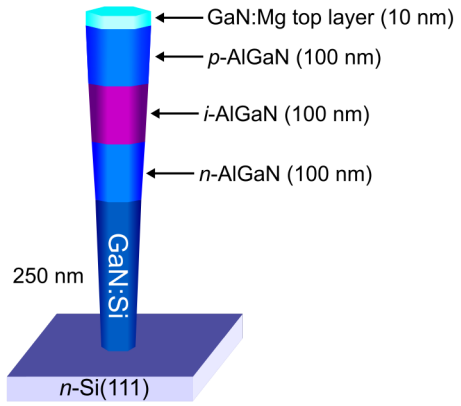

Figure 5.1: Schematic illustration of the AlGaN *p*-*i*-*n* nanowire structure for both low and high Al-concentration AlGaN nanowire samples (Sample A and B), consisting of 250 nm *n*-GaN nanowire base, 100 nm each of *n*-AlGaN/*i*-AlGaN/*p*-AlGaN making up the homojunction, and 10 nm *p*-GaN top contact layer.

5.2.2 Scanning Transmission Electron Microscopy

5.2.2.1 Nano-Cathodoluminescence

Nanometer-resolution STEM-cathodoluminescence (nanoCL) spectral imaging on individual nanowire structures was performed using a custom-built system on a VG HB-501 dedicated STEM at the Université Paris-Sud XI. The in-house high collection efficiency CL spectrum imaging detection set-up is described in detail by Zagonel et al. [122] and Tizei et al. [201]. The microscope is equipped with a high-brightness cold field-emission gun, operated at 60 kV with typical probe currents of 5 – 10 pA with ∼1 nm probe size. Specimens were cooled to ∼150 K with liquid nitrogen to further minimize effects of beam damage and concurrently increase radiative emission efficiency by surpressing phonon-assisted non-radiative recombination. Photons are collected by a parabolic mirror with a large solid-angle, coupled into a fibre optic bundle and dispersive optical spectrometer (300 grooves per mm diffraction grating blazed to 300 nm) read-out in parallel onto an electron-multiplying charge-coupled device (EMCCD). Such a set-up allows for high-speed acquisition while maintaining high-spectral resolution and high signal-to-noise ratio in the full emission spectrum. Experimental parameters provide a spectral resolution of 0.17 nm in wavelength ($\Delta\lambda$), or specifically ∼1.6 meV at the GaN bandgap energy and ∼2.9 meV at an energy of 4.59 eV relevant to the AlGaN studied. Experiments were performed in spectrum imaging mode for concurrent acquisition of spatial information from bright-field (BF) and annular dark-field (marked ADF in figures for simplicity) signals, allowing for a point-to-point comparison between the full CL emission spectrum collected at every pixel. In the absence of aberration-correction, typical spatial resolution obtained is ∼1 nm. Calibration of the dispersive grating and the parallel-detection onto the CCD is carried out using pairs of emission lines from a Hg vapour lamp for the ultraviolet wavelengths. The as-grown nanowires samples were mechanically exfoliated from the Si substrate, dispersed in anhydrous ethanol, and deposited on carbon-coated TEM support

grids for observation.

5.2.2.2 High-Resolution STEM

Subsequent structural characterization of the same homojunction nanowires was carried out using aberration-corrected scanning transmission electron microscopy (STEM). The possible generation of point defects due to knock-on damage in GaN is undesirable for CL signal collection, as they greatly quench the radiative recombination. The threshold for such electron-beam damage in GaN has been reported as 120 keV [185], therefore the STEM-CL experiments below threshold were performed first, then followed by the high-resolution (HR)STEM to study the atomic structure and elemental distribution. The high-resolution experiments were performed with a FEI Titan Cubed 80-300, fitted with a high-brightness field-emission gun (X-FEG), aberration-correctors on both the probe- and image-forming lens systems, a monochromator, and a high-resolution electron energy-loss spectrometer (Gatan GIF Quantum 966). All experiments were carried out at an accelerating voltage of 200 kV with 19 mrad convergence angle. Atomic-number, Z-contrast sensitive high-angle annular dark-field (HAADF) images were obtained using a detector angular range of 63.8 – 200 mrad. Elemental mapping by electron energy-loss spectroscopy (EELS) in STEM mode was done with the Ga $L_{2,3}$, and Al K-edges at 1115 eV and 1560 eV, respectively, using the spectrum imaging technique with a collection semi-angle of 28 mrad. Weighted-principal components analysis (PCA) was applied for noise reduction of the spectrum images using the multivariate statistical analysis (MSA) plugin implemented within DigitalMicrograph by HREM Research Inc.

5.3 Low Al-Concentration AlGaN Nanowires

Low-Al content $Al_xGa_{1-x}N$ nanowires (Sample A), with a nominal Al-concentration of $x = 0.11$, exhibit structural characterisitics and elemental distribution expected of AlGaN homojunction nanowires in this range of composition reported in literature. Some common features include an Al-rich AlGaN shell that can passivate the surface, and a high degree of compositional homogeneity within the AlGaN core region, as observed from high-angle annular dark-field (HAADF) Z-contrast imaging in Figure 5.2(a). It is also seen that the nanowire has a slight inversely tapered geometry, *i.e.* the nanowire is slowly increasing in diameter along the c-axis growth direction. Shown in Figure 5.2(e) is a high-magnification HAADF image taken from the marked region in Figure 5.2(a). The aforementioned Al-rich AlGaN shell near the nanowire surface (dark band) can be observed, within which 1:1 c-plane bilayer atomic-ordering of the AlGaN alloy is also demonstrated (analogous to the InGaN

alloys discussed in Chapter 3). In addition, this Al-rich AlGaN shell is further surrounded by a few atomic-plane thick Ga-rich AlGaN outermost shell (bright planes). Also notable for the low Al-content Sample A, is the prominent presence of basal plane stacking faults in the *p*-AlGaN region as indicated in detail by arrows within the insets of Figure 5.2(e). The Al-rich AlGaN shell show discontinuities in the atomic-ordering (segments of brighter (0001) layers) within the *p*-AlGaN region that appears to be correlated with the stacking faults. Similar contrast variations at the Al-rich shell in Ni-catalysed $Al_{0.21}Ga_{0.79}N$ nanowires have also been previously reported [235], describing irregular interruptions in the Al-rich (0001) layers intersecting with the radial growth component along the *m*-plane facets.

5.3.1 Alloy Homogeneity within Nanowire Core

Electron energy-loss spectroscopy (EELS) spectrum imaging was further performed to study the elemental distribution. Shown in Figure 5.2(b), the RGB composite false-colour image of Ga- and Al-signals suggests a low Al-concentration in the core region and a high Al-concentration in the shell region. The presence of an Al-rich AlGaN shell surrounding the nanowire structure is consistent with previous studies [232, 233, 236, 237]. The formation of such core-shell nanowire structures can significantly suppress non-radiative surface recombination and increase the carrier injection efficiency of nanowire LEDs and lasers. The surface mobility differences between the Ga and Al cation species can induce compositional inhomogeneity in AlGaN alloys [238], caused by the disparity in cohesive energies (Ga–N bond energy 2.2 eV, Al–N bond energy 2.88 eV) [239]. The spontaneous enrichment of Al at the nanowire sidewalls is one form of inhomogeneity specific to the additional free surfaces in nanowires. The direct impingement of Al-adatoms, which with their lower diffusivity, do not fully migrate back up to the *c*-plane growth front and instead incorporate locally at the sidewalls forming the core-shell structure.

Line profiles of the Ga-map (Figure 5.2(c)) at various positions along the nanowire laterally, as presented in Figure 5.2(d), suggest that a hexagonal cross-section with *m*-plane facets is maintained all along the nanowire. The Ga-signal measured from EELS increases monotonically with increasing concentration as well as projected thickness, therefore the shape of the signal profile directly infers the cross-sectional thickness. It is evident that along this *a*-plane viewing direction of $\langle 11\bar{2}0 \rangle$, the resulting projected Ga-signal intensity profiles shown in Figure 5.2(d) suggest *m*-plane sidewall facets, matching similar HAADF image intensity analysis by Arbiol et al. [240] in the GaN cores of their GaN/AlN nanowires. This confirms that the low Al-content AlGaN nanowires (Sample A) maintain a hexagonal cross-section of *m*-plane facets between the *n*-GaN base to the various *n*-, *i*, and *p*-AlGaN

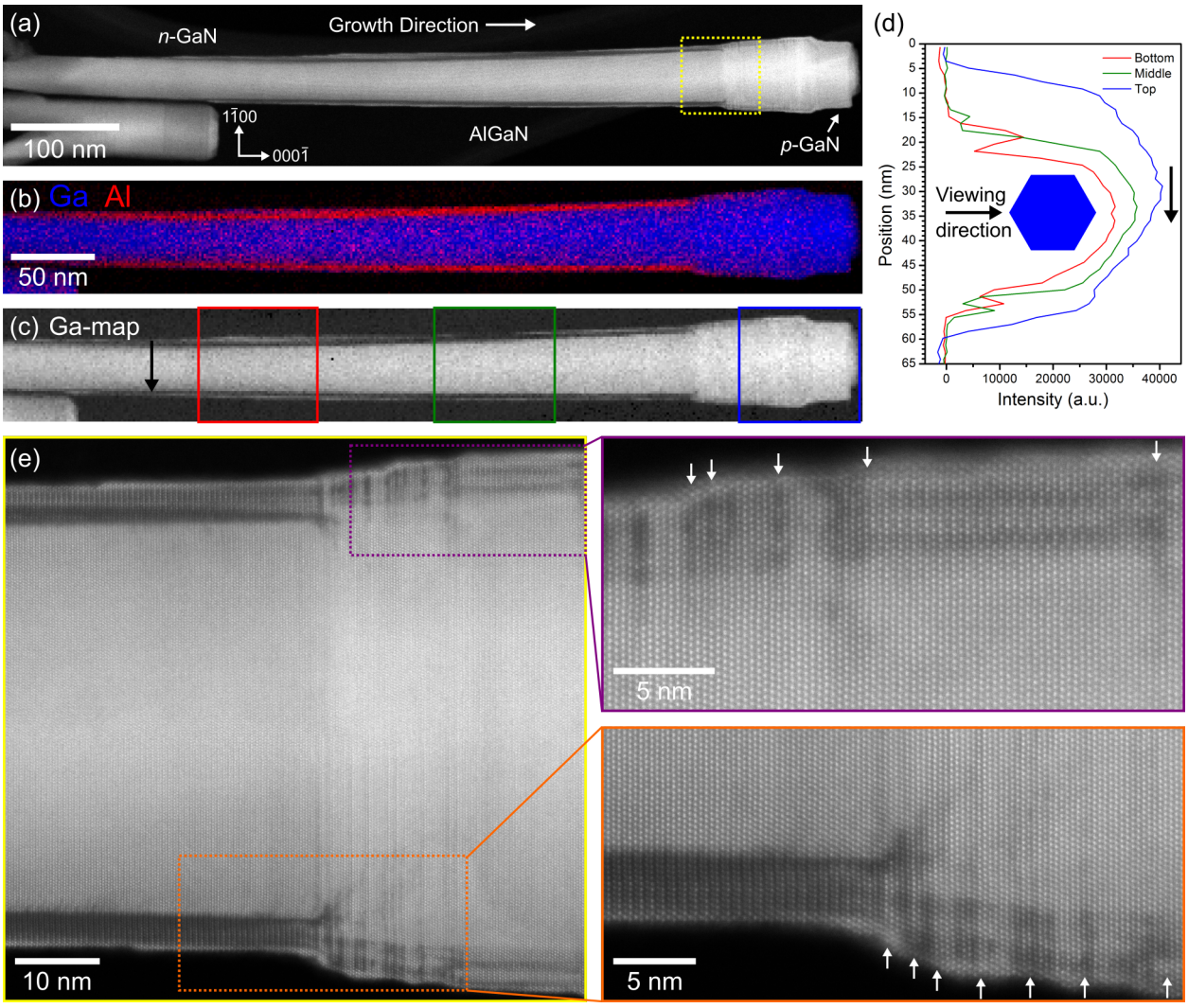

Figure 5.2: **(a)** STEM-HAADF image of a low-Al content AlGaN nanowire, Sample A. **(b)** Composite false-colour EELS map showing Ga and Al elemental distribution of the same nanowire viewed along a-plane orientation, with weighted-PCA applied for noise reduction, **(c)** Ga-distribution map only, same as the blue component in **(b)**. **(d)** Integrated intensity line profiles in the direction of the arrow of the projected Ga-signal from the boxed regions in **(c)** along different segments of the nanowire that show a tendency towards m-plane facets based on the projected profile shape. **(e)** High-magnification image from the boxed region in **(a)** showing uniform image intensity in the nanowire core, and the presence of the Al-rich shell and Ga-rich outermost shell. Detailed insets of the sidewall surface regions in the p-AlGaN region exhibits multiple stacking faults as arrowed.

layers grown subsequently, contrary to the high Al-content AlGaN nanowires (Sample B) to be discussed later in Section 5.4.2.1. An illustration for the hexagonal cross-section relative to the viewing direction is shown inset within Figure 5.2(d).

5.3.2 Elemental Confirmation of Al-Incorporation into Wire Core

Elemental quantification for the composition in the low Al-concentration AlGaN nanowires was carried out on PCA-treated STEM-EELS spectrum images, as shown in Figure 5.3 of the same representative nanowire from Figure 5.2. Using the relative quantification methods (atomic ratio of two elements) shown in Equation (5.1) [114] to determine the true group III composition in III-nitrides is valid due to the 1:1 stoichiometry in these compound semiconductors. The scattering cross-sections of the Ga $L_{2,3}$ and Al K-edges collected simultaneously in each spectrum image was calculated using the Hartree-Slater models available within DigitalMicrograph based on the scattering geometry parameters used. The resulting Ga- and Al-fraction maps are generated, which represent the chemical composition averaged through the AlGaN core and the Al-rich AlGaN shell within the projected thickness, are presented in Figures 5.3(b) and 5.3(c). The sum of the intensity from the two maps in each pixel adds up to unity (*i.e.* $N_{Al} + N_{Ga} = 1$). A lateral line profile of the intensities for both species integrated along the central region of the AlGaN segment is displayed in Figure 5.3(d). The shell region is highly Al-rich, up to 85 – 95% in Al-concentration, while the core region has ∼30 – 35% measured Al-concentration.

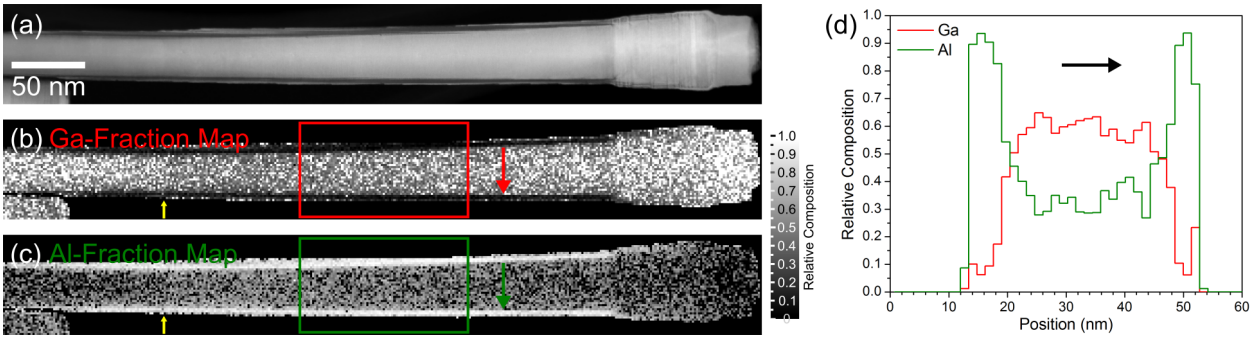

Figure 5.3: **(a)** ADF image the same low-Al content AlGaN nanowire (Sample A) from Figure 5.2 collected concurrently during the EELS spectrum image. EELS quantification of the relative Al/Ga-composition on dataset with weighted-PCA applied for noise reduction, using the Ga $L_{2,3}$ and Al K-edges collected simultaneously: **(b)** relative Ga-fraction map, and **(c)** relative Al-fraction map, both scaled between 0 – 1. A visible boundary with sudden changes in composition marks the n-GaN/n-AlGaN interface arrowed in yellow. **(d)** Integrated line profiles of the relative composition from the Ga-fraction and Al-fraction maps from the boxed regions in **(b)** and **(c)**, respectively.

$$\frac{N_{Al}}{N_{Ga}} = \frac{I_{Al}(\beta,\Delta)\sigma_{Al}(\beta,\Delta)}{I_{Ga}(\beta,\Delta)\sigma_{Ga}(\beta,\Delta)} \tag{5.1}$$

where

N : the areal density [atoms/nm^2]
I : the integrated edge signal intensity (can include plural scattering)
σ : the "partial" scattering cross-section [barns]
β : the collection semi-angle [mrad]
Δ : the integration energy window

A more accurate estimation of the Al-concentration within the AlGaN core (x_{core}) can be separated by taking into account the fractional core and shell thicknesses (d_{core} and t_{shell}, respectively) when considering a few simple assumptions [236]. Firstly, the hexagonal cross-section of the nanowires are simplified to a circular geometry. Secondly, the core-shell structure is assumed to be concentric in the through-thickness direction, and maintains the same proportion of fractional core/shell thicknesses. Considering these assumptions that are illustrated in the schematic in Figure 5.4, Equation (5.2) was derived accordingly to describe the fractional core and shell contributions along the projected thickness at the centre.

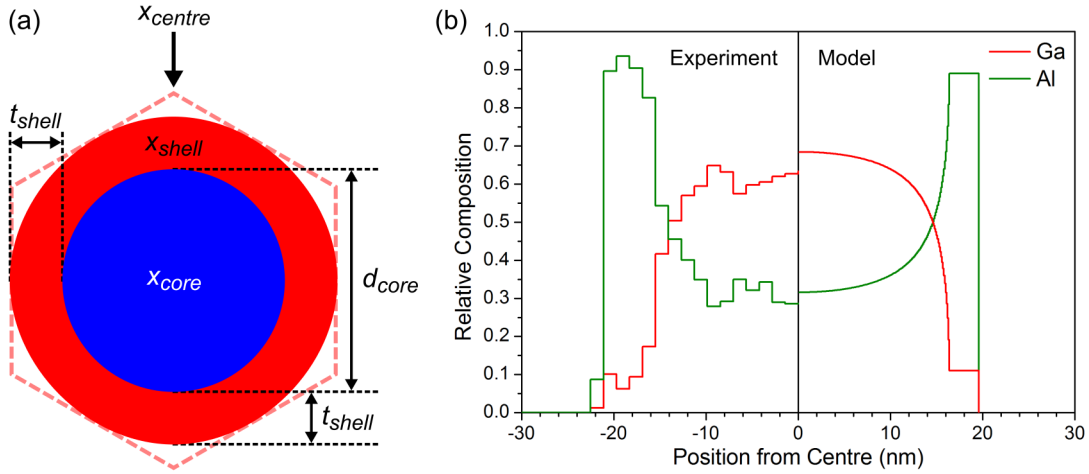

Figure 5.4: **(a)** Schematic model of the AlGaN nanowire simplified as a circular concentric core-shell structure in cross-section relative to the hexagonal outline (dashed red line) in this viewing direction. Equation (5.2) is derived according to the assumed proportions of core-to-shell along the centre of the nanowire through the projected thickness. **(b)** Comparison between the measured relative Ga- and Al-composition (from Figure 5.3(d)) and a projected profile calculated according to the model using parameters: x_{shell} = 89%, x_{core} = 20.1%, t_{shell} = 3.5 nm, and d_{core} = 32.5 nm.

$$x_{core} = \frac{x_{centre} \times (2t_{shell} + d_{core}) - x_{shell} \times 2t_{shell}}{d_{core}} \tag{5.2}$$

The Al-content can be extracted from the Al-fraction map of Figure 5.3(c), defining x_{shell} and x_{centre} as the measured Al-content at the shell and nanowire centre. For example, the quantification analysis gives: $x_{shell} = 89\%$ and $x_{centre} = 33\%$ from Figure 5.3(b), and local $t_{shell} = 3.5$ nm and $d_{core} = 32.5$ nm from the concurrent ADF signal (Figure 5.3(a)). Using Equation (5.2), the calculated Al-concentration at the AlGaN core, $x_{core} = 20.1\%$. A projected profile of the expected relative Ga/Al-composition calculated according to the cross-section model in Figure 5.4(a) is presented in Figure 5.4(b) (right panel) to illustrate the good correspondence to the experimentally-measured profile (left panel). Same treatment of the raw EELS data (not PCA-treated), with the exception of having a higher noise-level between adjacent pixels, also arrives at similar averaged quantities of composition at the AlGaN core. Despite the Al-signal in AlGaN core region appears low in an elemental map (red signal in the RGB composite of Figure 5.2(b)), the Al-concentration estimated from quantification following the projection-correction is substantial. Such that the AlGaN region in Sample A is expected to emit at distinguishably shorter wavelengths than if the core was pure GaN only, as also disproved later in Section 5.3.3.1 taking into account the presence of strain.

5.3.3 Delocalized Cathodoluminescence Signals over Long-Range

The optical properties of the AlGaN nanowires were also investigated using nanoscale STEM-CL spectrum imaging, followed by high-resolution STEM (HRSTEM) imaging to correlate to the spatial distribution of luminescence bands to structural features. Two of the low Al-concentration AlGaN nanowires from Sample A were examined and the results are summarized in Figure 5.5. NW 1 and NW 2 are shown viewed along their respective $\{11\bar{2}0\}$ a-plane and $\{1\bar{1}00\}$ m-plane orientations in the HRSTEM-HAADF images of Figures 5.5(a) and 5.5(h). The n-GaN/n-AlGaN interface is not easily identifiable in all nanowires from HAADF imaging (*e.g.* NW 2), inferring a relatively non-abrupt interface where the composition is graded or due to the small composition difference in the Ga-rich core region. The presence of stacking faults in the p-AlGaN region are detailed in the high-magnification images in Figures 5.5(f) and 5.5(g).

Individual nanowires in the low Al-content AlGaN Sample A typically show the presence of up to three CL emission peaks highly delocalized along the nanowire length over distances on the order of 0.2 μm (Figure 5.5(c)–Figure 5.5(d), Figure 5.5(j)–Figure 5.5(k)). Two peaks originate from the AlGaN region (sharp ~336 nm band-edge peak, broad and asymmetric peak with ~360 nm maximum), and one from the n-GaN base (weak intensity at ~357.6 nm, but on an adjacent overlapping nanowire). The very small blueshift in the GaN near

band-edge (NBE) emission energy of ∼10 meV from the *n*-GaN base can be assigned to the presence of strain induced by coverage of the Al-rich AlGaN shell with Al-content upwards of 95 at.% (Figure 5.3). The discrimination of emission from a strained GaN core and a low Al-concentration AlGaN core, both covered by an Al-rich AlGaN shell, will be detailed in a later section (Section 5.3.3.1).

Some wire-to-wire variation in the AlGaN band-edge peak wavelength exists, as evidenced in the comparison of CL spectra from regions of interest (ROIs) between NW 1 and NW 2

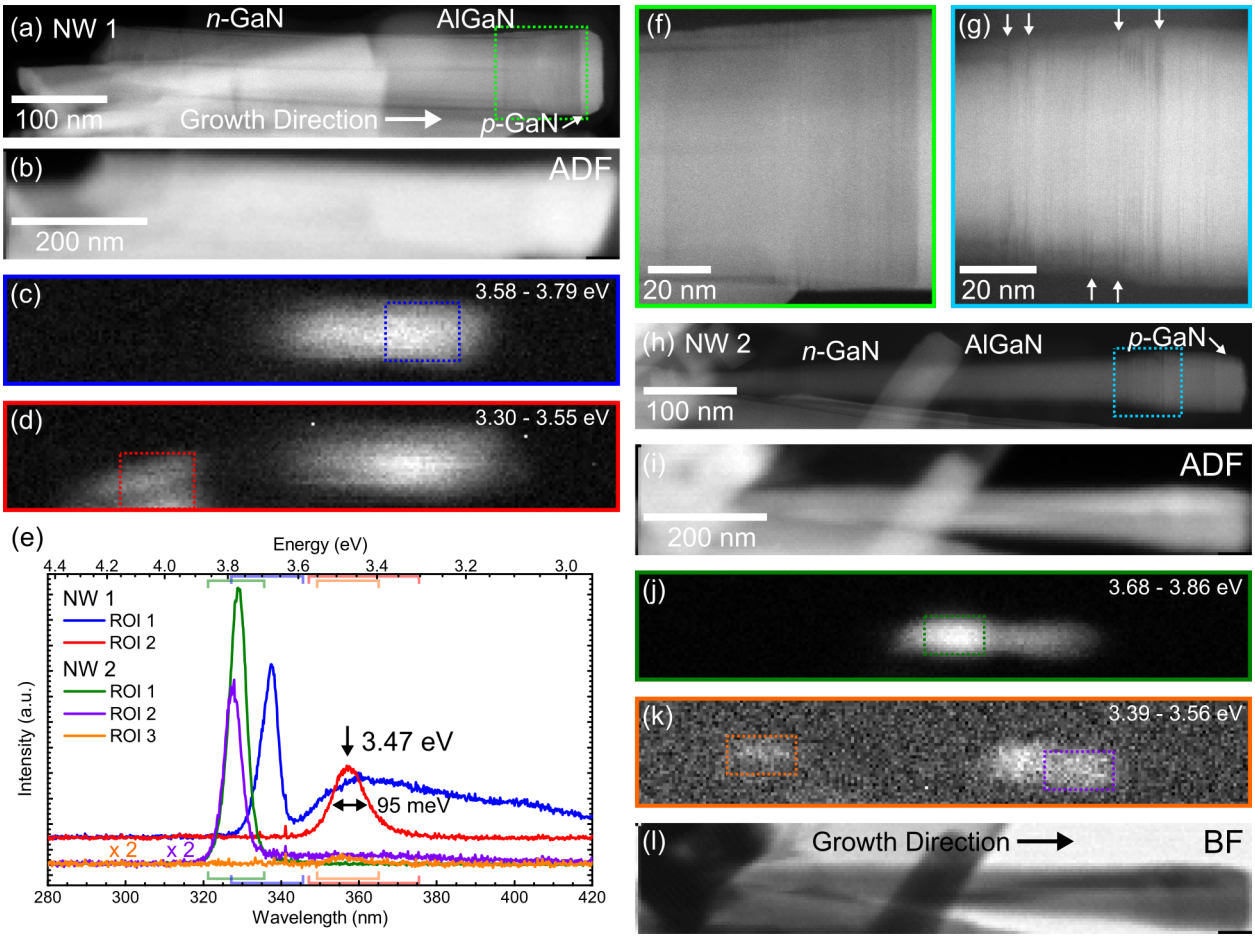

Figure 5.5: HRSTEM-HAADF images of low Al-content AlGaN nanowires (Sample A), **(a, f)** NW 1 viewed along *a*-plane and **(g, h)** NW 2 viewed along *m*-plane orientations. The presence of some stacking faults in the *p*-AlGaN region are marked by arrows in the detailed views of NW 1 and NW 2 in **(f)** and **(g)**, respectively. STEM-CL spectrum image of NW 1: **(b)** ADF image acquired concurrently with the CL spectrum image, and **(c, d)** wavelength-integrated CL maps of spectral features centred about the wavelengths labeled in **(e)** with energy integration window of each CL map also indicated. **(e)** Unique CL spectra from (region of interest) ROIs in NW 1 marked colour-coded in **(c, d)** and in NW 2 marked in **(j, k)**. Spectra of NW 1 (red, blue) have been shifted vertically for clarity. STEM-CL spectrum image of NW 2: **(i)** ADF and **(l)** BF image, and **(j, k)** wavelength-integrated CL maps of spectral features centred about the wavelengths labeled in **(e)**.

in Figure 5.5(e), showing a blueshift of 100 meV between NW 1 (ROI 1 in blue) and NW 2 (ROI 1 in green). Additionally, the full-width half-maximum of the AlGaN band-edge peak shows an average of approximately 5 nm (∼55 meV) at 150 K. The spread in the peak maximum and bandwidth observed in single low Al-concentration AlGaN nanowires using STEM-CL is consistent with temperature-variable PL spectroscopy carried out over a macroscopic ensemble of self-organized AlGaN nanowires [229]. The room-temperature PL spectrum of Sample A is shown in a later section alongside the high Al-concentration Sample B for comparison (Figure 5.12(b)). Similar AlGaN nanowires of the same range of Al-content have demonstrated room-temperature luminescence efficiency of ∼50%, as derived by comparing the integrated PL emission intensity at low-temperatures (10 K) and room-temperature at constant excitation power, assuming that the internal quantum efficiency (IQE) is unity at 10 K [241]. The estimated IQE is relatively high for AlGaN structures (both planar and nanowire geometries) of similar compositional range, and attributed to the Al-rich core-shell structure that can effectively suppress non-radiative recombination at the nanowire surfaces [121, 122, 176, 242]. The origin of such non-radiative recombination at surface states includes Ga-dangling bonds and other impurities at the non-polar nanowire sidewalls [243].

In all Sample A nanowires, CL emission intensity from the AlGaN region is peaked across the base *n*- and *i*-doped segments, and negligible intensity observed from the *p*-AlGaN regions. The *p*-AlGaN region is assumed to be where the nanowire diameter shows step-wise increases at the locations of stacking faults, which is consistent with the segment length expected from its growth duration. Other interfaces, such as *n*-GaN/*n*-AlGaN and *n*-AlGaN/*i*-AlGaN, are not distinguishable from HAADF imaging Z-contrast, and therefore doped AlGaN segments are not labeled in the images of the HRSTEM/nanoCL results shown in Figures 5.5 and 5.6. The continuity of the Al-rich AlGaN shell at the *p*-AlGaN region is disrupted, as compared to the *n*- and *i*-AlGaN segments, most evidently seen in Figure 5.2(e) and somewhat in Figures 5.5(f) and 5.6(b). An incomplete or locally discontinuous Al-rich shell can contribute to the local CL quenching observed at the *p*-AlGaN within single nanowires, because of the additional pathways to non-radiative recombination from the inferior surface passivation. The abrupt changes in sidewall incorporation of Al/Ga in these areas are likely due to the changes in sidewall surface energy in the presence of stacking errors that produced the faults [53]. The influence of Mg-doping on the relative growth rate between *c*- and *m*-plane terminating facets in GaN nanowires has been widely recognized [101, 104]. Consecutive stacking errors within a wurtzite (WZ) structure can lead to the formation of rotation twins about the *c*-axis or zinc-blende (ZB) insertions depending on the number of repeating units. ZB GaN (as well as binary InN and AlN) has a smaller bandgap

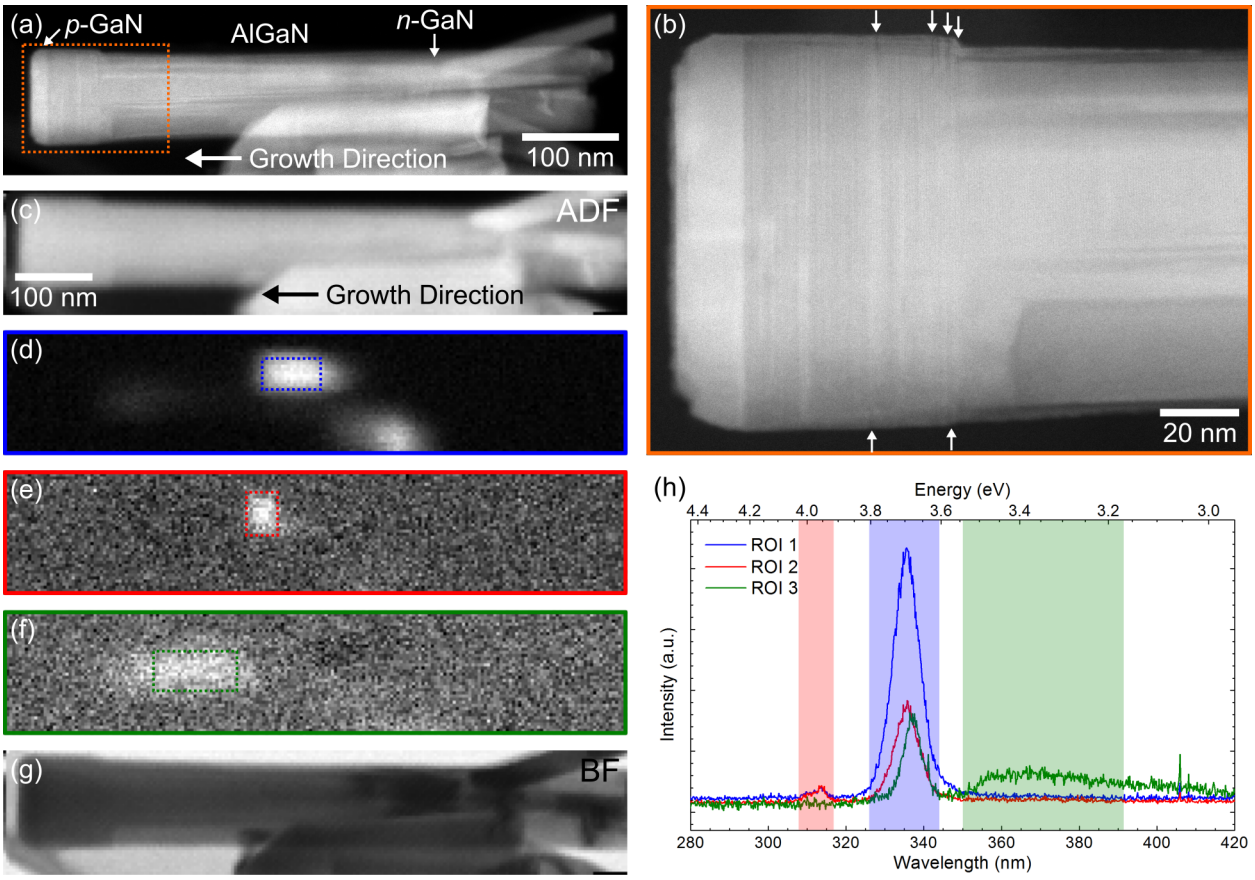

Figure 5.6: **(a – b)** HRSTEM-HAADF images of a low Al-content AlGaN nanowire (Sample A). The presence of some stacking faults in the *p*-AlGaN region are marked by arrows in the detailed view in **(b)**. STEM-CL spectrum image of the same nanowire. **(c)** ADF and **(g)** BF images acquired concurrently with the CL spectrum image, and **(d – f)** wavelength-integrated CL maps of spectral features centred about the wavelengths labeled in **(h)**. **(h)** Unique CL spectra from ROIs marked using colour-coded dashed boxes in **(d – f)**.

than its WZ phase counterpart [53], such that together with a staggered band alignment, ZB inclusions in an overall WZ GaN nanowire form quantum well-like heterostructures [55, 195].

Another nanowire examined from Sample A is shown viewed along an *a*-plane orientation in the HRSTEM-HAADF image in Figure 5.6(a). This Sample A nanowire showed no noticeable emission from the *n*-GaN base itself, but other emission peak intensities (Figures 5.6(d) and 5.6(f)) are similarly delocalized along the nanowire length over ∼0.1 μm in size as NW 1 and NW 2 from Figure 5.5. With the exception for an additional weak intensity peak at ∼314 nm from the AlGaN region shown in Figure 5.6(e), which originates from a confined central area within the AlGaN segment. However, no specific structural or chemical feature was identified using HRSTEM to correlate to this localized emission, so its emission origin remains unknown. The broad low-energy emission peak at 360 nm (∼3.44 eV) from

the i-AlGaN region in Figure 5.6(f) is considered of the same origin as NW 1's ROI 2 (blue spectrum in Figure 5.5(e)). In addition, a similar low-energy shoulder has been observed in room-temperature PL spectra of Sample A but overlaps with the expected emission from the n-GaN nanowire bases. This broad band can be ascribed to recombination of neutral donor acceptor pairs D^0A^0 in AlGaN at low (cryogenic) temperatures, which evolves towards a free electron-neutral acceptor transition eA^0 due to the thermal ionization of donors at temperatures above 100 K [128]. Its emission energy difference with the AlGaN NBE (FX_A) emission suggests a 236 meV deep acceptor level above the valence band, which is consistent with a Mg-acceptor activation energy (E_A) for AlGaN at the Sample A Al-composition (recall $E_A^{GaN} \approx 170$ meV [219], $E_A^{AlN} \approx 510$ meV [218]). Silicon substituting a nitrogen atom (Si_N) is another possible shallow acceptor in this case, as commonly observed in Si-doped GaN, Si_N has a binding energy $E_A \approx 224$ meV in GaN [244]. The asymmetric low-energy tail in the broad band is assigned to longitudinal-optical (LO) phonon replicas of the eA^0 transition [202]. CL emission from the n-GaN base is in general extremely weak in other (Al,In)GaN nanowire samples when surface passivation from the spontaneously-formed Al-rich AlGaN shell is absent. The strong presence of stacking faults in the p-AlGaN region are again noted in the high-magnification image in Figure 5.6(b). No defect-related emission at the p-AlGaN region that can be associated with the presence of stacking faults was observed.

5.3.3.1 Discriminating Emission from Strain or Composition in Nanowire Core

As a comparison to distinguish GaN emission from AlGaN emission in the Sample A, CL emission from the n-GaN bases in GaN p-n junction nanowires, in the absence of an Al(Ga)N shell, is presented in Figure 5.7. CL intensity is only observed in the n-GaN base portion of the nanowire (Figure 5.7(b)), but was detectable only when the carrier generation rate is maximized by increasing the probe current by up to ~90 times the currents used for the AlGaN nanowires. The corresponding spectrum in Figure 5.7(d) shows a narrow peak centred at 3.46 eV (358 nm), suggesting its contribution from a NBE transition of excitonic origin (involving free exciton or bound exciton recombination) or other shallow donor levels [202], and is in close agreement with literature values for CL emission from unstrained GaN at 150 K [122, 199, 245]. At low-temperatures, recombination of neutral donor-bound excitons (D^0X, due to shallow Si_{Ga} or O_N donors [104]) is the dominant NBE transition for undoped GaN [128]. With increasing temperature, such as at T = 150 K for the CL experiments, the D^0X lines are quenched giving way to free A exciton (FX_A) and even free B exciton (FX_B) lines observable with the spectral resolution from PL spectroscopy [128].

Analogous to coherent AlN/GaN core-shell nanowire heterostructures [246], an Al-rich AlGaN shell can inflict a *nearly uniaxial* compressive strain onto the n-GaN core along the

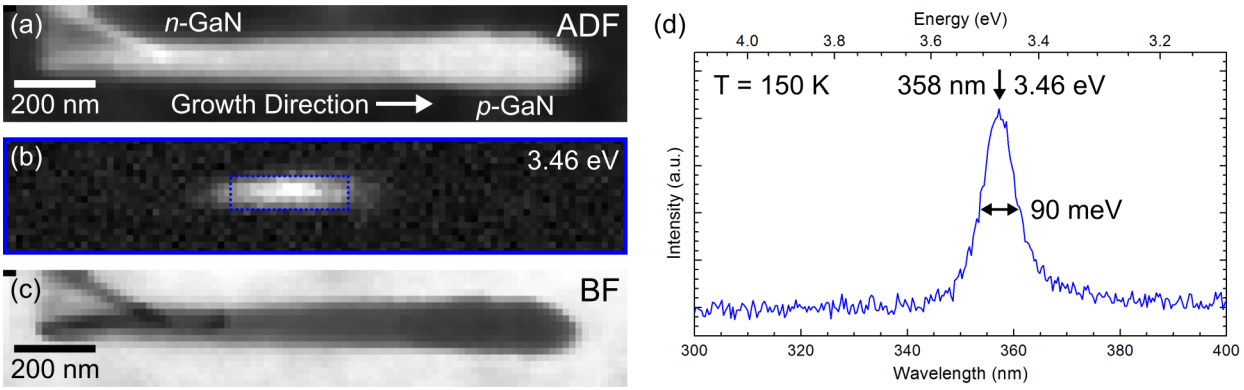

Figure 5.7: **(a)** ADF and **(c)** BF image of a GaN p-n junction nanowire from the STEM-CL spectrum image acquired at 150 K, **(b)** CL map extracted at E = 3.46 eV from the n-GaN region, and **(d)** CL spectrum showing the GaN NBE emission peak at 3.46 eV (358 nm) with 90 meV FWHM from the n-GaN region marked in **(b)**.

axial direction in Sample A nanowires [247]. The uniaxial-like strain condition is because the magnitude of the in-plane components, $\epsilon_{plane} = \frac{\epsilon_{xx}+\epsilon_{yy}}{2}$, is negligibly small compared to the out-of-plane strain ϵ_{zz} [248]. The uniaxial compression induces modifications to the GaN band structure that results in a blueshifting of the excitonic transition energies [249]. A dependence of the blueshift in luminescence energy on the thickness of the AlN shell has been reported by Rigutti et al. [246], or more specifically, on the degree of unixial strain which can be expressed as a function of the shell-to-core volumetric ratio V_{AlN}/V_{GaN}. In order to fulfill the criterion for continuity at the coherent GaN/AlN interface (according to continuum elastic theory), the out-of-plane strain in the GaN core ϵ^{zz}_{core} can be described as an analytical function of the nanowire geometrical parameters as in Equation (5.3) [248].

$$\epsilon^{zz}_{core} = \frac{F}{1+F}\frac{c_0^{AlN} - c_0^{GaN}}{c_0^{GaN}} \tag{5.3}$$

$$F = \frac{V_{AlN}}{V_{GaN}}\frac{C_{33}^{AlN}}{C_{33}^{GaN}}\left(\frac{c_0^{GaN}}{c_0^{AlN}}\right)^2 \tag{5.4}$$

$$\frac{V_{AlN}}{V_{GaN}} = \frac{t_s^2 + 2R_c t_s}{R_c^2} \tag{5.5}$$

where c_0 is the relaxed axial lattice parameter, C_{33} is the elastic constant, R_c is the nanowire core radius, and t_s is the shell thickness. The energy of excitonic transitions, including that of free A exciton (FX_A) can be calculated as a function of uniaxial strain ϵ^{zz}_{core} following Equation (5.6) for type A (heavy holes, HH), B excitons (light holes, LH) and similarly Equation (5.7) for type C excitons (split-off holes, CH).

Table 5.1: Material parameters for AlN and GaN used to describe the band structure of strained GaN, including valence-band deformation potentials (D_1 and D_3) and conduction-band hydrostatic deformation potential (a_{cz}) of wurtzite GaN from Ishii et al. [250]. The remaining parameter values are from Vurgaftman and Meyer [30].

Parameters	AlN	GaN
Axial lattice constant c_0 (Å)	4.982	5.185
Elastic constant C_{33} (GPa)	373	398
Crystal-field splitting Δ_{cr} (meV)	−169	10
Unstrained exciton energy $E_A(0)$ (eV)		3.478
Unstrained exciton energy $E_C(0)$ (eV)		3.5
Deformation potential $a_{cz} - D_1$ (eV)		−6.5
Deformation potential D_3 (eV)		4.9

$$E_{A,B}(\epsilon^{zz}_{core}) = E_{A,B}(0) + \Big[a_{cz} - D_1 - D_3\Big]\epsilon^{zz}_{core} \tag{5.6}$$

$$E_C(\epsilon^{zz}_{core}) = E_C(0) + \Big[a_{cz} - D_1\Big]\epsilon^{zz}_{core} \tag{5.7}$$

The low Al-content AlGaN nanowires (Sample A) presented in Figures 5.3, 5.5 and 5.6 exhibit an Al-rich shell with thickness ranging from 2 – 5 nm and core diameters varying from 30 – 100 nm along the nanowire length. The EELS elemental quantification for Sample A nanowires have already demonstrated in Section 5.3.2 that ∼20% Al is present within the AlGaN nanowire core. To further disprove the possibility of no Al incorporated within the nanowire core, the blueshift of the CL emission peak is assessed in the following. Under the hypothetical assumption that the cores are 100% GaN in the AlGaN segment (no Al was incorporated into the core) and the shells are 100% AlN, it suffices to isolate the extreme mismatch limits for simplicity. The blueshift in the "GaN core" emission (such as green NW 2 spectrum in Figure 5.5 and blue ROI 1 spectrum in Figure 5.6), which are at energies centred about 3.68 – 3.77 eV, is then 200 – 290 meV. Using Equation (5.6) to calculate the uniaxial strain needed to produce the smallest blueshift observed of 200 meV, it comes to −1.75% compressive strain when only considering type A excitons (X_A, electrons bound with HH), which translates to a shell-to-core volume ratio of $V_{AlN}/V_{GaN} = 0.80$ using Equations (5.3) and (5.4). It is worthwhile to mention that at such high magnitudes of uniaxial compression, there exists a cross-over between type A and C exciton energies at $\epsilon_{zz} \approx -0.5\%$, beyond which type C excitons (X_C, electrons bound to CH) becomes the lowest-lying energy transition at the valence band maximum [246, 249]. The deformation potentials that govern the blueshift are even smaller for type C exciton transitions (*cf.* Equation (5.7) and Table 5.1), therefore the calculated compressive strain required to

produce the observed minimum blueshift would not be realistic ($V_{AlN}/V_{GaN} = 3.62$). This calculated hypothetical scenario is therefore not in agreement with the observed shell-to-core volume ratio ($V_{AlN}/V_{GaN} < 0.50$) and the resulting CL emission energy (and hence assumed strain-induced blueshift).

The crossing of the valence band maximum is caused by changes in the internal displacement parameter u due to strain, which sensitively affects the crystal-field splitting (Δ_{cr}) that, along with the c/a lattice parameter ratios, governs the order of the Γ_6 (HH, LH) and Γ_1 (CH) hole bands (notation without taking into account spin-orbit coupling effect) [27, 249]. The sequence of Γ_6 and Γ_1 levels at the top of the valence band in wurtzite GaN is reversed with respective to wurtzite AlN, as described by the opposite signs in Δ_{cr} values (Table 5.1). Γ_6 and Γ_1 bands have wave functions that differ in character: Γ_6 is $p_{x,y}$-like and Γ_1 is p_z-like. The practical relevance of this band structure property difference is the switch in light polarization from TE-dominant in relaxed GaN to TM-dominant in uniaxially compressed GaN, given the change in $p_{x,y}$- to p_z-like character of the top-most valence band [251]. As already described in the introduction in this chapter, this change in light emission polarization has implications on the light extraction efficiency along the c-plane growth axis.

To illustrate this argument, a calculation for the Sample A nanowire presented in Figures 5.2 and 5.3 with an average $R_c = 16.25$ nm and $t_s = 3.5$ nm has $V_{AlN}/V_{GaN} = 0.48$ following Equation (5.5). In order for an AlN shell to inflict $\epsilon^{zz}_{core} = -1.75\%$ strain into the GaN core of the same size, the shell thickness would have to be 5.6 nm or greater. More recent work by Hetzl et al. [252] of Al(Ga)N/GaN core-shell nanowires with core diameters of ∼50 nm ($R_c = 25$ nm) and $Al_{0.95}Ga_{0.05}N$ shell thickness of up to 60 nm, or $V_{AlN}/V_{GaN} = 11.96$, demonstrates directly that even such an extreme case showed a strain-induced blueshift emission energy from the GaN core to only 3.63 eV for room-temperature luminescence. Therefore in conjunction with the elemental quantification outlined previously in Section 5.3.2 for these low Al-concentration AlGaN nanowires, the CL emission at energies beyond 3.68 eV can be undoubtly ascribed to an alloy composition effect at the AlGaN core with sufficient incorporated-Al.

5.4 High Al-Concentration AlGaN Nanowires

The second half of this chapter focuses on $Al_xGa_{1-x}N$ nanowires with drastically higher nominal Al-concentration of $x = 0.88$ (Sample B), which were also investigated in order to pursue shorter wavelength emission towards the UV-B band. A representative STEM-HAADF image of a high Al-content Sample B nanowire is shown in Figure 5.8(a). The n-GaN, p-i-n AlGaN (darker region), and p-GaN segments along the growth direction can be

clearly identified. It should be remarked that the various *p*-*i*-*n* doped AlGaN regions do not show unique HAADF contrast to be easily discernible when observing at low-magnifications, similar to the previous Sample A nanowires. However additional nanoscale features later discussed show changes in their nature along the nanowire length, which are assumed to be related to changes in doping and used to infer the differently doped regions. As compared to the low-Al content Sample A nanowires, the high-Al content AlGaN nanowires also exhibit a similar but more severe inversely tapered geometry, showing a drastic increase in diameter along the growth direction. The Sample B nanowires have a wurtzite crystal structure, as confirmed using the fast Fourier transform of the image (not shown). High-resolution images of the *p*-doped AlGaN region indicate the presence of extensive modulations in the image intensity at the atomic-scale, as shown in Figure 5.8(b). The alternating brighter and darker bands in the HAADF intensity observed shows some local short-range order, and can be

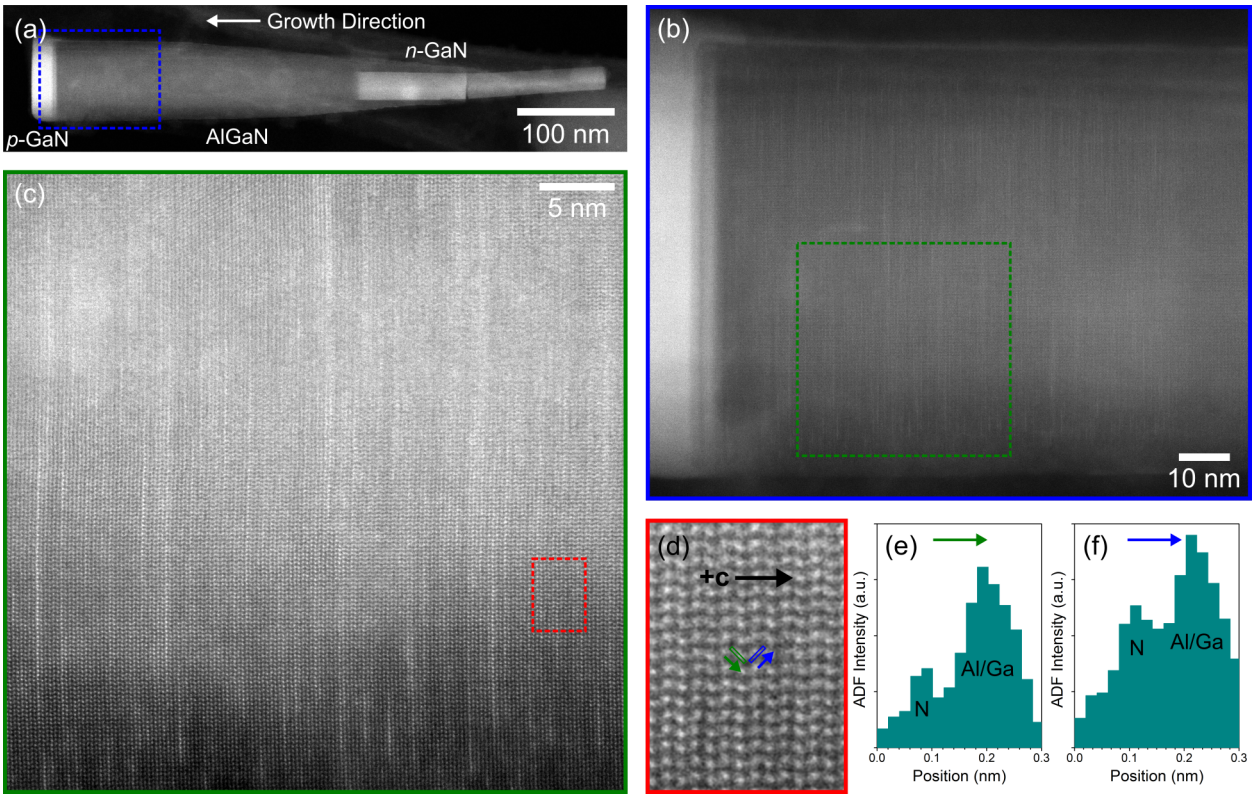

Figure 5.8: STEM-HAADF Z-contrast images of a single high-Al content AlGaN nanowire, Sample B. **(a)** An overview of the AlGaN *p*-*i*-*n* nanowire laser structures along a $\langle 11\bar{2}0 \rangle$ zone-axis, **(b)** a more detailed view of the *p*-AlGaN region (boxed in blue dashed line in **(a)**) showing the modulating image intensity along the *c*-axis. **(c)** Atomic-resolution image of the selected region within *p*-AlGaN (boxed in green dashed line) in **(b)** showing the discontinuous Ga-rich atomic-layers that show some short-range periodicity. Detailed atomic structure in **(d)** with line profiles across pairs of adjacent atomic dumbbells **(e, f)** directly confirms the N-polarity. Gaussian blur was applied to **(c)** and **(d)**.

directly attributed to local changes in composition, leading to modulating chemically-ordered Ga-rich/Al-rich bands. Seen in detail in Figure 5.8(c), these Ga-rich AlGaN layers exhibit discontinuities in the lateral direction (perpendicular to the growth direction) and do not span the full nanowire diameter, as most evident in the near surface region of the nanowire (at the bottom of the image). Further characterization of the compositional fluctuations in the high-Al content AlGaN alloy will be discussed in a later section (Section 5.4.2).

5.4.1 Crystal Polarity of AlGaN Nanowires

The crystal polarity of the nanowires was directly determined from the HAADF image intensity across adjacent atomic dumbbells within the high Al-content AlGaN when observed along the $\langle 11\bar{2}0 \rangle$ orientation (a-plane). The low-Z N-atoms are visible in the proximity of the weaker scattering from Al-atoms in comparison to the strong scattering from Ga-atoms in GaN [48, 116]. A detailed analysis of the atomic structure in the nanowire from Figure 5.8 shows elongation of the group III atomic columns alternating diagonally left and diagonally right. The corresponding line profiles of the HAADF intensity from a pair of marked atomic dumbbells in Figure 5.8(d) are displayed in Figures 5.8(e) and 5.8(f), confirming that the presented AlGaN nanowires are N-polar. All Sample B nanowires examined along $\langle 11\bar{2}0 \rangle$ orientation that allowed for this direct and facile polarity determination demonstrate N-face polarity. This is in good agreement with previous studies reporting polarity determination using (S)TEM methods on similar GaN nanowires grown under nitrogen-rich conditions [46, 49, 113]. Due to the N-face polarity, the polarization-induced electric field is anti-parallel to the built-in electric field of the p-n junction (along [0001] and $[000\bar{1}]$, respectively), thus can improve the carrier transport under electrical injection and reduce the operation voltage of the LEDs or laser of these nanowire structures relative to conventional Ga-polar AlGaN epilayer structures [225].

5.4.2 Atomic-Scale Compositional Modulations in AlGaN Alloy

In contrast to Sample A (low Al-concentration AlGaN sample), the strong atomic-scale compositional fluctuations that were formed within the AlGaN segments in Sample B requires additional characterization to understand their nature and formation. Illustrated in Figure 5.9(b) is a high-magnification HAADF image from the p-AlGaN region (boxed region in Figure 5.9(a)) of one AlGaN nanowire from Sample B, showing strongly modulated image intensity along the c-axis direction that can be attributed to local changes in Ga-concentration. The presence of extensive atomic-scale Ga-rich/Al-rich modulations along the growth direction can be clearly observed in the detailed view in Figure 5.9(c). Recall that atomic-scale

chemical ordering was also observed in the Sample A nanowires (Figure 5.2(e)), though quite exclusively within the Al-rich AlGaN shell discussed in Section 5.3. Further chemical evidence validating the compositional origin of the observed Z-contrast intensity modulations is provided by EELS spectrum imaging carried out at atomic-resolution. The Ga-map and the concurrently acquired ADF signal in Figure 5.9(d) show a distinct enrichment in the Ga-signal that corresponds to the local increase in the ADF signal within single *c*-planes. An overlay of the integrated intensity line profiles of the ADF signal (blue) and the Ga-signal (red) in Figure 5.9(e) further emphasizes their unequivocal correspondence. The localized variations in the Ga-concentration are estimated to be at minimum ∼5 – 10 at.%.

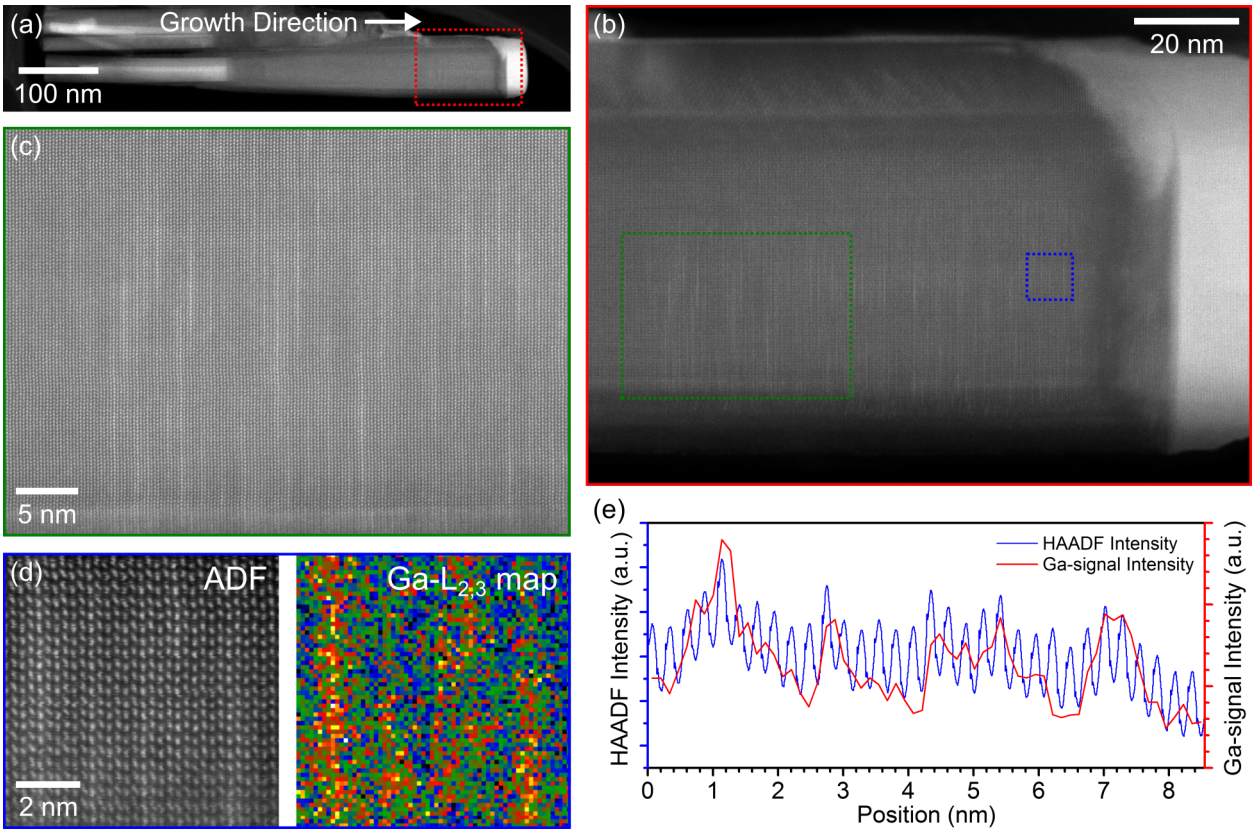

Figure 5.9: **(a)** STEM-HAADF image of an overview of one nanowire, highlighting the *n*- and *p*-GaN segments in bright contrast. **(b)** High-magnification image from the *p*-AlGaN region (boxed in red dashed line in **(a)**), showing intensity modulations along the *c*-axis, indicative of local changes of Ga-composition. **(c)** Detailed view from the blue dashed box region in **(b)**, showing highly localized compositional modulations of alternating Ga-rich/Al-rich planes at the atomic-scale. **(d)** The Ga-map (displayed in temperature-scale) and concurrently acquired ADF signal from EELS spectrum image at atomic-resolution (boxed in green dashed line in **(b)**), showing a direct correspondence between the local increases in Ga-signal with the ADF signal within single atomic-planes. Weighted-PCA was applied for noise reduction. **(e)** Integrated intensity line profiles of the ADF signal (blue) overlaid with the Ga-signal (red) across the entire EELS spectrum image in **(d)**, further emphasizes that the HAADF intensity modulations are attributed to local enrichment of Ga-composition.

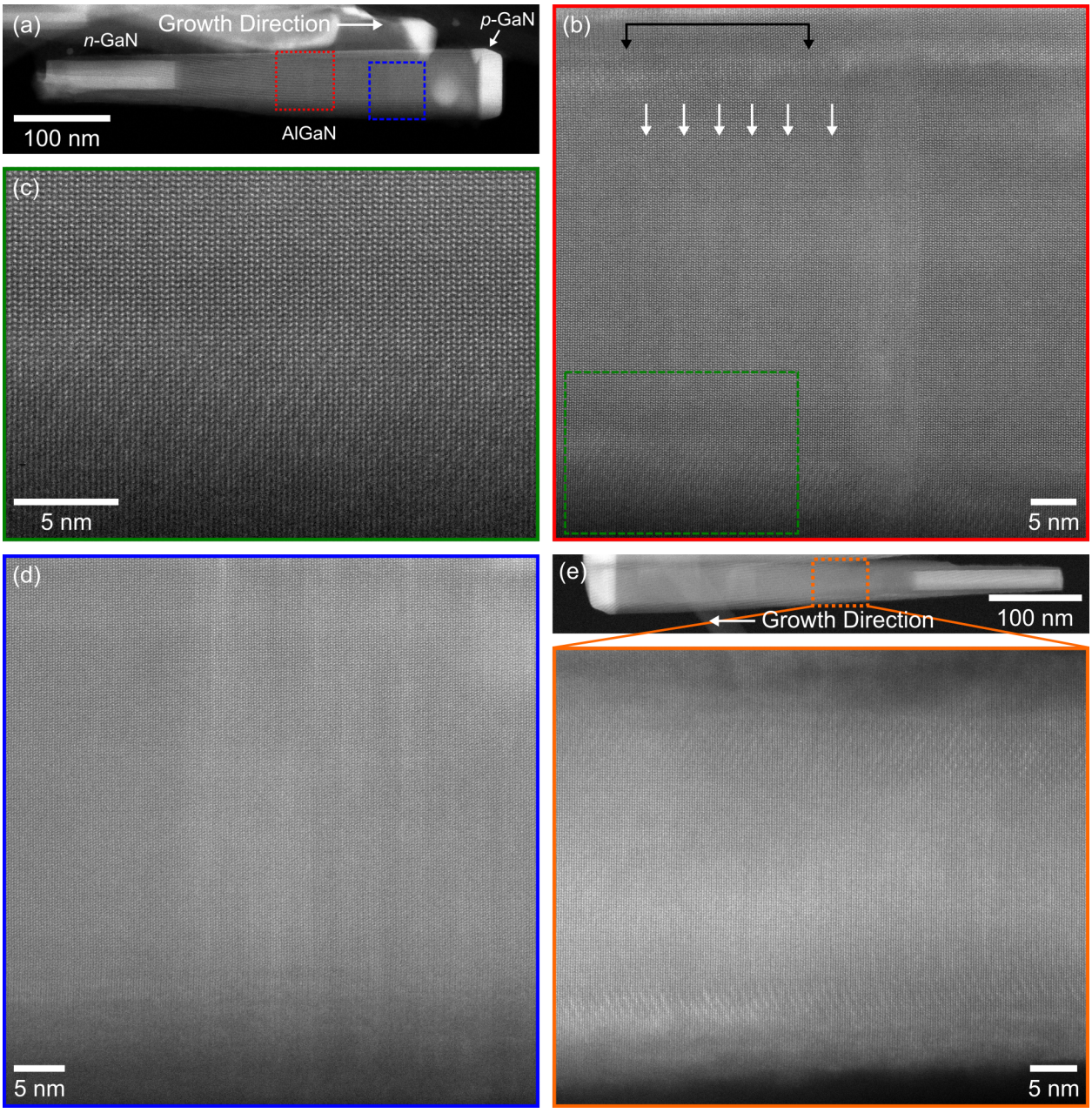

Figure 5.10: STEM-HAADF images of other high-Al content AlGaN nanowire structures (Sample B), showing compositional fluctuations of different nature in other regions. **(a)** An overview of a nanowire, highlighting the n- and p-GaN segments in bright contrast. **(b)** Detailed view of the i-AlGaN (boxed in red dotted line in **(a)**) showing modulating image intensity for planes inclined from the c-axis, and along c-planes of two length-scales (atomic-level between black arrows, and 2 nm arrowed white). **(c)** Atomic-resolution image of the selected region within i-AlGaN (boxed in green dashed line) in **(b)** showing the atomic-scale Ga-rich striations inclined along semi-polar $\{10\bar{1}3\}$ planes. **(d)** Detailed view of the compositional modulations in the p-AlGaN region along c-axis (boxed in blue dashed line in **(a)**). **(e)** A separate nanowire featuring similar atomic-scale compositional fluctuations along semi-polar $\{10\bar{1}3\}$ planes at the near-surface regions in n-AlGaN.

In addition, it should again be emphasized that the Ga-rich AlGaN bands (brighter regions) are not continuous along the lateral direction (perpendicular to the growth direction), as exemplified in Figure 5.9(c). Such Ga-rich AlGaN regions have sizes varying from a single atomic layer (0.25 nm) to 2 nm along the c-axis growth direction, such as bands arrowed in white in Figure 5.10(b), and lateral sizes varying from 2 – 10 nm. It is further noted that similar atomic-scale compositional modulations can be also observed at the near-surface regions in i- and n-AlGaN simultaneously in other nanowires presented in Figure 5.10. The nature of the compositional fluctuations shows varying characteristics in the different p-i-n-doped AlGaN regions. The single Ga-rich c-planes are prevalent predominantly within the p-AlGaN, with some also occuring inclined along semi-polar $\{10\bar{1}3\}$ planes (*cf.* the top near-surface region in the nanowire in Figure 5.9(b)). A large majority of the Ga-rich planes in n- and i-AlGaN are periodic single $\{10\bar{1}3\}$ planes inclined with respect to the growth direction near the nanowire sidewalls as in Figures 5.10(c) and 5.10(e), with lateral dimensions of ∼5 – 10 nm when observed edge-on along a $\langle 11\bar{2}0\rangle$ zone-axis. Other nanoscale Ga-rich regions are also prone to occur simultaneously in the i-AlGaN region near the centre of the nanowire, as shown in the example in Figure 5.10(b).

5.4.2.1 Dimensionality of Ga-rich Chemically-Ordered AlGaN

In order to deduce the approximate lateral dimensions of the Ga-rich regions within the high Al-content AlGaN nanowires (Sample B), multiple orientation views of the p-AlGaN segment as presented in Figure 5.11 were used. The observed lateral discontinuities suggest that the Ga-rich regions in the p-AlGaN segment make up a small fraction of the nanowire diameter in one direction, and may occupy a substantial portion of the projected thickness within the nanowire diameter (in order to be detectable). Alternatively, the Ga-rich/Al-rich planes could exhibit detectable HAADF intensity differences if the Ga-rich planes have a very high Ga-content (large compositional variation to Al-rich planes), but are small in dimension along the through-thickness seen in projection. This indicates that the atomic-scale compositional fluctuations would possess quantum dot/dash-like structural characteristics within the nanowires. In Figure 5.11, both a- and m-plane orientation views (adjacent zone-axes 30° tilt apart about the c-axis) of the same nanowire are displayed to illustrate the lateral extent of such atomic-scale Ga-rich regions within the p-AlGaN. Along both a- and m-plane views, the Ga-rich regions make up approximately half the nanowire diameter, bounded by the pairs of arrows in Figures 5.11(b) and 5.11(e), respectively. Such a two-image projection allows to delimit the approximate size of the Ga-rich regions as the purple shaded area, based on the intersected red and blue dashed line boundaries, in the schematic illustration of the c-plane direction in Figure 5.11(d). Uncertainty in the approximate size is

along the through-thickness direction, indicated by the gradation in the opacity within the purple shaded area in Figure 5.11(d), which can only be determined by a projection tilted 60° further and not possible in the current experimental set-up. This result confirms that the atomic-scale compositional fluctuations possess quantum dot-like or, at most, quantum dash-like structural characteristics within the high Al-concentration AlGaN nanowires.

With increased Al-concentration in Sample B, the presence of a few nm-thick Al-rich AlGaN shell (darker region) near the sidewall surface can also be observed when viewing along the $\langle 1\bar{1}00 \rangle$ orientation (m-plane), which is further surrounded by a Ga-rich outermost shell as presented in Figures 5.11(e) and 5.11(f). This is similar to that observed in the low Al-concentration nanowires (Sample A). The nanowires in the present study are ∼50 – 75 nm in diameter, and the nucleation density of the nanowires is high, therefore effects of beam shadowing by neighbouring nanowires are likely at play. Notable evidence of shadowing effect occurring during the growth of these Sample B nanowires includes the decreasing thickness of the Al-rich AlGaN shell visible in Figures 5.11(e) and 5.11(f). The thickness of the Al-rich AlGaN shell is noted by a double-ended black arrow in Figure 5.11(e), which shows a gradual narrowing towards the p-GaN contact layer marked by the black arrow. The variation in shell thickness is more noticeable at high-magnification in Figure 5.11(f), with the shell thickness also marked by double-ended black arrows. A mechanism coupling the narrowing of the Al-rich AlGaN shell thickness in AlGaN/GaN nanowires during continuous growth of longer AlGaN segments to simultaneous increases in nanowire diameter has been explained using geometrical shadowing [236]. This effect was explained by the facile sidewall incorporation of Al-atoms that increases the nanowire diameter, and progressively enhances the shadowing effect, such that sidewall diffusion and hence deposition rate of the shell diminishes. A similar behaviour of an Al-rich AlGaN shell decreasing in thickness has also been observed by Pierret et al. [231]. The Al-rich AlGaN shell also surrounds a large portion of the n-GaN base, further evidencing sidewall impingement and supporting the possibility of shadowing. Additionally, the Ga-rich outermost shell that encompasses the aforementioned Al-rich shell in both low and high Al-content nanowires (Sample A and B), visible in Figure 5.9(b) and Figure 5.11(e), extends beyond 75 – 150 nm below the top p-GaN segment. Its formation due to the sidewall diffusion of Ga-adatoms from the directly impinging flux at the nanowire tops is likely, but the direct impingement of adatoms onto the sidewalls is also possible for shells that form over long distances along the nanowire length.

The nature of the nanowire sidewall faceting, which can reflect the effects of the adatom mobility differences during AlGaN nanowire growth, should warrant some discussion. The low Al-content AlGaN nanowires (Sample A) exhibit hexagonal cross-sections with m-plane sidewall facets, as expected from GaN nanowires [101, 107] and shown previously in Fig-

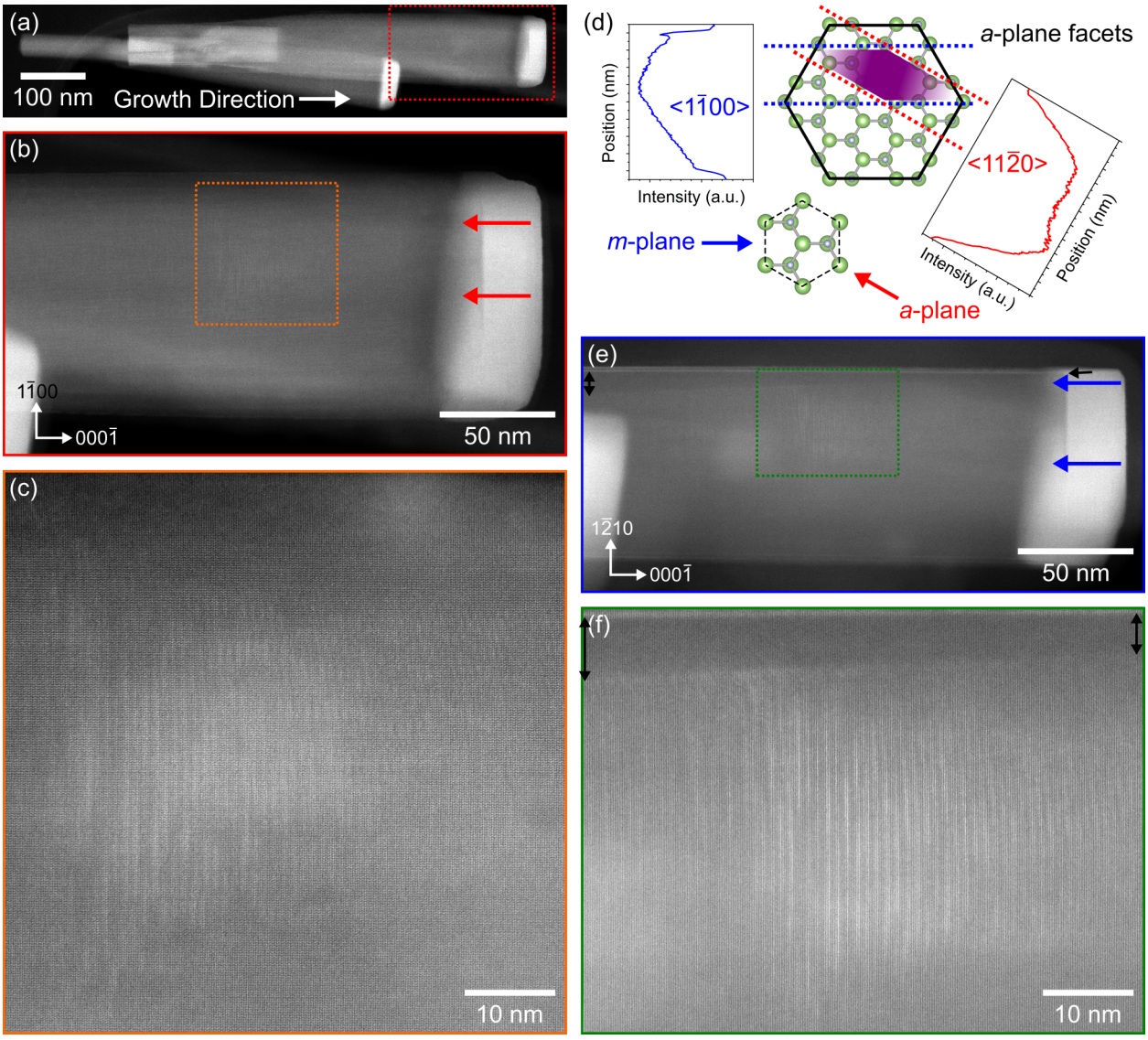

Figure 5.11: **(a – c)**, *a*-plane orientation view along $\langle 11\bar{2}0 \rangle$ of an AlGaN nanowire of Sample B. **(a)** is a low-magnification overview of the full nanowire, **(b)** shows the lateral extent of the Ga-rich regions within the *p*-AlGaN segment (boxed in red dashed line in **(a)**) marked by the red arrows, the atomic-scale Ga-rich layers (as boxed in orange dashed line) are shown in detail in **(c)**. **(d)** schematic illustration of the *c*-plane view of the nanowire, depicting the proposed macroscopic faceting (thick solid black hexagonal outline) from the HAADF intensity profiles (red for *a*-plane, blue for *m*-plane orientations), and the maximum size of the Ga-rich region as purple shaded area delimited by the red and blue dashed line boundaries from the two STEM projections. A wurtzite unit cell of GaN bound by *m*-plane surfaces (dashed black line) is also shown in **(d)**. **(e – f)** *m*-plane orientation view along $\langle 1\bar{1}00 \rangle$ of the same nanowire. **(e)** shows the lateral extent of the Ga-rich regions within the *p*-AlGaN segment marked by the blue arrows, and the modulated Ga-rich layers (boxed in green dashed line) are shown in detail in **(f)**.

ure 5.2(d). In contrast, the high Al-content AlGaN nanowires (Sample B) have a projected shape that deviates from what would result from a hexagonal cross-section terminated by m-plane sidewall facets. This is in agreement with the GaN/Al(Ga)N nanowire heterostructures of Ristić et al. [101] and Furtmayr et al. [253] where the GaN core is highly prismatic, while the surrounding AlN layer exists as an irregular rounded shell due to differences in surface kinetics of Ga and Al. The formation energies of m-plane surfaces for both GaN and AlN are reported to be only lower than a-plane by ∼10 meV [254].

The macroscopic shape of the high Al-content AlGaN nanowire in Figure 5.11 was assessed based on the lateral projected shape from the integrated HAADF intensity profile along both a- and m-plane views, as presented in Figure 5.11(d) as the red and blue plots, respectively. HAADF image intensity increases monotonically with thickness, such that the shape of the HAADF intensity profile reflects the projected cross-sectional thickness. The blue half-hexagon house-shaped profile viewing down m-plane orientation, and red isoceles trapezoid-shaped profile viewing down a-plane orientation in Figure 5.11(d) are reversed from the expected outcome if assuming a m-plane terminated hexagonal cross-section for the nanowire. Therefore the two projected shape profiles not only confirm non-m-plane surface facets, but they are in fact also suggestive of the presence of a-plane surface facets. The proposed macroscopic shape is shown viewed down the c-plane as the thick solid black hexagonal outline in Figure 5.11(d) overlaying the atomic-structure model deduced from the STEM observations along the two non-polar orientations. A wurtzite unit cell of GaN (dashed black hexagon) viewed down the c-plane with m-plane faces is also shown alongside for comparison in Figure 5.11(d) to note the 30° rotation relative to the macroscopic shape/facets determined from experimental results. Identical macroscopic lateral faceting behaviour in AlN/GaN nanowires grown by the McGill MBE group using similar growth temperatures and nitrogen-rich conditions have also been observed (*cf.* Appendix A.2), indicating that the high Al-content AlGaN nanowires have surface kinetics effects dominated by Al-adatoms.

Both an irregular shape (*i.e.* non-hexagonal cross-section with mixtures of m- and a-plane facets) or atypical a-plane surface termination could strongly affect the diffusion of Al and Ga atoms along the sidewalls during the subsequent growth process, altering the supply of atoms at the axial growth front that leads to non-uniform incorporation. Such a reasoning is further supported by the more recent growth of high Al-concentration AlGaN nanowires under nitrogen-reduced conditions and higher growth temperatures (895 – 960 °C) that maintains a high degree of atomic-scale and nanoscale alloy homogeneity across the various doped AlGaN regions (shown in Appendix A.3). (Al,In)GaN nanowires are typically grown under nitrogen-rich conditions, which has been described as a fundamental component for

achieving disparity between axial to radial growth rates. As early as during the nucleation stage for catalyst-free growth, the usual excess of active nitrogen reduces the mobility of adsorbed group III species on the substrate surface [255]. At the same time, the elevated growth temperatures provide sufficient enhancement for adatom migration along nanowire sidewalls towards the axial growth front, in particular the Al-adatoms [256]. This is evidenced by the lack of a Al-rich core-shell structure, which was otherwise present in both Sample A and B nanowires grown under nitrogen excess, as well as m-plane sidewall facets with reduced-nitrogen in contrast to the high-Al content Sample B. Additionally, at such high growth temperatures above the decomposition temperature of GaN (750 °C), Ga-adatoms readily desorb and its incorporation rate are significantly less than 0.1 [239]. Therefore the competitive incorporation of Ga and Al become then dominated by Al-species due to the overall difference in bond cohesive energy [239]. Together with the decreased nitrogen flux, there is less active nitrogen available for the Ga-incorporation, and the Ga-adatoms tend to accumulate as a reservoir at the growth front. However because of the desorption at very high temperatures, an accumulated Ga-adlayer that can otherwise lead to lateral and axial compositional fluctuations in AlGaN alloys [232, 239] does not form.

5.4.2.2 Formation Mechanism of Quantum Dot/Dash Features

The formation process of the Ga-rich quantum dot/dash-like features within the AlGaN segments is likely related to the interplay between spontaneous chemical ordering and anisotropic adatom migration from the irregular top/lateral surfaces of the nanowire arrays under nitrogen-rich conditions. The spontaneous formation of nanometer-scale long-range ordering of Al-rich and Ga-rich layers has been observed in nanowires [231, 233] and thin films [257], which was explained by the significantly different binding energies between Ga–N and Al–N. Such spontaneous chemical ordering alone, however, cannot explain the formation of quantum dot/dash-like nanostructures that are discontinuous in-plane. The macroscopic faceting in the high Al-content AlGaN nanowires was assessed from HAADF intensity profiles (Figure 5.11(d)) in the preceding section, invalidating the presence of m-plane sidewall facets and revealing a-plane surfaces. Due to the random nucleation and formation process as well as the beam shadowing and coalescence effects of neighbouring nanowires, self-organized AlGaN nanowires tend to develop into non-symmetric shapes with such irregular sidewall facets (which can be seen from the SEM image in Figure 5.12(a)). An irregular non-hexagonal cross-section can be due to an intermediate regime between having both m-plane and a-plane surface facets.

Both a non-symmetric shape and the nature of the surface facets strongly affect the diffusion of Al and Ga atoms along the sidewalls [257] that can alter the supply of atoms to

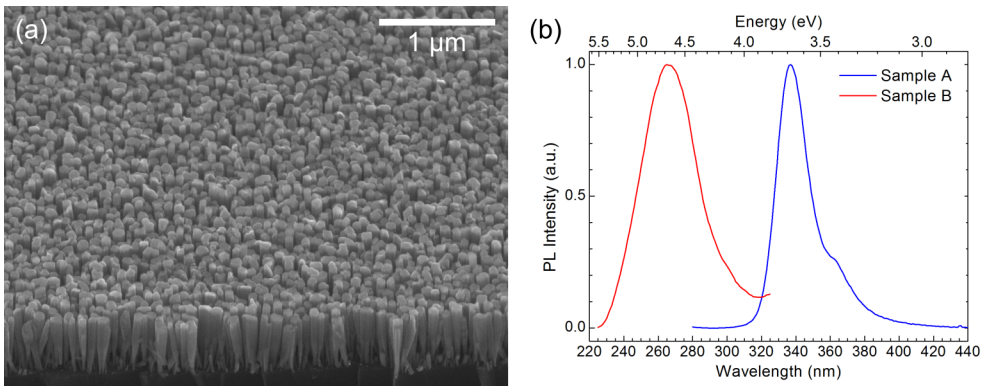

Figure 5.12: **(a)** SEM image of Sample B taken at a 45° tilt angle. **(b)** Normalized room-temperature PL spectra of low and high Al-concentration AlGaN nanowires (Sample A and B, respectively), noting the approximately twice as broad spectral linewidth in Sample B.

the top of the nanowire during the subsequent growth process. For AlN shells grown on GaN bases in AlN/GaN core-shell nanowires, it was determined empirically in the work of Hestroffer and Daudin [258] that approximately 55 – 60% of the Al-atoms impinging onto the sidewalls do not get incorporated and diffuse to the top surface growth front, then subsequently contribute to the axial growth rate. Surface diffusion barrier energies calculated from density functional theory for Ga-atoms on GaN and Al-atoms on AlN on the expected m-plane sidewall termination in nanowires are summarized in Table 5.2. Both respective systems show that diffusion along the nanowire length [0001] direction is unfavourable compared to across the m-plane facet in the $[11\bar{2}0]$ direction. The trends for both systems are reversed on the other non-polar a-plane (also shown in Table 5.2). Hestroffer and Daudin [258] proposed the possibility of narrow a-plane ridges connecting two adjacent m-plane sidewall facets that can facilitate a zig-zag motion of adatoms (along a-axis on m-plane to along c-axis on a-plane) globally towards the [0001] direction to the top surface. This description of the Ga/Al-atom surface diffusion can be a good parallel for the low Al-concentration AlGaN nanowires (Sample A), previously discussed to exhibit m-plane sidewall surfaces in Section 5.3. On the other hand, the a-plane termination for the high Al-concentration Sample B can shift the fraction of Al-atoms impingent onto the sidewalls that diffuse to the top surface, due to differences in a-plane surface diffusion barriers favouring motion along the nanowire length [0001] direction over laterally along $[1\bar{1}00]$ direction.

Additionally, it is worth mentioning that the role of dopant impurity atoms in ternary III-N nanowire growth is also not well-known. In the case of GaN nanowires, Mg-doping can induce changes in the ratio of c- to m-plane growth rates, encouraging coalescence due to enhanced radial growth [55, 104, 259], as well as the formation of stacking error-induced twin defects [55]. These effects, together with the difference in surface migration and desorption

Table 5.2: Calculated surface diffusion barrier energies of Ga on GaN [257] and Al on AlN [254] along directions parallel and perpendicular to [0001] on non-polar *m*-plane and *a*-plane surfaces.

	On *m*-plane $\{1\bar{1}00\}$		On *a*-plane $\{11\bar{2}0\}$	
(eV)	along [0001]	along $\langle 11\bar{2}0\rangle$	along [0001]	along $\langle 1\bar{1}00\rangle$
Ga on GaN	0.93	0.21	0.32	0.63
Al on AlN	2.79	0.11	0.56	2.12

rates between Ga and Al atoms [231], can strongly modulate the competitive nature between Al- and Ga-incorporation [232], driving the spontaneous chemical ordering process at the growth front. As such, quantum dot/dash-like nanostructures can be formed in self-organized AlGaN nanowire arrays due to the kinetically-driven nanoscale alloy inhomogeneity. Effects of such compositional variations on the optical properties of AlGaN nanowires are manifested by the broad PL spectral linewidth, shown in Figure 5.12(b), as well as the extremely high luminescence efficiency (∼80%) at room-temperature. Due to the large effective mass of charge carriers in Al-rich AlGaN, the Bohr radii are only 1 – 2 nm, which is comparable to the size variations of the observed quantum dots/dashes. As a consequence, the quantum dot/dash structures can even provide strong 3D quantum confinement. Moreover, such local compositional variations also induce strong perturbation to the energy band due to the changes in the spontaneous polarization fields.

5.4.3 Nanoscale Carrier Localization at Alloy Fluctuations

With increased Al-concentration in Sample B AlGaN nanowires (nominally $x = 0.88$), the extensive atomic-scale HAADF intensity fluctuations present in the AlGaN regions are indicative of strong Ga-rich/Al-rich compositional modulations, as validated using EELS elemental mapping at atomic-resolution in the previous Section 5.4.2. Such (sub-)nanoscale alloy fluctuations can present as localization potentials in the energy band landscape, leading to the enhanced spatial confinement of carriers. This aids to explain the unexpectedly high PL IQE of the Sample B nanowires, where by decreasing the effective carrier diffusion, diffusion to non-radiative recombination centres are prevented. In order to gain more insight into the assorted nature of compositional fluctuations throughout the variously doped AlGaN segments and their corresponding optical properties, combined nanoCL and HRSTEM on the high Al-content AlGaN nanowires was performed and discussed in this section. The nanoCL results of high Al-concentration Sample B demonstrate that the local optical behaviour in the presence of marked compositional fluctuations drastically differ from the low Al-concentration Sample A that exhibit a high degree of alloy homogeneity in the nanowire

core. Aside from an expected blueshifting in emission energy due to change in composition, numerous sharp emission lines originate from the AlGaN regions, whose spatial distribution of CL intensity is locally peaked across nanometer-sized areas.

The first example of such correlative HRSTEM and nanoCL analysis carried out on high Al-concentration AlGaN nanowires is presented in Figure 5.13, and the reproducible trends representative of other Sample B nanowires examined are summarized in the following. The nature of the laterally discontinuous compositional fluctuations varies between *p*-, *i*-, *n*-doped AlGaN regions: single atomic layers occurring on *c*-planes along the growth direction in *p*-AlGaN (Figures 5.13(c) and 5.13(e)) and on semi-polar $\{10\bar{1}3\}$ planes in *i*-AlGaN (Figure 5.13(b)) and *n*-AlGaN (Figures 5.13(a) and 5.13(d)). Other nm-sized compositional modulations and segregation effects can be also observed. Nanowires in Sample B display

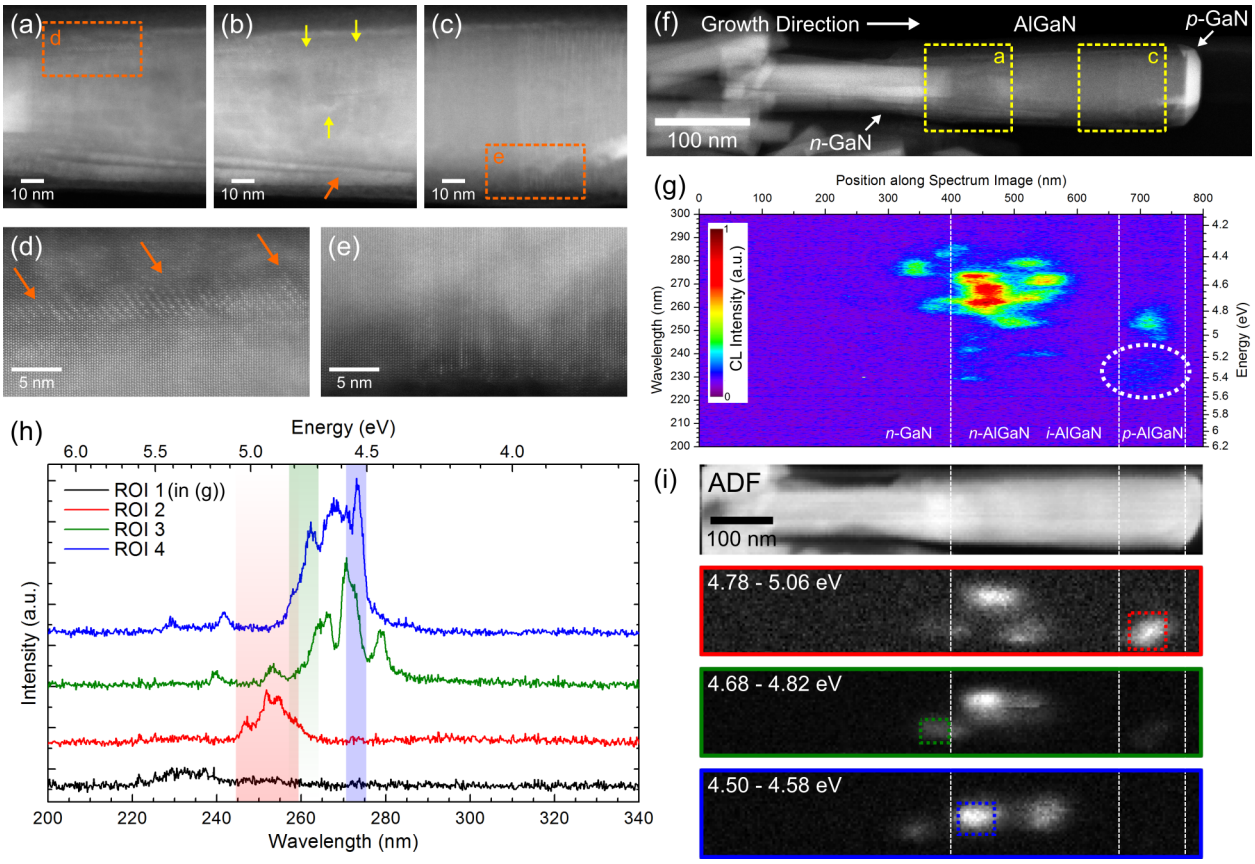

Figure 5.13: **(a – f)** HRSTEM-HAADF images showing detailed views of the atomic-scale compositional fluctuations in *i*-AlGaN **(b)**, *n*-AlGaN **(d)** and along *c*-planes in *p*-AlGaN **(e)**. STEM-CL spectrum image of the same nanowire: **(g)** CL spectral profile integrated across the nanowire diameter as a function of the emission wavelength/energy and position along the nanowire axis in the spectrum image, **(h)** selected CL spectra from ROIs marked in **(g, i)**, and **(i)** CL maps extracted about peak maxima marked in **(h)** with energy integration window also indicated, and the concurrently recorded ADF image. Dashed lines are visual boundary guides for separating the regions.

a spectrally dense series of narrow emission lines extended between 4.1 – 5.6 eV from the AlGaN regions (representative exemplaries in Figure 5.13(h) and Figure 5.14(c)), which are blueshifted (230 – 300 nm) relative to the low Al-content AlGaN Sample A. The origins of the emission peaks are also drastically more spatially localized within the AlGaN regions, confined to within 50 – 100 nm-sized regions both along and transverse to the *c*-axis growth direction. Demonstrated in the wavelength-filtered CL images shown in 5.13(i) is direct evidence of carrier localization visualized at the nanoscale. Subsequent HRSTEM on these nanowires shows that the different spectral behaviours (emission energy) can be correlated to positions along the nanowire with different types of compositional fluctuations. Specifically, the shortest wavelength peaks (230 – 240 nm) originate from volumes with atomic-scale Ga-rich *c*-planes in *p*-AlGaN (Figure 5.13(c), ROI 1 circled in 5.13(g)). The overall CL intensities from these regions are low (*cf.* ROI 1 spectrum in Figure 5.13(h)) and composed of multiple peaks that cannot be spectrally resolved. Other single sharp emission peaks at intermediate wavelengths (240 – 260 nm) also originate from the atomic-scale Ga-rich alloy modulations in the *p*-AlGaN region, such as ROI 2 in Figure 5.13(h) or red-dash-boxed area in Figure 5.13(i), which corresponds to the area in Figure 5.13(e). Multiple high intensity sharp peaks (250 – 290 nm) can be assigned to regions with atomic-scale modulations on inclined $\{10\bar{1}3\}$ planes (arrowed in orange in Figure 5.13(d)) or other nm-sized segregation (arrowed in yellow in Figure 5.13(b)).

The nanoCL of another single high Al-content AlGaN nanowire (Sample B) is also presented in Figure 5.14 and Figure 5.15 for comparison. At first glance, inspecting the CL spectra alone illustrates that the localization potential population induced by compositional fluctuations does depend on the individual nanowire. However, an overall trend confirming the correlation between the nature of the Ga-enrichment that have been observed along specific doped AlGaN regions can also be drawn, as outlined in the subsequent paragraphs. Numerous sharp CL lines are also observed in the selected unique spectra in Figure 5.14(c), a majority of which originate from withn the AlGaN regions. The *n*-GaN base and *p*-GaN top generally emit weakly or do not luminesce at all, both of which can be directly related to the partial presence or absence of an Al-rich AlGaN shell, respectively. The near band-edge (NBE) emission at ∼3.54 eV (Spectrum F in Figure 5.14(c) with 92 meV FWHM) from the *n*-GaN base in the case of this nanowire is relatively strong, as shown in the corresponding CL map in Figure 5.14(b)'s Map F. The slight blueshifting in the GaN NBE energy relative to what is expected of the GaN bandgap at T = 150 K (3.46 eV) can be accounted for by the presence of the Al-rich AlGaN shell. As already described in Section 5.3.3.1, the Al-rich AlGaN shell can inflict a nearly uniaxial compressive strain (magnitude of in-plane components are negligibly small) into the *n*-GaN core along the axial direction [247]. A dependence of

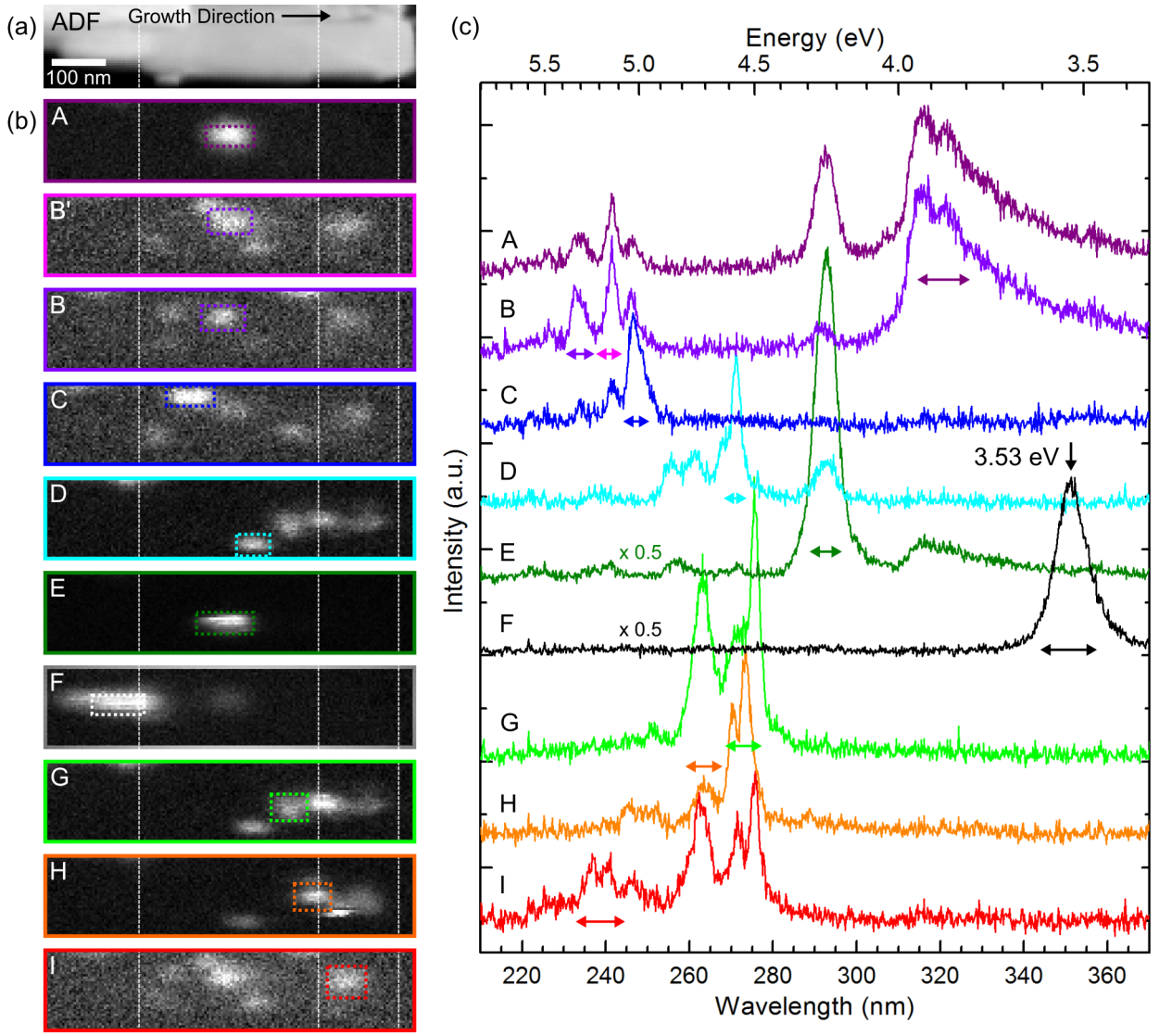

Figure 5.14: **(a)** ADF image of a high Al-content AlGaN nanowire (Sample B) from the STEM-CL spectrum image, **(b)** wavelength-integrated CL maps extracted about peak maxima marked by double-ended arrows in corresponding colours in the spectra of **(c)** labeled A – I. Dashed lines are boundary guides for the separate regions to match Figure 5.15. **(c)** selected CL spectra from ROIs marked as colour-coded and labeled A – I in the CL maps of **(b)**. Intensity scaling of spectra, when applicable, is indicated by a multiplier.

the blueshift in luminescence energy from the n-GaN base on the thickness of the Al(Ga)N shell can be estimated from the degree of uniaxial strain determined as a function of the shell-to-core volume ratio V_{shell}/V_{core} [246]. Conversely, the measured 80 meV blueshift from the n-GaN base can be used to estimate the uniaxial compression imposed by the Al(Ga)N shell as $\epsilon^{zz}_{core} = -0.7\%$ or $\epsilon^{zz}_{core} = -1.2\%$ when considering the type A/B and C valence band maximum cross-over.

The emission from the AlGaN is again clearly localized to small regions of 50 – 100 nm in size, with changes transverse to the growth direction particularly evident when comparing nearby localization centres, such as in the CL Maps D, G, H in Figure 5.14(b). Similar to the Sample B nanowire presented in Figure 5.13 and reproduced in other single nanowires of the same sample, the shortest wavelength peaks (220 – 240 nm) that are not fully resolved spectrally originate from the *p*-AlGaN region (ROI boxed in Figure 5.14(b)'s Map I and its spectrum in (c)). When compared to the HRSTEM-HAADF images of this local emitting area, the images reveal volumes with atomic-scale Ga-rich *c*-planes in *p*-AlGaN at the centre of the nanowire (Figure 5.15(e)), and along semi-polar $\{10\bar{1}3\}$ planes at the near-surface region of the nanowire (Figure 5.15(g)). Other well-resolved short wavelength emission lines with energy values of 5.3 eV, 5.15 eV, and 5.05 eV also arise from the approximate interfacial region between *n*-AlGaN/*i*-AlGaN in Map B, B', C of Figure 5.14(b). Also evident in all of Spectra A, B, and E of Figure 5.14(b), whose ROIs are close in proximity to each other, is the low-energy broad band at 3.93 eV (316 nm) paired with the high intensity sharp peak

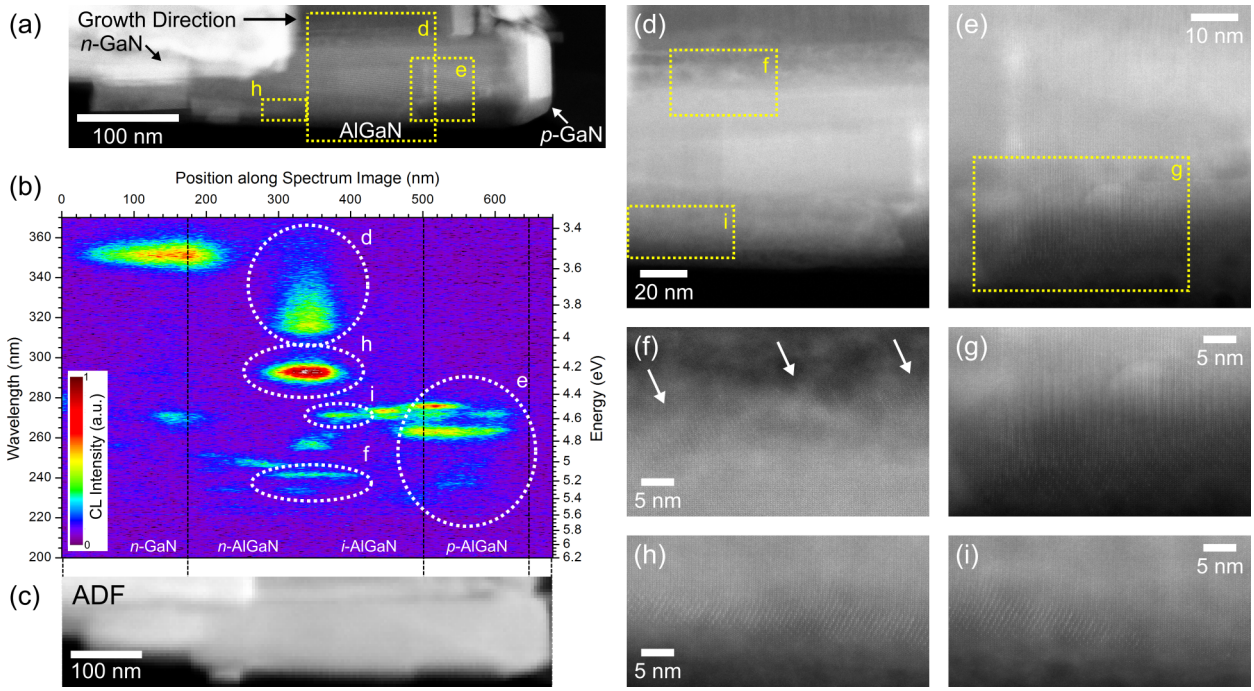

Figure 5.15: (a, d – i) HRSTEM-HAADF images of the high Al-content AlGaN nanowire in Figure 5.14, showing detailed views of the atomic-scale compositional fluctuations on semi-polar planes in *i*-AlGaN **(d, f, h, i)** and along *c*-planes in *p*-AlGaN **(e, g)**. STEM-CL spectrum image of the same nanowire: **(b)** CL spectral profile integrated across the nanowire diameter, and **(c)** concurrently recorded ADF image. Dotted ellipses in **(b)** are marked to correlate the emission peaks and their corresponding locations using the same label from the HRSTEM images. Dashed lines are boundary guides for the separate regions identified in HRSTEM.

at 4.23 eV (293 nm). Analogous to the broad band observed in the low Al-content Sample A detailed in Section 5.3.3, this broad asymmetric band in Sample B can also be assigned to a free electron-neutral acceptor transition (eA^0) and its LO phonon replicas. Assuming the 4.23 eV line is an AlGaN NBE transition (FX_A), the relative energy difference with the eA^0 transition of 310 meV translates to a Mg-acceptor activation energy for $Al_xGa_{1-x}N$ with Al-content of $x \approx 0.4$. Recall also that Si_N-acceptor has a binding energy $E_A \approx 224$ meV in GaN [244].

A two-dimensional spectral profile, plotted as a function of the emission energy/wavelength and probe position along the nanowire growth axis within the spectrum image, provides a more quantitative visualization of carrier localization at the emission centres in the high Al-content AlGaN nanowires. Specifically from the CL spectral profile in Figure 5.15(b), a few features are notable: a) the *i*- and *n*-AlGaN segments emit the strongest overall in a lower-energy band (ellipse *h*); b) the *p*-AlGaN segment emit the shortest wavelengths with highest intensity (ellipse *e*), while is still only a fraction of the emission intensity from the lower-energy bands.[1] High intensity luminescence bands that lay horizontally along a constant emission energy extend less than 100 nm in size, such as bands marked by ellipses *e, f, i*, reflect both spectral and spatial localization. The corresponding HRSTEM-HAADF images of the approximate locations of various localization centres (marked by ellipses in Figure 5.15(b), labeled with their image pair) have been identified with the aid of the unprojected CL maps and spectra in Figure 5.14(b) and (c), and presented in Figure 5.15(d)–(i).

5.4.3.1 Optical Properties of Extended Defects

There has been sufficient interest in extended defect-induced luminescence within GaN in the past, including threading dislocations [204], inversion domain boundaries [260, 261], and stacking faults [53, 262]. The prevalence for basal plane stacking faults in the *p*-AlGaN segment in the low Al-concentration AlGaN nanowires of Sample A was already discussed in Sections 5.3.1 and 5.3.3. Therefore one example of a high Al-concentration AlGaN nanowire from Sample B with confirmed presence of stacking faults is explored in Figure 5.16. It should be emphasized that a large majority of the Sample B nanowires examined with combined nanoCL and HRSTEM or HRSTEM only did not contain any stacking faults within the AlGaN regions, but it is still of relevance to discuss the role of stacking faults as localization centres. HRSTEM-HAADF images of that high Al-content AlGaN nanowire viewed along $\{1\bar{1}00\}$ *m*-plane orientation (Figures 5.16(e) and 5.16(f)) show adjacent *c*-planes that have reduced and enhanced image intensities relative to the nearby area within the AlGaN region, as marked by the pair of red brackets in Figure 5.16(e). As a first approximation, it is

[1] There is some non-linear droop in detector response towards lower wavelength that should be considered.

straightforward to associate these Z-contrast intensity variations to alloy fluctuations based on prior observations in Sample B. However, viewing along *m*-plane orientation does not allow to deduce the *ABAB* stacking sequence expected in a wurtzite structure because of the mirror symmetry about *c*-axis.

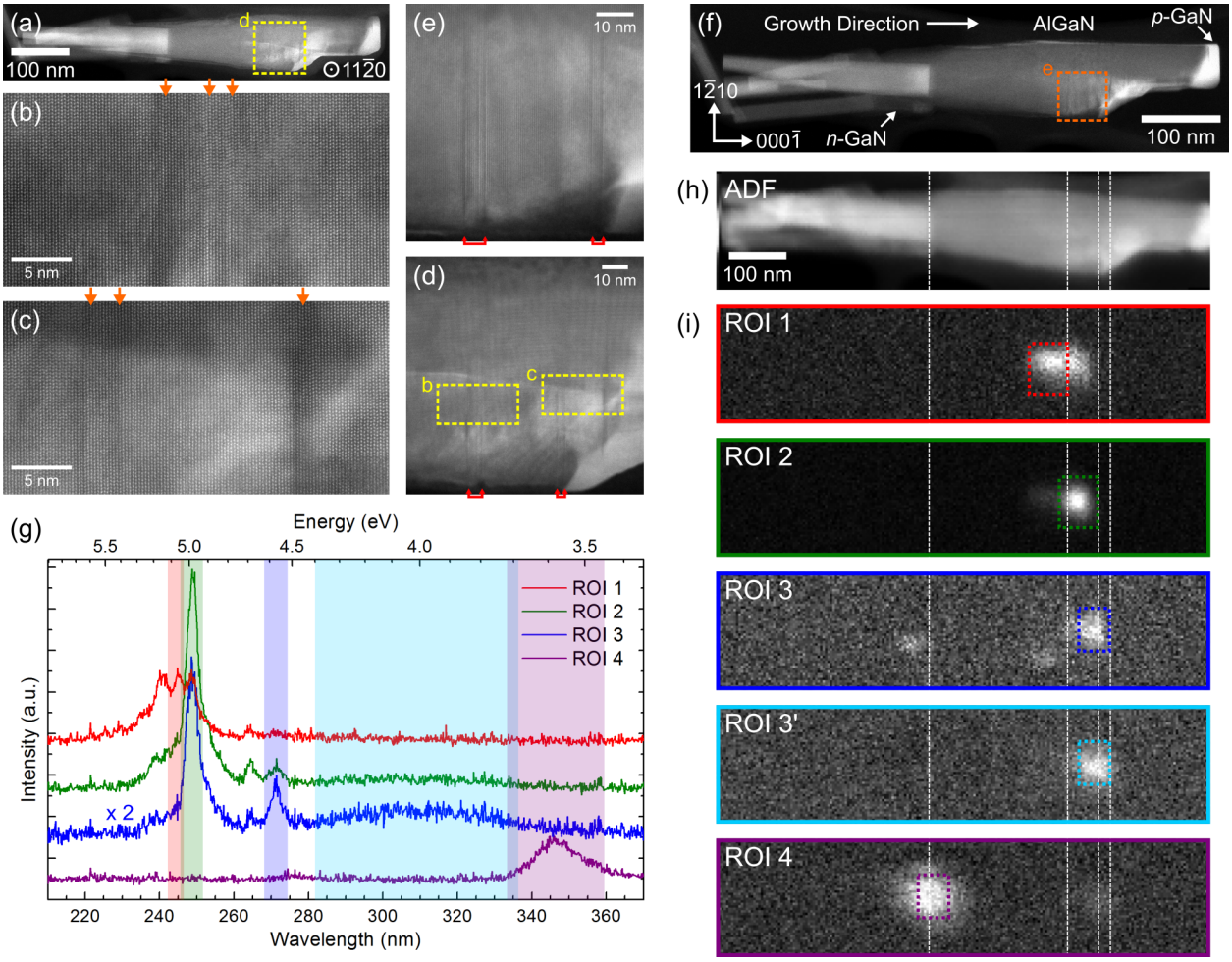

Figure 5.16: High Al-content AlGaN nanowire (Sample B) containing stacking faults. **(a – f)** HRSTEM-HAADF images showing detailed views of the stacking faults within the AlGaN segments viewed along ⟨11$\bar{2}$0⟩ zone-axis **(a – d)** and ⟨1$\bar{1}$00⟩ zone-axis **(e – f)**. Red arrowed-brackets in images **(d)** and **(e)** label the groups of stacking faults in common between the two images of different zone-axes. STEM-CL spectrum image of the same nanowire: **(g)** selected CL spectra from ROIs marked in **(i)**, **(h)** the concurrently recorded ADF image, and **(i)** CL maps extracted about peak maxima marked in **(g)**. Intensity scaling of spectra in **(g)**, when applicable, is indicated by a multiplier. Dashed lines in **(i)** are visual guides for the approximate locations of stacking faults or interfaces.

Consequently, *a*-plane orientation (adjacent zone-axis 30° tilt away about *c*-axis) views of the same nanowire presented in Figure 5.16(a)–(d) enable the examination of the stacking sequence. The detailed views of the areas in question from boxed regions in Figure 5.16(d) clearly outline multiple planes with errors in the stacking sequence, as marked by orange

arrows in Figures 5.16(b) and 5.16(c). It should be noted that some image intensity variations still exist at the stacking faults in the *a*-plane orientation view. However, there was no consistent image intensity change observed in this case, which could be related to different types of basal stacking faults. Tischer et al. [53] have previously demonstrated using correlative CL/electron beam induced current (EBIC) measurements in a scanning electron microscope and TEM that cubic insertions in semi-polar AlGaN electron-blocking layers in an LED structure decreased the Al-content locally at the stacking sequence interruption. It is possible that some alloy fluctuation was likewise induced at the stacking faults within the AlGaN nanowires in the current study, but this could not be verified using elemental analysis. The nanoCL of this Sample B nanowire shows a total of six unique emission peaks localized to 50 – 100 nm sized regions within the AlGaN. Due to the close spatial proximity of the emission centres at the location with stacking faults identified, a few of the peaks are recurrent across the ROI 1 – 3 spectra in Figure 5.16(g). Again, ROI 4 spectrum in Figure 5.16(g) is assigned to the NBE of the strained *n*-GaN base. A dependence of the CL intensity drop-off towards the growth direction with respect to the position of the few stacking faults can be observed in the CL maps of Figure 5.16(i), including the broad low-energy peak in the ROI 3 spectrum (Figure 5.16(g) and ROI 3' map pair in 5.16(i)) that is likely of defect-origin. At this stage, it is premature to conclude whether the emission is due solely to the presence of the confirmed stacking faults in this particular Sample B nanowire, or if there is a contribution from compositional fluctuations associated with the emission at such extended defects.

5.5 Conclusion

In summary, low and high Al-concentration AlGaN nanowires show strikingly different behaviour in their elemental distribution, which has a strong impact on the resulting optical properties. The low-Al content AlGaN exhibits a high degree of alloy homogeneity within the core of the nanowires, whose CL emission is strong due to the presence of a surface passivating Al-rich AlGaN shell, but delocalized across hundreds of nanometers. In the high Al-concent AlGaN nanowires, a simular core-shell structure that allows for better carrier confinement radially is also observed. The most substantial evidence with increased Al-concentration is the strong compositional fluctuations of different nature and spatial scales down to single atomic planes that can be classified as quantum dots/dashes prevalent across the differently doped AlGaN regions. NanoCL reveals a high spectral density of sharp emission lines from the AlGaN, evidencing carrier localization in the presence of energy band fluctuations given the nanoscale variations in composition. A position-dependence in the CL emission over specific

wavelength ranges suggests that distinct bands correspond to specific types of the compositional fluctuations at spatially defined regions in the high Al-content AlGaN nanowires. Specifically, atomic-scale Ga-rich *c*-planes in the *p*-AlGaN emit the shortest wavelengths, while Ga-rich semi-polar planes in *i*- and *n*-AlGaN emit strongly in a lower-energy band. Due to the kinetic nature of the growth process governing the spontaneous formation of these nano-/atomic-scale compositional fluctuations, variation in growth parameters can be optimized to further exploit the alloy inhomogeneity and the associated carrier localization. As such, emission in the DUV range, pushing towards the NBE of AlN, can be greatly enhanced using such AlGaN nanowire structures for application as electrically-injected lasers and LEDs operating at room-temperature.

Chapter 6

Summary and Outlook

In this thesis, the experimental work focused on the investigation of ternary III-nitride nanowire heterostructures by analytical techniques in scanning transmission electron microscopy (STEM), namely electron energy-loss spectroscopy (EELS) for chemical information and cathodoluminescence (CL) spectroscopy for measurement of optical properties at the nanoscale. The aim was to examine the luminescence from individual nanostructures, and derive a fundamental understanding of the material features contributing to specific optical responses. This thesis work can be subcategorized into the two main structure types studied, with majority of the focus on the first topic: i) structure-property relationship in InGaN/(Al)GaN dot-in-a-wire embedded heterostructures, and ii) alloy inhomogeneity in AlGaN nanowires.

Ternary InGaN alloys continue to generate a lot of interest because of their anomalous alloy behaviours, and how they contribute to carrier localization and the exceptional quantum efficiencies despite of high defect densities. The growth of InGaN/GaN heterostructures in a nanowire geometry is proposed to alleviate much of the lattice mismatch strain that governs the piezoelectric polarization. Evidence of suppressed internal polarization field has been deduced from carrier dynamics using time-resolved photoluminescence (PL) spectroscopy that have a two orders of magnitude smaller decay times [17]. Furthermore, early reports observed minimal blue-shift in the PL peak emission energy with high excitation density to support the reduction of polarization field-induced quantum-confined Stark effect [9, 18]. It was later contradicted by Lähnemann et al. [140], where micro-PL on single nanowires systematically showed a blue-shift indicating progressive screening of the internal polarization field. Supporting finite element calculations estimated substantial values of piezoelectric polarization that are only partially reduced relative to their planar counterparts. However, such calculations were carried out based on composition inputs determined from lattice spacing measurements averaged within an ensemble using X-ray diffraction mixed with strain from

TEM-based lattice spacing measurements [15]. These earlier studies also determined the InGaN composition with prior assumptions about the strain state, and not the two attributes independently.

It was discussed in Chapter 2 that the strain partitioning behaviour in short-period InGaN/GaN nanowire heterostructures plays a dominant role in the incorporation of indium during the formation of InGaN quantum dots (QDs). The misfit strain between InGaN and GaN is accommodated elastically, and increased normal strain within GaN barriers are balanced out by enhancing In-incorporation in the subsequent QD, ultimately leading to the non-uniformity of In-content within individual nanowires. Notably, the strain relaxation in the embedded InGaN QDs is actually hydrostatic, because of the sidewall overgrowth by GaN that adds another out-of-plane constraint in the embedded structures in order to maintain coherency. It is the out-of-plane stress that is limiting the reduction in piezoelectric polarization expected in nanowire heterostructures. However, the omnipresent spontaneous polarization in compressively strained $In_xGa_{1-x}N$ alloys has its vector anti-parallel to the piezoelectric polarization vector, with magnitudes that remain variant only across a small range ($P_{sp} = -0.029$ – 0.032 C/m^2 for $x = 0-1$). Therefore, non-zero values of piezoelectric polarization can be sufficient to match and counterbalance the spontaneous polarization within the InGaN QDs.

Alloy effects continue to be a topic of concern in nanowire structures and how the inhomogeneity influences carrier localizaton, in particular evidence of composition pulling in thicker InGaN insertions [13, 15]. Atomic-level chemical ordering of InGaN alloys was confirmed within nanowire heterostructures in Chapter 3, proposed to circumvent other larger scale compositional variability due to their mutually exclusive occurrence. Atomically-ordered InGaN alloys with its alternating In-rich/Ga-rich c-plane layers can be thought of as monolayer units of strain partitioning, and provide more flexibility in accommodating bond lengths. As such, the first InGaN QD that experiences the highest degree of in-plane strain exhibits a prevalence for atomic ordering, further exemplified in the single InGaN dot nanowires. In addition, the semi-polar vicinal growth surfaces within the nanowire heterostructures promotes the energetically-favourable incorporation of In-adatoms into lower-coordination surface sites. The optical consequences of atomic ordering in InGaN alloys are intrinsically difficult to isolate, but the low defect density of nanowires makes them a viable platform to carry out such investigations.

Chapter 4 examines the luminescence of individual nanowire heterostructures. It was demonstrated that the polychromatic emission characteristics originate from single nanowires caused by the compositional non-uniformity between InGaN QDs. It does not, however, overlook the contribution of the inhomogeneous strain distribution to the intrinsic broadening

to individual emission peaks. Various structural features have been identified to factor into the overall emission rate, including the presence of the GaN or Al-rich AlGaN surface passivating shells, and basal plane stacking faults and the related zinc-blende insertions within the active region. The passivating shell positively impacts that lateral carrier confinement in QDs and suppresses non-radiative recombination at the nanowire surface. The enhanced carrier confinement becomes especially evident with the addition of Al into the barrier layers in the InGaN/AlGaN dot-in-a-wire structures. On the other hand, I_1-type stacking faults and zinc-blende insertions can be pinpointed to specific InGaN QDs that exhibit locally quenched CL intensity. Furthermore, evidence for the presence of polarization fields was revealed in the single and multiple InGaN/GaN heterostructures from excitation density dependent non-linearities, which were inferred from an observed proximity-related blue-shift in peak emission energy. Finally, the built-in potential within these N-face polar InGaN/GaN *p-i-n* light-emitting diode (LED) structures has adverse effects on the hole drift, which limits the spatial resolution of STEM-CL technique on the current nanostructures.

On the second topic of AlGaN nanowires in Chapter 5, significant compositional undulations of varying nature and spatial scales down to single atomic planes have been exacerbated by differences in Ga- and Al-adatom diffusion during nanowire growth. The alloy inhomogeneity appears to be dominated by Al-adatoms in the presence of excess active nitrogen and impacts the high Al-composition regime. It should also be emphasized that doping impurities, in particular Mg-dopants, can strongly modify the surface energy that altered the Ga-enrichment to along *c*-planes in the *p*-AlGaN segment. The compositional fluctuations in AlGaN give rise to a high spectral density of sharp emission lines that demonstrate carrier localization in the presence of energy band fluctuations. Most notable is the dominance of distinct emission bands correspond to specific types of the compositional fluctuations, including the shortest wavelengths at the *c*-plane variant and emitting strongest in a lower-energy band at the semi-polar plane variant.

Outlook Looking ahead at some relevant topics and questions that could become of interest for future studies. The investigation of InGaN/GaN nanowires has revealed sufficient nanowire-to-nanowire scatter in the emission characteristics. While this work on short-period InGaN/GaN nanowire heterostructures has not solved the issue of controlling the indium incorporation, it has demonstrated the significance of the three-dimensional strain relaxation and how that influences with local composition and the expected piezoelectric polarization. These attributes were instead employed to produce the broad emission necessary for phosphor-free white light-emitting diodes without any need for down-conversion [11, 19, 41]. The variability in nanowire spacing, diameter, length, and composition control

for self-organized nanowire growth makes the achievement of large area uniformity difficult. Templated selective area growth could be more a suitable alternative to achieve uniformity within nanowire ensembles.

Significant interest has been generated in recent years to realize III-N semiconductor quantum dots as reliable single photon emitters operable at room-temperature for future quantum information applications [263, 264]. The enhanced hole localization expected at atomically-ordered InGaN alloys [89] could offer the carrier confinement needed to sustain excitons up to room-temperature. It has yet to be confirmed whether the ordered InGaN quantum dot nanowires continues to mimic a two-level atom-like emission behaviour.

Due to the kinetic nature of the process governing the spontaneous formation of the nano- and atomic-scale compositional fluctuations in the AlGaN nanowires, growth parameters can be optimized to further exploit the alloy inhomogeneity and the associated carrier localization. Thereby, it provides another approach to obtain high-efficiency luminescence at emission wavelengths deeper into the ultraviolet spectral range for application as electrically-injected lasers and LEDs operating at room-temperature. Additionally, the Ga-rich/Al-rich AlGaN atomic-layers embody the appropriate strain-state and quantum confinement to be able to engineer the emission polarization to achieve the more desirable TE polarization ($E \perp c$) towards high Al-content [221].

Appendix A

Examples of Other Related III-Nitride Nanowires

A.1 Low-Temperature InGaN Nanowire Growth

$In_xGa_{1-x}N$ nanowire photoelectrodes with high indium composition of $x = 0.5$ to have optimal conduction band minimum and valence band maximum for water splitting have also been developed. Typical nitrogen-rich growth conditions, such as those used to produce InGaN/GaN dot-in-a-wire structures from Chapters 2 to 4, promotes such InGaN nanowire to form spontaneously InGaN/GaN core-shell structures with nanometers-thick GaN shell due to the higher surface desorption rate of In than that of Ga. As demonstrated in Chapter 4, the presence of a higher bandgap GaN shell is beneficial against non-radiative surface recombintation for emitters. However, it is detrimental to the photocatalytic activity of nanowires as photoanode because of the poor extraction of minority carriers. Instead, near unity V/III flux ratio together with a low substrate temperature (520 °C) can be used to enhance In-incorporation while suppressing the aforementioned strain-induced In-segregation at the core. The growth temperature of 520 °C is lower than the dissociation temperature of In–N bond (∼550 °C), leading to relatively low In-volatility. While the V/III ratio ∼ 1 eliminates the formation of a GaN shell in nanowires due to decreased surface desorption of In. As a consequence, the modified growth conditions demonstrated significant impact on the structural, optical and photoelectrochemical properties of InGaN nanowires [265]. Nanowire diameters are increased up to ∼300 nm, and surface texturing, which increases the effective surface area, is prevalent on the nanowire sidewalls.

Structural properties of the temperature and nitrogen-flow reduced grown InGaN nanowires were studied by aberration-corrected scanning transmission electron microscopy (STEM).

The STEM high-angle annular dark-field (STEM-HAADF) image of an InGaN nanowire is shown in Figure A.1(a). Elemental mapping over the nanowire by EELS was further performed and the indium composition was quantified according to the methods described in Chapter 2. The indium-content map (normalized to thickness in projection) displayed in pseudocolour in Figure A.1(b) shows similar variations as the STEM-HAADF image in Figure A.1(a), indicating the absence of an InGaN/GaN core-shell structure. Also from Figure A.1(b), the average indium composition is estimated as ∼50% within the bulk of the nanowire. While there are some deviations towards the nanowire surface, the indium composition locally remains high at ∼30% close to the surface.

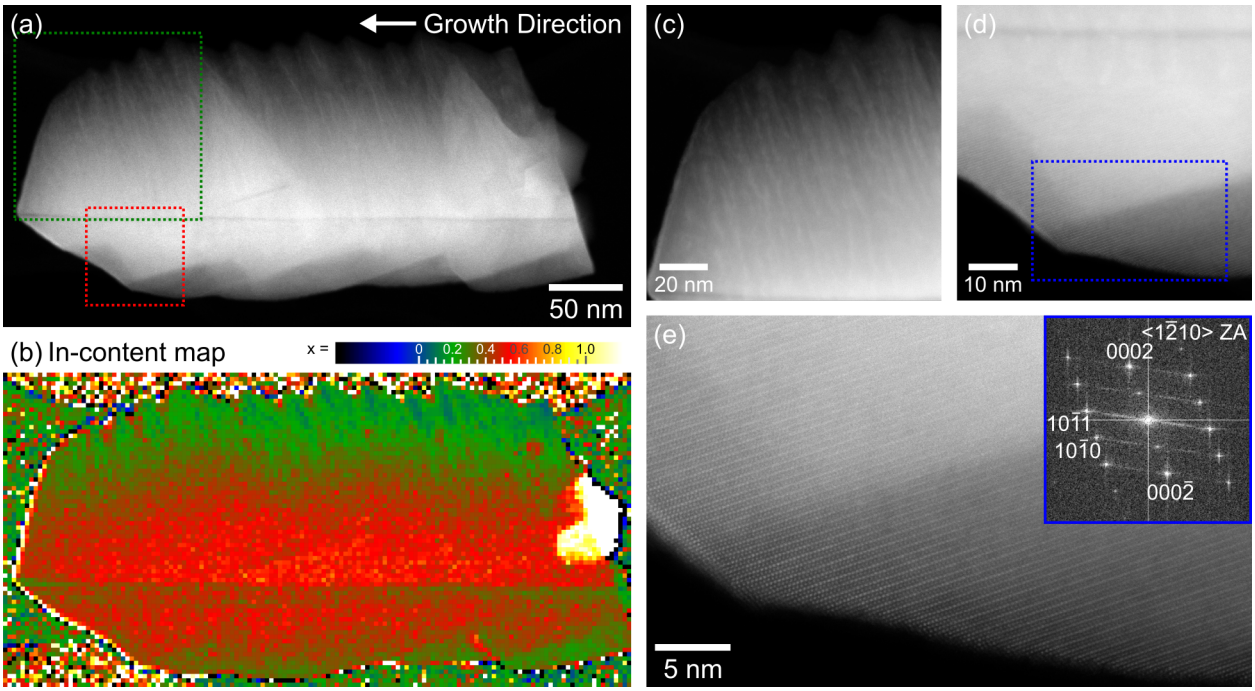

Figure A.1: **(a)** STEM-HAADF of an InGaN nanowire viewed along $\langle 1\bar{2}10 \rangle$ zone-axis, showing evidence of contrast at sidewalls due to the strong surface texturing. **(b)** The thickness-projected indium-content map derived using STEM-EELS spectrum imaging, displayed in pseudocolour, indicative of relatively uniform distribution of indium in the nanowire (∼50% in the bulk, ∼30% at the near-surface region). **(c)**–**(e)** High-magnification images of the regions in the **(c)** green and **(d)** red dashed boxes from **(a)**, and in **(e)** the blue dashed box area in **(d)**, highlighting the presence of atomic ordering along *c*-axis direction on the bottom surface of the nanowire in **(d,e)**. Additional inset in **(e)** shows the image's fast-Fourier transform (FFT) confirming various crystallographic directions.

Some instances of compositional fluctuations are evident, such as the atomic ordering (alternating indium-rich/gallium-rich *c*-planes) prominent on one side of the InGaN nanowire in Figures A.1(d) and A.1(e), or resemblance of phase segregation at the top sidewall in Figure A.1(c). The coexistence of such nanoscale phase separation processes in a single nanowire, while remaining spatially isolated, suggests that the driving force promoting atomic order-

ing indeed simultaneously suppresses phase separation [162] discussed in Chapter 3. It is also noteworthy to mention that the nanowire presented in Figure A.1(a) has a growth axis along $\langle 10\bar{1}1 \rangle$, as shown in the image's FFT in the inset of Figure A.1(e). A majority of other nanowires examined in STEM also exhibit a non-c-plane growth axis (such as $\langle 10\bar{1}2 \rangle$ or $\langle 10\bar{1}0 \rangle$). This is in agreement with the high-resolution X-ray diffraction $\theta/2\theta$ scan (not shown) that exhibits (102) and (203) peaks in addition to the (002) and (004) basal plane reflections of wurtzite-structured InGaN.

A.2 Nitrogen-Rich Flux AlN Nanowire Growth

AlN nanowires grown on GaN nanowire templates using similar growth temperatures (800 – 900 °C) and typical nitrogen-rich flux (1.0 sccm) as Sample A and B AlGaN nanowires from Chapter 5 have also been investigated. Figures A.2(a) and A.2(e) show low-magnification STEM-HAADF images of two separate nanowires viewed along m- and a-plane orientations, respectively. The macroscopic shape of the AlN/GaN nanowires grown under nitrogen-rich conditions in Figure A.2 was assessed based on the lateral projected shape from the integrated profile of the Al-signal from EELS along both m- and a-plane views (Figures A.2(b) and A.2(c)), as presented in Figure A.2(d) as the blue and red plots for the first nanowire, respectively. The blue half-hexagon house-shaped profile viewing down m-plane orientation, and red isoceles trapezoid-shaped profile viewing down a-plane orientation in Figure A.2(d) are reversed from the expected outcome if assuming a m-plane terminated hexagonal cross-section for the nanowire (such as from Figure A.3(d)). Also notable for the second AlN/GaN nanowire in Figure A.2(e), is the difference in projected shape shown in Figure A.2(h) between the Al-signal from AlN segment and Ga-signal from the GaN bases from Figures A.2(f) and A.2(g), respectively. Viewing along a-plane orientation, the GaN base exhibits a half-hexagon house-shaped profile indicative of m-plane faceting, while the AlN exhibits the same isoceles trapezoid-shaped profile as the red a-plane profile in Figure A.2(d). The lateral projected shape from these two AlN/GaN nanowires is clearly indicative of a change from m-plane faceting in the GaN nanowire template to a-plane faceting in the AlN segments.

Further evidence of the sidewall faceting is confirmed by a third AlN/GaN nanowire viewed down c-plane orientation in Figure A.2(i). A high-magnification image of the bottom vertex (marked in Figure A.2(i)) shown in Figure A.2(j) allows for visualization of the atomic columns down [0001]. A corresponding FFT of the local area (inset in Figure A.2(j)) indexes the macroscopic facets to belong to the $\{11\bar{2}0\}$ a-plane family. The macroscopic faceting deduced from the STEM observations along the three orientations (two non-polar and one polar) is demonstrated schematically viewed down the c-plane as the thick solid

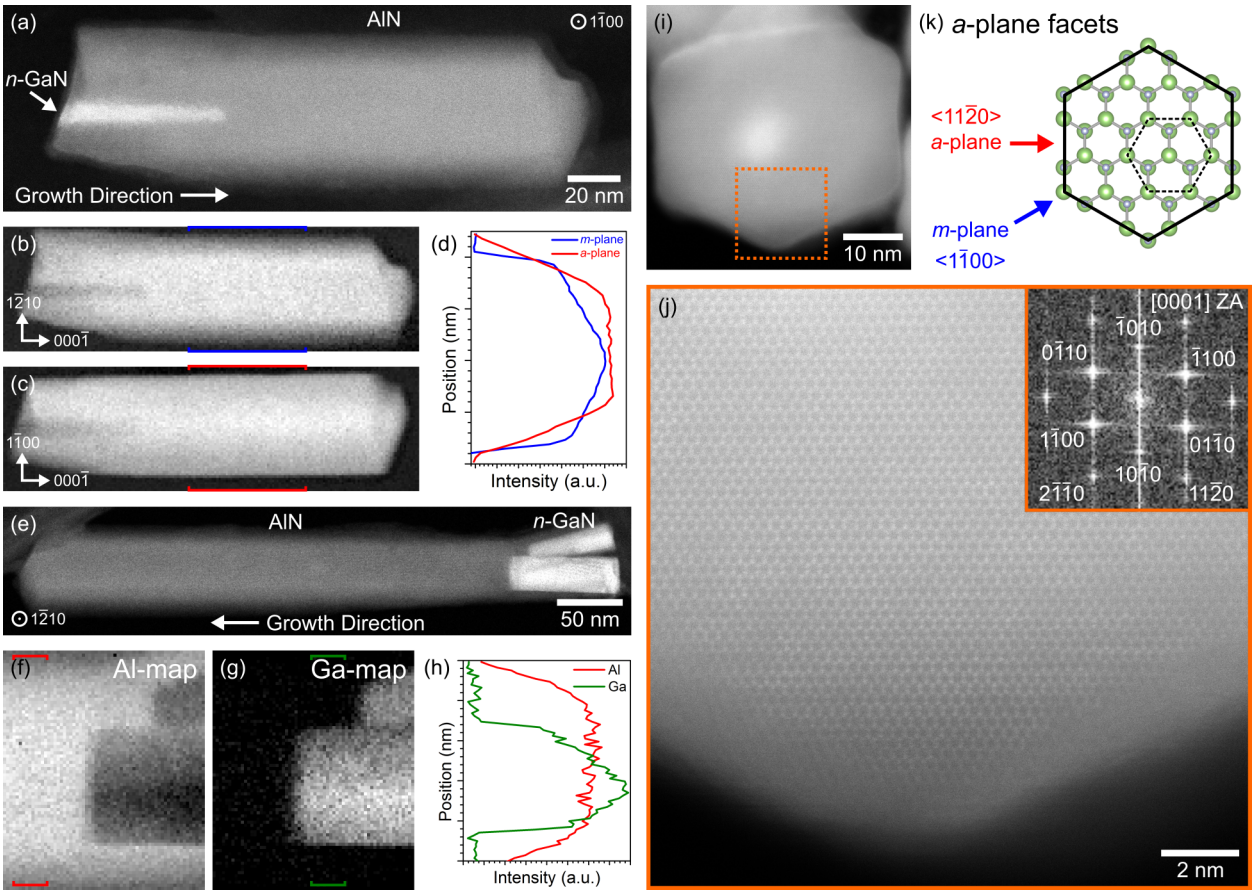

Figure A.2: AlN/GaN nanowires grown under typical nitrogen-rich conditions (1.0 sccm flow rate). **(a)** A low-magnification STEM-HAADF image of a nanowire viewed along $\langle 1\bar{1}00 \rangle$ zone-axis, **(b, c)** EELS maps generated using the Al $L_{2,3}$-edge for the Al-distribution when viewing along **(b)** m-plane, and **(c)** a-plane orientation, and **(d)** the corresponding integrated line profiles of the Al-signal colour-coded according to their marked regions. **(e)** A low-magnification STEM-HAADF image of a second nanowire viewed along $\langle 11\bar{2}0 \rangle$ zone-axis, **(f, g)** EELS maps from Al K and Ga $L_{2,3}$-edges showing the elemental distribution of Al and Ga at the interfacial region, and **(h)** the corresponding integrated line profiles of the Al (red) and Ga (green) signals from the marked regions. **(i)** c-plane orientation view of another nanowire of the same sample, seen at high-magnification in **(j)** showing clear a-plane termination at the sidewall surfaces. Inset in **(j)** is the FFT confirming various crystallographic directions. **(k)** Schematic illustration of the c-plane view of the nanowire, depicting the macroscopic faceting (thick solid black hexagonal outline) from **(i, j)**, and a wurtzite unit cell of GaN bound by m-plane surfaces (dashed black line).

black hexagonal outline in Figure A.2(k) overlaying the atomic-structure model. A wurtzite unit cell of GaN (dashed black hexagon) viewed down the c-plane with m-plane faces is also outlined within the atomic-structure model for comparison in Figure A.2(k). It is important to note the 30° relative rotation between the unit cell and the macroscopic shape/facets determined from experimental results, which is identical to the relationship observed in the high Al-concentration AlGaN nanowires (Sample B) from Section 5.4.2.1.

A.3 Low Nitrogen-Flow AlGaN Nanowire Growth

An alternative III-N nanowire growth regime of low nitrogen flow rate (approaching close to V/III $\approx$ 1) was more recently proposed to enhance the surface migration of Al adatoms and thus the uniformity of Al/Ga compositional distribution [266]. Shown in Figure A.3(a) is a low-magnification STEM-HAADF image of a single AlGaN/GaN nanowire grown with a nitrogen flow rate of 0.4 sccm and a substrate temperature of 950 °C. It is seen that AlGaN nanowire segment (darker region) is grown on GaN nanowire template (brighter region). The corresponding colour-coded EELS elemental mapping shown in Figure A.3(b) highlights the Ga (red) and Al (blue) distributions within the nanowire. A sharp GaN/AlGaN interface is also measured, indicating the superior crystalline quality of the AlGaN nanowire segment. Figure A.3(c) shows a high-resolution STEM-HAADF image near the top region of the AlGaN nanowire shown in Figure A.3(a). It is seen that the AlGaN segment exhibits relatively homogeneous image intensity, indicative of relatively uniform Al distribution, including the absence of an Al-rich shell.

The macroscopic shape of the high Al-content AlGaN nanowire grown under nitrogen-reduced conditions in Figure A.3(a) was assessed based on the lateral projected shape from the integrated HAADF intensity profile along its m-plane orientation, as presented in Figure A.3(d). HAADF image intensity increases monotonically with thickness, such that the shape of the HAADF intensity profile reflects the projected cross-sectional thickness. The blue isoceles trapezoid-shaped profile viewing down $\langle 1\bar{1}00 \rangle$ zone-axis in Figure A.3(d) match the expected outcome of a m-plane terminated hexagonal cross-section for the nanowire. Furthermore, the sidewall faceting is confirmed by another nitrogen-reduced AlGaN nanowire nanowire viewed down c-plane orientation in Figure A.3(e). An atomically-resolved image of the top-right region (marked in Figure A.3(e)) shown in Figure A.3(f) and the corresponding FFT of the local area (inset in Figure A.3(f)) indexes the macroscopic facets belong instead to the $\{1\bar{1}00\}$ m-plane family. Similar to before, the macroscopic faceting is illustrated schematically according to the STEM observations, presented as the thick solid black hexagonal outline in Figure A.3(g) overlaying the atomic-structure model viewing along [0001], together with a wurtzite unit cell of GaN (dashed black hexagon) with m-plane faces. For the nitrogen-reduced AlGaN nanowires, the unit cell and the determined macroscopic facets have outlines that are concentric, and therefore m-plane surface facets are confirmed.

(Al,In)GaN nanowires are typically grown under nitrogen-rich conditions, which has been described as a fundamental component for achieving disparity between axial to radial growth rates. As early as during the nucleation stage for catalyst-free growth, the usual excess of active nitrogen reduces the mobility of adsorbed group III species on the substrate surface

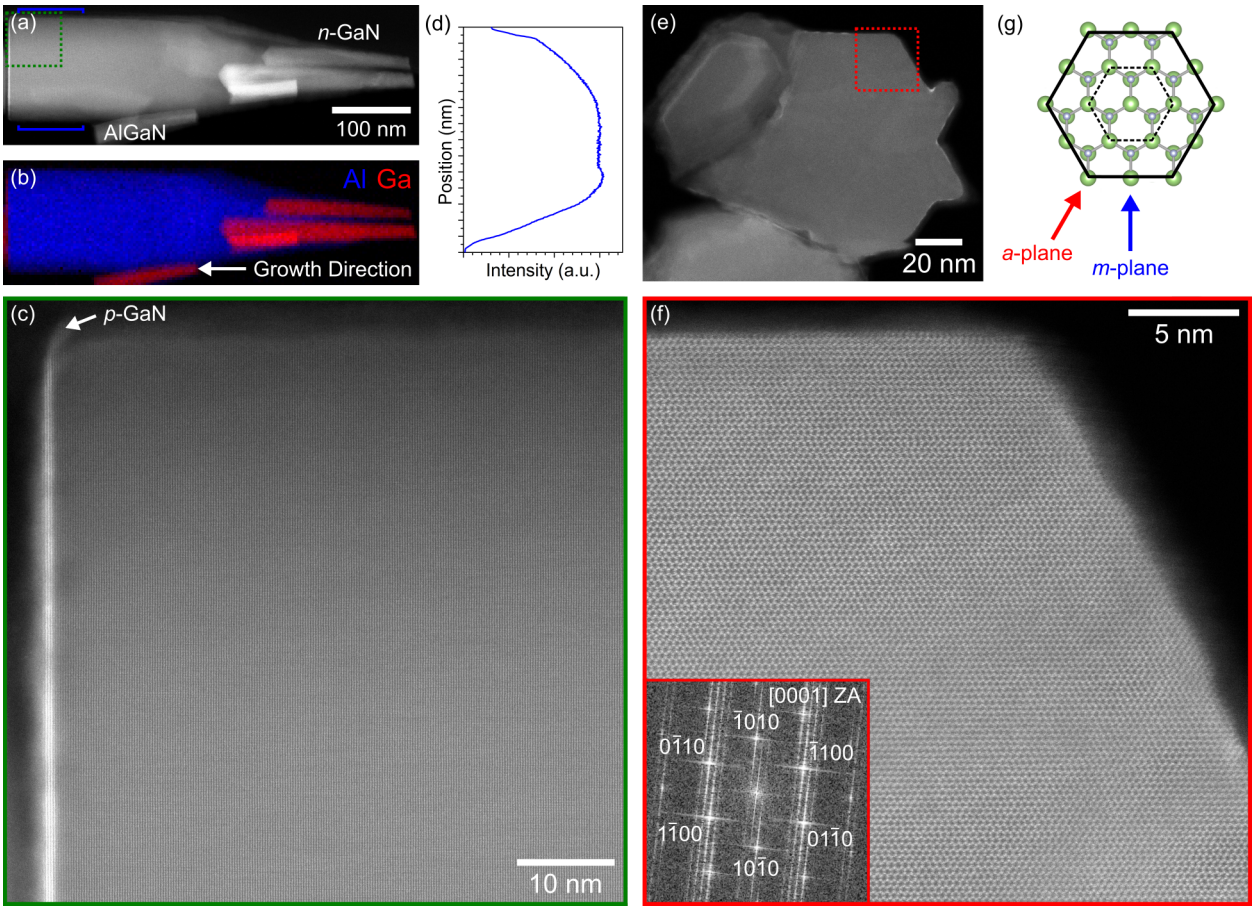

Figure A.3: GaN/AlGaN nanowires grown with a low nitrogen flow rate (0.4 sccm). **(a)** A low-magnification STEM-HAADF image of a nanowire viewed along $\langle 1\bar{1}00 \rangle$, and **(b)** the corresponding colour-coded EELS maps showing the elemental distribution of Ga and Al in red and blue, respectively. **(c)** A high-resolution image taken from the AlGaN segment marked in **(a)**, highlighting the relatively uniform Al distribution. The thin bright band is the *p*-GaN contact layer. **(d)** HAADF intensity profile for the *m*-plane orientation view of the AlGaN segment from the nanowire in **(a)**. **(e)** *c*-plane orientation view of the same sample, seen at high-magnification in **(f)** showing clear *m*-plane termination at the sidewall surfaces. Inset in **(f)** is the FFT confirming various crystallographic directions. **(g)** Schematic illustration of the *c*-plane view of the nanowire, depicting the macroscopic faceting (thick solid black hexagonal outline) from **(e, f)**, and a wurtzite unit cell of GaN bound by *m*-plane surfaces (dashed black line).

[255]. At the same time, the elevated growth temperatures provide sufficient enhancement for adatom migration along nanowire sidewalls towards the axial growth front, in particular the Al-adatoms [256]. This is evidenced by the lack of a Al-rich core-shell structure, as well as *m*-plane sidewall facets for AlGaN nanowires grown using with reduced-nitrogen.

Bibliography

[1] F. A. Ponce and D. P. Bour. Nitride-based semiconductors for blue and green light-emitting devices. *Nature*, 386(6623):351–359, mar 1997. doi: 10.1038/386351a0. URL http://www.nature.com/doifinder/10.1038/386351a0.

[2] E. Ertekin, P. A. Greaney, D. C. Chrzan, and T. D. Sands. Equilibrium limits of coherency in strained nanowire heterostructures. *Journal of Applied Physics*, 97(11):114325, 2005. doi: 10.1063/1.1903106. URL http://aip.scitation.org/doi/10.1063/1.1903106.

[3] F. Glas. Critical dimensions for the plastic relaxation of strained axial heterostructures in free-standing nanowires. *Physical Review B*, 74(12):121302, 2006. doi: 10.1103/PhysRevB.74.121302. URL http://link.aps.org/doi/10.1103/PhysRevB.74.121302.

[4] S. Chichibu, T. Azuhata, T. Sota, and S. Nakamura. Spontaneous emission of localized excitons in InGaN single and multiquantum well structures. *Applied Physics Letters*, 69(27):4188–4188, 1996. doi: 10.1063/1.116981. URL http://aip.scitation.org/doi/10.1063/1.116981.

[5] Y. Narukawa, Y. Kawakami, M. Funato, S. Fujita, S. Fujita, and S. Nakamura. Role of self-formed InGaN quantum dots for exciton localization in the purple laser diode emitting at 420 nm. *Applied Physics Letters*, 70(8):981–983, 1997. doi: 10.1063/1.118455. URL http://aip.scitation.org/doi/10.1063/1.118455.

[6] S. Albert, A. Bengoechea-Encabo, M. A. Sánchez-García, X. Kong, A. Trampert, and E. Calleja. Selective area growth of In(Ga)N/GaN nanocolumns by molecular beam epitaxy on GaN-buffered Si(111): from ultraviolet to infrared emission. *Nanotechnology*, 24(17):175303, 2013. doi: 10.1088/0957-4484/24/17/175303. URL http://stacks.iop.org/0957-4484/24/i=17/a=175303.

[7] Y.-H. Ra, R. Wang, S. Y. Woo, M. Djavid, S. Md. Sadaf, J. Lee, G. A. Botton, and Z. Mi. Full-Color Single Nanowire Pixels for Projection Displays. *Nano Letters*, 16(7):4608–4615, 2016. doi: 10.1021/acs.nanolett.6b01929. URL http://pubs.acs.org/doi/abs/10.1021/acs.nanolett.6b01929.

[8] A. Kikuchi, M. Kawai, M. Tada, and K. Kishino. InGaN/GaN multiple quantum disk nanocolumn light-emitting diodes grown on (111) Si substrate. *Japanese Journal of Applied Physics*, 43(12A):L1524–L1526, 2004. doi: 10.1143/JJAP.43.L1524. URL http://iopscience.iop.org/1347-4065/43/12A/L1524.

[9] R. Armitage and K. Tsubaki. Multicolour luminescence from InGaN quantum wells grown over GaN nanowire arrays by molecular-beam epitaxy. *Nanotechnology*, 21(19):195202, 2010.

doi: 10.1088/0957-4484/21/19/195202. URL http://iopscience.iop.org/article/10.1088/0957-4484/21/19/195202.

[10] Y.-L. Chang, J. L. Wang, F. Li, and Z. Mi. High efficiency green, yellow, and amber emission from InGaN/GaN dot-in-a-wire heterostructures on Si(111). *Applied Physics Letters*, 96(1): 013106, 2010. doi: 10.1063/1.3284660. URL http://aip.scitation.org/doi/10.1063/1.3284660.

[11] H.-W. Lin, Y.-J. Lu, H.-Y. Chen, H.-M. Lee, and S. Gwo. InGaN/GaN nanorod array white light-emitting diode. *Applied Physics Letters*, 97(7):073101, 2010. doi: 10.1063/1.3478515. URL http://aip.scitation.org/doi/10.1063/1.3478515.

[12] W. Guo, M. Zhang, A. Banerjee, and P. Bhattacharya. Catalyst-Free InGaN/GaN Nanowire Light Emitting Diodes Grown on (001) Silicon by Molecular Beam Epitaxy. *Nano Letters*, 10(9):3355–3359, 2010. doi: 10.1021/nl101027x. URL http://pubs.acs.org/doi/abs/10.1021/nl101027x.

[13] G. Tourbot, C. Bougerol, A. Grenier, M. I. den Hertog, D. Sam-Giao, D. Cooper, P. Gilet, B. Gayral, and B. Daudin. Structural and optical properties of InGaN/GaN nanowire heterostructures grown by PA-MBE. *Nanotechnology*, 22(7):075601, 2011. doi: 10.1088/0957-4484/22/7/075601. URL http://iopscience.iop.org/0957-4484/22/7/075601/.

[14] M. Wölz, V. M. Kaganer, O. Brandt, L. Geelhaar, and H. Riechert. Analyzing the growth of $In_xGa_{1-x}N$/GaN superlattices in self-induced GaN nanowires by x-ray diffraction. *Applied Physics Letters*, 98(26):261907, 2011. doi: 10.1063/1.3604810. URL http://scitation.aip.org/content/aip/journal/apl/98/26/10.1063/1.3604810.

[15] M. Knelangen, M. Hanke, E. Luna, L. Schrottke, O. Brandt, and A. Trampert. Monodisperse (In, Ga)N insertions in catalyst-free-grown GaN(0001) nanowires. *Nanotechnology*, 22(36): 365703, 2011. doi: 10.1088/0957-4484/22/36/365703. URL http://iopscience.iop.org/0957-4484/22/46/469501/.

[16] D. Cherns, R. F. Webster, S. V. Novikov, C. T. Foxon, A. M. Fischer, F. A. Ponce, and S. J. Haigh. Compositional variations in $In_{0.5}Ga_{0.5}N$ nanorods grown by molecular beam epitaxy. *Nanotechnology*, 25:215705, 2014. doi: 10.1088/0957-4484/25/21/215705. URL http://iopscience.iop.org/0957-4484/25/21/215705/.

[17] Y. Kawakami, S. Suzuki, A. Kaneta, M. Funato, A. Kikuchi, and K. Kishino. Origin of high oscillator strength in green-emitting InGaN/GaN nanocolumns. *Applied Physics Letters*, 89(16):163124, 2006. doi: 10.1063/1.2363958. URL http://aip.scitation.org/doi/10.1063/1.2363958.

[18] R. Bardoux, A. Kaneta, M. Funato, Y. Kawakami, A. Kikuchi, and K. Kishino. Positive binding energy of a biexciton confined in a localization center formed in a single $In_xGa_{1-x}N$/GaN quantum disk. *Physical Review B*, 79(15):155307, 2009. doi: 10.1103/PhysRevB.79.155307. URL https://link.aps.org/doi/10.1103/PhysRevB.79.155307.

[19] H. P. T. Nguyen, S. Zhang, K. Cui, X. Han, S. Fathololoumi, M. Couillard, G. A. Botton, and Z. Mi. p-Type modulation doped InGaN/GaN dot-in-a-wire white-light-emitting diodes monolithically grown on Si(111). *Nano Letters*, 11(5):1919–1924, 2011. doi: 10.1021/nl104536x. URL http://pubs.acs.org/doi/abs/10.1021/nl104536x.

[20] J. Bruckbauer, P. R. Edwards, J. Bai, T. Wang, and R. W. Martin. Probing light emission from quantum wells within a single nanorod. *Nanotechnology*, 24(36):365704, 2013. doi: 10.1088/0957-4484/24/36/365704. URL http://stacks.iop.org/0957-4484/24/i=36/a=365704?key=crossref.6796a2fa0455075e403569c8e1e1718c.

[21] R. Calarco, M. Marso, T. Richter, A. I. Aykanat, R. Meijers, A. v.d. Hart, T. Stoica, and H. Lüth. Size-dependent Photoconductivity in MBE-Grown GaN–Nanowires. *Nano Letters*, 5(5):981–984, may 2005. doi: 10.1021/nl0500306. URL http://pubs.acs.org/doi/abs/10.1021/nl0500306.

[22] J. Ristić, E. Calleja, A. Trampert, S. Fernández-Garrido, C. Rivera, U. Jahn, and K. H. Ploog. Columnar AlGaN/GaN Nanocavities with AlN/GaN Bragg Reflectors Grown by Molecular Beam Epitaxy on Si(111). *Physical Review Letters*, 94(14):146102, 2005. doi: 10.1103/PhysRevLett.94.146102. URL http://link.aps.org/doi/10.1103/PhysRevLett.94.146102.

[23] C. Rivera, U. Jahn, T. Flissikowski, J. Pau, E. Muñoz, and H. T. Grahn. Strain-confinement mechanism in mesoscopic quantum disks based on piezoelectric materials. *Physical Review B*, 75(4):045316, 2007. doi: 10.1103/PhysRevB.75.045316. URL http://link.aps.org/doi/10.1103/PhysRevB.75.045316.

[24] J. Wu, W. Walukiewicz, K. M. Yu, J. W. Ager, E. E. Haller, H. Lu, and W. J. Schaff. Small band gap bowing in $In_{1-x}Ga_xN$ alloys. *Applied Physics Letters*, 80(25):4741–4743, 2002. doi: 10.1063/1.1489481. URL http://aip.scitation.org/doi/10.1063/1.1489481.

[25] E. F. Schubert. *Light emitting diodes*. Cambridge University Press, Cambridge, UK, 2nd edition, 2006. ISBN 978-0-521-86538-8.

[26] S. Nakamura, T. Mukai, and M. Senoh. Candela-class high-brightness InGaN/AlGaN double-heterostructure blue-light-emitting diodes. *Applied Physics Letters*, 64(13):1687–1689, 1994. doi: 10.1063/1.111832. URL http://aip.scitation.org/doi/10.1063/1.111832.

[27] S. Nakamura, S. Pearton, and G. Fasol. *The Blue Laser Diode: The Complete Story*. Springer, Berlin, Heidelberg, 2000. ISBN 978-3-642-08579-6. doi: 10.1007/978-3-662-04156-7. URL http://link.springer.com/10.1007/978-3-662-04156-7.

[28] A. Kitai. *Light Emitting Diodes*. Wiley, Chichester, West Sussex, U.K., 2011. ISBN 978-1-1199-7454-3. doi: 10.1002/9781119974543.ch5. URL http://dx.doi.org/10.1002/9781119974543.ch5.

[29] J. Wu. When group-III nitrides go infrared: New properties and perspectives. *Journal of Applied Physics*, 106(1):011101, 2009. doi: 10.1063/1.3155798. URL http://aip.scitation.org/doi/10.1063/1.3155798.

[30] I. Vurgaftman and J. R. Meyer. Band parameters for nitrogen-containing semiconductors. *Journal of Applied Physics*, 94(6):3675–3696, 2003. doi: 10.1063/1.1600519. URL http://aip.scitation.org/doi/10.1063/1.1600519.

[31] H. Morkoç. *General Properties of Nitrides*. Wiley-VCH Verlag GmbH and Co. KGaA, 2009. ISBN 978-3-5276-2843-8. doi: 10.1002/9783527628438. URL http://dx.doi.org/10.1002/9783527628438.

[32] H. Amano, N. Sawaki, I. Akasaki, and Y. Toyoda. Metalorganic vapor phase epitaxial growth of a high quality GaN film using an AlN buffer layer. *Applied Physics Letters*, 48(5):353–355, 1986. doi: 10.1063/1.96549. URL http://aip.scitation.org/doi/10.1063/1.96549.

[33] I. Akasaki, H. Amano, Y. Koide, K. Hiramatsu, and N. Sawaki. Effects of ain buffer layer on crystallographic structure and on electrical and optical properties of GaN and $Ga_{1-x}Al_xN$ ($0 < x < 0.4$) films grown on sapphire substrate by MOVPE. *Journal of Crystal Growth*, 98 (1):209 – 219, 1989. doi: 10.1016/0022-0248(89)90200-5. URL http://www.sciencedirect.com/science/article/pii/0022024889902005.

[34] H. Amano, M. Kito, K. Hiramatsu, and I. Akasaki. P-Type Conduction in Mg-Doped GaN Treated with Low-Energy Electron Beam Irradiation (LEEBI). *Japanese Journal of Applied Physics*, 28(12A):L2112, 1989. doi: 10.1143/JJAP.28.L2112. URL http://stacks.iop.org/1347-4065/28/i=12A/a=L2112.

[35] S. Nakamura, N. Iwasa, M. Senoh, and T. Mukai. Hole Compensation Mechanism of p-Type GaN Films. *Japanese Journal of Applied Physics*, 31(5R):1258, 1992. doi: 10.1143/JJAP.31.1258. URL http://stacks.iop.org/1347-4065/31/i=5R/a=1258.

[36] S. Nakamura and T. Mukai. High-Quality InGaN Films Grown on GaN Films. *Japanese Journal of Applied Physics*, 31(10B):L1457, 1992. doi: 10.1143/JJAP.31.L1457. URL http://stacks.iop.org/1347-4065/31/i=10B/a=L1457.

[37] S. Nakamura, Y. Harada, and M. Seno. Novel metalorganic chemical vapor deposition system for GaN growth. *Applied Physics Letters*, 58(18):2021–2023, 1991. doi: http://dx.doi.org/10.1063/1.105239. URL http://aip.scitation.org/doi/10.1063/1.105239.

[38] J. Hader, J. V. Moloney, and S. W. Koch. Temperature-dependence of the internal efficiency droop in GaN-based diodes. *Applied Physics Letters*, 99(18):181127, 2011. doi: 10.1063/1.3658031. URL http://aip.scitation.org/doi/10.1063/1.3658031.

[39] M.-H. Kim, M. F. Schubert, Q. Dai, J. K. Kim, E. F. Schubert, J. Piprek, and Y. Park. Origin of efficiency droop in GaN-based light-emitting diodes. *Applied Physics Letters*, 91(18):183507, 2007. doi: 10.1063/1.2800290. URL http://aip.scitation.org/doi/10.1063/1.2800290.

[40] Y. C. Shen, G. O. Mueller, S. Watanabe, N. F. Gardner, A. Munkholm, and M. R. Krames. Auger recombination in InGaN measured by photoluminescence. *Applied Physics Letters*, 91(14):141101, 2007. doi: 10.1063/1.2785135. URL http://aip.scitation.org/doi/10.1063/1.2785135.

[41] W. Guo, M. Zhang, P. Bhattacharya, and J. Heo. Auger recombination in III-nitride nanowires and its effect on nanowire light-emitting diode characteristics. *Nano Letters*, 11(4):1434–1438, 2011. doi: 10.1021/nl103649d. URL http://pubs.acs.org/doi/abs/10.1021/nl103649d.

[42] J. Iveland, L. Martinelli, J. Peretti, J. S. Speck, and C. Weisbuch. Direct measurement of auger electrons emitted from a semiconductor light-emitting diode under electrical injection: Identification of the dominant mechanism for efficiency droop. *Physical Review Letters*, 110 (17):177406, 2013. doi: 10.1103/PhysRevLett.110.177406. URL https://link.aps.org/doi/10.1103/PhysRevLett.110.177406.

[43] X. Ni, Q. Fan, R. Shimada, Ü. Özgür, and H. Morkoç. Reduction of efficiency droop in InGaN light emitting diodes by coupled quantum wells. *Applied Physics Letters*, 93(17):171113, 2008. doi: 10.1063/1.3012388. URL http://aip.scitation.org/doi/10.1063/1.3012388.

[44] Y.-K. Kuo, T.-H. Wang, and J.-Y. Chang. Advantages of blue InGaN light-emitting diodes with InGaN-AlGaN-InGaN barriers. *Applied Physics Letters*, 100(3):031112, 2012. doi: 10.1063/1.3678341. URL http://aip.scitation.org/doi/10.1063/1.3678341.

[45] O. Ambacher, J. Smart, J. R. Shealy, N. G. Weimann, K. Chu, M. Murphy, W. J. Schaff, L. F. Eastman, R. Dimitrov, L. Wittmer, M. Stutzmann, W. Rieger, and J. Hilsenbeck. Two-dimensional electron gases induced by spontaneous and piezoelectric polarization charges in N- and Ga-face AlGaN/GaN heterostructures. *Journal of Applied Physics*, 85(6):3222–3233, 1999. doi: 10.1063/1.369664. URL http://aip.scitation.org/doi/10.1063/1.369664.

[46] K. Hestroffer, C. Leclere, C. Bougerol, H. Renevier, and B. Daudin. Polarity of GaN nanowires grown by plasma-assisted molecular beam epitaxy on Si(111). *Physical Review B*, 84(24):245302, 2011. doi: 10.1103/PhysRevB.84.245302. URL http://link.aps.org/doi/10.1103/PhysRevB.84.245302.

[47] D. Huang, P. Visconti, M.A. Reshchikov, F. Yun, T. King, A.A. Baski, C.W. Litton, J. Jasinski, Z. Liliental-Weber, and H. Morkoç. Polarity of GaN Grown on Sapphire by Molecular Beam Epitaxy with Different Buffer Layers. *Physica Status Solidi (a)*, 188(2):571–574, 2001. doi: 10.1002/1521-396X(200112)188:2⟨571::AID-PSSA571⟩3.3.CO;2-6. URL http://doi.wiley.com/10.1002/1521-396X(200112)188:2{%}3C571::AID-PSSA571{%}3E3.3.CO;2-6.

[48] G. Radtke, M. Couillard, G. A. Botton, D. Zhu, and C. J. Humphreys. Scanning transmission electron microscopy investigation of the Si(111)/AlN interface grown by metalorganic vapor phase epitaxy. *Applied Physics Letters*, 97(25):251901, 2010. doi: 10.1063/1.3527928. URL http://aip.scitation.org/doi/10.1063/1.3527928.

[49] M. de la Mata, C. Magén, J. Gazquez, M. I. B. Utama, M. Heiss, S. Lopatin, F. Furtmayr, C. J. Fernández-Rojas, B. Peng, J. R. Morante, R. Rurali, M. Eickhoff, A. Fontcuberta i Morral, Qi. Xiong, and J. Arbiol. Polarity assignment in ZnTe, GaAs, ZnO, and GaN-AlN nanowires from direct dumbbell analysis. *Nano Letters*, 12(5):2579–2586, 2012. doi: 10.1021/nl300840q. URL http://pubs.acs.org/doi/abs/10.1021/nl300840q.

[50] V. Fellmann, P. Jaffrennou, D. Sam-Giao, B. Gayral, K. Lorenz, E. Alves, and B. Daudin. Ternary AlGaN Alloys with High Al Content and Enhanced Compositional Homogeneity Grown by Plasma-Assisted Molecular Beam Epitaxy. *Japanese Journal of Applied Physics*, 50(3):031001, 2011. doi: 10.1143/JJAP.50.031001. URL http://stacks.iop.org/1347-4065/50/031001.

[51] A. Gutiérrez-Sosa, U. Bangert, A. J. Harvey, C. J. Fall, R. E. Jones, P. Briddon, and M. I. Heggie. Band-gap-related energies of threading dislocations and quantum wells in group-III nitride films as derived from electron energy loss spectroscopy. *Physical Review B*, 66(3):035302, 2002. doi: 10.1103/PhysRevB.66.035302. URL http://link.aps.org/doi/10.1103/PhysRevB.66.035302.

[52] C. Hahn, Z. Zhang, A. Fu, C. H. Wu, Y. J. Hwang, D. J. Gargas, and P. Yang. Epitaxial growth of InGaN nanowire arrays for light emitting diodes. *ACS Nano*, 5(5):3970–3976, 2011. doi: 10.1021/nn200521r. URL http://pubs.acs.org/doi/abs/10.1021/nn200521r.

[53] I. Tischer, M. Hocker, B. Neuschl, M. Madel, M. Feneberg, M. Schirra, M. Frey, M. Knab, P. Maier, T. Wunderer, R. A. R. Leute, J. Wang, F. Scholz, J. Biskupek, J. Bernhard, U. Kaiser, U. Simon, L. Dieterle, H. Groiss, E. Müller, D. Gerthsen, and K. Thonke. Optical properties of defects in nitride semiconductors. *Journal of Materials Research*, 30(20): 2977–2990, 2015. doi: 10.1557/jmr.2015.273. URL http://www.journals.cambridge.org/abstract_S0884291415002733.

[54] C. Stampfl and Chris G. Van de Walle. Energetics and electronic structure of stacking faults in AlN, GaN, and InN. *Physyical Review B*, 57:R15052–R15055, 1998. doi: 10.1103/PhysRevB.57.R15052. URL https://link.aps.org/doi/10.1103/PhysRevB.57.R15052.

[55] J. Arbiol, S. Estradé, J. D. Prades, A. Cirera, F. Furtmayr, C. Stark, A. Laufer, M. Stutzmann, M. Eickhoff, M. H. Gass, A. L. Bleloch, F. Peiró, and J. R. Morante. Triple-twin domains in Mg doped GaN wurtzite nanowires: structural and electronic properties of this zinc-blende-like stacking. *Nanotechnology*, 20(14):145704, 2009. doi: 10.1088/0957-4484/20/14/145704. URL http://iopscience.iop.org/article/10.1088/0957-4484/20/14/145704.

[56] K. Lawniczak-Jablonska, T. Suski, Z. Liliental-Weber, E. M. Gullikson, J. H. Underwood, R. C. C. Perera, and T. J. Drummond. Anisotropy of the nitrogen conduction states in the group III nitrides studied by polarized X-ray absorption. *Applied Physics Letters*, 70(20):2711, 1997. doi: 10.1063/1.119000. URL http://aip.scitation.org/doi/10.1063/1.119000.

[57] C. Wood and D. Jena. *Polarization Effects in Semiconductors*. Springer, Berlin, Heidelberg, 2008. ISBN 978-0-387-68319-5. doi: 10.1007/978-0-387-68319-5. URL http://link.springer.com/10.1007/978-0-387-68319-5.

[58] G. Burns. *Solid State Physics*. Academic Press, Orlando, 1985. ISBN 978-0121460709.

[59] A. Zoroddu, F. Bernardini, P. Ruggerone, and V. Fiorentini. First-principles prediction of structure, energetics, formation enthalpy, elastic constants, polarization, and piezoelectric constants of AlN, GaN, and InN: Comparison of local and gradient-corrected density-functional theory. *Physical Review B*, 64:045208, 2001. doi: 10.1103/PhysRevB.64.045208. URL http://link.aps.org/doi/10.1103/PhysRevB.64.045208.

[60] F. Bernardini, V. Fiorentini, and D. Vanderbilt. Spontaneous polarization and piezoelectric constants of III-V nitrides. *Physical Review B*, 56(16):R10024–R10027, oct 1997. doi: 10.1103/PhysRevB.56.R10024. URL http://link.aps.org/doi/10.1103/PhysRevB.56.R10024.

[61] D. L. Smith and C. Mailhiot. Optical properties of strained-layer superlattices with growth axis along [111]. *Physical Review Letters*, 58(12):1264–1267, 1987. doi: 10.1103/PhysRevLett.58.1264. URL https://link.aps.org/doi/10.1103/PhysRevLett.58.1264.

[62] T. Takeuchi, S. Sota, M. Katsuragawa, M. Komori, H. Takeuchi, H. Amano, and I. Akasaki. Quantum-Confined Stark Effect due to Piezoelectric Fields in GaInN Strained Quantum Wells. *Japanese Journal of Applied Physics*, 36(Part 2, No. 4A):L382–L385, 1997. doi: 10.1143/JJAP.36.L382. URL http://stacks.iop.org/1347-4065/36/L382.

[63] D. A. B. Miller, D. Chemla, T. Damen, A. Gossard, W. Wiegmann, T. Wood, and C. Burrus. Band-Edge Electroabsorption in Quantum Well Structures: The Quantum-Confined Stark Effect. *Physical Review Letters*, 53(22):2173–2176, 1984. doi: 10.1103/PhysRevLett.53.2173. URL http://link.aps.org/doi/10.1103/PhysRevLett.53.2173.

[64] J. Renard, R. Songmuang, G. Tourbot, C. Bougerol, B. Daudin, and B. Gayral. Evidence for quantum-confined Stark effect in GaN/AlN quantum dots in nanowires. *Physical Review B*, 80(12):121305(R), 2009. doi: 10.1103/PhysRevB.80.121305. URL http://link.aps.org/doi/10.1103/PhysRevB.80.121305.

[65] D. Camacho Mojica and Y. M. Niquet. Stark effect in GaN/AlN nanowire heterostructures: Influence of strain relaxation and surface states. *Physical Review B*, 81(19):195313, 2010. doi: 10.1103/PhysRevB.81.195313. URL http://link.aps.org/doi/10.1103/PhysRevB.81.195313.

[66] F. Bernardini and V. Fiorentini. Macroscopic polarization and band offsets at nitride heterojunctions. *Physical Review B*, 57(16):R9427–R9430, apr 1998. doi: 10.1103/PhysRevB.57.R9427. URL http://link.aps.org/doi/10.1103/PhysRevB.57.R9427.

[67] D. Cherns, J. S. Barnard, and F. A. Ponce. Measurement of the piezoelectric field across strained InGaN/GaN layers by electron holography. *Solid State Communications*, 111(5):281–285, 1999. doi: 10.1016/S0038-1098(99)00130-1. URL http://linkinghub.elsevier.com/retrieve/pii/S0038109899001301.

[68] S. Pereira, M. R. Correia, E. Pereira, K. P. O'Donnell, C. Trager-Cowan, F. Sweeney, and E. Alves. Compositional pulling effects in $In_xGa_{1-x}N$/GaN layers: A combined depth-resolved cathodoluminescence and Rutherford backscattering/channeling study. *Physical Review B*, 64(20):205311, nov 2001. doi: 10.1103/PhysRevB.64.205311. URL http://link.aps.org/doi/10.1103/PhysRevB.64.205311.

[69] A. Armigliato, R. Balboni, G. P. Carnevale, G. Pavia, D. Piccolo, S. Frabboni, A. Benedetti, and A. G. Cullis. Application of convergent beam electron diffraction to two-dimensional strain mapping in silicon devices. *Applied Physics Letters*, 82(13):2172–2174, 2003. doi: 10.1063/1.1565181. URL http://aip.scitation.org/doi/10.1063/1.1565181.

[70] M. Naito, M. Ishimaru, Y. Hirotsu, and M. Takashima. Local structure analysis of Ge-Sb-Te phase change materials using high-resolution electron microscopy and nanobeam diffraction. *Journal of Applied Physics*, 95(12):8130–8135, 2004. doi: 10.1063/1.1728316. URL http://aip.scitation.org/doi/10.1063/1.1728316.

[71] M. J. Hÿtch, E. Snoeck, and R. Kilaas. Quantitative measurement of displacement and strain fields from HREM micrographs. *Ultramicroscopy*, 74(3):131–146, 1998. doi: 10.1016/S0304-3991(98)00035-7. URL http://linkinghub.elsevier.com/retrieve/pii/S0304399198000357.

[72] P. L. Galindo, S. Kret, A. M. Sanchez, J.-Y. Laval, A. Yáñez, J. Pizarro, E. Guerrero, T. Ben, and S. I. Molina. The Peak Pairs algorithm for strain mapping from HRTEM images. *Ultramicroscopy*, 107(12):1186–1193, 2007. doi: 10.1016/j.ultramic.2007.01.019. URL http://linkinghub.elsevier.com/retrieve/pii/S0304399107000204.

[73] M. Hÿtch, F. Houdellier, F. Hüe, and E. Snoeck. Nanoscale holographic interferometry for strain measurements in electronic devices. *Nature*, 453(7198):1086–1089, 2008. doi: 10.1038/nature07049. URL http://www.nature.com/doifinder/10.1038/nature07049.

[74] J. L. Rouvière and E. Sarigiannidou. Theoretical discussions on the geometrical phase analysis. *Ultramicroscopy*, 106(1):1–17, 2005. doi: 10.1016/j.ultramic.2005.06.001. URL http://www.sciencedirect.com/science/article/pii/S0304399105001038.

[75] F. Houdellier, M. J. Hÿtch, E. Snoeck, and M. J. Casanove. High-resolution electron holography for the study of composition and strain in thin film semiconductors. *Materials Science and Engineering B*, 135(3):188–191, 2006. doi: 10.1016/j.mseb.2006.08.035. URL http://linkinghub.elsevier.com/retrieve/pii/S092151070600451X.

[76] C. Kisielowski, Z. Liliental-Weber, and S. Nakamura. Atomic Scale Indium Distribution in a GaN/$In_{0.43}Ga_{0.57}N$/$Al_{0.1}Ga_{0.9}N$ Quantum Well Structure. *Japanese Journal of Applied Physics*, 36:6932–6936, 1997. doi: 10.1143/JJAP.36.6932.

[77] T. M. Smeeton, M. J. Kappers, J. S. Barnard, M. E. Vickers, and C. J. Humphreys. Electron-beam-induced strain within InGaN quantum wells: False indium "cluster" detection in the transmission electron microscope. *Applied Physics Letters*, 83(26):5419–5421, 2003. doi: 10.1063/1.1636534.

[78] D. Korakakis, K. F. Ludwig, and T. D. Moustakas. Long range order in $Al_xGa_{1-x}N$ films grown by molecular beam epitaxy. *Applied Physics Letters*, 71(1):72, 1997. doi: 10.1063/1.119916. URL http://aip.scitation.org/doi/10.1063/1.119916.

[79] P. Ruterana, G. Nouet, W. Van der Stricht, I. Moerman, and L. Considine. Chemical ordering in wurtzite $In_xGa_{1-x}N$ layers grown on (0001) sapphire by metalorganic vapor phase epitaxy. *Applied Physics Letters*, 72(14):1742–1744, 1998. doi: 10.1063/1.121170. URL http://aip.scitation.org/doi/10.1063/1.121170.

[80] C. Tessarek, S. Figge, T. Aschenbrenner, S. Bley, A. Rosenauer, M. Seyfried, J. Kalden, K. Sebald, J. Gutowski, and D. Hommel. Strong phase separation of strained $In_xGa_{1-x}N$ layers due to spinodal and binodal decomposition: Formation of stable quantum dots. *Physical Review B*, 83(11):115316, 2011. doi: 10.1103/PhysRevB.83.115316. URL http://link.aps.org/doi/10.1103/PhysRevB.83.115316.

[81] D. A. Porter and K. E. Easterling. *Phase Transformation in Metals and Alloys*. Taylor & Francis, Boca Raton, 2nd edition, 1992. ISBN 9780748757411.

[82] J. W. Cahn and J. E. Hilliard. Free Energy of a Nonuniform System. I. Interfacial Free Energy. *The Journal of Chemical Physics*, 28(2):258–267, 1958. doi: 10.1063/1.1744102. URL http://aip.scitation.org/doi/10.1063/1.1744102.

[83] S. Yu. Karpov. Suppression of phase separation in InGaN due to elastic strain. *MRS Internet Joural of Nitride Semiconductor Research*, 3(1998):16, 1998. doi: 10.1557/S1092578300000831. URL http://journals.cambridge.org/abstract_S1092578300000880.

[84] Q. Y. Wei, T. Li, Y. Huang, J. Y. Huang, Z. T. Chen, T. Egawa, and F. A. Ponce. Compositional instability in InAlN/GaN lattice-matched epitaxy. *Applied Physics Letters*, 100(9): 092101, 2012. doi: 10.1063/1.3690890. URL http://aip.scitation.org/doi/10.1063/1.3690890.

[85] H. P. T. Nguyen, K. Cui, S. Zhang, M. Djavid, A. Korinek, G. A. Botton, and Z. Mi. Controlling Electron Overflow in Phosphor-Free InGaN/GaN Nanowire White Light-Emitting Diodes. *Nano Letters*, 12(3):1317–1323, 2012. doi: 10.1021/nl203860b. URL http://pubs.acs.org/doi/abs/10.1021/nl203860b.

[86] S. F. Chichibu, T. Azuhata, T. Sota, and T. Mukai. Localized excitons in an $In_{0.06}Ga_{0.94}N$ multiple-quantum-well laser diode lased at 400 nm. *Applied Physics Letters*, 79(3):341–343, 2001. doi: 10.1063/1.1385583. URL http://aip.scitation.org/doi/10.1063/1.1385583.

[87] R. A. Oliver, S. E. Bennett, T. Zhu, D. J. Beesley, M. J. Kappers, D. W. Saxey, A. Cerezo, and C. J. Humphreys. Microstructural origins of localization in InGaN quantum wells. *Journal of Physics D: Applied Physics*, 43(35):354003, 2010. doi: 10.1088/0022-3727/43/35/354003. URL http://stacks.iop.org/0022-3727/43/i=35/a=354003?key=crossref.777e6d01ce0582a1a78c9294f749a30c.

[88] L. Bellaiche, T. Mattila, L.-W. Wang, S.-H. Wei, and A. Zunger. Resonant hole localization and anomalous optical bowing in InGaN alloys. *Applied Physics Letters*, 74(13):1842–1844, 1999. doi: 10.1063/1.123687. URL http://aip.scitation.org/doi/10.1063/1.123687.

[89] L.-W. Wang. Calculations of carrier localization in $In_xGa_{1-x}N$. *Physical Review B*, 63: 245107, 2001. doi: 10.1103/PhysRevB.63.245107. URL https://link.aps.org/doi/10.1103/PhysRevB.63.245107.

[90] S. F. Chichibu, A. Uedono, T. Onuma, B. A. Haskell, A. Chakraborty, T. Koyama, P. T. Fini, S. Keller, S. P. DenBaars, J. S. Speck, U. K. Mishra, S. Nakamura, S. Yamaguchi, S. Kamiyama, H. Amano, I. Akasaki, J. Han, and T. Sota. Origin of defect-insensitive emission probability in In-containing (Al,In,Ga)N alloy semiconductors. *Nature Materials*, 5 (10):810–816, 2006. doi: 10.1038/nmat1726. URL http://www.nature.com/doifinder/10.1038/nmat1726.

[91] D. Gerthsen, E. Hahn, B. Neubauer, A. Rosenauer, O. Schön, M. Heuken, and A. Rizzi. Composition Fluctuations in InGaN Analyzed by Transmission Electron Microscopy. *Physica Status Solidi (a)*, 177(1):145–155, 2000. doi: 10.1002/(SICI)1521-396X(200001)177:1⟨145::AID-PSSA145⟩3.0.CO;2-0. URL http://dx.doi.org/10.1002/(SICI)1521-396X(200001)177:1<145::AID-PSSA145>3.0.CO;2-0.

[92] M. J. Galtrey, R. A. Oliver, M. J. Kappers, C. J. Humphreys, D. J. Stokes, P. H. Clifton, and A. Cerezo. Three-dimensional atom probe studies of an $In_xGa_{1-x}N$/GaN multiple quantum well structure: Assessment of possible indium clustering. *Applied Physics Letters*, 90(6): 061903, 2007. doi: 10.1063/1.2431573. URL http://aip.scitation.org/doi/10.1063/1.2431573.

[93] R. Zimmermann. Theory of exciton linewidth in II–VI semiconductor mixed crystals. *Journal of Crystal Growth*, 101(1):346–349, 1990. doi: 10.1016/0022-0248(90)90993-U. URL http://www.sciencedirect.com/science/article/pii/002202489090993U.

[94] D. M. Graham, A. Soltani-Vala, P. Dawson, M. J. Godfrey, T. M. Smeeton, J. S. Barnard, M. J. Kappers, C. J. Humphreys, and E. J. Thrush. Optical and microstructural studies of InGaN/GaN single-quantum-well structures. *Journal of Applied Physics*, 97(10):103508, 2005. doi: 10.1063/1.1897070. URL http://aip.scitation.org/doi/10.1063/1.1897070.

[95] G. Steude, B. K. Meyer, A. Göldner, A. Hoffmann, F. Bertram, J. Christen, H. Amano, and I. Akasaki. Optical investigations of AlGaN on GaN epitaxial films. *Applied Physics Letters*, 74(17):2456–2458, 1999. doi: 10.1063/1.123879. URL http://aip.scitation.org/doi/10.1063/1.123879.

[96] S. F. Chichibu, A. Uedono, T. Onuma, B. A. Haskell, A. Chakraborty, T. Koyama, P. T. Fini, S. Keller, S. P. Denbaars, J. S. Speck, U. K. Mishra, S. Nakamura, S. Yamaguchi, S. Kamiyama, H. Amano, I. Akasaki, J. Han, and T. Sota. Origin of localized excitons in In-containing three-dimensional bulk (Al,In,Ga)N alloy films probed by time-resolved photoluminescence and monoenergetic positron annihilation techniques. *Philosophical Magazine*, 87(13):2019–2039, 2007. doi: 10.1080/14786430701241689.

[97] Y.-H. Cho, G. H. Gainer, A. J. Fischer, J. J. Song, S. Keller, U. K. Mishra, and S. P. DenBaars. "S-shaped" temperature-dependent emission shift and carrier dynamics in InGaN/GaN multiple quantum wells. *Applied Physics Letters*, 73(10):1370–1372, 1998. doi: 10.1063/1.122164. URL http://aip.scitation.org/doi/10.1063/1.122164.

[98] S. Chichibu, K. Wada, and S. Nakamura. Spatially resolved cathodoluminescence spectra of InGaN quantum wells Spatially resolved cathodoluminescence spectra of InGaN quantum wells. *Applied Physics Letters*, 71(16):2346–2348, 1997. doi: 10.1063/1.120025. URL http://aip.scitation.org/doi/10.1063/1.120025.

[99] U. Jahn, J. Ristić, and E. Calleja. Cathodoluminescence spectroscopy and imaging of GaN/(Al,Ga)N nanocolumns containing quantum disks. *Applied Physics Letters*, 90(16):161117, 2007. doi: 10.1063/1.2724913. URL http://aip.scitation.org/doi/10.1063/1.2724913.

[100] R. S. Wagner and W. C. Ellis. Vapor-liquid-solid mechanism of single crystal growth. *Applied Physics Letters*, 4(5):89–90, 1964. doi: 10.1063/1.1753975. URL http://aip.scitation.org/doi/10.1063/1.1753975.

[101] J. Ristić, E. Calleja, S. Fernández-Garrido, L. Cerutti, A. Trampert, U. Jahn, and K. H. Ploog. On the mechanisms of spontaneous growth of III-nitride nanocolumns by plasma-assisted molecular beam epitaxy. *Journal of Crystal Growth*, 310(18):4035–4045, 2008. doi: 10.1016/j.jcrysgro.2008.05.057. URL http://linkinghub.elsevier.com/retrieve/pii/S0022024808004430.

[102] R. Songmuang, O. Landré, and B. Daudin. From nucleation to growth of catalyst-free GaN nanowires on thin AlN buffer layer. *Applied Physics Letters*, 91(25):251902, 2007. doi: 10.1063/1.2817941. URL http://aip.scitation.org/doi/10.1063/1.2817941.

[103] V. Consonni, M. Knelangen, L. Geelhaar, A. Trampert, and H. Riechert. Nucleation mechanisms of epitaxial GaN nanowires: Origin of their self-induced formation and initial radius. *Physical Review B*, 81:085310, 2010. doi: 10.1103/PhysRevB.81.085310. URL https://link.aps.org/doi/10.1103/PhysRevB.81.085310.

[104] F. Furtmayr, M. Vielemeyer, M. Stutzmann, J. Arbiol, S. Estradé, F. Peirò, J. R. Morante, and M. Eickhoff. Nucleation and growth of GaN nanorods on Si (111) surfaces by plasma-assisted molecular beam epitaxy - The influence of Si- and Mg-doping. *Journal of Applied Physics*, 104(3):034309, 2008. doi: 10.1063/1.2953087. URL http://aip.scitation.org/doi/10.1063/1.2953087.

[105] V. Consonni, M. Hanke, M. Knelangen, L. Geelhaar, A. Trampert, and H. Riechert. Nucleation mechanisms of self-induced GaN nanowires grown on an amorphous interlayer. *Physical Review B*, 83:035310, 2011. doi: 10.1103/PhysRevB.83.035310. URL https://link.aps.org/doi/10.1103/PhysRevB.83.035310.

[106] M. A. Sanchez-Garcia, E. Calleja, E. Monroy, F. J. Sanchez, F. Calle, E. Muñoz, and R. Beresford. The effect of the III/V ratio and substrate temperature on the morphology and properties of GaN- and AlN-layers grown by molecular beam epitaxy on Si(111). *Journal of Crystal Growth*, 183(1-2):23–30, 1998. doi: 10.1016/S0022-0248(97)00386-2. URL http://linkinghub.elsevier.com/retrieve/pii/S0022024897003862.

[107] K. A. Bertness, A. Roshko, L. M. Mansfield, T. E. Harvey, and N. A. Sanford. Mechanism for spontaneous growth of GaN nanowires with molecular beam epitaxy. *Journal of Crystal Growth*, 310(13):3154–3158, 2008. doi: 10.1016/j.jcrysgro.2008.03.033. URL http://linkinghub.elsevier.com/retrieve/pii/S0022024808002534.

[108] S. Fernández-Garrido, J. Grandal, E. Calleja, M. A. Sánchez-García, and D. López-Romero. A growth diagram for plasma-assisted molecular beam epitaxy of GaN nanocolumns on Si(111). *Journal of Applied Physics*, 106(12):126102, 2009. doi: 10.1063/1.3267151. URL http://aip.scitation.org/doi/10.1063/1.3267151.

[109] R. K. Debnath, R. Meijers, T. Richter, T. Stoica, R. Calarco, and H. Lüth. Mechanism of molecular beam epitaxy growth of GaN nanowires on Si(111). *Applied Physics Letters*, 90(12):123117, 2007. doi: 10.1063/1.2715119. URL http://aip.scitation.org/doi/10.1063/1.2715119.

[110] V. G. Dubrovskii, V. Consonni, L. Geelhaar, A. Trampert, and H. Riechert. Scaling growth kinetics of self-induced GaN nanowires. *Applied Physics Letters*, 100(15):153101, 2012. doi: 10.1063/1.3701591. URL http://dx.doi.org/10.1063/1.3701591.

[111] K. A. Grossklaus, A. Banerjee, S. Jahangir, P. Bhattacharya, and J. M. Millunchick. Misorientation defects in coalesced self-catalyzed GaN nanowires. *Journal of Crystal Growth*, 371:142–147, 2013. doi: 10.1016/j.jcrysgro.2013.02.019. URL http://dx.doi.org/10.1016/j.jcrysgro.2013.02.019.

[112] M. D. Brubaker, I. Levin, A. V. Davydov, D. M. Rourke, N. A. Sanford, V. M. Bright, and K. A. Bertness. Effect of AlN buffer layer properties on the morphology and polarity of GaN nanowires grown by molecular beam epitaxy. *Journal of Applied Physics*, 110(5):053506, 2011. doi: 10.1063/1.3633522. URL http://aip.scitation.org/doi/110.1063/1.3633522.

[113] S. Fernández-Garrido, X. Kong, T. Gotschke, R. Calarco, L. Geelhaar, A. Trampert, and O. Brandt. Spontaneous Nucleation and Growth of GaN Nanowires: The Fundamental Role of Crystal Polarity. *Nano Letters*, 12(12):6119–6125, 2012. doi: 10.1021/nl302664q. URL http://pubs.acs.org/doi/abs/10.1021/nl302664q.

[114] R. F. Egerton. *Electron Energy-Loss Spectroscopy in the Electron Microscope*. Springer, New York, 3rd edition, 2011. ISBN 978-1-4419-9582-7. doi: 10.1007/978-1-4419-9583-4_1.

[115] P. D. Nellist. *Scanning Transmission Electron Microscopy*. Springer US, New York, NY, 2011. ISBN 978-1-4419-7199-9. doi: 10.1007/978-1-4419-7200-2. URL http://link.springer.com/10.1007/978-1-4419-7200-2.

[116] K. A. Mkhoyan, P. E. Batson, J. Cha, W. J. Schaff, and J. Silcox. Direct Determination of Local Lattice Polarity in Crystals. *Science*, 312(5778):1354–1354, 2006. doi: 10.1126/science.1124511. URL http://www.sciencemag.org/cgi/doi/10.1126/science.1124511.

[117] S. D. Findlay, N. Shibata, H. Sawada, E. Okunishi, Y. Kondo, and Y. Ikuhara. Dynamics of annular bright field imaging in scanning transmission electron microscopy. *Ultramicroscopy*, 110(7):903–923, 2010. doi: 10.1016/j.ultramic.2010.04.004. URL http://www.sciencedirect.com/science/article/pii/S0304399110001129.

[118] S. D. Findlay, N. Shibata, H. Sawada, E. Okunishi, Y. Kondo, T. Yamamoto, and Y. Ikuhara. Robust atomic resolution imaging of light elements using scanning transmission electron microscopy. *Applied Physics Letters*, 95(19):191913, 2009. doi: 10.1063/1.3265946. URL http://aip.scitation.org/doi/10.1063/1.3265946.

[119] B. G. Yacobi and D. B. Holt. *Cathodoluminescence Microscopy of Inorganic Solids*. Springer US, Boston, MA, 1990. ISBN 978-0-306-43314-6. doi: 10.1007/978-1-4757-9595-0. URL http://link.springer.com/10.1007/978-1-4757-9595-0.

[120] M. Merano, S. Sonderegger, A. Crottini, S. Collin, P. Renucci, E. Pelucchi, A. Malko, M. H. Baier, E. Kapon, B. Deveaud, and J.-D. Ganière. Probing carrier dynamics in nanostructures by picosecond cathodoluminescence. *Nature*, 438(7067):479–482, 2005. doi: 10.1038/nature04298. URL http://www.nature.com/doifinder/10.1038/nature04298.

[121] S. K. Lim, M. Brewster, F. Qian, Y. Li, C. M. Lieber, and S. Gradečak. Direct correlation between structural and optical properties of III-V nitride nanowire heterostructures with nanoscale resolution. *Nano Letters*, 9(11):3940–3944, 2009. doi: 10.1021/nl9025743. URL http://pubs.acs.org/doi/abs/10.1021/nl9025743.

[122] L. F. Zagonel, S. Mazzucco, M. Tencé, K. March, R. Bernard, B. Laslier, G. Jacopin, M. Tchernycheva, L. Rigutti, F. H. Julien, R. Songmuang, and M. Kociak. Nanometer scale spectral imaging of quantum emitters in nanowires and its correlation to their atomically resolved structure. *Nano Letters*, 11(2):568–573, 2011. doi: 10.1021/nl103549t. URL http://pubs.acs.org/doi/abs/10.1021/nl103549t.

[123] G. Schmidt, M. Müller, P. Veit, F. Bertram, J. Christen, M. Glauser, J.-F. Carlin, G. Cosendey, R. Butté, and N. Grandjean. Nano-scale luminescence characterization of individual InGaN/GaN quantum wells stacked in a microcavity using scanning transmission electron microscope cathodoluminescence. *Applied Physics Letters*, 105(3):032101, 2014. doi: 10.1063/1.4890670. URL http://aip.scitation.org/doi/10.1063/1.4890670.

[124] J. T. Griffiths, S. Zhang, B. Rouet-Leduc, W. Y. Fu, A. Bao, D. Zhu, D. J. Wallis, A. Howkins, I. Boyd, D. Stowe, M. J. Kappers, C. J. Humphreys, and R. A. Oliver. Nanocathodoluminescence Reveals Mitigation of the Stark Shift in InGaN Quantum Wells by Si Doping. *Nano Letters*, 15(11):7639–7643, 2015. doi: 10.1021/acs.nanolett.5b03531. URL http://pubs.acs.org/doi/10.1021/acs.nanolett.5b03531.

[125] D. Volm, K. Oettinger, T. Streibl, D. Kovalev, M. Ben-Chorin, J. Diener, B. K. Meyer, J. Majewski, L. Eckey, A. Hoffmann, H. Amano, I. Akasaki, K. Hiramatsu, and T. Detchprohm. Exciton fine structure in undoped gan epitaxial films. *Phys. Rev. B*, 53:16543–16550, 1996. doi: 10.1103/PhysRevB.53.16543. URL https://link.aps.org/doi/10.1103/PhysRevB.53.16543.

[126] Z. Mahfoud, A. T. Dijksman, C. Javaux, P. Bassoul, A.-L. Baudrion, J. Plain, B. Dubertret, and M. Kociak. Cathodoluminescence in a Scanning Transmission Electron Microscope: A Nanometer-Scale Counterpart of Photoluminescence for the Study of II–VI Quantum Dots. *The Journal of Physical Chemistry Letters*, 4(23):4090–4094, 2013. doi: 10.1021/jz402233x. URL http://pubs.acs.org/doi/abs/10.1021/jz402233x.

[127] S. Meuret, L. H. G. Tizei, T. Auzelle, R. Songmuang, B. Daudin, B. Gayral, and M. Kociak. Lifetime Measurements Well below the Optical Diffraction Limit. *ACS Photonics*, 3(7):1157–1163, 2016. doi: 10.1021/acsphotonics.6b00212. URL http://pubs.acs.org/doi/abs/10.1021/acsphotonics.6b00212.

[128] M. Leroux, N. Grandjean, B. Beaumont, G. Nataf, F. Semond, J. Massies, and P. Gibart. Temperature quenching of photoluminescence intensities in undoped and doped GaN. *Journal of Applied Physics*, 86(7):3721–3728, 1999. doi: 10.1063/1.371242. URL http://aip.scitation.org/doi/10.1063/1.371242.

[129] B. G. Yacobi and D. B. Holt. Cathodoluminescence scanning electron microscopy of semiconductors. *Journal of Applied Physics*, 59(4):R1–R24, 1986. doi: 10.1063/1.336491. URL http://aip.scitation.org/doi/10.1063/1.336491.

[130] A. Gustafsson. Nanowire-based structures for infrared to ultraviolet emitters studied by cathodoluminescence. *Journal of Microscopy*, 262(2):134–141, 2016. doi: 10.1111/jmi.12296. URL http://doi.wiley.com/10.1111/jmi.12296.

[131] D. Drouin, A. R. Couture, D. Joly, X. Tastet, V. Aimez, and R. Gauvin. CASINO V2.42—A Fast and Easy-to-use Modeling Tool for Scanning Electron Microscopy and Microanalysis Users. *Scanning*, 29(3):92–101, 2007. doi: 10.1002/sca.20000. URL http://onlinelibrary.wiley.com/doi/10.1002/sca.20000/abstract.

[132] K. Kanaya and S. Okayama. Penetration and energy-loss theory of electrons in solid targets. *Journal of Physics D: Applied Physics*, 5(1):43–58, 1972. doi: 10.1088/0022-3727/5/1/308. URL http://stacks.iop.org/0022-3727/5/i=1/a=308.

[133] D. B. Wittry and D. F. Kyser. Cathodoluminescence at p-n Junctions in GaAs. *Journal of Applied Physics*, 36(4):1387–1389, 1965. doi: 10.1063/1.1714315. URL http://aip.scitation.org/doi/10.1063/1.1714315.

[134] S. J. Rosner, G. Girolami, H. Marchand, P. T. Fini, J. P. Ibbetson, L. Zhao, S. Keller, U. K. Mishra, S. P. DenBaars, and J. S. Speck. Cathodoluminescence mapping of epitaxial lateral overgrowth in gallium nitride. *Applied Physics Letters*, 74(14):2035–2037, 1999. doi: 10.1063/1.123748. URL http://aip.scitation.org/doi/10.1063/1.123748.

[135] J. Barjon, J. Brault, B. Daudin, D. Jalabert, and B. Sieber. Cathodoluminescence study of carrier diffusion in AlGaN. *Journal of Applied Physics*, 94(4):2755–2757, 2003. doi: 10.1063/1.1593797. URL http://aip.scitation.org/doi/10.1063/1.1593797.

[136] A. Gustafsson, J. Bolinsson, N. Sköld, and L. Samuelson. Determination of diffusion lengths in nanowires using cathodoluminescence. *Applied Physics Letters*, 97(7):072114, 2010. doi: 10.1063/1.3473829. URL http://aip.scitation.org/doi/10.1063/1.3473829.

[137] S. Strite and H. Morkoç. GaN, AlN, and InN: A review. *Journal of Vacuum Science & Technology B: Microelectronics and Nanometer Structures*, 10(4):1237–1266, 1992. doi: 10.1116/1.585897. URL http://aip.scitation.org/doi/10.1116/1.585897.

[138] I-hsiu Ho and G. B. Stringfellow. Solid phase immiscibility in GaInN. *Applied Physics Letters*, 69(18):2701–2703, 1996. doi: 10.1063/1.117683. URL http://aip.scitation.org/doi/10.1063/1.117683.

[139] Y. J. Hong, C.-H. Lee, A. Yoon, M. Kim, H.-K. Seong, H. J. Chung, C. Sone, Y. J. Park, and G.-C. Yi. Visible-color-tunable light-emitting diodes. *Advanced Materials*, 23(29):3284–3288, 2011. doi: 10.1002/adma.201100806. URL http://onlinelibrary.wiley.com/doi/10.1002/adma.201100806/abstract.

[140] J. Lähnemann, O. Brandt, C. Pfüller, T. Flissikowski, U. Jahn, E. Luna, M. Hanke, M. Knelangen, A. Trampert, and H. T. Grahn. Coexistence of quantum-confined Stark effect and localized states in an (In,Ga)N/GaN nanowire heterostructure. *Physical Review B*, 84(15):155303, 2011. doi: 10.1103/PhysRevB.84.155303. URL http://link.aps.org/doi/10.1103/PhysRevB.84.155303.

[141] G. Tourbot, C. Bougerol, F. Glas, L. F. Zagonel, Z. Mahfoud, S. Meuret, P. Gilet, M. Kociak, B. Gayral, and B. Daudin. Growth mechanism and properties of InGaN insertions in GaN nanowires. *Nanotechnology*, 23(13):135703, 2012. doi: 10.1088/0957-4484/23/13/135703. URL http://iopscience.iop.org/0957-4484/23/13/135703/.

[142] M. Wölz, J. Lähnemann, O. Brandt, V. M. Kaganer, M. Ramsteiner, C. Pfüller, C. Hauswald, C .N. Huang, L. Geelhaar, and H. Riechert. Correlation between In content and emission wavelength of $In_xGa_{1-x}N$/GaN nanowire heterostructures. *Nanotechnology*, 23(45):455203, 2012. doi: 10.1088/0957-4484/23/45/455203. URL http://iopscience.iop.org/0957-4484/23/45/455203/.

[143] Th. Kehagias, G. P. Dimitrakopulos, P. Becker, J. Kioseoglou, F. Furtmayr, T. Koukoula, I. Häusler, A. Chernikov, S. Chatterjee, Th. Karakostas, H.-M. Solowan, U. T. Schwarz, M. Eickhoff, and Ph. Komninou. Nanostructure and strain in InGaN/GaN superlattices grown in GaN nanowires. *Nanotechnology*, 24(43):435702, 2013. doi: 10.1088/0957-4484/24/43/435702. URL http://iopscience.iop.org/0957-4484/24/43/435702/.

[144] A. P. Vajpeyi, A. O. Ajagunna, K. Tsagaraki, M. Androulidaki, and A. Georgakilas. InGaN nanopillars grown on silicon substrate using plasma assisted molecular beam epitaxy. *Nanotechnology*, 20(32):325605, 2009. doi: 10.1088/0957-4484/20/32/325605. URL http://iopscience.iop.org/0957-4484/20/32/325605/.

[145] T. Böttcher, S. Einfeldt, V. Kirchner, S. Figge, H. Heinke, D. Hommel, H. Selke, and P. L. Ryder. Incorporation of indium during molecular beam epitaxy of InGaN. *Applied Physics Letters*, 73(22):3232–3234, 1998. doi: 10.1063/1.122728. URL http://aip.scitation.org/doi/10.1063/1.122728.

[146] J. Palisaitis, C.-L. Hsiao, M. Junaid, J. Birch, L. Hultman, and P. O. Å. Persson. Effect of strain on low-loss electron energy loss spectra of group-III nitrides. *Physical Review B*, 84(24):245301, 2011. doi: 10.1103/PhysRevB.84.245301. URL http://link.aps.org/doi/10.1103/PhysRevB.84.245301.

[147] A. Rosenauer, T. Mehrtens, K. Müller, K. Gries, M. Schowalter, P. Venkata Satyam, S. Bley, C. Tessarek, D. Hommel, K. Sebald, M. Seyfried, J. Gutowski, A. Avramescu, K. Engl, and S. Lutgen. Composition mapping in InGaN by scanning transmission electron microscopy. *Ultramicroscopy*, 111(8):1316–1327, 2011. doi: 10.1016/j.ultramic.2011.04.009. URL http://www.sciencedirect.com/science/article/pii/S0304399111001598.

[148] R. D. Leapman and C. R. Swyt. Separation of overlapping core edges in electron energy loss spectra by multiple-least-squares fitting. *Ultramicroscopy*, 26(4):393–403, 1988. doi: 10.1016/0304-3991(88)90239-2. URL http://linkinghub.elsevier.com/retrieve/pii/0304399188902392.

[149] P. Wang, A. L. Bleloch, M. Falke, P. J. Goodhew, J. Ng, and M. Missous. Direct measurement of composition of buried quantum dots using aberration-corrected scanning transmission electron microscopy. *Applied Physics Letters*, 89(7):072111, 2006. doi: 10.1063/1.2335361. URL http://aip.scitation.org/doi/10.1063/1.2335361.

[150] D. Zubia, S. D. Hersee, and T. Khraishi. Strain partitioning in coherent compliant heterostructures. *Applied Physics Letters*, 80(5):740–742, 2002. doi: 10.1063/1.1445803. URL http://aip.scitation.org/doi/10.1063/1.1445803.

[151] V. Potin, E. Hahn, A. Rosenauer, D. Gerthsen, B. Kuhn, F. Scholz, A. Dussaigne, B. Damilano, and N. Grandjean. Comparison of the In distribution in InGaN/GaN quantum well structures grown by molecular beam epitaxy and metalorganic vapor phase epitaxy. *Journal of Crystal Growth*, 262(1-4):145–150, 2004. doi: 10.1016/j.jcrysgro.2003.10.082. URL http://linkinghub.elsevier.com/retrieve/pii/S0022024803019742.

[152] W. Jiao, W. Kong, J. Li, K. Collar, T.-H. Kim, and A. S. Brown. The relationship between depth-resolved composition and strain relaxation in InAlN and InGaN films grown by molecular beam epitaxy. *Applied Physics Letters*, 103(16):162102, 2013. doi: 10.1063/1.4825143. URL http://aip.scitation.org/doi/10.1063/1.4825143.

[153] C. H. Wang, S. P. Chang, W. T. Chang, J. C. Li, Y. S. Lu, Z. Y. Li, H. C. Yang, H. C. Kuo, T. C. Lu, and S. C. Wang. Efficiency droop alleviation in InGaN/GaN light-emitting diodes by graded-thickness multiple quantum wells. *Applied Physics Letters*, 97(18):181101, 2010. doi: 10.1063/1.3507891. URL http://aip.scitation.org/doi/10.1063/1.3507891.

[154] Z. G. Ju, W. Liu, Z.-H. Zhang, S. T. Tan, Y. Ji, Z. B. Kyaw, X. L. Zhang, S. P. Lu, Y. P. Zhang, B. B. Zhu, N. Hasanov, X. W. Sun, and H. V. Demir. Improved hole distribution in InGaN/GaN light-emitting diodes with graded thickness quantum barriers. *Applied Physics Letters*, 102(24):243504, 2013. doi: 10.1063/1.4811698. URL http://aip.scitation.org/doi/10.1063/1.4811698.

[155] O. Landré, D. Camacho, C. Bougerol, Y. M. Niquet, V. Favre-Nicolin, G. Renaud, H. Renevier, and B. Daudin. Elastic strain relaxation in GaN/AlN nanowire superlattice. *Physical Review B*, 81(15):153306, 2010. doi: 10.1103/PhysRevB.81.153306. URL http://link.aps.org/doi/10.1103/PhysRevB.81.153306.

[156] M. Wölz, M. Ramsteiner, V. M. Kaganer, O. Brandt, L. Geelhaar, and H. Riechert. Strain engineering of nanowire multi-quantum well demonstrated by Raman spectroscopy. *Nano Letters*, 13(9):4053–4059, 2013. doi: 10.1021/nl401306q. URL http://pubs.acs.org/doi/abs/10.1021/nl401306q.

[157] O. Marquardt, C. Hauswald, M. Wölz, L. Geelhaar, and O. Brandt. Luminous Efficiency of Axial $In_xGa_{1-x}N$/GaN Nanowire Heterostructures: Interplay of Polarization and Surface Potentials. *Nano Letters*, 13:3298–3304, 2013. doi: 10.1021/nl4015183. URL http://pubs.acs.org/doi/abs/10.1021/nl4015183.

[158] L. K. Teles, L. G. Ferreira, J. R. Leite, L. M. R. Scolfaro, A. Kharchenko, O. Husberg, D. J. As, D. Schikora, and K. Lischka. Strain-induced ordering in $In_xGa_{1-x}N$ alloys. *Applied Physics Letters*, 82(24):4274–4276, 2003. doi: 10.1063/1.1583854. URL http://aip.scitation.org/doi/10.1063/1.1583854.

[159] O. Ambacher, J Majewski, C Miskys, A. Link, M. Hermann, M. Eickhoff, M. Stutzmann, F. Bernardini, V. Fiorentini, V Tilak, B Schaff, and L. F. Eastman. Pyroelectric properties of Al(In)GaN/GaN hetero- and quantum well structures. *Journal of Physics: Condensed Matter*, 14(13):3399–3434, 2002. doi: 10.1088/0953-8984/14/13/302. URL iopscience.iop.org/article/10.1088/0953-8984/14/13/302/.

[160] S. Nakamura and G. Fasol. *The Blue Laser Diode: The Complete Story*. Springer, Berlin, Heidelberg, 1997. ISBN 978-3-662-04156-7.

[161] D. Doppalapudi, S. N. Basu, K. F. Ludwig, and T. D. Moustakas. Phase separation and ordering in InGaN alloys grown by molecular beam epitaxy. *Journal of Applied Physics*, 84 (3):1389–1395, 1998. ISSN 00218979. doi: 10.1063/1.368251. URL http://link.aip.org/link/JAPIAU/v84/i3/p1389/s1&Agg=doi.

[162] L. K. Teles, L. G. Ferreira, L. M. R. Scolfaro, and J. R. Leite. Theoretical study of strain-induced ordering in cubic $In_xGa_{1-x}N$ epitaxial layers. *Physical Review B*, 69:245317, 2004. ISSN 01631829. doi: 10.1103/PhysRevB.69.245317. URL http://journals.aps.org/prb/abstract/10.1103/PhysRevB.69.245317.

[163] M. Gao, Y. Lin, S. T. Bradley, S. A. Ringel, J. Hwang, W. J. Schaff, and L. J. Brillson. Spontaneous compositional superlattice and band-gap reduction in Si-doped $Al_xGa_{1-x}N$ epilayers. *Applied Physics Letters*, 87(19):191906, 2005. ISSN 00036951. doi: 10.1063/1.2126127. URL http://scitation.aip.org/content/aip/journal/apl/87/19/10.1063/1.2126127.

[164] G. B. Stringfellow and G. S. Chen. Atomic ordering in III/V semiconductor alloys. *Journal of Vacuum Science & Technology B: Microelectronics and Nanometer Structures*, 9:2182–2188, 1991. ISSN 0734211X. doi: 10.1116/1.585761. URL http://scitation.aip.org/content/avs/journal/jvstb/9/4/10.1116/1.585761.

[165] M. Albrecht, L. Lymperakis, J. Neugebauer, J. Northrup, L. Kirste, M. Leroux, I. Grzegory, S. Porowski, and H. Strunk. Chemically ordered $Al_xGa_{1-x}N$ alloys: Spontaneous formation of natural quantum wells. *Physical Review B*, 71(3):035314, January 2005. ISSN 1098-0121. doi: 10.1103/PhysRevB.71.035314. URL http://link.aps.org/doi/10.1103/PhysRevB.71.035314.

[166] E. Iliopoulos, K. F. Ludwig, and T. D. Moustakas. Complex ordering in ternary wurtzite nitride alloys. *Journal of Physics and Chemistry of Solids*, 64(9-10):1525–1532, September 2003. ISSN 00223697. doi: 10.1016/S0022-3697(03)00094-5. URL http://linkinghub.elsevier.com/retrieve/pii/S0022369703000945.

[167] H. Chen, R. M. Feenstra, J. E. Northrup, T. Zywietz, and J. Neugebauer. Spontaneous formation of indium-rich nanostructures on InGaN(0001) surfaces. *Physical Review Letters*, 85(9):1902–1905, August 2000. ISSN 1079-7114. URL http://journals.aps.org/prl/abstract/10.1103/PhysRevLett.85.1902.

[168] H. K. Cho, J. Y. Lee, K. S. Kim, and G. M. Yang. Superlattice-like stacking fault and phase separation of $In_xGa_{1-x}N$ grown on sapphire substrate by metalorganic chemical vapor deposition. *Applied Physics Letters*, 77(2):247–249, 2000. ISSN 00036951. doi: 10.1063/1.126939. URL http://link.aip.org/link/APPLAB/v77/i2/p247/s1&Agg=doi.

[169] Z. Liliental-Weber, D. N. Zakharov, K. M. Yu, J. W. Ager, W. Walukiewicz, E. E. Haller, H. Lu, and W. J. Schaff. Compositional modulation in $In_xGa_{1-x}N$: TEM and X-ray studies. *Journal of Electron Microscopy*, 54(3):243–250, June 2005. ISSN 0022-0744. doi: 10.1093/jmicro/dfi033. URL http://jmicro.oxfordjournals.org/cgi/pmidlookup?view=long&pmid=16123056.

[170] J. E. Northrup, L. T. Romano, and J. Neugebauer. Surface energetics, pit formation, and chemical ordering in InGaN alloys. *Applied Physics Letters*, 74(16):2319, 1999. ISSN 00036951. doi: 10.1063/1.123837. URL http://link.aip.org/link/APPLAB/v74/i16/p2319/s1&Agg=doi.

[171] I. Gorczyca, K. Skrobas, T. Suski, N. E. Christensen, and A. Svane. Band gaps in InN/GaN superlattices: Nonpolar and polar growth directions. *Journal of Applied Physics*, 114(22):223102, 2013. ISSN 00218979. doi: 10.1063/1.4843015. URL http://scitation.aip.org/content/aip/journal/jap/114/22/10.1063/1.4843015.

[172] S. V. Dudiy and A. Zunger. Optical consequences of long-range order in wurtzite $Al_xGa_{1-x}N$ alloys. *Physical Review B*, 68(4):041302, July 2003. ISSN 0163-1829. doi: 10.1103/PhysRevB.68.041302. URL http://link.aps.org/doi/10.1103/PhysRevB.68.041302.

[173] A. Al-Yacoub and L. Bellaiche. Piezoelectricity of ordered (Ga0.5In0.5)N alloys. *Applied Physics Letters*, 79(14):2166–2168, 2001. ISSN 00036951. doi: 10.1063/1.1406983. URL http://scitation.aip.org/content/aip/journal/apl/79/14/10.1063/1.1406983.

[174] S. Lee, C. Freysoldt, and J. Neugebauer. Ordering phenomena and formation of nanostructures in $In_xGa_{1-x}N$ layers coherently grown on GaN(0001). *Physical Review B*, 90(24):245301, 2014. doi: 10.1103/PhysRevB.90.245301. URL http://link.aps.org/doi/10.1103/PhysRevB.90.245301.

[175] Y. Cui, S. Lee, C. Freysoldt, and J. Neugebauer. Role of biaxial strain and microscopic ordering for structural and electronic properties of $In_xGa_{1-x}N$. *Physical Review B*, 92(8):085204, aug 2015. ISSN 1098-0121. doi: 10.1103/PhysRevB.92.085204. URL http://link.aps.org/doi/10.1103/PhysRevB.92.085204.

[176] H. P. T. Nguyen, S. Zhang, A. T. Connie, M. G. Kibria, Q. Wang, I. Shih, and Z. Mi. Breaking the carrier injection bottleneck of phosphor-free nanowire white light-emitting diodes. *Nano Letters*, 13(11):5437–5442, November 2013. ISSN 1530-6992. doi: 10.1021/nl4030165. URL http://pubs.acs.org/doi/abs/10.1021/nl4030165.

[177] S. Y. Woo, N. Gauquelin, H. P. T. Nguyen, Z. Mi, and G. A. Botton. Interplay of strain and indium incorporation in InGaN/GaN dot-in-a-wire nanostructures by scanning transmission electron microscopy. *Nanotechnology*, 26(34):344002, 2015. ISSN 0957-4484. doi: 10.1088/0957-4484/26/34/344002. URL http://iopscience.iop.org/0957-4484/26/34/344002/.

[178] J. C. Woicik, K. F. Ludwig, and T. D. Moustakas. Composition dependent bilayer atomic ordering in $Al_xGa_{1-x}N$ films examined by polarization-dependent extended X-ray absorption fine structure. *Applied Physics Letters*, 100(16):162105, 2012. ISSN 00036951. doi: 10.1063/1.4704678. URL http://link.aip.org/link/APPLAB/v100/i16/p162105/s1&Agg=doi.

[179] E. Okunishi, I. Ishikawa, H. Sawada, F. Hosokawa, M. Hori, and Y. Kondo. Visualization of Light Elements at Ultrahigh Resolution by STEM Annular Bright Field Microscopy. *Microscopy and Microanalysis*, 15(Suppl 2):164, 2009. ISSN 1431-9276. doi: 10.1017/S1431927609093891.

[180] M. Rao, N. Newman, and S. Mahajan. The formation of ordered structures in InGaN layers. *Scripta Materialia*, 56(1):33–36, January 2007. ISSN 13596462. doi: 10.1016/j.scriptamat.2006.08.068. URL http://linkinghub.elsevier.com/retrieve/pii/S1359646206006695.

[181] J. E. Northrup and J. Neugebauer. Indium-induced changes in GaN(0001) surface morphology. *Physical Review B*, 60(12):R8473–R8476, September 1999. ISSN 0163-1829. doi: 10.1103/PhysRevB.60.R8473. URL http://link.aps.org/doi/10.1103/PhysRevB.60.R8473.

[182] Y. D. Zhuang, J. Bruckbauer, P. A. Shields, P. R. Edwards, R. W. Martin, and D. W. E. Allsopp. Influence of stress on optical transitions in GaN nanorods containing a single InGaN/GaN quantum disk. *Journal of Applied Physics*, 116(17):174305, 2014. doi: 10.1063/1.4898685. URL http://aip.scitation.org/doi/10.1063/1.4898685.

[183] X. Zhou, M.Y. Lu, Y.-J. Lu, E. Jones, S. Gwo, and S. Gradečak. Nanoscale Optical Properties of Indium Gallium Nitride/Gallium Nitride Nanodisk-in-Rod Heterostructures. *ACS Nano*, 9(3):2868–2875, 2015. doi: 10.1021/nn506867b. URL http://pubs.acs.org/doi/abs/10.1021/nn506867b.

[184] H. P. T. Nguyen, M. Djavid, S. Y. Woo, X. Liu, A. T. Connie, S. Sadaf, Q. Wang, G. A. Botton, I. Shih, and Z. Mi. Engineering the Carrier Dynamics of InGaN Nanowire White Light-Emitting Diodes by Distributed p-AlGaN Electron Blocking Layers. *Scientific Reports*, 5:7744, 2015. doi: 10.1038/srep07744. URL http://www.nature.com/doifinder/10.1038/srep07744.

[185] K. H. Baloch, A. C. Johnston-Peck, K. Kisslinger, E. A. Stach, and S. Gradečak. Revisiting the "In-clustering" question in InGaN through the use of aberration-corrected electron microscopy below the knock-on threshold. *Applied Physics Letters*, 102(19):191910, 2013. doi: 10.1063/1.4807122. URL http://aip.scitation.org/doi/10.1063/1.4807122.

[186] J. T. Griffiths, S. Zhang, J. Lhuillier, D. Zhu, W. Y. Fu, A. Howkins, I. Boyd, D. Stowe, D. J. Wallis, C. J. Humphreys, and R. A. Oliver. Nano-cathodoluminescence reveals the effect of electron damage on the optical properties of nitride optoelectronics and the damage threshold. *Journal of Applied Physics*, 120(16):165704, 2016. doi: 10.1063/1.4965989. URL http://aip.scitation.org/doi/10.1063/1.4965989.

[187] M. Boroditsky, I. Gontijo, M. Jackson, R. Vrijen, E. Yablonovitch, T. Krauss, Chuan-Cheng Cheng, A. Scherer, R. Bhat, and M. Krames. Surface recombination measurements on III–V candidate materials for nanostructure light-emitting diodes. *Journal of Applied Physics*, 87 (7):3497–3504, 2000. doi: 10.1063/1.372372. URL http://dx.doi.org/10.1063/1.372372.

[188] N. A. Sanford, P. T. Blanchard, K. A. Bertness, L. Mansfield, J. B. Schlager, A. W. Sanders, A. Roshko, B. B. Burton, and S. M. George. Steady-state and transient photoconductivity in c-axis GaN nanowires grown by nitrogen-plasma-assisted molecular beam epitaxy. *Journal of Applied Physics*, 107(3):034318, 2010. doi: 10.1063/1.3275888. URL http://aip.scitation.org/doi/10.1063/1.3275888.

[189] J. Lähnemann, C. Hauswald, M. Wölz, U. Jahn, M. Hanke, L. Geelhaar, and O. Brandt. Localization and defects in axial (In,Ga)N/GaN nanowire heterostructures investigated by spatially-resolved luminescence spectroscopy. *Journal of Physics D: Applied Physics*, 47(39): 394010, 2014. doi: 10.1088/0022-3727/47/39/394010. URL http://iopscience.iop.org/0022-3727/47/39/394010/.

[190] M. Kociak, O. Stéphan, A. Gloter, L. F. Zagonel, L. H. G. Tizei, M. Tencé, K. March, J. D. Blazit, Z. Mahfoud, A. Losquin, S. Meuret, and C. Colliex. Seeing and measuring in colours: Electron microscopy and spectroscopies applied to nano-optics. *Comptes Rendus Physique*, 15(2-3):158–175, 2014. doi: 10.1016/j.crhy.2013.10.003. URL http://dx.doi.org/10.1016/j.crhy.2013.10.003.

[191] H. Li, P. Li, J. Kang, Z. Li, Y. Zhang, Z. Li, J. Li, X. Yi, J. Li, and G. Wang. Quantum Efficiency Enhancement of 530 nm InGaN Green Light-Emitting Diodes with Shallow Quantum Well. *Applied Physics Express*, 6(5):052102, 2013. doi: 10.7567/APEX.6.052102. URL http://stacks.iop.org/1882-0786/6/i=5/a=052102?key=crossref.63a2a28b601c5bc11465e160d1c631f0.

[192] W.-C. Lai, C.-H. Yen, and S.-J. Chang. GaN-Based Green-Light-Emitting Diodes with InN/GaN Growth-Switched InGaN Wells. *Applied Physics Express*, 6(10):102101, 2013. ISSN 1882-0778. doi: 10.7567/APEX.6.102101. URL http://stacks.iop.org/1882-0786/6/i=10/a=102101?key=crossref.f03ca9a2fc297c77b75cdff255465ad6.

[193] G. L. Martinez, M. R. Curiel, B. J. Skromme, and R. J. Molnar. Surface recombination and sulfide passivation of gan. *Journal of Electronic Materials*, 29(3):325–331, 2000. doi: 10.1007/s11664-000-0072-x. URL http://link.springer.com/article/10.1007/s11664-000-0072-x.

[194] M. Zafar Iqbal, M. A. Reshchikov, L. He, and H. Morkoç. Effect of ambient on photoluminescence from gan grown by molecular-beam epitaxy. *Journal of Electronic Materials*, 32(5):346–349, 2003. doi: 10.1007/s11664-003-0156-5. URL http://link.springer.com/article/10.1007/s11664-003-0156-5.

[195] G. Jacopin, L. Rigutti, L. Largeau, F. Fortuna, F. Furtmayr, F. H. Julien, M. Eickhoff, and M. Tchernycheva. Optical properties of wurtzite/zinc-blende heterostructures in GaN nanowires. *Journal of Applied Physics*, 110(6):064313, 2011. doi: 10.1063/1.3638698. URL http://aip.scitation.org/doi/10.1063/1.3638698.

[196] M. Strassburg, A. Hoffmann, J. Holst, J. Christen, T. Riemann, F. Bertram, and P. Fischer. The origin of the PL photoluminescence Stokes shift in ternary group-III nitrides: field effects and localization. *Physica Status Solidi (C)*, 1845(6):1835–1845, 2003. doi: 10.1002/pssc.200303137. URL http://doi.wiley.com/10.1002/pssc.200303137.

[197] A.-L. Bavencove, G. Tourbot, J. Garcia, Y. Désières, P. Gilet, F. Levy, B. André, B. Gayral, B. Daudin, and L. S. Dang. Submicrometre resolved optical characterization of green nanowire-based light emitting diodes. *Nanotechnology*, 22(34):345705, 2011. doi: 10.1088/0957-4484/22/34/345705. URL http://iopscience.iop.org/article/10.1088/0957-4484/22/34/345705/.

[198] L. F. Zagonel, L. H. G. Tizei, G. Z. Vitiello, G. Jacopin, L. Rigutti, M. Tchernycheva, F. H. Julien, R. Songmuang, T. Ostasevicius, F. de la Peña, C. Ducati, P. A. Midgley, and M. Kociak. Nanometer-scale monitoring of quantum-confined Stark effect and emission efficiency droop in multiple GaN/AlN quantum disks in nanowires. *Physical Review B*, 93 (20):205410, 2016. doi: 10.1103/PhysRevB.93.205410. URL http://link.aps.org/doi/10.1103/PhysRevB.93.205410.

[199] L. F. Zagonel, L. Rigutti, M. Tchernycheva, G. Jacopin, R. Songmuang, and M. Kociak. Visualizing highly localized luminescence in GaN/AlN heterostructures in nanowires. *Nanotechnology*, 23(45):455205, 2012. doi: 10.1088/0957-4484/23/45/455205. URL http://iopscience.iop.org/0957-4484/23/45/455205/.

[200] F. Qian, M. Brewster, S. K. Lim, Y. Ling, C. Greene, O. Laboutin, J. W. Johnson, S. Gradečak, Y. Cao, and Y. Li. Controlled synthesis of AlN/GaN multiple quantum well nanowire structures and their optical properties. *Nano Letters*, 12(6):3344–3350, 2012. doi: 10.1021/nl301690e. URL http://pubs.acs.org/doi/abs/10.1021/nl301690e.

[201] L. H. G. Tizei, S. Meuret, K. March, K. Hestroffer, T. Auzelle, B. Daudin, and M. Kociak. A polarity-driven nanometric luminescence asymmetry in AlN/GaN heterostructures. *Applied Physics Letters*, 105:143106, 2014. doi: 10.1063/1.4897408. URL http://aip.scitation.org/doi/10.1063/1.4897408.

[202] X. Zhou, M.-Y. Lu, Y.-J. Lu, S. Gwo, and S. Gradečak. Correlation of doping, structure, and carrier dynamics in a single GaN nanorod. *Applied Physics Letters*, 102(25):253104, 2013. doi: 10.1063/1.4812241. URL http://aip.scitation.org/doi/10.1063/1.4812241.

[203] J.-S. Hwang, F. Donatini, J. Pernot, R. Thierry, P. Ferret, and L. S. Dang. Carrier depletion and exciton diffusion in a single ZnO nanowire. *Nanotechnology*, 22(47):475704, 2011. doi: 10.1088/0957-4484/22/47/475704. URL http://iopscience.iop.org/article/10.1088/0957-4484/22/47/475704/.

[204] M. Albrecht, H. P. Strunk, J. L. Weyher, I. Grzegory, S. Porowski, and T. Wosinski. Carrier recombination at single dislocations in GaN measured by cathodoluminescence in a transmission electron microscope. *Journal of Applied Physics*, 92(4):2000–2005, 2002. doi: 10.1063/1.1490618. URL http://aip.scitation.org/doi/10.1063/1.1490618.

[205] S. Jahangir, M. Mandl, M. Strassburg, and P. Bhattacharya. Molecular beam epitaxial growth and optical properties of red-emitting (lambda = 650 nm) InGaN/GaN disks-in-nanowires on silicon. *Applied Physics Letters*, 102(7):071101, 2013. doi: 10.1063/1.4793300.

[206] A. Hangleiter. Optical properties of nitride heterostructures. *Physica Status Solidi (C)*, 1834 (6):1816–1834, 2003. doi: 10.1002/pssc.200303127. URL http://doi.wiley.com/10.1002/pssc.200303127.

[207] R. Songmuang, T. Ben, B. Daudin, D. González, and E. Monroy. Identification of III–N nanowire growth kinetics via a marker technique. *Nanotechnology*, 21(29):295605, 2010. doi: 10.1088/0957-4484/21/29/295605. URL http://iopscience.iop.org/article/10.1088/0957-4484/21/29/295605/.

[208] E. Galopin, L. Largeau, G. Patriarche, L. Travers, F. Glas, and J.-C. Harmand. Morphology of self-catalyzed GaN nanowires and chronology of their formation by molecular beam epitaxy. *Nanotechnology*, 22(24):245606, 2011. doi: 10.1088/0957-4484/22/24/245606. URL http://iopscience.iop.org/article/10.1088/0957-4484/22/24/245606/.

[209] S. Schwaiger, S. Metzner, T. Wunderer, I. Argut, J. Thalmair, F. Lipski, M. Wieneke, J. Bläsing, F. Bertram, J. Zweck, A. Krost, J. Christen, and F. Scholz. Growth and coalescence behavior of semipolar (11-22) GaN on pre-structured r-plane sapphire substrates. *Physica Status Solidi (B)*, 248(3):588–593, 2011. doi: 10.1002/pssb.201046336. URL http://doi.wiley.com/10.1002/pssb.201046336.

[210] M. Hocker, I. Tischer, B. Neuschl, K. Thonke, M. Caliebe, M. Klein, and F. Scholz. Stacking fault emission in GaN: Influence of n-type doping. *Journal of Applied Physics*, 119(18):185703, 2016. doi: 10.1063/1.4949512. URL http://aip.scitation.org/doi/10.1063/1.4949512.

[211] A. Bhattacharyya, T. D. Moustakas, L. Zhou, D. J. Smith, and W. Hug. Deep ultraviolet emitting AlGaN quantum wells with high internal quantum efficiency. *Applied Physics Letters*, 94(18):181907, 2009. doi: 10.1063/1.3130755. URL http://aip.scitation.org/doi/10.1063/1.3130755.

[212] Y. Taniyasu, M. Kasu, and T. Makimoto. An aluminium nitride light-emitting diode with a wavelength of 210 nanometres. *Nature*, 441(7091):325–328, 2006. doi: 10.1038/nature04760. URL http://www.nature.com/doifinder/10.1038/nature04760.

[213] Y. Taniyasu and M. Kasu. Surface 210 nm light emission from an AlN p-n junction light-emitting diode enhanced by A-plane growth orientation. *Applied Physics Letters*, 96(22): 221110, 2010. doi: 10.1063/1.3446834. URL http://aip.scitation.org/doi/10.1063/1.3446834.

[214] H. Yoshida, Y. Yamashita, M. Kuwabara, and H. Kan. Demonstration of an ultraviolet 336 nm AlGaN multiple-quantum-well laser diode. *Applied Physics Letters*, 93(24):241106, 2008. doi: 10.1063/1.3050539. URL http://aip.scitation.org/doi/10.1063/1.3050539.

[215] T. Takano, Y. Narita, A. Horiuchi, and H. Kawanishi. Room-temperature deep-ultraviolet lasing at 241.5 nm of AlGaN multiple-quantum-well laser. *Applied Physics Letters*, 84(18): 3567–3569, 2004. doi: 10.1063/1.1737061. URL http://aip.scitation.org/doi/10.1063/1.1737061.

[216] J. Xie, S. Mita, Z. Bryan, W. Guo, L. Hussey, B. Moody, R. Schlesser, R. Kirste, M. Gerhold, R. Collazo, and Z. Sitar. Lasing and longitudinal cavity modes in photo-pumped deep ultraviolet AlGaN heterostructures. *Applied Physics Letters*, 102(17):171102, 2013. doi: 10.1063/1.4803689. URL http://aip.scitation.org/doi/10.1063/1.4803689.

[217] X.-H. Li, T. Detchprohm, T.-T. Kao, Md. M. Satter, S.-C. Shen, P. Douglas Yoder, R. D. Dupuis, S. Wang, Y. O. Wei, H. Xie, A. M. Fischer, F. A. Ponce, T. Wernicke, C. Reich, M. Martens, and M. Kneissl. Low-threshold stimulated emission at 249 nm and 256 nm from AlGaN-based multiple-quantum-well lasers grown on sapphire substrates. *Applied Physics Letters*, 105(14):141106, 2014. doi: 10.1063/1.4897527. URL http://aip.scitation.org/doi/10.1063/1.4897527.

[218] K. B. Nam, M. L. Nakarmi, J. Li, J. Y. Lin, and H. X. Jiang. Mg acceptor level in AlN probed by deep ultraviolet photoluminescence. *Applied Physics Letters*, 83(5):878–880, 2003. doi: 10.1063/1.1594833. URL http://aip.scitation.org/doi/10.1063/1.1594833.

[219] W. Götz, R. S. Kern, C. H. Chen, H. Liu, D. A. Steigerwald, and R. M. Fletcher. Hall-effect characterization of III–V nitride semiconductors for high efficiency light emitting diodes. *Materials Science and Engineering: B*, 59(1–3):211 – 217, 1999. doi: 10.1016/S0921-5107(98)00393-6. URL http://www.sciencedirect.com/science/article/pii/S0921510798003936.

[220] A. A. Toropov, E. A. Shevchenko, T. V. Shubina, V. N. Jmerik, D. V. Nechaev, M. A. Yagovkina, A. A. Sitnikova, S. V. Ivanov, G. Pozina, J. P. Bergman, and B. Monemar. Suppression of the quantum-confined Stark effect in $Al_xGa_{1-x}N/Al_yGa_{1-y}N$ corrugated quantum wells. *Journal of Applied Physics*, 114(12):124306, 2013. doi: 10.1063/1.4822155. URL http://aip.scitation.org/doi/10.1063/1.4822155.

[221] J. E. Northrup, C. L. Chua, Z. Yang, T. Wunderer, M. Kneissl, N. M. Johnson, and T. Kolbe. Effect of strain and barrier composition on the polarization of light emission from AlGaN/AlN quantum wells. *Applied Physics Letters*, 100(2):021101, 2012. doi: 10.1063/1.3675451. URL http://aip.scitation.org/doi/10.1063/1.3675451.

[222] Z. Mi, S. Zhao, S. Y. Woo, M. Bugnet, M. Djavid, X. Liu, J. Kang, X. Kong, W. Ji, H. Guo, Z. Liu, and G. A. Botton. Molecular beam epitaxial growth and characterization of Al(Ga)N nanowire deep ultraviolet light emitting diodes and lasers. *Journal of Physics D: Applied Physics*, 49(36):364006, 2016. doi: 10.1088/0022-3727/49/36/364006. URL http://iopscience.iop.org/article/10.1088/0022-3727/49/36/364006/.

[223] D. E. Perea, E. R. Hemesath, E. J. Schwalbach, J. L. Lensch-Falk, P. W. Voorhees, and L. J. Lauhon. Direct measurement of dopant distribution in an individual vapour-liquid-solid nanowire. *Nature Nanotechnology*, 4(5):315–319, 2009.

[224] P. Xie, Y. Hu, Y. Fang, J. Huang, and C. M. Lieber. Diameter-dependent dopant location in silicon and germanium nanowires. *Proceedings of the National Academy of Sciences*, 106 (36):15254–15258, 2009. URL www.pnas.org/content/106/36/15254.

[225] S. Zhao, A. T. Connie, M. H. T. Dastjerdi, X. H. Kong, Q. Wang, M. Djavid, S. Sadaf, X. D. Liu, I. Shih, H. Guo, and Z. Mi. Aluminum nitride nanowire light emitting diodes: Breaking the fundamental bottleneck of deep ultraviolet light sources. *Scientific Reports*, 5:8332, 2015. doi: 10.1038/srep08332. URL http://www.nature.com/articles/srep08332.

[226] S. Zhao, M. Djavid, and Z. Mi. Surface Emitting, High Efficiency Near-Vacuum Ultraviolet Light Source with Aluminum Nitride Nanowires Monolithically Grown on Silicon. *Nano Letters*, 15(10):7006–7009, 2015. doi: 10.1021/acs.nanolett.5b03040. URL http://pubs.acs.org/doi/10.1021/acs.nanolett.5b03040.

[227] M. Sakai, Y. Inose, K. Ema, T. Ohtsuki, H. Sekiguchi, A. Kikuchi, and K. Kishino. Random laser action in GaN nanocolumns. *Applied Physics Letters*, 97(15):151109, 2010. doi: 10.1063/1.3495993. URL http://aip.scitation.org/doi/10.1063/1.3495993.

[228] K. H. Li, X. Liu, Q. Wang, S. Zhao, and Z. Mi. Ultralow-threshold electrically injected AlGaN nanowire ultraviolet lasers on Si operating at low temperature. *Nature Nanotechnology*, 10 (2):140–144, 2015. doi: 10.1038/nnano.2014.308. URL http://www.nature.com/doifinder/10.1038/nnano.2014.308.

[229] S. Zhao, S. Y. Woo, M. Bugnet, X. Liu, J. Kang, G. A. Botton, and Z. Mi. Three-Dimensional Quantum Confinement of Charge Carriers in Self-Organized AlGaN Nanowires: A Viable Route to Electrically Injected Deep Ultraviolet Lasers. *Nano Letters*, 15(12):7801–7807, 2015. doi: 10.1021/acs.nanolett.5b02133. URL http://pubs.acs.org/doi/10.1021/acs.nanolett.5b02133.

[230] S. Zhao, X. Liu, S. Y. Woo, J. Kang, G. A. Botton, and Z. Mi. An electrically injected AlGaN nanowire laser operating in the ultraviolet-C band. *Applied Physics Letters*, 107(4):043101, 2015. doi: 10.1063/1.4927602. URL http://aip.scitation.org/doi/10.1063/1.4927602.

[231] A. Pierret, C. Bougerol, M. I. den Hertog, B. Gayral, M. Kociak, H. Renevier, and B. Daudin. Structural and optical properties of $Al_xGa_{1-x}N$ nanowires. *Physica Status Solidi (RRL) - Rapid Research Letters*, 7(10):868–873, 2013. doi: 10.1002/pssr.201308009. URL http://doi.wiley.com/10.1002/pssr.201308009.

[232] A. Pierret, C. Bougerol, S. Murcia-Mascarós, A. Cros, H. Renevier, B. Gayral, and B. Daudin. Growth, structural and optical properties of AlGaN nanowires in the whole composition range. *Nanotechnology*, 24:115704, 2013. doi: 10.1088/0957-4484/24/11/115704. URL http://iopscience.iop.org/0957-4484/24/11/115704/.

[233] C. Himwas, M. I. den Hertog, L. S. Dang, E. Monroy, and R. Songmuang. Alloy inhomogeneity and carrier localization in AlGaN sections and AlGaN/AlN nanodisks in nanowires with 240–350nm emission. *Applied Physics Letters*, 105:241908, 2014. doi: 10.1063/1.4904989. URL http://aip.scitation.org/doi/10.1063/1.4904989.

[234] M. Belloeil, B. Gayral, and B. Daudin. Quantum Dot-Like Behavior of Compositional Fluctuations in AlGaN Nanowires. *Nano Letters*, 16(2):960–966, 2016. doi: 10.1021/acs.nanolett.5b03904. URL http://pubs.acs.org/doi/abs/10.1021/acs.nanolett.5b03904.

[235] L. Lari, T. Walther, M. H. Gass, L. Geelhaar, C. Chèze, H. Riechert, T. J. Bullough, and P. R. Chalker. Direct observation by transmission electron microscopy of the influence of Ni catalyst-seeds on the growth of GaN-AlGaN axial heterostructure nanowires. *Journal of Crystal Growth*, 327(1):27–34, 2011. doi: 10.1016/j.jcrysgro.2011.06.004. URL http://www.sciencedirect.com/science/article/pii/S0022024811005057.

[236] R. F. Allah, T. Ben, R. Songmuang, and D. González. Imaging and Analysis by Transmission Electron Microscopy of the Spontaneous Formation of Al-Rich Shell Structure in $Al_xGa_{1-x}N$/GaN Nanowires. *Applied Physics Express*, 5:045002, 2012. doi: 10.1143/APEX.5.045002. URL http://stacks.iop.org/1882-0786/5/045002.

[237] Q. Wang, A. T. Connie, H. P. T. Nguyen, M. G. Kibria, S. Zhao, S. Sharif, I. Shih, and Z. Mi. Highly efficient, spectrally pure 340 nm ultraviolet emission from $Al_xGa_{1-x}N$ nanowire based light emitting diodes. *Nanotechnology*, 24(34):345201, 2013. doi: 10.1088/0957-4484/24/34/345201. URL http://iopscience.iop.org/article/10.1088/0957-4484/24/34/345201.

[238] R. F. Allah, T. Ben, and D. González. Structural and Chemical Evolution of the Spontaneous Core-Shell Structures of $Al_xGa_{1-x}N$/GaN Nanowires. *Microscopy and Microanalysis*, 20:1254–1261, 2014. doi: 10.1017/S1431927614000634. URL http://dx.doi.org/10.1017/S1431927614000634.

[239] E. Iliopoulos and T. D. Moustakas. Growth kinetics of AlGaN films by plasma-assisted molecular-beam epitaxy. *Applied Physics Letters*, 81(2):295–297, 2002. doi: 10.1063/1.1492853. URL http://aip.scitation.org/doi/10.1063/1.1492853.

[240] J. Arbiol, C. Magén, P. Becker, G. Jacopin, A. Chernikov, S. Schäfer, F. Furtmayr, M. Tchernycheva, L. Rigutti, J. Teubert, S. Chatterjee, J. R. Morante, and M. Eickhoff. Self-assembled GaN quantum wires on GaN/AlN nanowire templates. *Nanoscale*, 4:7517–7524, 2012. doi: 10.1039/c2nr32173d. URL http://xlink.rsc.org/?DOI=c2nr32173d.

[241] Q. Wang, H. P. T. Nguyen, K. Cui, and Z. Mi. High efficiency ultraviolet emission from $Al_xGa_{1-x}N$ core-shell nanowire heterostructures grown on Si (111) by molecular beam epitaxy. *Applied Physics Letters*, 101(4):043115, 2012. doi: 10.1063/1.4738983. URL http://aip.scitation.org/doi/10.1063/1.4738983.

[242] O. Demichel, M. Heiss, J. Bleuse, H. Mariette, and A. Fontcuberta i Morral. Impact of surfaces on the optical properties of gaas nanowires. *Applied Physics Letters*, 97(20):201907, 2010. doi: 10.1063/1.3519980. URL http://aip.scitation.org/doi/10.1063/1.3519980.

[243] C. G. Van de Walle and D. Segev. Microscopic origins of surface states on nitride surfaces. *Journal of Applied Physics*, 101(8):081704, 2007. doi: 10.1063/1.2722731. URL http://aip.scitation.org/doi/10.1063/1.2722731.

[244] M. A. Reshchikov and H. Morkoç. Luminescence properties of defects in GaN. *Journal of Applied Physics*, 97(6):061301, 2005. doi: 10.1063/1.1868059. URL http://aip.scitation.org/doi/10.1063/1.1868059.

[245] G. Jacopin, A. De Luna Bugallo, P. Lavenus, L. Rigutti, F. H. Julien, L. F. Zagonel, M. Kociak, C. Durand, D. Salomon, X. J. Chen, J. Eymery, and M. Tchernycheva. Single-Wire Light-Emitting Diodes Based on GaN Wires Containing Both Polar and Nonpolar InGaN/GaN Quantum Wells. *Applied Physics Express*, 5(1):014101, 2012. doi: 10.1143/APEX.5.014101. URL http://apex.jsap.jp/link?APEX/5/014101/.

[246] L. Rigutti, G. Jacopin, L. Largeau, E. Galopin, A. De Luna Bugallo, F. H. Julien, J.-C. Harmand, F. Glas, and M. Tchernycheva. Correlation of optical and structural properties of GaN/AlN core-shell nanowires. *Physical Review B*, 83(15):155320, 2011. doi: 10.1103/PhysRevB.83.155320. URL http://link.aps.org/doi/10.1103/PhysRevB.83.155320.

[247] S. L. Chuang and C. S. Chang. k·p method for strained wurtzite semiconductors. *Phys. Rev. B*, 54:2491–2504, 1996. doi: 10.1103/PhysRevB.54.2491. URL http://link.aps.org/doi/10.1103/PhysRevB.54.2491.

[248] K. Hestroffer, R. Mata, D. Camacho, C. Leclere, G. Tourbot, Y. M. Niquet, A. Cros, C. Bougerol, H. Renevier, and B. Daudin. The structural properties of GaN/AlN core–shell nanocolumn heterostructures. *Nanotechnology*, 21(41):415702, 2010. doi: 10.1088/0957-4484/21/41/415702. URL http://iopscience.iop.org/article/10.1088/0957-4484/21/41/415702.

[249] Q. Yan, P. Rinke, M. Scheffler, and C. G. Van de Walle. Strain effects in group-III nitrides: Deformation potentials for AlN, GaN, and InN. *Applied Physics Letters*, 95(12):121111, 2009. doi: 10.1063/1.3236533. URL http://aip.scitation.org/doi/10.1063/1.3236533.

[250] R. Ishii, A. Kaneta, M. Funato, Y. Kawakami, and A. A. Yamaguchi. All deformation potentials in gan determined by reflectance spectroscopy under uniaxial stress: Definite breakdown of the quasicubic approximation. *Physical Review B*, 81:155202, 2010. doi: 10.1103/PhysRevB.81.155202. URL http://link.aps.org/doi/10.1103/PhysRevB.81.155202.

[251] G. Jacopin, L. Rigutti, S. Bellei, P. Lavenus, F. H. Julien, A. V. Davydov, D. Tsvetkov, K. A. Bertness, N. A. Sanford, J. B. Schlager, and M. Tchernycheva. Photoluminescence polarization in strained GaN/AlGaN core/shell nanowires. *Nanotechnology*, 23(32):325701, 2012. doi: 10.1088/0957-4484/23/32/325701. URL http://iopscience.iop.org/article/10.1088/0957-4484/23/32/325701.

[252] M. Hetzl, M. Kraut, J. Winnerl, L. Francaviglia, M. Döblinger, S. Matich, A. Fontcuberta i Morral, and M. Stutzmann. Strain-Induced Band Gap Engineering in Selectively Grown GaN–(Al,Ga)N Core–Shell Nanowire Heterostructures. *Nano Letters*, 16(11):7098–7106, 2016. doi: 10.1021/acs.nanolett.6b03354. URL http://pubs.acs.org/doi/abs/10.1021/acs.nanolett.6b03354.

[253] F. Furtmayr, J. Teubert, P. Becker, S. Conesa-Boj, J. R. Morante, A. Chernikov, S. Schäfer, S. Chatterjee, J. Arbiol, and M. Eickhoff. Carrier confinement in GaN/$Al_xGa_{1-x}N$ nanowire heterostructures ($0 \leq x \leq 1$). *Physical Review B*, 84(20):205303, 2011. doi: 10.1103/PhysRevB.84.205303. URL http://link.aps.org/doi/10.1103/PhysRevB.84.205303.

[254] V. Jindal and F. Shahedipour-Sandvik. Density functional theoretical study of surface structure and adatom kinetics for wurtzite AlN. *Journal of Applied Physics*, 105(8):084902, 2009. doi: 10.1063/1.3106164. URL http://aip.scitation.org/doi/10.1063/1.3106164.

[255] C. Himwas, M. Den Hertog, F. Donatini, L. S. Dang, L. Rapenne, E. Sarigiannidou, R. Songmuang, and E. Monroy. AlGaN/AlN quantum dots for UV light emitters. *Physica Status Solidi (C)*, 10(3):285–288, 2013. doi: 10.1002/pssc.201200679. URL http://doi.wiley.com/10.1002/pssc.201200679.

[256] P. Pramanik, S. Sen, C. Singha, A. S. Roy, A. Das, S. Sen, A. Bhattacharyya, D. Kumar, and D.V. Sridhara Rao. Controlling the compositional inhomogeneities in $Al_xGa_{1-x}N/Al_yGa_{1-y}N$ MQWs grown by PA-MBE: Effect on luminescence properties. *Journal of Crystal Growth*, 439:60–65, 2016. doi: 10.1016/j.jcrysgro.2016.01.004. URL http://linkinghub.elsevier.com/retrieve/pii/S002202481600018X.

[257] L. Lymperakis and J. Neugebauer. Large anisotropic adatom kinetics on nonpolar GaN surfaces: Consequences for surface morphologies and nanowire growth. *Physical Review B*, 79(24):241308, 2009. doi: 10.1103/PhysRevB.79.241308. URL http://link.aps.org/doi/10.1103/PhysRevB.79.241308.

[258] K. Hestroffer and B. Daudin. A geometrical model for the description of the AlN shell morphology in GaN-AlN core-shell nanowires. *Journal of Applied Physics*, 114(24):244305, 2013. doi: 10.1063/1.4854495. URL http://aip.scitation.org/doi/10.1063/1.4854495.

[259] Q. Wang, X. Liu, M. G. Kibria, S. Zhao, H. P. T. Nguyen, K. H. Li, Z. Mi, T. Gonzalez, and M. P. Andrews. p-Type Dopant Incorporation and Surface Charge Properties of Catalyst-free GaN Nanowires Revealed by Micro-Raman Scattering and X-ray Photoelectron Spectroscopy. *Nanoscale*, 6:9970–9976, 2014. ISSN 2040-3372. doi: 10.1039/C4NR01608D. URL http://xlink.rsc.org/?DOI=C4NR01608D.

[260] T. Auzelle, B. Haas, M. Den Hertog, J.-L. Rouvière, B. Daudin, and B. Gayral. Attribution of the 3.45 eV GaN nanowires luminescence to inversion domain boundaries. *Applied Physics Letters*, 107(5):051904, 2015. doi: 10.1063/1.4927826. URL http://aip.scitation.org/doi/10.1063/1.4927826.

[261] M. Shahmohammadi, J.-D. Ganière, H. Zhang, R. Ciechonski, G. Vescovi, O. Kryliouk, M. Tchernycheva, and G. Jacopin. Excitonic diffusion in InGaN/GaN core–shell nanowires. *Nano Letters*, 16(1):243–249, 2016. doi: 10.1021/acs.nanolett.5b03611. URL http://pubs.acs.org/doi/10.1021/acs.nanolett.5b03611.

[262] J. Lähnemann, O. Brandt, U. Jahn, C. Roder, P. Dogan, F. Grosse, A. Belabbes, F. Bechstedt, A. Trampert, L. Geelhaar, and C. Pfüller. Direct experimental determination of the spontaneous polarization of GaN. *Physical Review B*, 86(8):081302(R), 2012. doi: 10.1103/PhysRevB.86.081302. URL http://link.aps.org/doi/10.1103/PhysRevB.86.081302.

[263] M. J. Holmes, K. Choi, S. Kako, M. Arita, and Y. Arakawa. Room-Temperature Triggered Single Photon Emission from a III-Nitride Site-Controlled Nanowire Quantum Dot. *Nano Letters*, 14(2):982–986, 2014. doi: 10.1021/nl404400d. URL http://pubs.acs.org/doi/abs/10.1021/nl404400d.

[264] S. Deshpande, T. Frost, A. Hazari, and P. Bhattacharya. Electrically pumped single-photon emission at room temperature from a single InGaN/GaN quantum dot. *Applied Physics Letters*, 105(14):141109, 2014. doi: 10.1063/1.4897640. URL http://aip.scitation.org/doi/10.1063/1.4897640.

[265] S. Fan, S. Y. Woo, S. Vanka, G. A. Botton, and Z. Mi. An $In_{0.5}Ga_{0.5}N$ nanowire photoanode for harvesting deep visible light photons. *APL Materials*, 4(7):076106, 2016. doi: 10.1063/1.4958964. URL http://scitation.aip.org/content/aip/journal/aplmater/4/7/10.1063/1.4958964.

[266] S. Zhao, S. Y. Woo, S. Md. Sadaf, Y. Wu, A. Pofelski, D. A. Laleyan, R. T. Rashid, Y. Wang, G. A. Botton, and Z. Mi. Molecular beam epitaxy growth of Al-rich AlGaN nanowires for deep ultraviolet optoelectronics. *APL Materials*, 4(8):086115, 2016. doi: 10.1063/1.4961680. URL http://scitation.aip.org/content/aip/journal/aplmater/4/8/10.1063/1.4961680.